Primary structure materials – Test results (2nd batch)

T. Batmalle, J. Berthe, P Beauchêne, V. Biasi, A. Deudon, C Huchette, P Lapeyronnie, G. Leplat,
A Mavel, G. Portemont, P. Reulet (ONERA)
A. Palacios, R. Tejerina (Airbus D&S)
J. Hodgkinson, C. Lourenço (Cranfield University)

Future Sky Safety is a Joint Research Programme (JRP) on Safety, initiated by EREA, the association of European Research Establishments in Aeronautics. The Programme contains two streams of activities: 1) coordination of the safety research programmes of the EREA institutes and 2) collaborative research projects on European safety priorities.

This deliverable is produced by the Project P7 “Mitigating Risks of Fire, Smoke and Fumes”, and aims at improving characterization capabilities and understanding with respect to the fire and high temperature behaviour of primary structure CFRP materials. Test results from a second batch of T700/M21 tests are presented in this report.

Programme Manager	Michel Piers, NLR
Operations Manager	Lennaert Speijker, NLR
Project Manager (P7)	Eric Deletombe ONERA
Grant Agreement No.	640597
Document Identification	D7.7
Status	Approved
Version	2.1
Classification	Public

This page is intentionally left blank

Future Sky Safety has received funding from the EU's Horizon 2020 Research and Innovation Programme, under Grant Agreement No. 640597.

Contributing partners

Company	Name
ONERA (DMAS)	J. Berthe, A. Deudon, G. Portemont
ONERA (DMPE)	T. Batmalle, V. Biasi, G. Leplat, P. Reulet
Cranfield University	J. Hodgkinson, C. Lourenço
Airbus D&S	A. Palacios, R. Tejerina

Document Change Log

Version	Issue Date	Remarks
1.0	22-12-2017	First formal release
2.0	29-12-2017	Second formal release
2.1	02-07-2018	Third formal release (extra test results)

Approval status

Prepared by: *(name)*	**Company**	**Role**	**Date**
Valentin Biasi, Gillian Leplat	ONERA	Main Authors	16-07-2018
Checked by: *(name)*	**Company**	**Role**	**Date**
Julien Berthe	ONERA	Quality assurance	16-07-2018
Approved by: *(name)*	**Company**	**Role**	**Date**
Eric Deletombe	ONERA	Project Manager (P7)	17-07-2018
Lennaert Speijker	NLR	Operations Manager	24-07-2018

ACRONYMS

Acronym	Definition
A/C	Aircraft (Commercial)
ASTM	American Society for Testing and Materials
CFRP	Carbon Fibre Reinforced Plastics
DSC	Differential Scanning Calorimetry
FSS	Future Sky Safety
JRI	Joint Research Initiative
P7	FSS Project n°7
PCRD	Programme-cadre de recherche et de développement:
TGA	Thermo Gravimetric Analysis
WP	Workpackage

EXECUTIVE SUMMARY

Problem Area

An objective of the Project P7 "Mitigating the risk of fire, smoke and fumes" of Future Sky Safety (FSS) is to support increasing safety - meaning here reducing the number of casualties - with respect to fire related issues (in-flight or post-crash). First, many studies on the current flights show that about 50% of the casualties in case of aircraft accidents are linked to situations where fire is involved. Hundreds of casualties could be saved per year if fire effects on the primary structure or in the cabin environment were mitigated. Second, the development of larger, more electric and more lightweight aircraft (with an increase use of Carbon Fibre Reinforced Plastics (CFRP) composite parts in aircraft design, such as fuselage panels, engine carters, engine exhausts,… *etc*) raises several safety questions with respect to unknown behaviours of the materials and structures when exposed to fire. But the scope of this problem is large, embracing a variety of problems and solutions: the use of fireproof and less toxic materials, the early detection of fire, the simulation of passengers' evacuation,… etc. In the FSS research programme, it was decided to address the fire issue as part of Theme 4: "Building the Ultra-resilient Vehicles". It means that the research work is focused on material and structural questions, and aims at mitigating fire related safety risks when/by introducing new generation of materials in future aircraft design (incl. possible eco-friendly ones). Considering this focus, it must be noticed that very few test results are available today to the research community, because of evident costs (test facilities, destructive tests, specimens and sensors) and industry confidentiality reasons. A large part of the project P7 – to which this deliverable relates - is dedicated to develop and share experimental testing facilities and test results, with a clear partnership added value between EU Research Establishments, Academia and Industry being reached.

For new aircraft concepts, the application of CFRP is considered in the primary structure of the wing and the fuselage. Such airplane exhibits novel or unusual design features leading to a gap with the technology envisioned in the airworthiness standards dedicated to transport category airplanes. A specific concern is for safety issue pertaining to aircraft passengers with respect to crashworthiness and to fire behaviour of composite materials. Enhancing the understanding of aircraft fire performance guarantees aircraft occupants a significant safety increase to come out unharmed in case of fire incident or in crash situation. More particularly, occupant safety improvements with regard to evacuation when engine kerosene fire is developing outside will be linked to an enhancement of knowledge about the carbon epoxy materials behaviour and degradation under severe temperature conditions and fire exposure. In terms of fumes toxicity, self-estinguishibility and heat generation, the use of carbon epoxy composite materials for primary structures not only brings specific questions regarding the passengers safety, but also regarding the rescue team efficiency and safety. In terms of structures design, it is crucial to accurately understand and compare the safe, damaged (impact, crash) and decomposed (fire) materials performances, in terms of mechanical strength (load carrying) and fireproof-ness.

Future Sky Safety has received funding from the EU's Horizon 2020 Research and Innovation Programme, under Grant Agreement No. 640597.

Description of Work

The objective of FSS P7 work package WP7.1 "Understanding and characterising the fire behaviour of primary structure composite materials (epoxy resins, standard CFRP)" is to enhance knowledge concerning the fire behaviour and performance of CFRP primary structure composite materials, in order to better predict safety and survivability issues in case of fire incident or post-crash situation. Such predictions rely on physical models and numerical tools which need to be developed based on exhaustive materials (characterisation) and components (validation) experimental testings. Moreover, WP7.1 produces a comprehensive experimental database for a reference material to be shared by the European research community as a basis for material model development of the fire behaviour and degradation of CFRP materials. The T700GC/M21 material has been proposed to be used in this WP7.1 because a lot of published results already exist about its standard mechanical behaviour which the project can build on. For this purpose, existing testing protocols have to be adapted, improved or invented. FSS P7 deliverable D7.1 "Plan of Experiments – Primary Structures Materials – Final Requirements, Selection and Specification of Materials and Tests" [1] includes a list of complementary tests which could be developed and performed to complete an already existing database with respect to:

- Mechanical and thermo-mechanical properties of virgin and charred material,
- Dynamic degradation phenomena (incl. ignition of combustible gases inside the CFRP laminate) during the fire exposure time,
- Fire resistance of damaged composite panels to direct exposure to flame impact.

This report presents the test results from a second batch of T700/M21 tests.

Results & Conclusions

In the last past years, ONERA has developed a test facility to provide thermo-physical properties characterisation of anisotropic materials. Especially, it can assess simultaneously the specific heat and the 3 main components of the thermal conductivity tensor as a function of temperature. It is based on thermographic measurements of the material thermal response subjected to a pure radiative laser heating. The test facility was carried out on the selected T700GC/M21 CFRP material that was studied in 2 stacking sequences to identify properties at the virgin state (i.e. below glass transition and pyrolysis thresholds) and above.

In precedent studies, the thermal decomposition of epoxy matrix reinforced by carbon fibre composite materials had been performed at ONERA. Three main chemical reactions had been identified: pyrolysis of the matrix, oxidation of the char produced by the pyrolysis of the matrix and oxidation of the fibres. To succeed in, Thermo Gravimetric Analysis (TGA) and Differential Scanning Calorimetry (DSC) experiments had been carried out in order to identify a thermal degradation model adapted to composite materials. In this deliverable, the complementary TGA results for the material manufactured and provided by CEiiA are under the scope.

Heating rates of TGA measurements have also been extended to reach thermal loads of the same order of magnitude than those experienced during a fire event. Kinetic modelling assessed at low heating rates is confronted to high heating rates measurements and shows a significant local thermal non-equilibrium that requires measurements to be analysed out of the conventional thermally thin assumption.

Thermal properties of the CFRP had been assessed experimentally in the previous deliverable for the virgin state of the material onto a temperature range where any chemical reaction is avoided. Complementary TGA measurements have provided kinetic modelling for defining a preparation protocol to reach a fully charred (pyrolysed) state of the material. The protocol has been successfully carried out and thermal characterisations of the charred state have been performed and are presented in this deliverable.

Laser induced decomposition has been developed at ONERA to analyse the thermal response of composite material subjected to a pure radiative heat load. Such original approach can provide relevant information about the material behaviour without any uncertainty regarding the heat flux distribution and its nature. Actually, a fire event induces a heat flux at the material surface the time and space distribution of which is very difficult to assess. Using a stable and coherent heat source provides a very accurate heat flux on the material surface so that the thermal response can be analysed confidently. The experimental facility offers also well controlled boundary conditions, non-intrusive and accurate temperature measurements and avoids any combustion of volatiles that can affect the material behaviour. Results are presented for different heat flux magnitudes and different laser exposure periods.

Applicability

The obtained test results are complementary to existing ones on T700GC/M21 which are available in the open literature. Once published in journal papers, they will permit code developers (academic) and users (industry) to:

- get input data for numerical simulations,
- address the question of the validity of the state-of-the-art models they apply (capability to reproduce the observed phenomena),
- propose future developments where lacks are identified.

Finally, the composite structures design capabilities could be improved either through increase of confidence in the existing tools, or thanks to new developments based on the so-gained knowledge.

This page is intentionally left blank

Future Sky Safety has received funding from the EU's Horizon 2020 Research and Innovation Programme, under Grant Agreement No. 640597.

TABLE OF CONTENTS

LIST OF FIGURES

LIST OF TABLES

Future Sky Safety has received funding from the EU's Horizon 2020 Research and Innovation Programme, under Grant Agreement No. 640597.

1 INTRODUCTION

1.1. The Programme

Horizon 2020 is the biggest EU Research and Innovation platform ever with nearly €80 billion of funding available over 7 years (2014 to 2020) – in addition to the private investment that this money will attract. Within this frame, EREA, the association of European Research Establishments in Aeronautics has proposed Future Sky program: a Joint Research Initiative in which development and integration of aviation technologies is taken to the European level. Future Sky is based on the alignment of national institutional research for aviation by setting up joint research programs: the first one to be launched in 2015 was the Future Sky Safety programme (http://www.futuresky.eu/projects/safety), because safety is a transverse domain of common interest to all stakeholders and with reduced competitive aspects. Four themes and seven projects (5 have already started) were identified (Runway Excursions, Total System Risk Assessment, Human Performance Envelope, Organizational Accidents, and Fire Smoke and Fumes). The work presented in this document belongs to the P7 project “Mitigating Risks of Fire, Smoke and Fumes”.

1.2. Project context

The reason of the “Mitigating Risks of Fire, Smoke and Fumes” project proposal came from the development of larger, more electric and more lightweight aircraft (with an increase use of CFRP composite parts in A/C design, such as fuselage panels, wings, engine carters, engine exhausts,… etc). Such airplane exhibits novel or unusual design features leading to a gap with the technology envisioned in the airworthiness standards dedicated to transport category airplanes, which also raises several safety questions with respect to unknown behaviors of the materials and structures. A specific concern is for safety issue pertaining to aircraft passengers with respect to crashworthiness and to fire behavior of composite aircraft structures. But the scope of this problem is large, embracing a variety of problems and solutions: the use of fireproof and less toxic materials, the early detection of fire, the simulation of passengers’ evacuation, etc. And few researches have been funded yet by the EU commission on this subject. It was decided to address the fire issue in the FSS research program as part of Theme 4: “Building the Ultra-resilient Vehicles”. It means that the research work focuses on material and structural questions, and aims at mitigating fire related safety risks when/by introducing new generation of materials in future aircraft design (incl. possible eco-friendly ones).

Enhancing the understanding of aircraft fire performance guarantees aircraft occupants a significant safety increase to come out unharmed in case of fire incident or in crash situation. More particularly, occupant safety improvements with regard to evacuation when engine kerosene fire is developing outside will be linked to an enhancement of knowledge about the carbon epoxy materials behavior and degradation under severe temperature conditions and fire exposure. In terms of fumes toxicity, self-extinguishibility, heat generation and degradation products under elevated temperature or fire exposure, the use of composite materials in cabin environment also brings specific questions regarding passengers

and crew safety. Beside of this some concerns also exist about the impact of various innovations on on-board air quality. Multiple investigations have been carried out on hypothetical air contamination by oil ingredients and on the potential impact of such contamination on occupants' health, both in short term and in long term. The more general question of any possible kinds of impact on on-board air quality then raised, that can be due for instance to the introduction of new materials in the design that could react with more and more electrical heating or new engine systems.

The objectives of the EU in terms of increasing air transport safety are reminded in the annual EASA Safety Plan. In this perspective, the P7 objective is to contribute to the reduction of the number of air transport casualties with respect to fire related issues (in-flight or post-crash). Indeed many studies show that about 50% of the fatalities in case of aircraft accidents are linked to situations where fire is involved. Many casualties could be prevented per year if fire effects on the primary structure or in the cabin environment were mitigated.

In this context, the mechanical behavior and decomposition of organic matrix and carbon fibres of composite materials at elevated temperature or under fire exposure have to be better known, for safety reasons and also health (onboard air quality) issues. Improved material solutions (for primary structures or cabin environment) should also be proposed when needed.

The P7 project "Mitigate risks of fire, smoke and fumes" [2] addresses on the one hand effects of fire on materials (production of heat, toxic fumes and smokes), and on the other hand effects of fire on structures (burnthrough, strength) that can endanger the passengers' life directly (exposure) or indirectly (evacuation). The scope of the works covers both primary structures materials (e.g. epoxy resin, carbon fiber reinforced polymers) and cabin materials (e.g. phenolic polymers, glass fiber reinforced plastics). The P7 project has been split into three work packages according to the expected impacts that were claimed for this 3 years research work:

- WP7.1: the first work package aims at improving the knowledge about effects of fire on materials and structures. It would mainly concern standard epoxy resins and carbon fibers reinforced polymer materials (primary structures),
- WP7.2: the second work package aims at proposing improved materials solutions, mainly to mitigate fire, smoke and fumes. It would concern new materials (primary structures and cabin), the properties of which will be compared to standard ones,
- WP7.3: the third work package aims at analyzing possible effects on the on-board air quality that the introduction of such new materials in the aircraft structure and cabin could have.

The FSS P7 project is led by ONERA, as its experience covers both Crash and Fire worthiness of A/C composite materials and structures. ONERA also leads the first work package which aims at better understanding and characterizing the fire and high temperature behavior of primary structure CFRP materials. DLR leads the second work package which is dedicated to the improvement of current material solutions to mitigate fire, smoke and fumes in the cabin environment. Last, NLR leads the third work package where objectives are to study the indirect effects of such new materials, technologies and fuel

systems on the on-board aircraft air quality. Bridges between the different tasks and partners are implemented by CEIIA (WP 7.1 and WP7.3), VZLU (WP7.2) and Cranfield University (WP7. 1 and WP7.3), and access to the industry is reached in all tasks thanks to the contribution of Airbus-military (AIRBUS D&S, WP7.1), ALENIA (WP7.2) and EMBRAER (WP7.1 and WP7.3) companies. The overall project consistency will be increased by CAA UK providing regulatory advice and guidance to all the project tasks.

1.3. Research objectives

The objective of FSS P7 work package WP7.1 "Understanding and characterising the fire behaviour of primary structure composite materials (epoxy resins, standard CFRP)" is to enhance knowledge concerning the fire behaviour and performance of CFRP primary structure composite materials, in order to better predict safety and survivability issues in case of fire incident or post-crash situation. Such predictions rely on physical models and numerical tools which need to be developed based on exhaustive materials (characterisation) and components (validation) experimental testing. The objective of WP7.1 is to produce a comprehensive experimental database for a reference material to be shared by the European research community as a basis for material model development of the fire behaviour and degradation of CFRP materials. The T700GC/M21 material has been proposed to be used in this WP7.1 because a lot of published results already exist about its standard mechanical behaviour which the project can build on.

Earlier work in FSS WP7.1 included a list of complementary tests which could be developed and performed to complete the already existing database with respect to:

- Mechanical and thermo-mechanical properties of virgin and charred material,
- Dynamic degradation phenomena (incl. ignition of combustible gases inside the CFRP laminate) during the fire exposure time,
- Fire resistance of damaged composite panels to direct exposure to flame impact.

This objective of this study is to present the test results from a second and complementary batch of T700GC/M21 tests.

1.4. Approach

The objective of WP7.1 is to enhance knowledge concerning the fire behavior and performance of CFRP primary structure composite materials, in order to better predict safety and survivability issues in case of fire incident or post-crash situation. Such predictions rely on physical models and numerical tools which need to be developed based on exhaustive materials (characterization) and components (validation) experimental testings. The objective of WP7.1 is also to produce a comprehensive experimental database for a reference material to be shared by the European research community as a basis for material model development of the fire behavior and degradation of CFRP materials. The T700GC/M21 material has been proposed to be used in this WP7.1 because a lot of published results already exist about its standard mechanical behavior which the project can build on. Partners' state-of-the-art models and simulation

tools will be assessed according to this comprehensive set of experimental data. FSS P7 WP7.1 was split into 3 tasks:

- T7.1.1. Definition of tests, manufacturing of test coupons and panels, preparation of tests (incl. instrumentation), led by CEiiA (see deliverable FSS P7 D7.1)
- T7.1.2. Test and model the thermo-chemical, thermo-physical and thermo-mechanical properties of composite materials according to temperature, fire exposure (time), and material state (virgin and charred), led by ONERA,
- T7.1.3. Test and model resilience to temperature/fire effects at structural levels (incl. on damaged panels), led by CASA.

The present FSS P7 D7.4 deliverable "Primary structure materials – Test results (second batch)" refers to task T7.1.2 of WP7.1.

1.5. Structure of the document

The introduction being done, the next sections of the document are sub-divided according to the following topics:

- Kinetic properties characterising the decomposition reactions the material undergoes as a function of temperature, gas atmospheres, heating rates and the associated energies involved in each reaction;
- Protocol definition for preparation and conditioning of homogeneously charred test specimens;
- Thermo-physical properties (specific heat and thermal conductivity tensor) at the charred state and as a function of temperature;
- Thermal behaviour under laser-induced decomposition.

In precedent studies [5], the thermal degradation of epoxy matrix reinforced by carbon fibre composite materials had been performed at ONERA. During these studies, three main chemical reactions had been identified: pyrolysis of the matrix, oxidation of the char produced by the pyrolysis of the matrix and oxidation of the fibres. To succeed in, TGA and DSC experiments had been carried out in order to identify a thermal degradation model adapted to composite material. In this deliverable, complementary and exhaustive TGA results for the material manufactured and provided by CEiiA are presented.

In the last past years, ONERA has developed a test facility to provide thermo-physical properties characterisation of anisotropic materials. Especially, it can assess simultaneously the specific heat and the 3 main components of the thermal conductivity tensor as a function of temperature. It is based on thermographic measurements of the material thermal response subjected to a pure radiative laser heating. The test facility was carried out on the selected T700GC/M21 CFRP material studied considering 2 stacking sequences (unidirectional and quasi-isotropic laminates). Properties have been identified at the

virgin state (*i.e.* below glass transition and pyrolysis) in the previous deliverable (D7.4 [10]). This second technical report is dedicated to the assessment of the properties of the charred state only. The preparation protocol to get the fully charred test specimen will be defined.

The same experimental facility can also be used to analyse the thermal response during decomposition of charring materials subjected to the laser heating at high power. Dedicated but similar specimens are tested from the room temperature at the virgin state. Different heat flux magnitudes, exposure durations, stacking sequences are investigated in order to cover the whole behavioural range of the material subjected to significant heat loads.

2 MATERIAL

The study is focused on one material used in the aeronautical industry for primary and secondary aircraft structures. The T700GC/M21 is a composite laminate made of carbon fibres (T700GC by TORAY) and epoxy resin reinforced by thermoplastic nodules (M21 by HEXCEL).

Plies of M21 / 35% / 268 / T700GC unidirectional, $260\ \mu m$-thick, prepregs are stacked and cured to provide the different composite laminates studied hereafter.

The material density is given at the virgin state: $\rho = 1580\ kg/m^3$.

Fibres average diameter is $7\ \mu m$ and the volume fraction of fibres is 0.567 for the cured material. The final laminate thickness is about $2.08 - 2.10\ mm$ for 8 ply laminates and $4.16 - 4.20\ mm$ for 16 ply laminates.

CEiiA was in charge of manufacturing T700GC/M21 plates for ONERA. They were provided to ONERA in December 2015.

3 THERMO-GRAVIMETRIC ANALYSIS

3.1. Approach description and associated technical objectives

TGA measurements correspond to the first test phase when investigating thermal behaviour and stability of composite materials. Such tests are performed at the condensed matter scale regarding few mg and mm of material. The objective is the assessment of physical quantities such as:

- mass loss and mass loss rate as a function of temperature, atmosphere and heating rates;
- number of decomposition reactions;
- temperature onset;
- residual mass;
- reaction enthalpies (if combined with DSC).

The analysis of the physical quantities measured with the device provides important information about:

- thermo-chemical kinetics defining each reaction with Arrhenius equations and associated parameters;
- thermally thin assumption validity with respect to the heating rate;
- isothermal preparation protocols to reach specific decomposition state of the material for thermal properties characterisation.

3.2. Experimental apparatus and data analysis tools

3.2.1. TGA/DSC

Measurements are performed with a METTLER TOLEDO TGA/DSC3+ device. It combines a conventional but very accurate thermo-gravimetric analyser with a differential scanning calorimetric sensor onto the weighing module in order to assess simultaneously the mass loss and the reaction enthalpies during the decomposition process. However, the accuracy of the DSC measurement with METTLER TOLEDO TGA/DSC3+ coupled device is lower than with conventional dedicated DSC devices ($\pm 10\,\%$) but the measurement is directly correlated to the mass loss onto the full range of temperature up to $1100\,°C$.

Figure 1 - METTLER TOLEDO TGA/DSC3+ device

3.2.2. Adethec

Adethec is a toolbox developed at ONERA to analyse and model thermo-chemical reactions occurring in a decomposing material from TGA and DSC signals measured using the METTLER-TOLEDO TGA/DSC3+ device. Adethec is developed in Python using the Qt graphic library and consists of three stackable and movable sub-windows: a database detailing all experimental conditions, a plot zone and a parameters' selection zone (cf. Figure 2). The database is composed of the TGA and DSC experimental measurements. From a set of experiments selected by the user, four main functions are available:

- A simple plot function that can plot the mass loss, relative mass loss, mass loss rate or the calorimetric signal. Smoothing functions and buoyancy compensation (if measured) can be performed;
- A DSC analyser to integrate reaction enthalpies from the calorimetric signal, where minimum and maximum integration temperatures are specified by sliders. Different methods are available to evaluate the baseline calorimetric signal.
- A TGA fitting function from a user-defined set of reactions. The user can define a set of n solid species and m reactions. Each species is defined by its initial mass fraction and each reaction is defined by one solid reactant R and one optional solid product P. All remaining products are gases G and are assumed inert. The mass stoichiometric coefficient ν defines the mass fraction of a solid reactant transformed into a solid product as described by the following equation:

$$R \rightarrow \nu P + (1-\nu)G$$

Each reaction can be either oxidative (activated by the presence of O_2) or not, and is modelled with Arrhenius kinetics model using a set of (A, E_A, n) parameters as:

$$\frac{\partial Y_{ij}}{\partial t} = -A.\exp\left(-\frac{E_A}{RT}\right).Y_{ij}^{n}$$

where Y_{ij} is the mass fraction of the species i involved as reactant in the decomposing reaction j. From a set of thermally activated reactions, the total mass fraction rate of the species i is determined by:

$$\frac{\partial Y_i}{\partial t} = \sum_{j=1}^{m} \frac{\partial Y_{ij}}{\partial t} - \sum_{k=1}^{m} \nu_k \frac{\partial Y_{ik}}{\partial t}$$

where the first term represents the contributions of reactions where i is a reactant and the second term represents the contributions where i is a product. The total mass loss m/m_0 can be detailed as:

$$\frac{m}{m_0} = \sum_{i=1}^{n} Y_i$$

The set of m parameters interacting with n solid species is expressed as a set of differential equations solved in Adethec by a 2nd order Runge-Kutta method. The set of Arrhenius parameters $(A,\ E_A,\ n)_j$ is optimised by a bounded quasi-Newton method in order to have the best fit between the model and the experimental results.

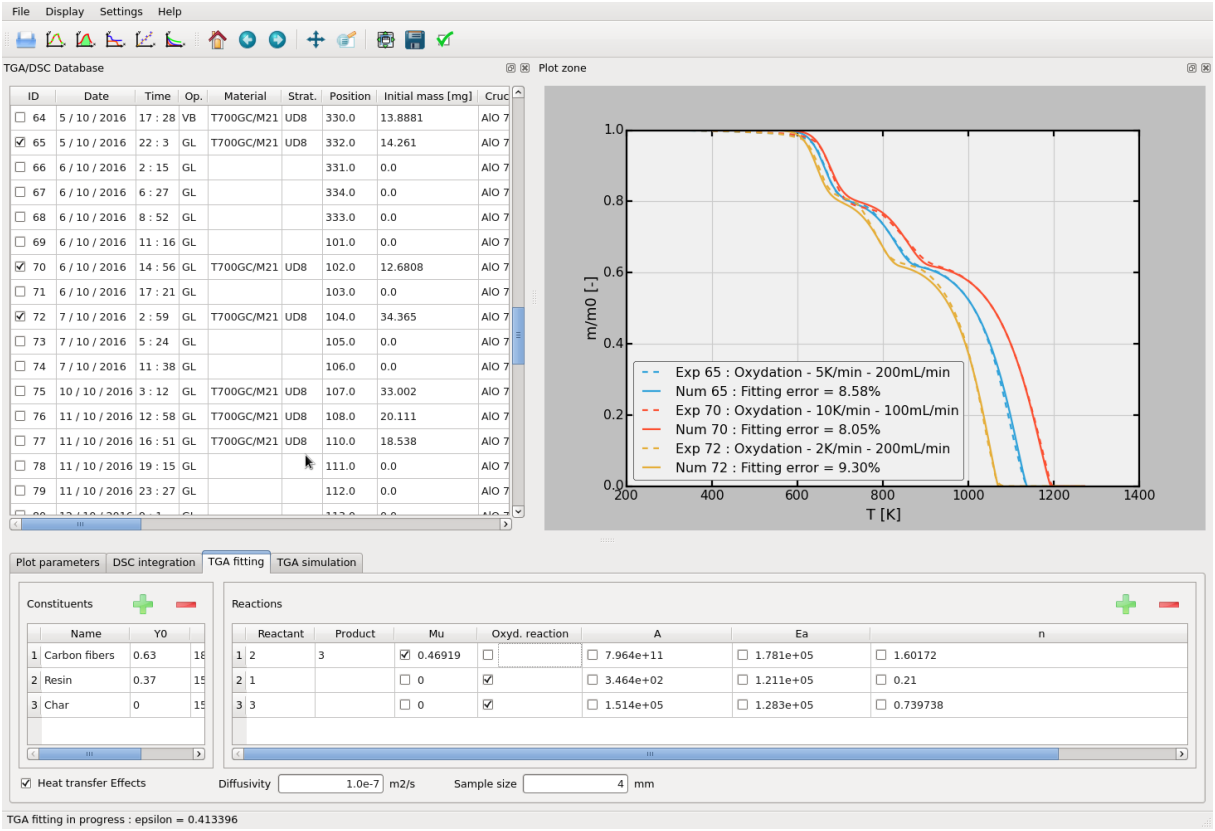

Figure 2 - Screenshot of Adethec graphic user interface for TGA fitting of a carbon-epoxy composite laminate decomposition under air atmosphere using a 3-stage Arrhenius model (Resin pyrolysis into char > Char oxidation > Fibre oxidation)

3.2.3. Fast TGA

In order to check the validity of the model presented in the next section (§3.2.2) for high temperature ramps, experiments have been performed on the ONERA Fast-TGA apparatus (Figures 3-4). By this device, it is possible to heat small samples in inert environment (Helium, nitrogen or vacuum) up to 100°C/s and to measure the evolution of the mass loss as function of the temperature applied thanks to on the hang-down design. This system provides the highest level of stability and the best limit of detection. The furnace is in graphite and uses Joule heating principle to apply the temperature on the coupon. The measure the temperature is achieved by a thermocouple positioned close to the sample (Figures 4). It is important to notice that due the heating ramp, the temperature in the sample could not be considered as homogeneous and 3D simulations are mandatory to compare the model proposed in the previous section with the experimental data obtained by this technic.

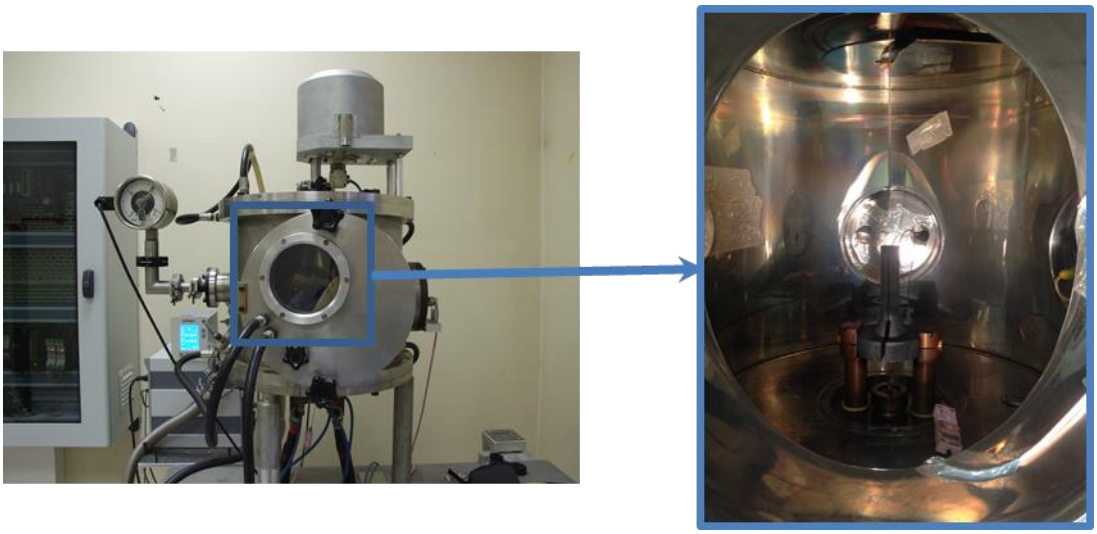

Figure 3 – Fast ATG apparatus developed at Onera

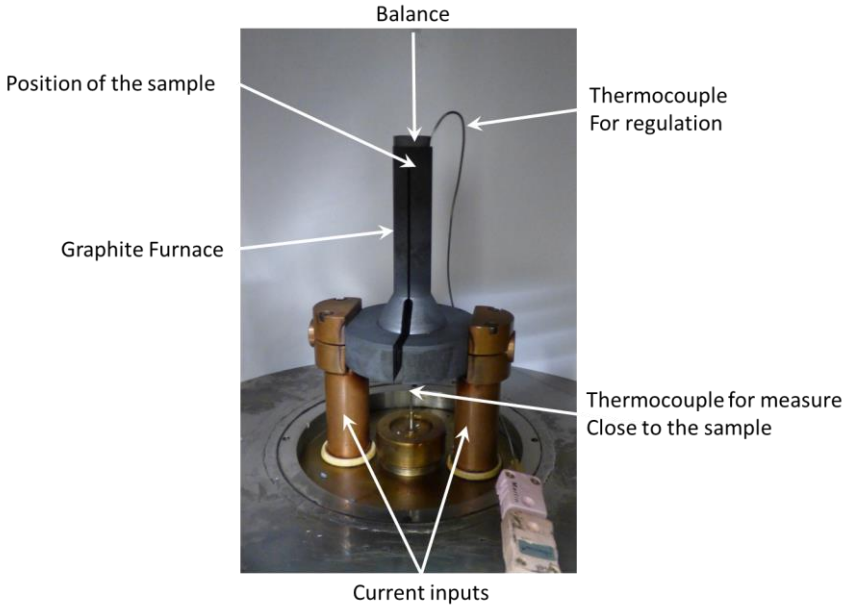

Figure 4 – Fast ATG apparatus developed at Onera : description of the graphite furnace and the principle of the measure

3.3. Experimental results analysis

3.3.1. Under inert atmosphere

Figure 5 shows relative mass loss (m/m_0) as a function of temperature resulting from thermo-gravimetric analyses under inert atmosphere (N_2) at different heating rates ($2, 5$ and $10K/\text{min}$). The studied material is a carbon/epoxy laminate whose commercial name is T700GC/M21. Figure 6 shows results of normalized mass loss rate, named hereafter MLR, and assessed using the following relation:

$$MLR = -\frac{1}{m_0}\frac{\partial m}{\partial T}$$

where m is the mass, m_0 the initial mass and T the temperature. Each TGA experiment is repeated twice and exhibits a very satisfying reproducibility, except after $900K$ where unexpected mass losses are measured, probably due to low oxidative gas flow during the experiments or to the release of O_2 by the material itself at high temperature. Mass loss rates shows only one global reaction around $T = 650\ K$ and transforming 23% of the solid material into gaseous species. The MLR plots point out one global reaction and confirm that the occurring reaction is very reproducible.

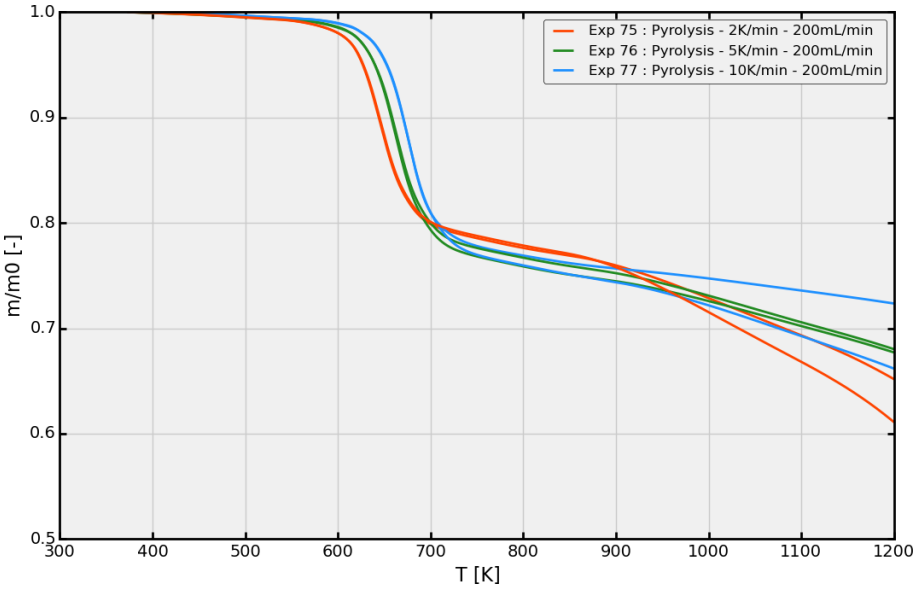

Figure 5 - Relative mass loss reproducibility in N_2 atmosphere at $2, 5$ and $10K/min$

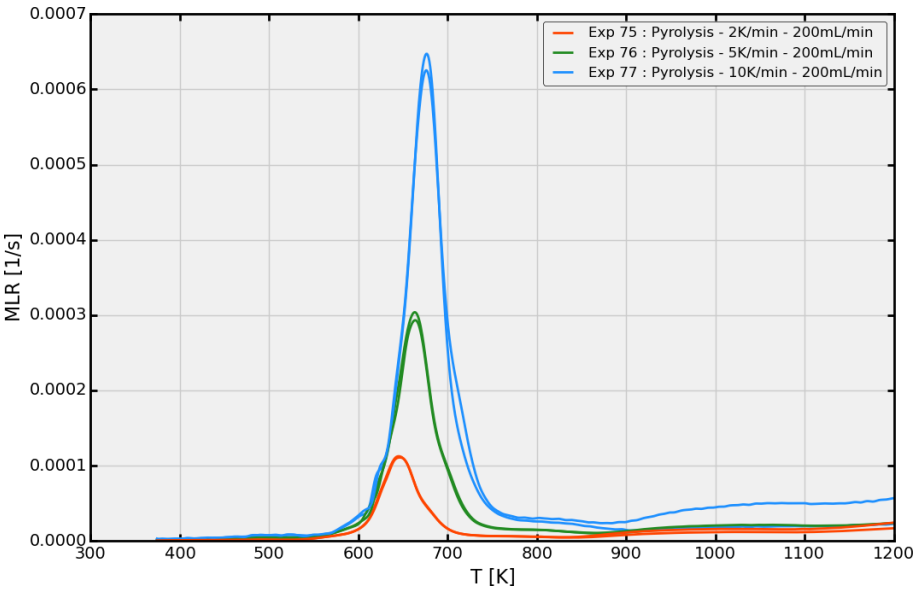

Figure 6 - Mass Loss Rate reproducibility in N_2 atmosphere at $2, 5$ and $10K/min$

Figure 7 shows the results of heat flux signal (HF) during DSC analyses under N_2 atmosphere at $2,\ 5$ and $10K/\text{min}$. Duplicate measurements have been performed but are not plotted here. Integration of heat flux signals provides reaction energies occurring in a decomposing material using the following relation:

$$Q_{reac} = \frac{1}{m_0}\int_{T_i}^{T_f} (HF(T) - HF_{base}(T))\, dT$$

where T_i is the lower temperature integration bound and T_f the higher temperature integration bound of the considered reaction. HF_{base} represents the baseline heat flux signal (without any reaction), evaluated with a spline based on HF (dashed lines) between T_i and T_f. Figure 7 shows that one reaction energy can be identified by DSC analysis under inert atmosphere, associated to the pyrolysis reaction and with a relatively low value. The low signal shows a high uncertainty due to the signal noise of the DSC sensor. The reader can note that standard DSC sensors have better precisions than DSC sensors embedded in a TGA/DSC apparatus. Quality of DSC signals can be improved by a standardised method for coupon preparation (similar masses and shapes) in order to have better contact quality between the coupon and the thermocouple sensors within the crucible. In practice, high precision machining for CFRP is very hard to obtain on such millimetric disc-shaped samples.

The average value of the pyrolysis reaction energy for the set of analyses is:

$$Q_{pyro} = 2.9 \times 10^4 kJ/kg$$

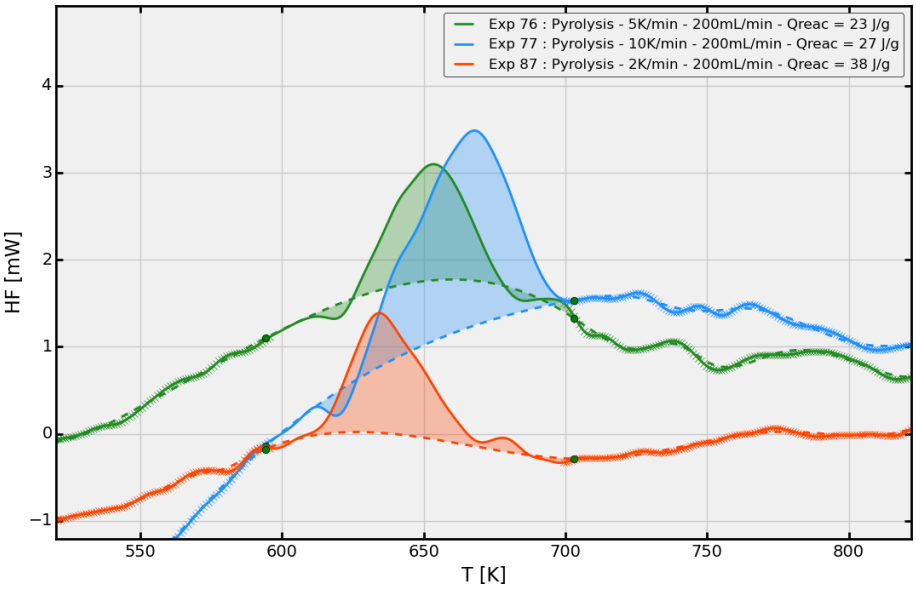

Figure 7 - DSC signal in N_2 atmosphere at $2,5$ and $10K/min$

3.3.2. Under oxidizing atmosphere

Figure 8 and Figure 9 plot reproducibility TGA tests in air atmosphere in the same plot style as previously. Figure 8 shows the relative mass loss (m/m_0) and Figure 9 exhibits the MLR as a function of temperature for different heating rates ($2,5$ and $10K/\text{min}$). 3 successive decomposition reactions occur when the temperature increases. The first reaction occurs around $650K$ and seems similar to the pyrolysis reaction under inert atmosphere. However, the relative mass loss is slightly lower than the one in inert atmosphere (20% instead of 23%). The second reaction takes place at around $800K$ and represents a relative mass loss of 18%. Finally, the third reaction decomposes the total remaining mass of the composite material at around $1100K$. Reproducibility of these TGA analyses is very satisfying, despite the relative mass loss after the first reaction that differs by 3%.

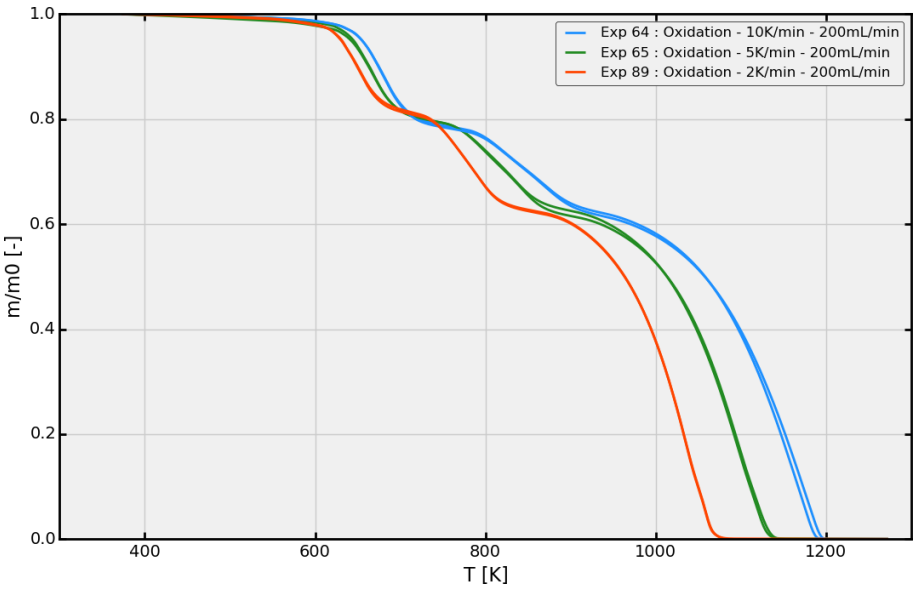

Figure 8 - Relative mass loss reproducibility in air atmosphere at $2, 5$ and $10 K/min$

MLR curves on Figure 9 reveal that the 3 global reactions could be divided into sub-reactions, as the multiple peaks for each global reaction shows.

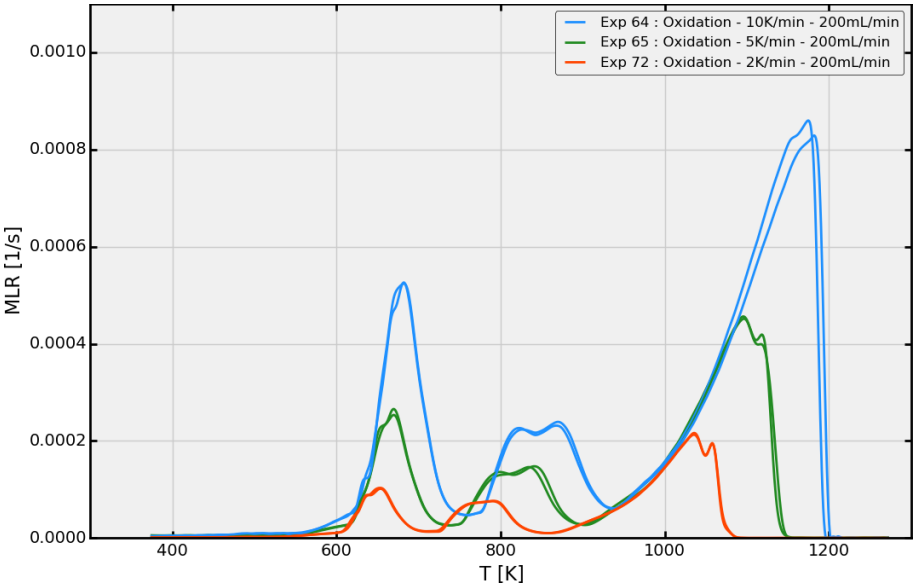

Figure 9 - Mass Loss Rate reproducibility in air atmosphere at $2, 5$ and $10 K/min$

Figure 10 shows the results of the DSC analyses under air atmosphere at different heating rates ($2,\ 5$ and $10\ K/min$). Only the 2 last reactions can be noticed in heat flux curves as the first pyrolysis

reaction has very low reaction energy (cf. previous section). The integration of HF curves in oxidizing atmosphere allows to evaluate the reaction energy of the 2 oxidation reactions:

$$Q_{oxy1} = 2.65 \times 10^6\ J/kg$$

$$Q_{oxy2} = 9.85 \times 10^6\ J/kg$$

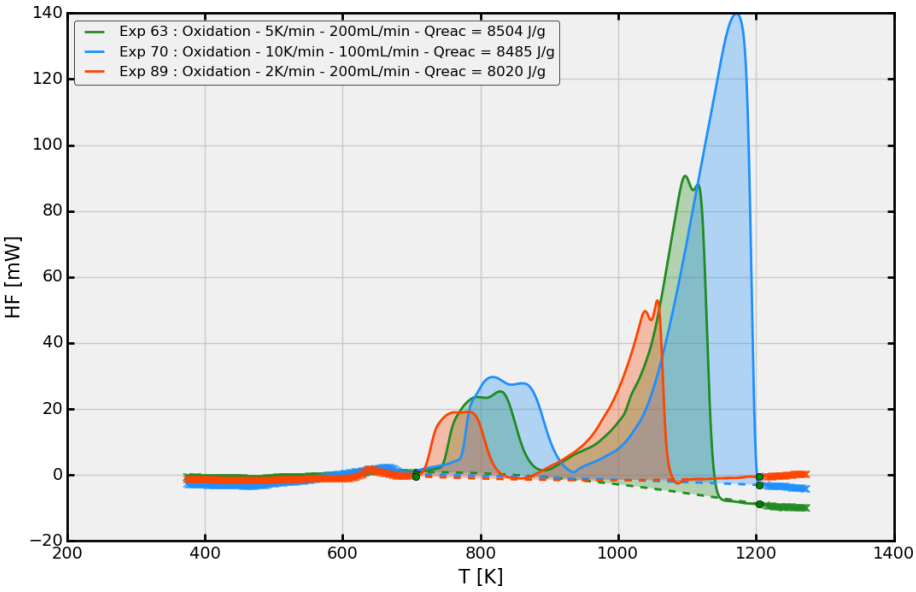

Figure 10 - DSC signal in air atmosphere at $2, 5$ and $10 K/min$

3.3.3. Under dual atmosphere: inert then oxidative

Figure 11 and Figure 12 show relative mass loss and MLR in a specific case where the atmosphere changes during the analysis. For the experiment, the environment atmosphere surrounding the sample material is switched from N_2 under $T = 720\ K$ to air above. This unusual protocol, named *pyroxy*, is plotted with equivalent analyses under classical N_2 and air atmospheres.

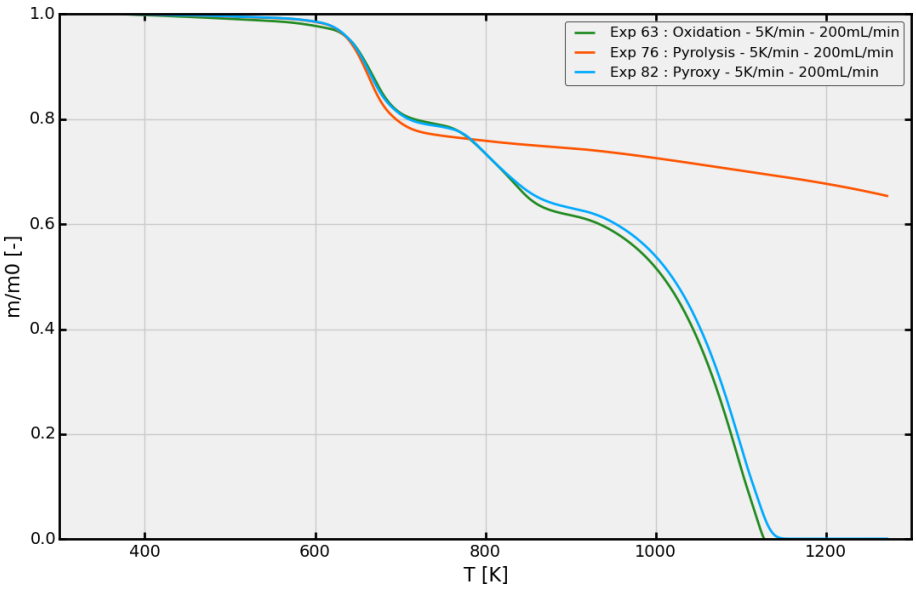

Figure 11 - Relative mass loss at $5K/min$ in dual atmosphere (inert then oxidative), compared to standard N_2 and air atmospheres

The *pyroxy* analysis shows that the first reaction is identical than the first reaction under and close to the single reaction in inert atmosphere. The pyrolysis mass loss curve points out a slightly different intermediate mass loss but this is probably due to differences of the resin/fibres ratio of the sample materials. Basically, the kinetic of the first decomposition reaction is similar whether the atmosphere is oxidative or inert. The next reactions in oxidative atmosphere have the same kinetic parameters, demonstrating that intermediate products can be considered as equivalent whatever the atmosphere.

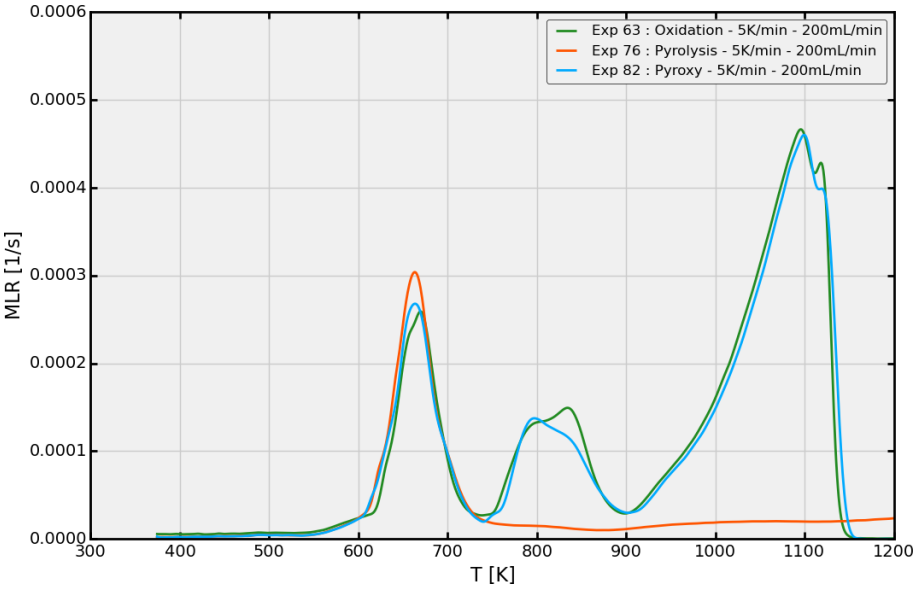

Figure 12 - Mass Loss Rate at $5K/min$ in dual atmosphere (inert then oxidative), compared to standard N_2 and air atmospheres

3.3.4. Under inert atmosphere at high temperature ramp

In order to evaluate the influence of high temperature rates on the thermal degradation, 6 coupons have been tested at 3 different heating rates. The test matrix is presented in Table 1. This table reports the geometry of the coupons, the heating rate and the sample mass before and after the test. For tests #1 and #3, the coupon is dropped during the test and it then impossible to measure its final mass. Nevertheless, the evolution of the mass loss before the drop has been monitored.

Coupon reference	Stacking sequence	Dimensions [mm^3]	Heating ramp [K/min]	m_0 [mg]	m_f [mg]	Δm [mg]
3809A_FSS_P7_P206-01_SS02#01	$[0]_8$	$5 \times 4.5 \times 2.23$	300	69.0	4.1	-
3809A_FSS_P7_P206-01_SS02#02	$[0]_8$	$5 \times 4.5 \times 2.23$	600	73.2	49.5	23.7
3809A_FSS_P7_P206-01_SS02#03	$[0]_8$	$5 \times 4.5 \times 2.23$	1200	75.7	0.2	-
3809A_FSS_P7_P206-01_SS02#04	$[0]_8$	$5 \times 4.5 \times 2.23$	300		48.1	21.4
3809A_FSS_P7_P206-01_SS02#05	$[0]_8$	$5 \times 4.5 \times 2.23$	300		49.9	22.5
3809A_FSS_P7_P206-01_SS02#06	$[0]_8$	$5 \times 4.5 \times 2.23$	600		46.5	21.7

Table 1 – Test matrix for Fast ATG tests

Due the thermal degradation, the initial geometry of the coupon is highly modified. A pristine and degraded coupon is presented on Figure 13. We can observe a high expansion of the volume and a collapse of the coupon due to pyrolysis of the matrix and the formation of char and voids.

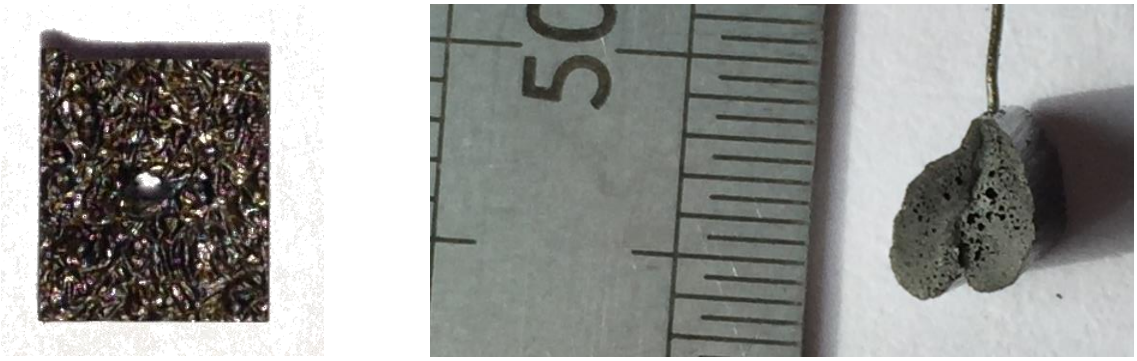

Figure 13 – Pristine coupon in T700GC/M21 and after fast ATG tests

Figures 14-15- present impose the time evolution of the setpoint temperature and the temperature measured close to the coupon for the different coupons. We can observe a very good repeatability for the experiment. During the cooling phase, the evolution of the measured temperature is quite far from the

impose condition due to the thermal inertia of the system. Nevertheless, the repeatability of the test is excellent and a comparison between each test could be done.

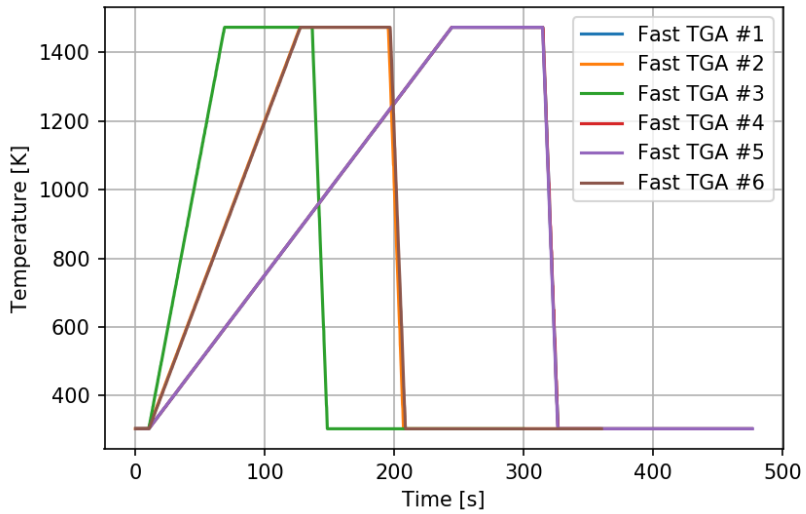

Figure 14 – Time evolution of the setpoint temperature for Fast ATG experiments

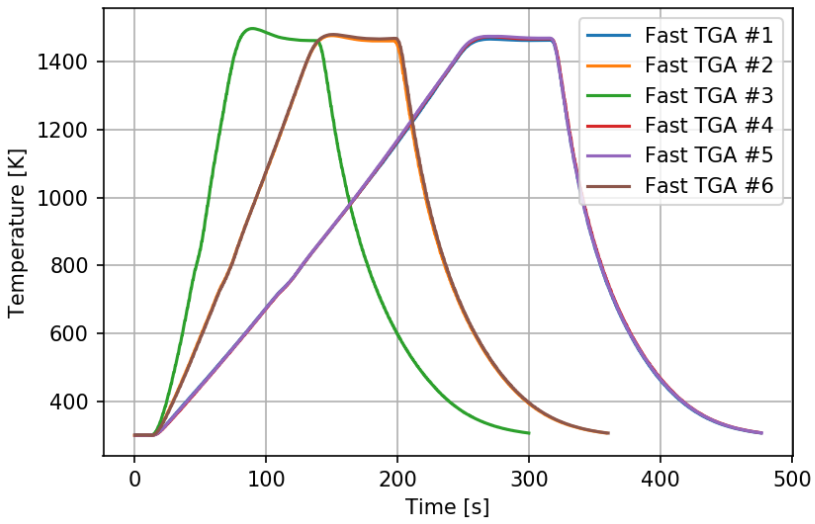

Figure 15 – Time evolution of the measured temperature close to the sample for the Fast ATG experiments

Figure 16 shows the evolution of the mass loss as a function of temperature resulting from thermo-gravimetric analyses under inert atmosphere (He) at different heating rates (300, 600 and 1200 K/min). The studied material is a carbon/epoxy laminate whose commercial name is T700GC/M21.

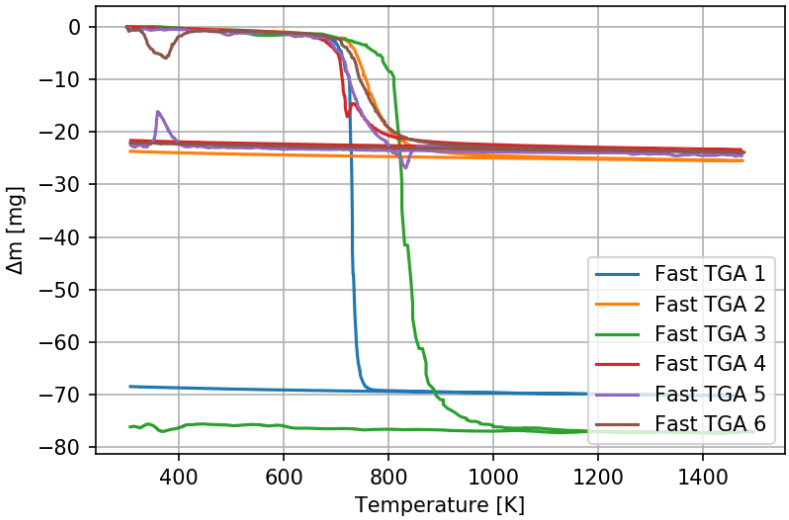

Figure 16 – Time evolution of the mass loss for the different coupons

This evolution doesn't take into account the influence of the Archimedes' buoyancy in the evolution of the mass loss. In order to estimate it, we consider that during the cooling phase the mass loss is null and then an estimation of this phenomenon can be achieved. The Figure 17 presents the evolution of the mass loss measured during the cooling phase as function of the temperature and the fitting curve uses in Figure 21 to estimate the relative mass loss. We can observe a very good repeatability of this phenomenon on all the coupons. An error on the mass measurement of around 2 mg can be made by neglecting this phenomenon.

We can observe on the precedent figure the sudden drop of the mass for coupon #1 and #3. This is due to the rupture of the coupon by thermal degradation and the drop of the coupon from the hang system during the test.

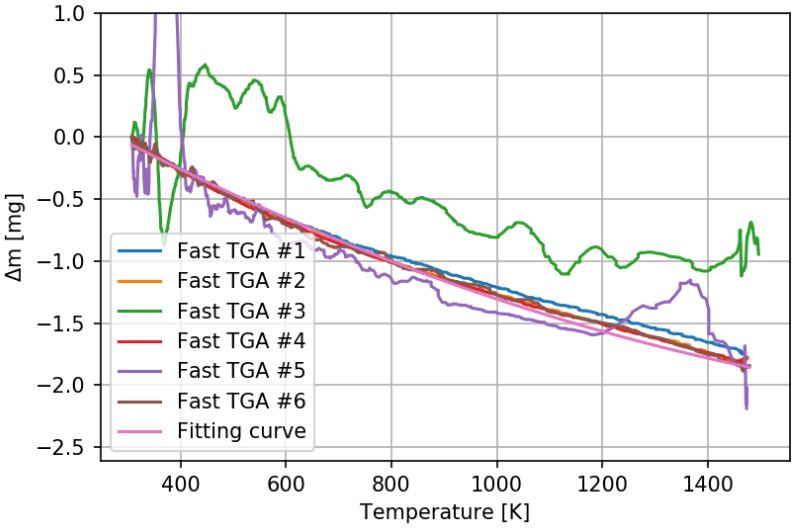

Figure 17 – Estimation of the Archimedes' buoyancy

Figures 18-21 shows relative mass loss (m/m_0) as a function of temperature resulting from thermo-gravimetric analyses under inert atmosphere (He) at 300, 600 and 1200 K/min). The first remark concerns the repeatability of the experiment. The repeatability of the result is excellent even if a rupture of the coupon occurs. In such case, the evolution of the relative mass loss is similar to the over samples (see for example the coupon #1 on Figure 18) before the drop of the sample.

For heating ramp of 300 K/min and 600 K/min, the different curve are quasi similar and the major differences are only due to noise on the measurement technics. For 300 K/min, the mass loss is maximal at around 710 K, at 760 K for 600 K/min and 800 K for 1200 K/min. These observations confirm the influence even at very high temperature rate, the influence of the heating rate on the thermal degradation kinetics. Figure 21 overlays the relative mass loss (m/m_0) as a function of temperature for these different heating rates (300, 600 and 1200 K/min) and exihbits the influence of the temperature rate. The Figure 22 shows the final percentage of relative mass loss ($1 - m/m_0$). It underlines a very small influence on the final mass loss due to the temperature.

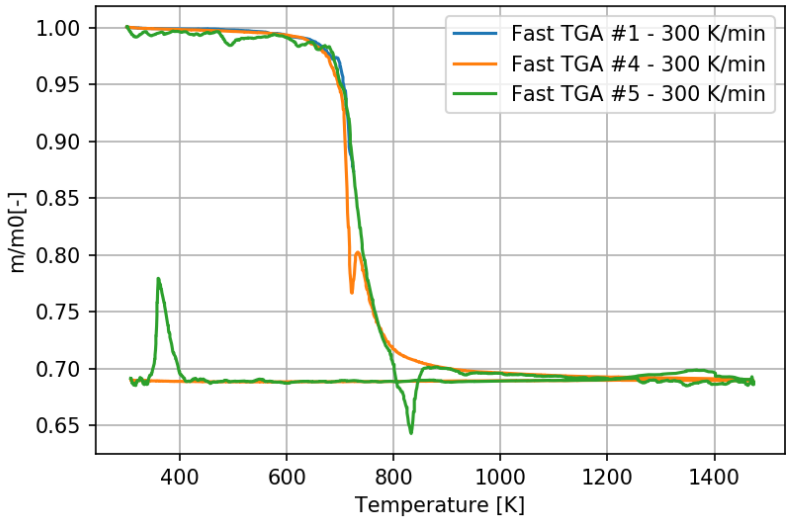

Figure 18 – Evolution of the mass loss at 300 K/min for fast ATG.

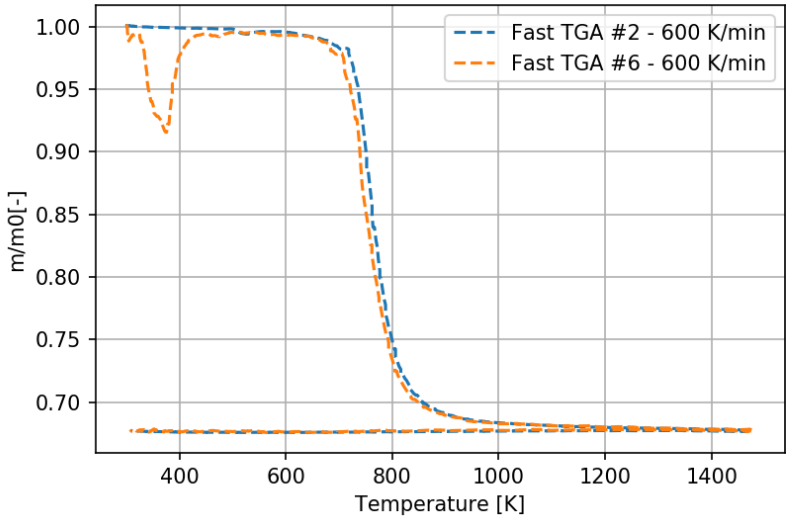

Figure 19 – Evolution of the mass loss at 600 K/min for fast ATG.

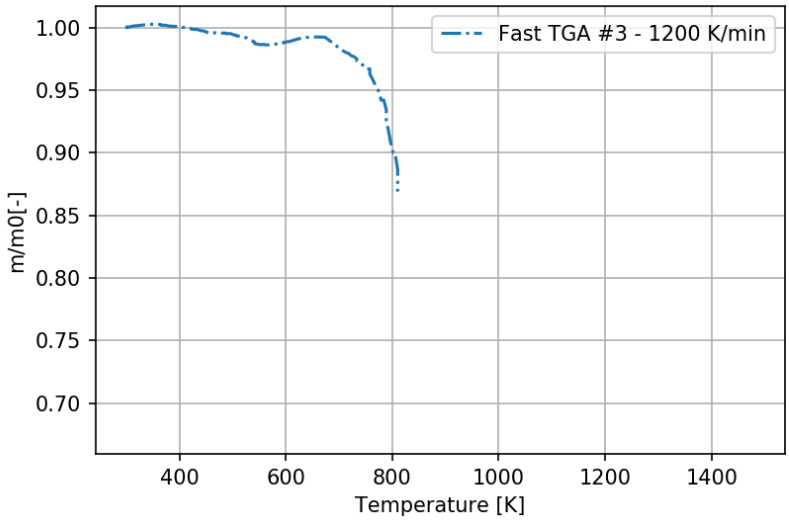

Figure 20 – Evolution of the mass loss at 1200 K/min for fast ATG.

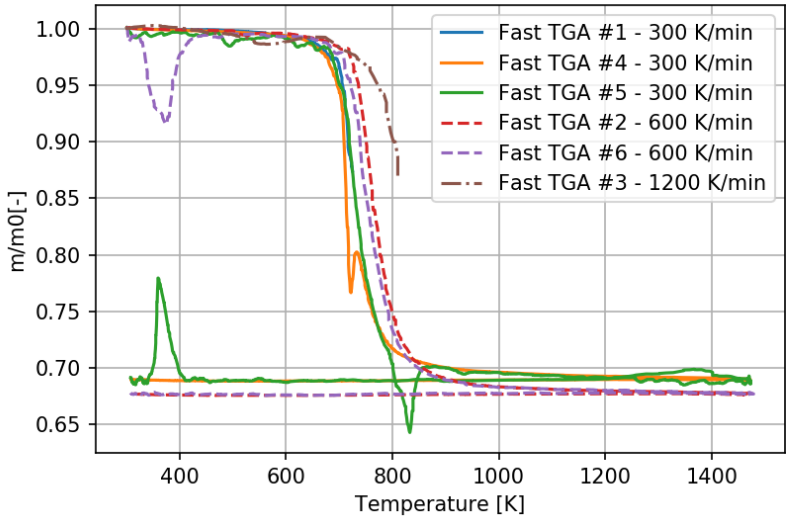

Figure 21 – Comparison for the evolution of the mass loss for 3 different heating rates (300, 600, 1200 K/min) for fast ATG.

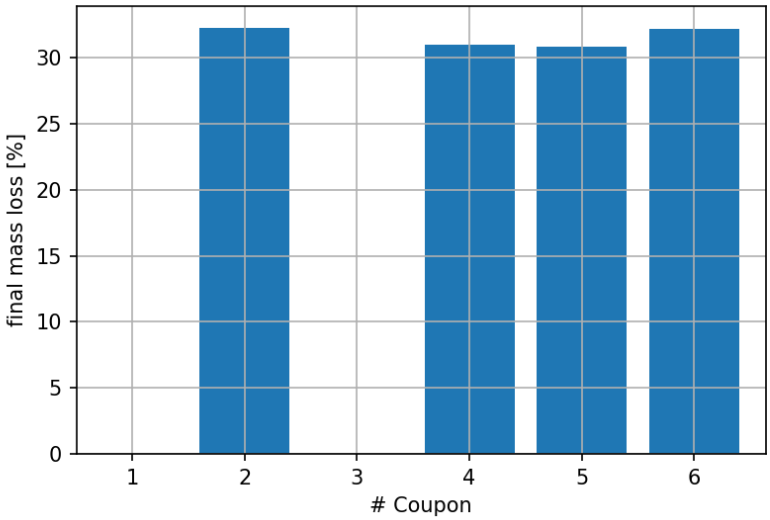

Figure 22 – Comparison of final the mass loss for the 6 different coupons.

3.4. Kinetics and energetics modelling of the thermo-chemical decomposition reactions

3.4.1. 1-stage-model: inert atmosphere only

As detailed by the T700GC/M21 manufacturer, the mass ratio of carbon fibres is equal to 62%. The commonly used chemical mechanism to model carbon fibres / epoxy resin composite material considers that carbon fibres are not subjected to reactions under inert atmosphere and that epoxy resin decomposes in an intermediate solid residue named *char* as well as decomposition gases:

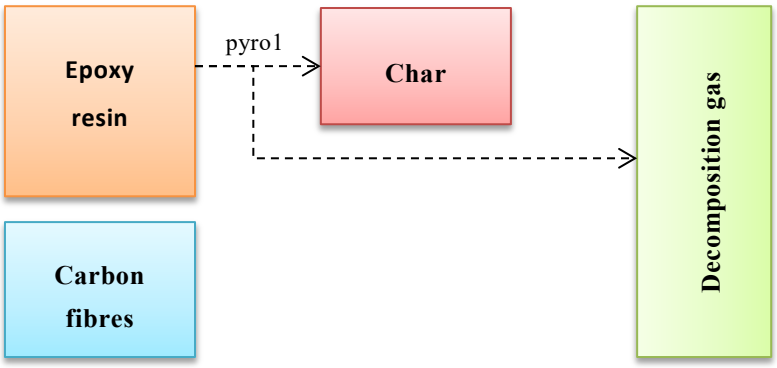

Figure 23 – 1 reaction thermo-chemical mechanism of T700GC/M21

This reaction mechanism is modeled with Arrhenius kinetic equations, as detailed in the section 3.2.2 and kinetic parameters are assessed through an optimization process using the Adethec toolbox. Parameters minimising the difference between the experimental and numerical values are:

Reaction	ν	A	E_A	n
pyro1	0.41	2.87e12	1.87e5	1.40

Table 2 - Arrhenius parameters of the thermo-chemical mechanism of T700GC/M21 in N_2 atmosphere

where ν is the mass stoichiometric coefficient that transforms virgin resin to *char* material. Figure 24 and Figure 25 show comparisons of the experimental values of relative mass loss and mass loss rate at different heating rates under inert atmosphere. Kinetic parameters are used to plot the numerical values of m/m_0 and MLR. It is important to note that the fitting of the Arrhenius parameters is global and valid whatever the heating rate while most optimisations are done with only one temperature heating rate. The relative mean fitting errors vary from 2.1% to 2.6% under $800K$ and from 3.02% to 10.1% on the whole range of temperature. The fitted chemical mechanism gives satisfactory results during the decomposition, but as the mass loss diverges from the theoretical final value at the highest temperatures, the fitting error increases consequently.

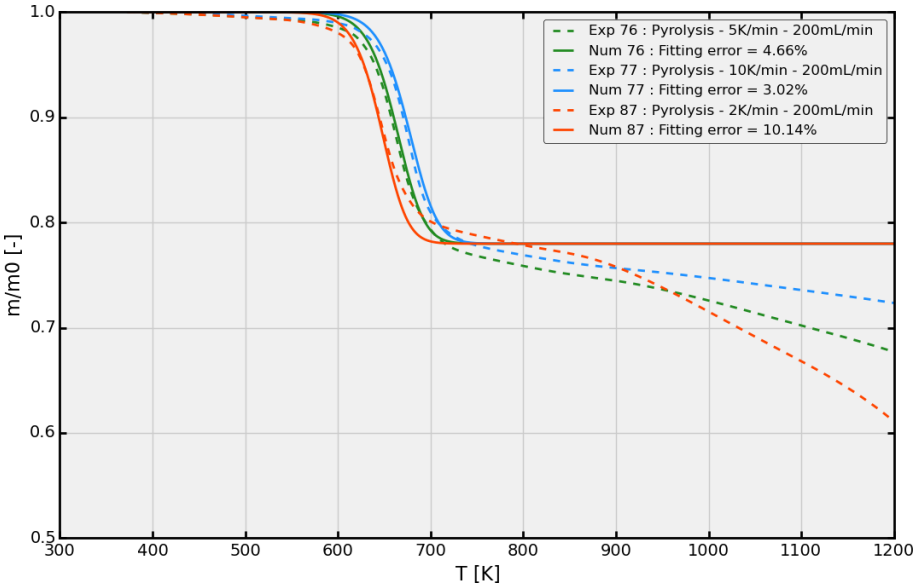

Figure 24 - Relative mass loss reconstruction at $2, 5$ and $10K/min$ in N_2 atmosphere using the 1-stage-model

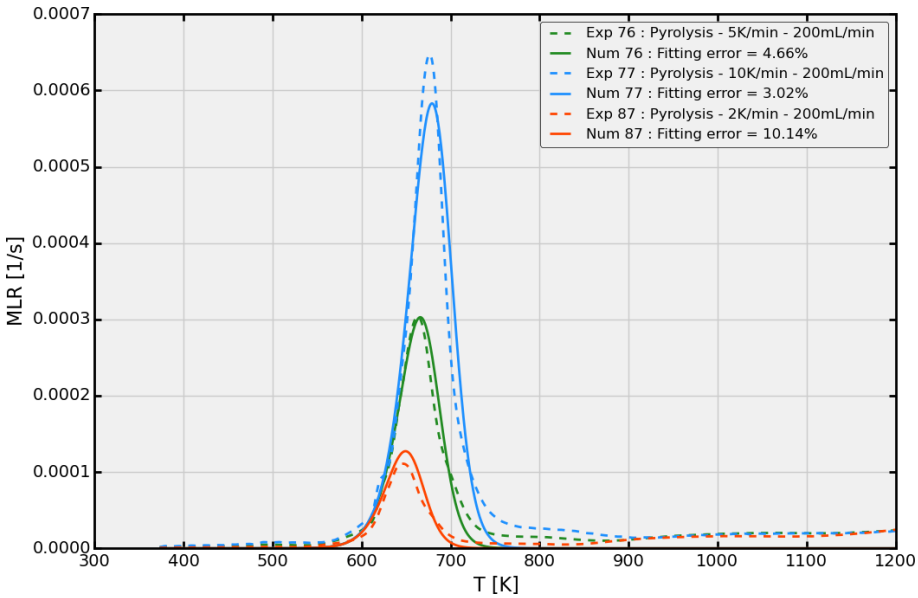

Figure 25 - Mass Loss Rate reconstruction at $2, 5$ and $10 K/min$ in N_2 atmosphere using the 1-stage-model

Figure 26 shows the evolution of solid species mass fraction at $5\,K/min$ considering the chemical mechanism detailed in Figure 23 (carbon fibers, epoxy resin and *char*). As the resin decomposes at about $T = 650\,K$, the *char* species is created with a mass ratio of $\nu = 0.41$. For higher temperatures, the mass fraction of the remaining species does not change.

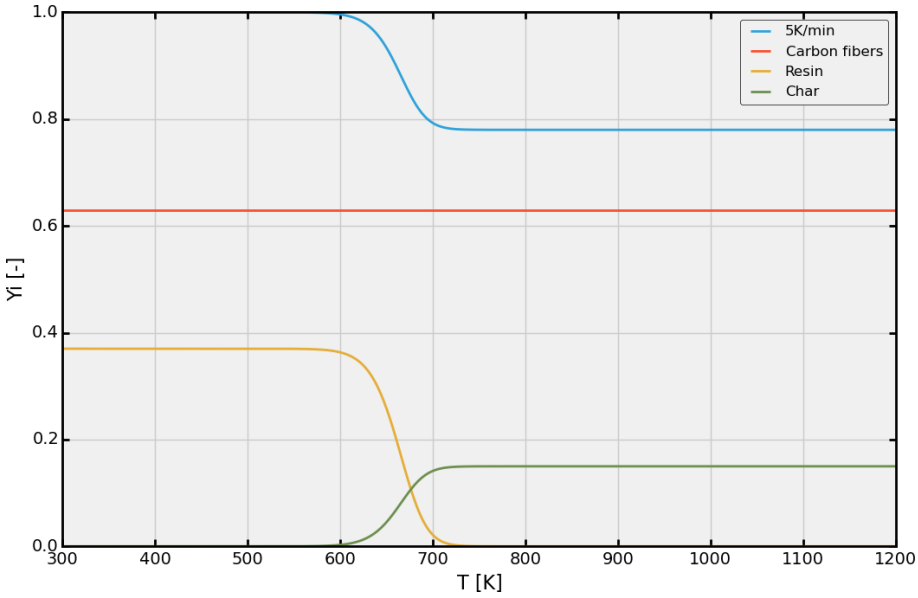

Figure 26 - Mass fraction reconstruction of solid species at $5 K/min$ in N_2 atmosphere using 1-stage-model

3.4.2. 3-stage-model: oxidative atmosphere only

The proposed chemical mechanism of the thermal decomposition of T700GC/M21 under oxidative atmosphere is presented in Figure 27. The pyrolysis model detailed in the previous section is unchanged as the behaviour of the material seems independent of the atmosphere for this particular reaction. The second reaction, named *oxy1*, models the decomposition of the *char* into volatiles and the third reaction, named *oxy2*, models the decomposition of the carbon fibres into volatiles. Gaseous species are not detailed and considered as *decomposition gases*.

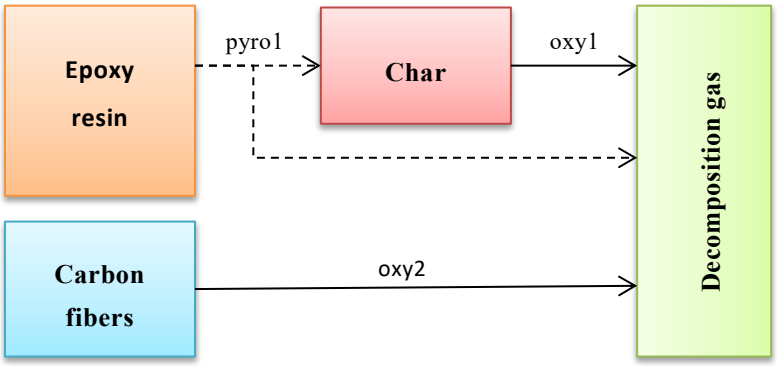

Figure 27 - 3 reactions thermo-chemical mechanism of T700GC/M21

The chemical mechanism is modeled using Arrhenius equations and parameters of *oxy1* and *oxy2* are optimised using the ADeTheC toolbox. Parameters that minimise the difference between experimental and numerical results are detailed in the following table:

Reaction	ν	A	E_A	n
pyro1	0.41	2.87e12	1.87e5	1.40
oxy1	-	6.70e4	1.21e5	0.85
oxy2	-	2.78e2	1.18e5	0.28

Table 3 - Arrhenius parameters of the 3 reactions thermo-chemical mechanism of T700GC/M21 in air atmosphere

Figure 28 and Figure 29 exhibits the reconstruction of the numerical values of m/m_0 and MLR in solid lines compared to experimental values in dashed lines. This optimised model seems to accurately fit the different decomposition reactions of the ATG analyses. The fitting errors vary from 1.8% to 2.2% depending on the heating rate level. It is important to note that the fitting of the experimental values could be improved by defining as set of minor reactions (decomposition of 2% of the initial mass from

$400K$ to $600K$) but such level of thermo-chemical modelling does not improve the macroscopic thermal decomposition behaviour.

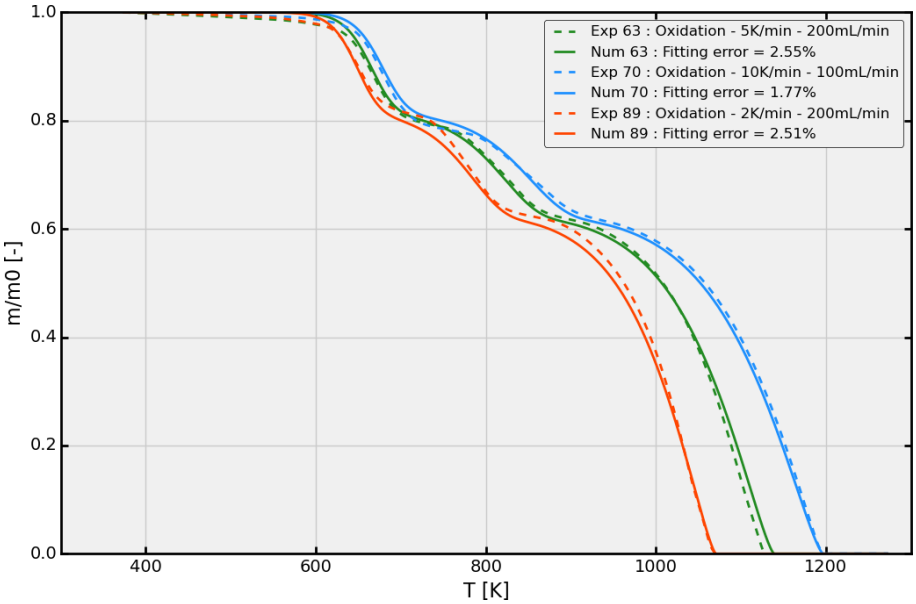

Figure 28 - Relative mass loss reconstruction at $2,5$ and $10K/min$ in air atmosphere using a 3-stage-model

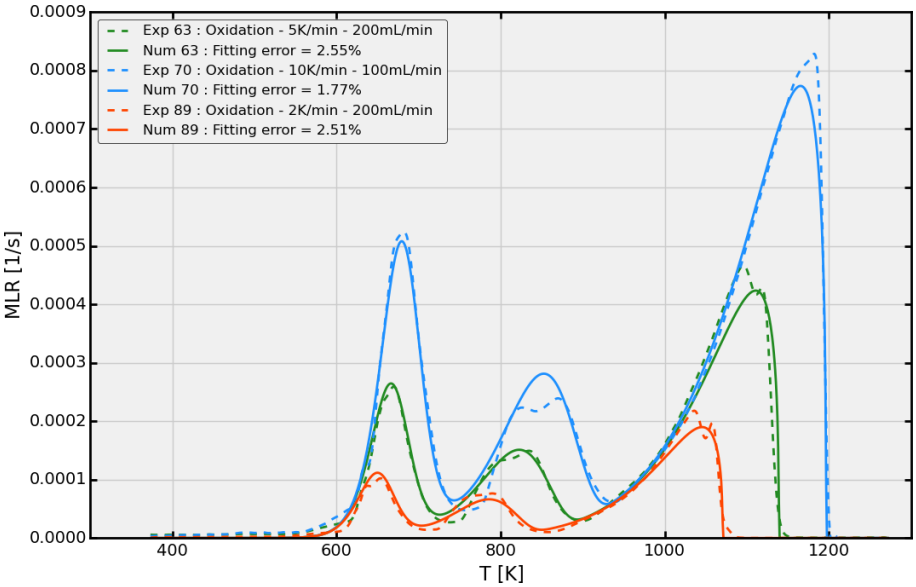

Figure 29 – Mass Loss Rate reconstruction at $2,5$ and $10K/min$ in air atmosphere using a 3-stage-model

Figure 30 shows the evolution of solid species mass fraction at $5\,K/min$ considering the chemical mechanism detailed in Figure 27 under oxidative atmosphere. Up to $T = 700K$, the behaviour is similar to

the decomposition in inert atmosphere. Then, the char decomposes into decomposition gases due to the reaction *oxy1*. Last reaction *oxy2* makes the carbon fibres decompose totally at around $T = 1050K$ without any solid residue.

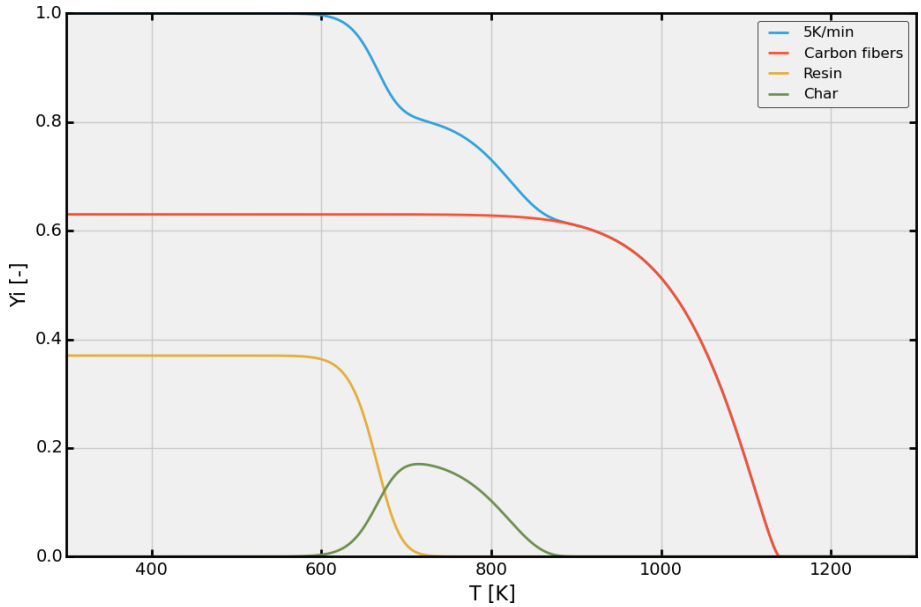

Figure 30 - Mass fraction reconstruction of solid species at $5K/min$ in air atmosphere using a 3 reactions model

3.5. Extrapolation of thermochemical kinetics from conventional thermogravimetric analysis at higher heating rates

Complementary TGA measurements are performed in order to identify the range of applicability of conventional analysis assuming thermally thin sample materials. The thermally-thin assumption has a direct consequence onto the sample material preparation. Indeed, (geometrically-) thin sample materials must be used at high heating rates while thicker sample materials could be used at lower heating rates. Actually, the thermal properties (specific heat and thermal conductivity) of the material are mandatory for an accurate sizing of the sample materials because low conductivity materials such as CFRP must require thinner sample materials than higher conductivity materials for TGA measurements at the same heating rate in order to avoid any temperature gradient during the test and get an expected homogeneous decomposition.

Another key point in performing relevant TGA measurements and analysis is to prepare sample materials that satisfy the representative elementary volume (REV) assumption. Indeed, a composite material is a heterogeneous material and the sample material extracted onto a panel must represent the composition of the entire panel, i.e. relevant fibre-to-resin ratio for instance. As a consequence, the sample material must be big enough to have the right and general composition.

The reader can thus easily understand that the two assumptions (REV and thermally thin) for relevant analysis are contradictory and a compromise has to be made in order to perform the measurements. The sample material preparation is crucial for reliable analysis.

But for composite materials, the REV may be difficult to define because of the complex composition of such materials involving polymeric resin, carbon fibres, thermoplastic nodules… In some cases, the REV can be way bigger than expected. The REV characteristic length can exceed $1\,cm$ for some CFRP such as 3D woven or interlock materials. Such size is not compatible with conventional crucible size and/or measurement range of the TGA device. The direct consequence of the big sample material size is that the thermally-thin assumption is no longer valid.

These complementary results are thus performed at heating rates from $2\,K/min$ up to $100\,K/min$ under nitrogen atmosphere for $20\,mg$ sample materials. So the size is not adjusted for each test for the thermally-thin assumption to be valid. The objective is to identify the effect of kinetics out of the thermally thin assumption as a function of the heating rate. However, for all tests, the REV assumption remains verified. Relative mass loss is plotted in Figure 31 and mass loss rate is plotted in Figure 32. Increasing the heating rate delays the MLR peak of the pyrolysis reaction towards the higher temperatures.

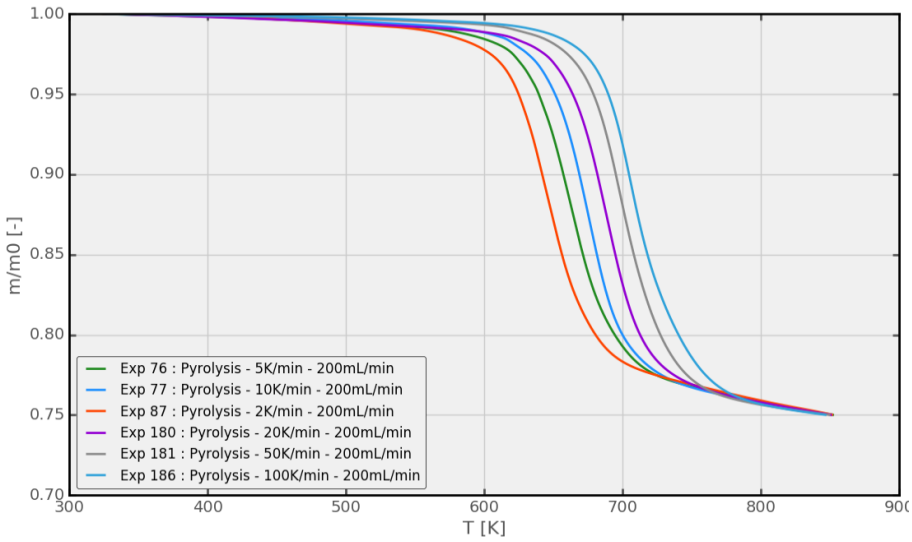

Figure 31 - Relative mass loss under inert atmosphere at heating rates from $2\,K/min$ up to $100\,K/min$

Future Sky Safety has received funding from the EU's Horizon 2020 Research and Innovation Programme, under Grant Agreement No. 640597.

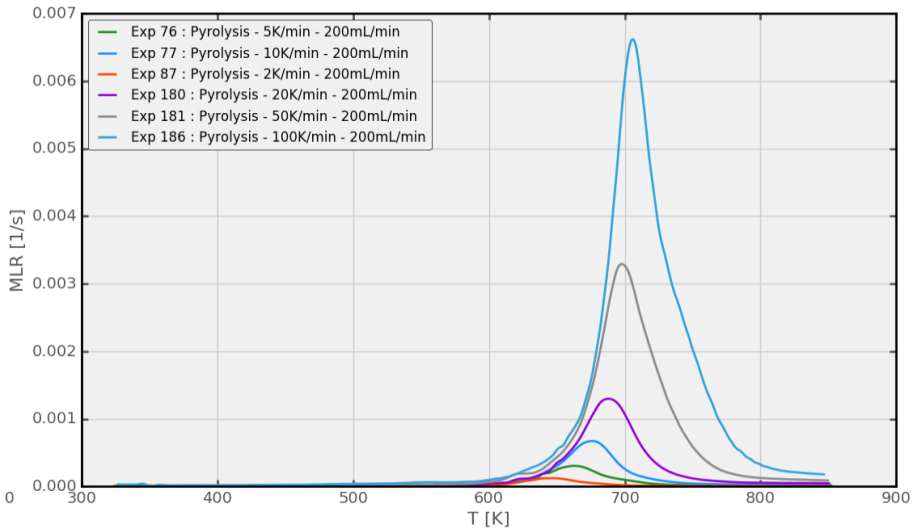

Figure 32 - Mass loss rate under inert atmosphere at heating rates from $2\ K/min$ up to $100\ K/min$

If the kinetics identified in section 3.4.1 is used for measurement reconstruction, discrepancies appear for tests at $20\ K/min$ and higher. Figure 33 and Figure 34 show the comparison between measurements (dashed lines) and kinetic modelling (plain lines). Obviously, the results up to $10\ K/min$ are good because those lowest heating rates have been used to identify the kinetic parameters. The model predicts decomposition at lower temperature than the measurements.

As a consequence, heat diffusion within thermally-thick sample materials delays decomposition at the highest heating rates.

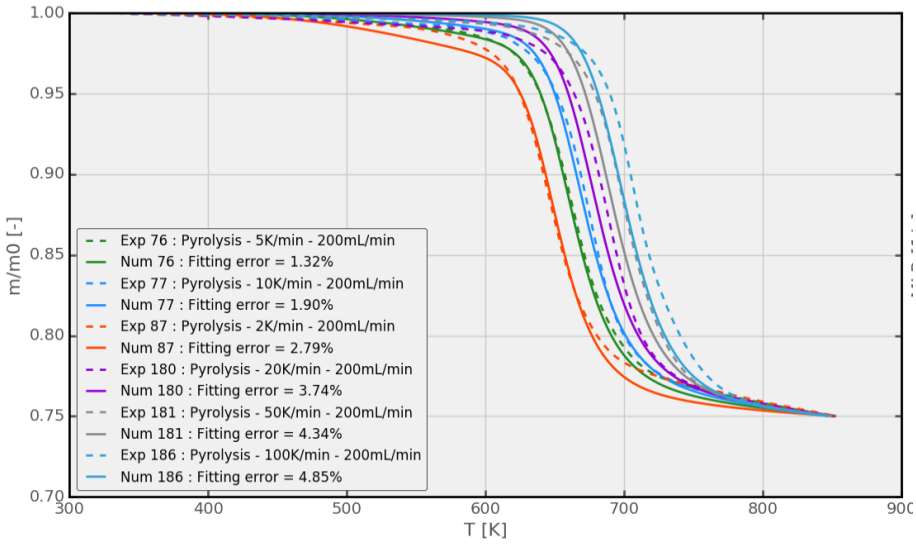

Figure 33 – Comparison of Arrhenius kinetics (plain lines) and measurements (dashed lines) of relative mass loss under inert atmosphere at heating rates from $2\ K/min$ up to $100\ K/min$

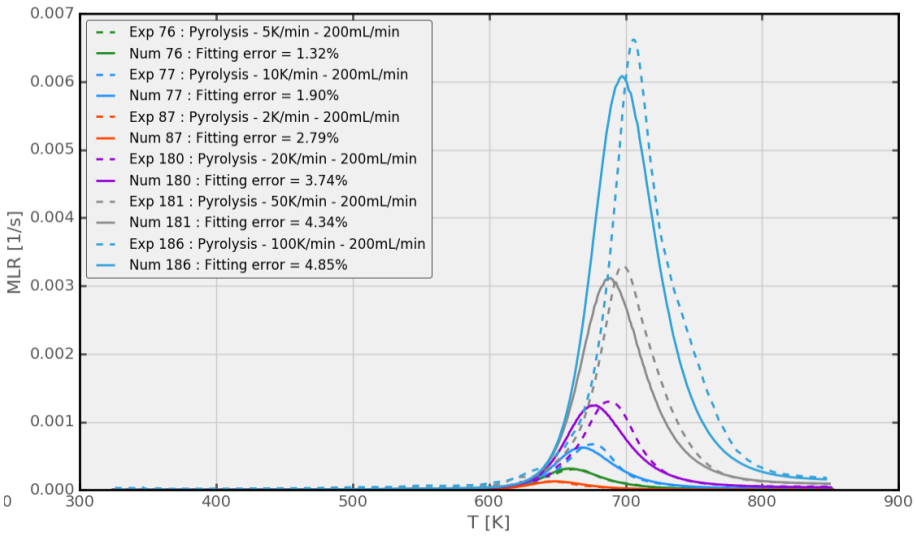

Figure 34 – Comparison of Arrhenius kinetics (plain lines) and measurements (dashed lines) of mass loss rate under inert atmosphere at heating rates from $2\ K/min$ up to $100\ K/min$

The Adethec toolbox provides simple models to take into account heat diffusion within the material during the integration of the Arrhenius equations. Currently, heat transfer models are limited to 1D modelling assuming spherical sample materials. This limitation is not the most relevant approach to model TGA results performed on the T700GC/M21 CFRP because sample materials are mostly parallelepiped-shaped. However, such simple model can consider heat diffusion from the edge to the core of the sample material if relevant characteristic size and thermal diffusivity is given. As a consequence of the 1D limitation, the thermal diffusivity can only be specified by an isotropic value.

Figure 35 and Figure 36 exhibit the comparison between measurements (dashed lines) and kinetic modelling with heat transfer effect (plain lines). A significant improvement on the highest heating rates can be noticed on the results while heat diffusion does not affect the lowest heating rates. It confirms that homogeneous decomposition occurs with negligible temperature gradients at the lowest heating rates because the thermally-thin assumption is still verified. Above, the heating rate is too high and temperature gradients appear within the sample material. The sample material surface decomposes first while the core remains protected temporarily.

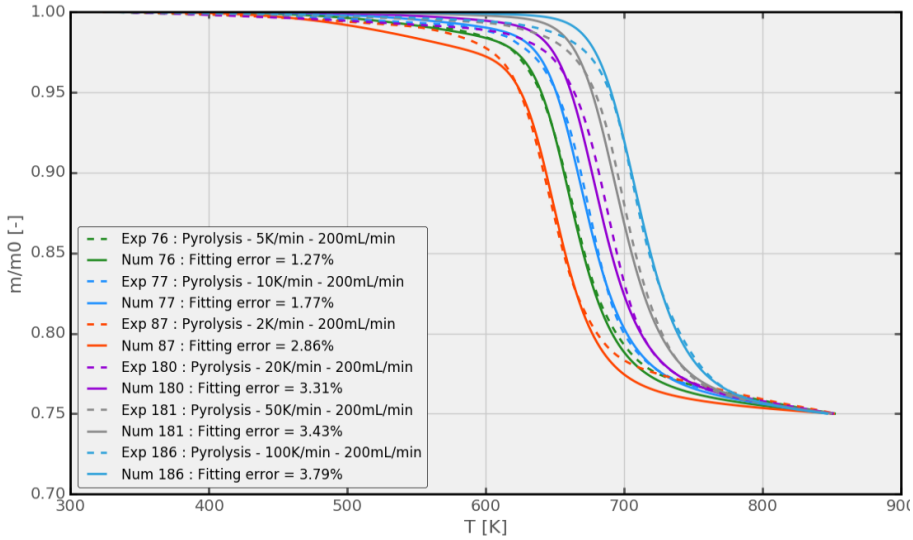

Figure 35 – Comparison of Arrhenius kinetics (plain lines) and measurements (dashed lines) of relative mass loss under inert atmosphere at heating rates from $2\ K/min$ up to $100\ K/min$ considering heat diffusion within the material

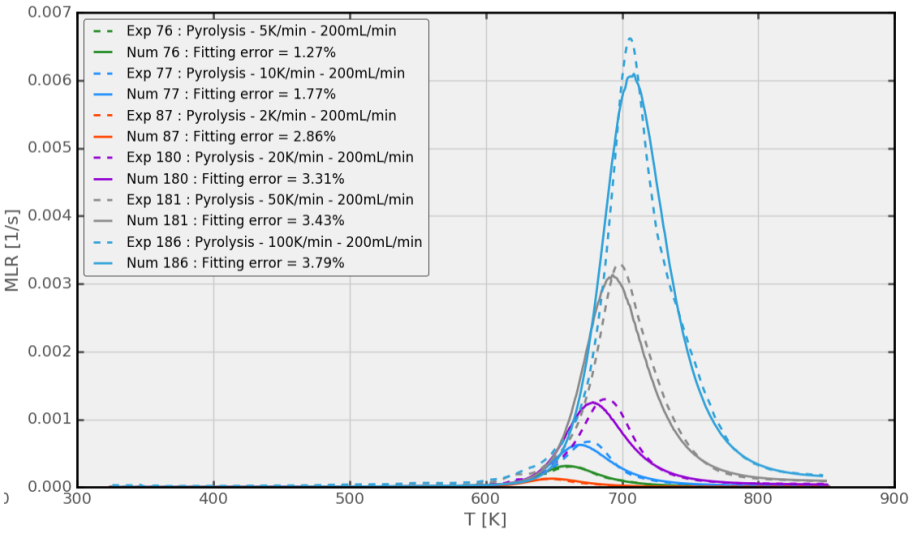

Figure 36 – Comparison of Arrhenius kinetics (plain lines) and measurements (dashed lines) of mass loss rate under inert atmosphere at heating rates from $2\ K/min$ up to $100\ K/min$ considering heat diffusion within the material

More complex and representative thermal model should be implemented in the Adethec solver to improve the result and the identification of Arrhenius kinetics whatever the heating rate or sample material size. Such model should take into account anisotropic heat diffusion and temperature-dependency of the thermal properties to provide more accurate and reliable results.

Such conclusion must be confirmed under oxidative atmosphere because thermal diffusion is associated to oxygen diffusion in order to activate oxidizing reactions. Fick mass diffusion within the solid and porous sample material should be quantified as well as heat diffusion for the approach to be complete and relevant.

3.6. Preliminary gas phase analysis

In order to evaluate the gaseous compounds released during decomposition in inert atmosphere, gaseous chromatography and mass spectrometry analyses are coupled to analyse the gas-phase out of a pyrolyser Double Shot 3030. These analyses have been done by SRA Instruments SA with a GC/MS Agilent 7890B/5977A device. It has been chosen to use a pyrolyser instead of a TGA device since the TGA device operates continuously and the GC takes samples at defined times or temperatures. Isothermal condition is then defined to decompose the sample and to operate the GC/MS measurements.

Three coupons of T700GC/M21 are pyrolysed at $550\,°C$ in N_2 atmosphere. The first pyrolysis reaction affected the composite as the temperature increases is identical whatever the atmosphere. This first decomposition reaction results in a solid charred residue as well as gaseous and possibly ignitable volatiles. The initial mass is $4\,mg$ for the first sample material and $2\,mg$ for the next two. The sample materials are extracted from the same piece of composite panel and cut in the through thickness direction in order to consider all plies of the laminate. The first sample material comes from the core of the laminate while the other two come from the edges.

The Multishot 3030 device is used in Flash Pyrolysis mode for isothermal decomposition at $550\,°C$ under inert atmosphere (Helium). The GC device is composed of a single column UA-5 ($30\,m \times 0.25\,mm \times 0.25\,\mu m$) with a constant mass flow rate of $1\,ml/min$.

The MS device is used in scan mode 1 - 500 amu with NIST and FSEARCH libraries.

Figure 37 - Multishot/GC-MS SRA (2013)

The analysis of the first sample material shows a composite polymer with rich and complex composition. Overall, about 140 compounds are detected in the chromatogram plotted on below.

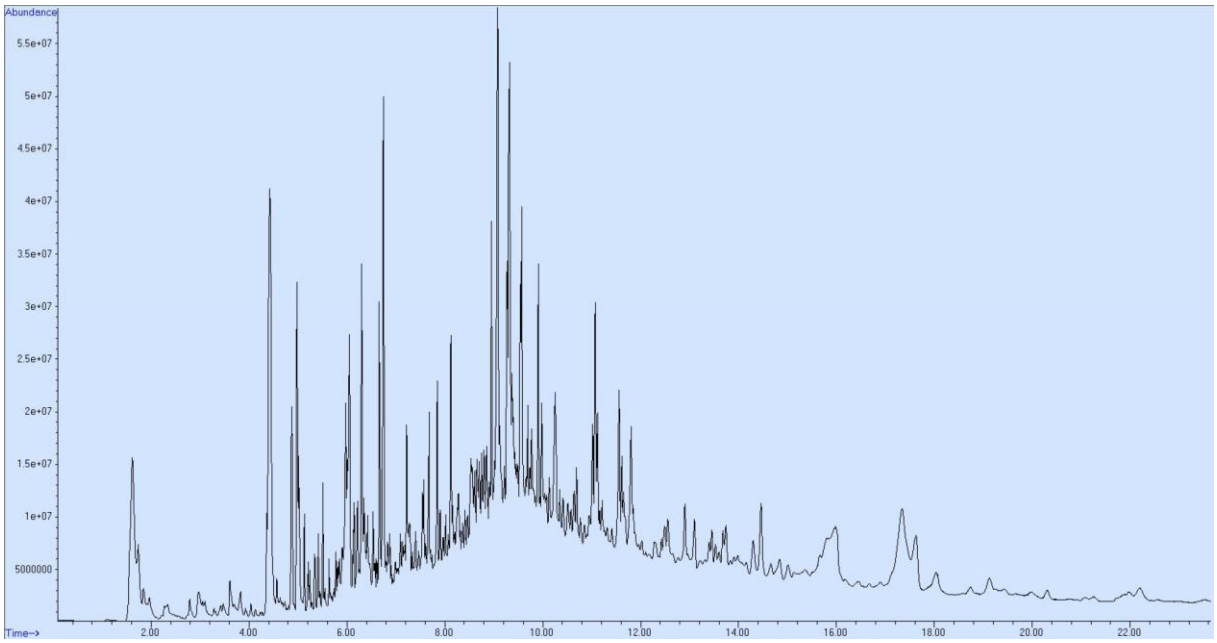

Figure 38 - Complete chromatogram for the first test, $4\ mg$, $550\ °C$

The baseline shows an unusual upward drift compared to other sample types. For better separation of the peaks, using a longer column might be considered for complementary results.

3 main compounds families are identified:

- PHENOL: main family with most intense signals. Phenol isomers are numerous as well as dimers. The most probable source comes from phenol-based resin. Epoxy resin Hexply 21 is formed by the reaction of phenol and epichlorohydrin. Thermal degradation of the resin will lead to the breakage of chemical bonds, i.e. the polymer structure, yielding the thermal degradation products propylene oxide and toluene.
- AMINE: minority. The analysers identifies many amine-based compounds such as Aniline and N-Methyl-. The most probable source is a minority base of amine resin.
- SULFUR: A strong presence of SO_2 is detected in the beginning of the chromatogram associated with Polyethersulfone that may come from PESF- or PSF-type polymers. It might be an additive. DAPSONE (diaminodiphenyl sulfone) is used as an additive in Hexcel's samples in order to increase the toughness of the epoxy resin. SO_2 will probably be a degradation product of DAPSONE. Amines are used as curing agents.
- ACID: ultra-minority. Traces of gas compounds with a base of carboxylic acid are detected with a very low signal.

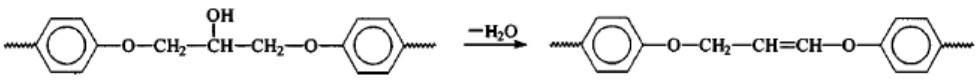

Figure 39 - Snapshot taken from Levchik et al 2004.

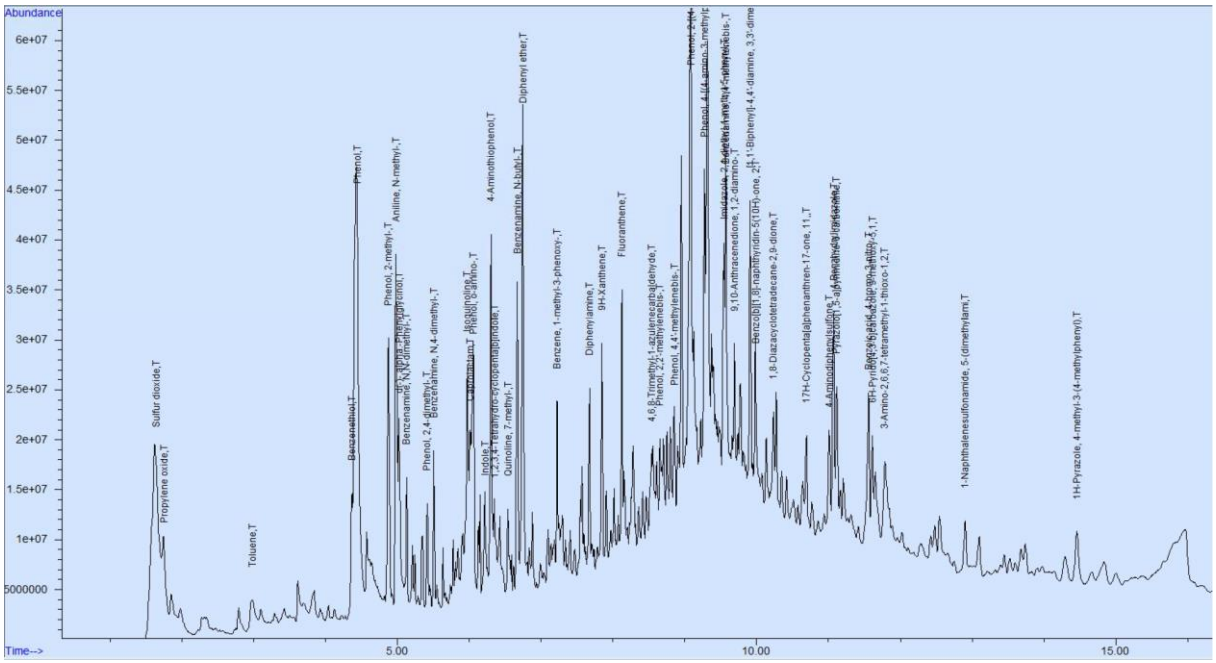

Figure 40 – Chromatogram with compounds name for the second test, 2 mg, 550 °C

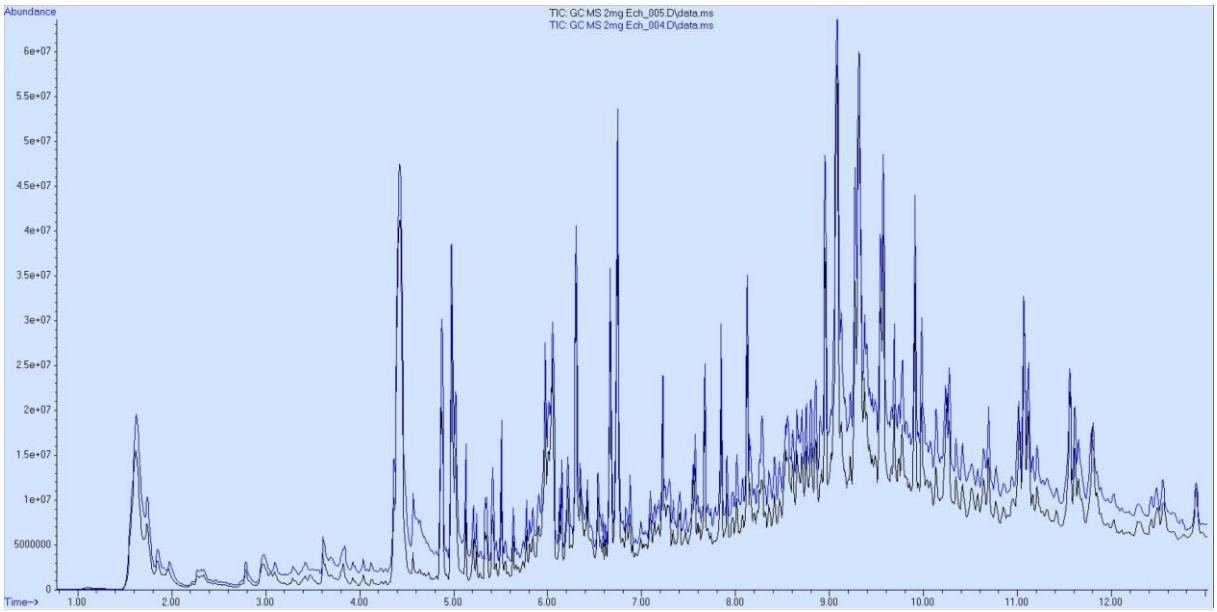

Figure 41 – Complete chromatograms comparison for the second and third tests, 2 mg, 550 °C

Same composition is detected for the 3 tests. It indicates that the material composition is homogeneous whatever the extracted samples. The sample materials size is then relevant for such measurement and the representative elementary volume assumption is valid.

The analysis performed with the flash pyrolyser has shown the different compounds released by the thermal decomposition of the T700GC/M21 at $550\,°C$ under inert atmosphere. The 40 most intense and detectable compounds are listed

#	Compound	Retention time (min)	Area	Confidence factor %
1	Sulfur dioxide	1.636	106937629	95
2	Propylene oxide	1.756	54302490	81
3	Toluene	2.976	84698754	99
4	Benzenethiol	4.368	83350120	81
5	Phenol	4.442	334247078	80
6	Phenol, 2-methyl-	4.878	127499926	99
7	Aniline, N-methyl-	4.981	170641877	70
8	Benzenamine, N,N-dimethyl	5.132	34321515	95
9	Phenol, 2,4-dimethyl-	5.418	23538192	94
10	Benzenamine, N,4-dimethyl	5.510	44205039	88
11	Isoquinoline	5.976	84411987	97
12	Caprolactam	6.019	73114395	93
13	Indole	6.220	50111020	99
14	4-Aminothiophenol	6.305	175771107	93
15	Quinoline, 7-methyl-	6.539	69424358	93
16	Benzenamine, N-butyl-	6.670	112274279	86
17	Diphenyl ether	6.747	132023777	89
18	Benzene, 1-methyl-3-phenoxy	7.227	50722058	64
19	Diphenylamine	7.674	57534353	99
20	9H-Xanthene	7.849	84192328	100
21	Fluoranthene	8.127	77803480	91
22	Phenol, 2,2'-methylenebis	8.655	13881603	96
23	Phenol, 4,4'-methylenebis	8.856	20426517	88

24	Phenol, 2,2'-methylenebis	8.955	106570175	81
25	Phenol, 2-[(4-hydroxyphenyl)methyl]-	9.085	290740412	91
26	Phenol, 4-[(4-amino-3-methylphenyl)amino]-	9.275	71675256	75
27	Phenol, 4,4'-methylenebis-	9.316	237213202	83
28	Imidazole, 2,4-diethyl-1-methyl-5-phenyl-	9.547	68730073	75
29	Benzenamine, 4,4'-methylenebis-	9.575	107350519	83
30	9,10-Anthracenedione, 1,2-diamino-	9.692	33826011	97
31	[1,1'-Biphenyl]-4,4'-diamine, 3,3'-dimethyl-	9.912	97723051	93
32	Benzo[b][1,8]-naphthyridin-5(10H)-one, 2,4,7-trimethyl-	9.985	26828582	71
33	1,8-Diazacyclotetradecane-2,9-dione	10.237	23583233	90
34	17H-Cyclopenta[a]phenanthren-17-one, 11,12,13,16-tetrahydro-3-methoxy-13-methyl-, (S)-	10.695	31508673	94
35	4-Aminodiphenylsulfone	11.013	39354113	93
36	4-Benzhydrylimidazole	11.071	98450760	90
37	Pyrazolo[1,5-a]pyrimidine-6-carbonitrile, 7-benzyl-2-methyl-	11.116	46317212	98
38	3-Amino-2,6,6,7-tetramethyl-1-thioxo-1,2,5,6,7,8-hexahydro-[2,7]naphthyridine-4-carbonitrile	11.788	37903515	83
39	1-Naphthalenesulfonamide, 5-(dimethylamino)-N-phenyl-	12.903	39538464	96
40	1H-Pyrazole, 4-methyl-3-(4-methylphenyl)-1,5-diphenyl-	14.460	30600621	98

Figure 42 - 40 most intense and detectable compounds

4 DEFINITION OF THE PREPARATION PROTOCOL TO GET FULLY AND HOMOGENEOUSLY CHARRED TEST SPECIMENS FOR BLADE MEASUREMENTS

In order to characterise the thermo-physical properties of the T700GC/M21 material in its fully charred state (fibres + char), it is necessary to define the experimental protocol to obtain coupons in an homogeneously charred state of decomposition. Due to the technical constraints and the available facilities, it was decided to decompose the material within a ceramic insulated furnace controlled in temperature under air atmosphere. The isothermal decomposition temperature condition should be identified to activate only the pyrolysis of the material and to prevent the oxidization of the *char*. Figure 43 shows the relative mass of the decomposing material in air for different isothermal conditions during $6\ hours$ using the Adethec toolbox and the 3-reactions model presented in the previous section 3.4.2. The theoretical asymptotic behaviour of pyrolysis decomposition is found at $m/m_0 = 80\%$ of the initial mass. An isothermal heating at $T = 603K$ (i.e. $T = 330°C$) does not pyrolyse completely the resin after 6 hours while a $T = 643K$ begins to oxidize the *char*. A compromise statement satisfying the theoretical condition is obtained for an intermediate temperature of $T = 623K$ (ie. $T = 350°C$).

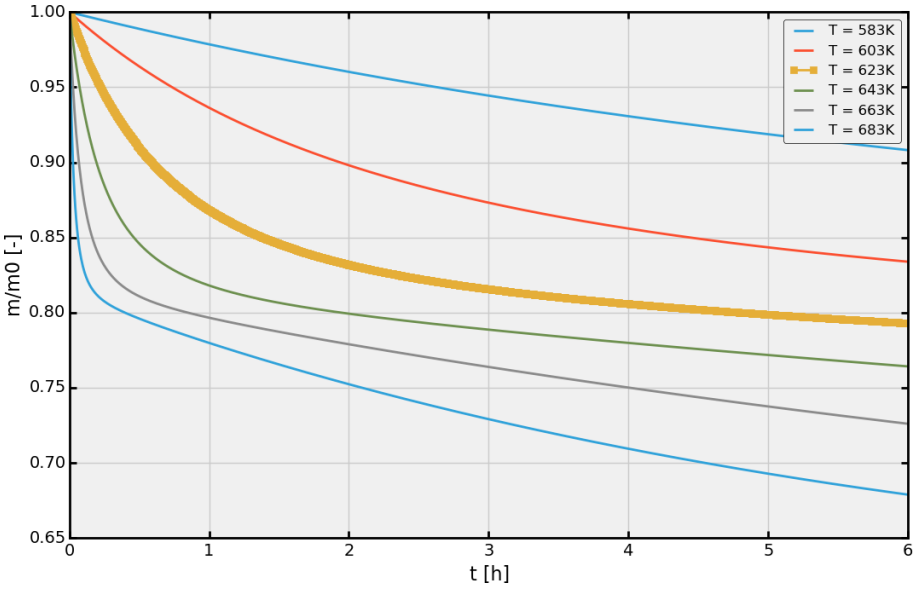

Figure 43 – Relative mass loss reconstruction in different isothermal conditions under air atmosphere during 6 hours

On Figure 44 the mass fraction evolution of the solid species of T700GC/M21 under air atmosphere at $T = 623K$ is plotted and confirms that all the resin has been decomposed with the mass fraction of *char* reaches an asymptotic value. The chosen protocol to prepare fully charred coupons thus consists in heating a sample material in a furnace controlled in temperature at $623K$ during 5 hours. The expected mass loss is then about 21%.

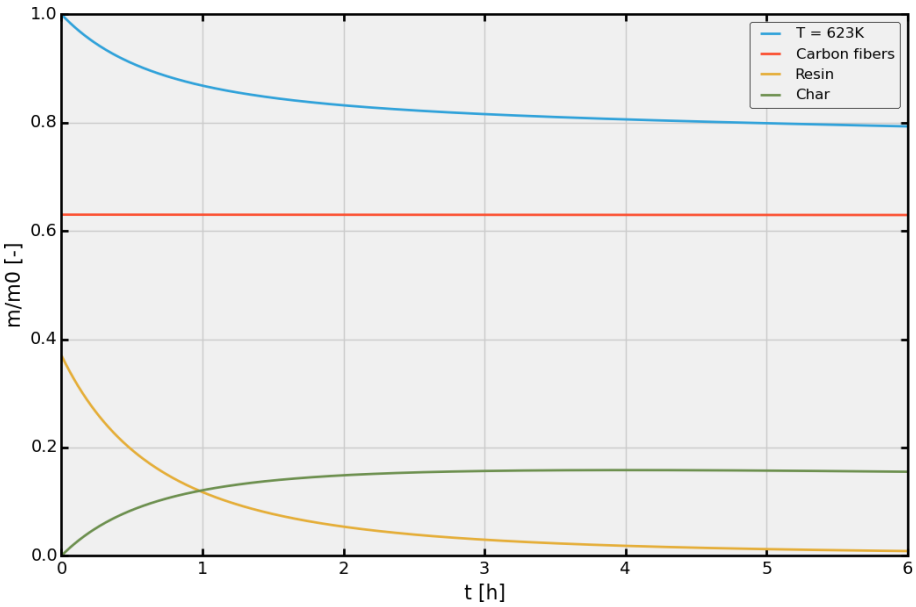

Figure 44 - Mass fraction reconstruction of solid species at $623K$ during 6 hour in air atmosphere

5 SPECTRAL EMISSIVITY

5.1. Experimental methodology

The approach used is a direct approach by comparison between the heat flux radiates from the sample surface and which from a black body at the same temperature of the sample. Excepting the presence of a folding mirror for the black body flux, the optical path for these two fluxes is similar. These fluxes are directed toward an Infrared Red Fourier Transform Spectrometer which analyses the spectral decomposition in the 2-20 µm range. The method principle is illustrated on the Figure 45.

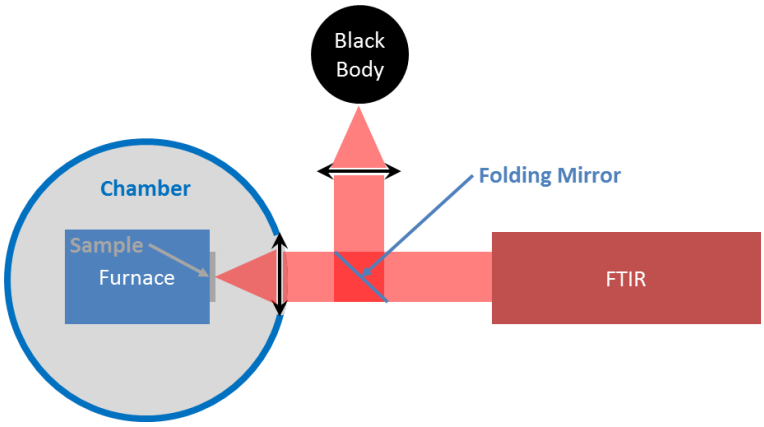

Figure 45 - Illustration of the emissivity principle

The temperature of the sample is imposed by the contact with a resistive heating furnace. The temperature range is limited by the emissivity of the material. In the case of the studied material, the lower temperature is around 150°C.

This furnace is positioned in a climate chamber in which the ambiance can be controlled in gas and pressure. In our case, all the results have been obtained by applying atmospheric pressure in air environment.

All samples have been cut from the 3809A_FSS_P7_P211-01_SS03 plate with the 7.9x18 mm^2 geometry. Samples in fibre direction and in the transverse direction has been cut has explained in the cutting plan e presented on Figure 46. Each sample is drilled in the thickness in order to include a thermocouple inside and monitor the temperature of the sample during the test (Figure 47).

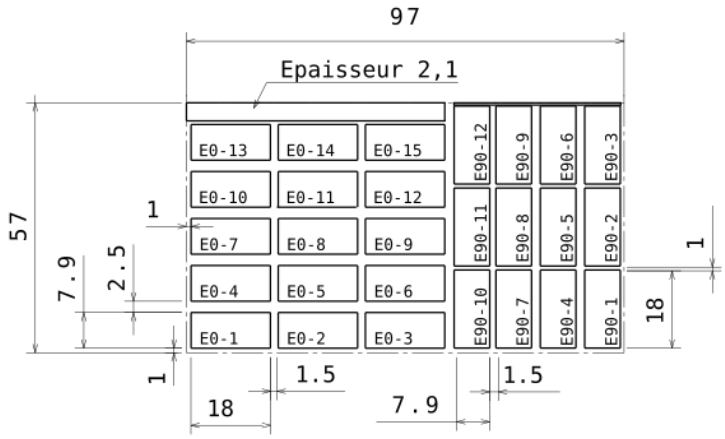

Figure 46 - Illustration of the cutting plane for emissivity samples

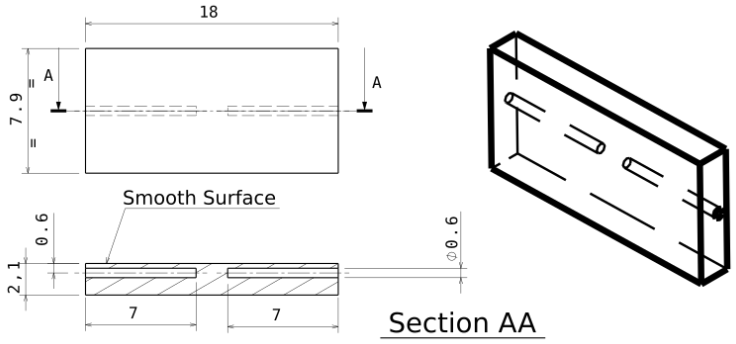

Figure 47 - Illustration of the position of the drill hole in each sample

In order to reduce the uncertainties of the temperature in the coupon, 2 holes are drilled. They also permit to characterize the offset between the furnace temperature which is monitored and the contact thermal resistance between the furnace and the sample (Figures 48). The emissivity of the sample is characterized on the smooth surface of the composite material.

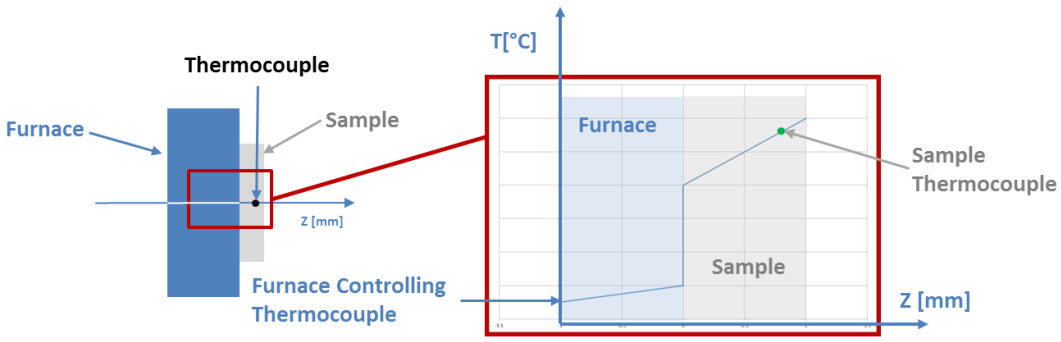

Figure 48 - Illustration of the evolution the temperature inside the sample and position of the thermocouples

5.2. Measurement technique

All the samples have been tested at 3 different temperatures (150°C, 175°C and 200°C) lower than the glass transition temperature (around 200-220°C) and sufficiently high for reducing the signal to noise ratio. For such temperatures, the black body signal is quite low at short wavelength in mid-infrared. Figures 49 present the evolution of the spectral radiance (thanks to the Planck law) and the useful spectrum which is determined from 0.5 λ_{Wien} to 4.5 λ_{Wien} (where λ_{Wien} is the Wien wavelength and corresponding to the maximum of the spectral radiance and defined by the Wien law).

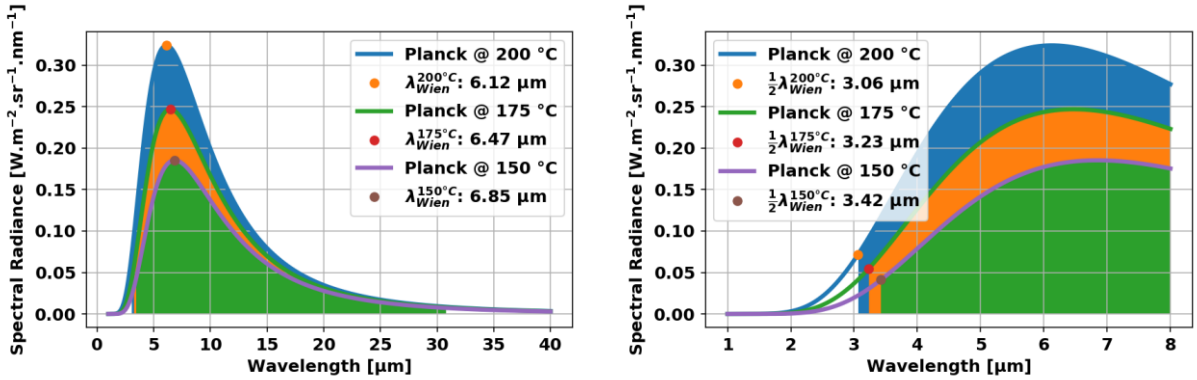

a/ Evolution of the spectral wavelength in mid-infrared for T= [150,175,200]°C

b/ Evolution of the spectral wavelength for short wavelength in the mid-infrared

Figure 49 – Useful spectrum in the mid-infrared for temperature [150,175,200]°C

Hence for wavelength lower than 0.5 $\lambda_{Wien}(T)$, the spectral emissivity measurement are very noisy. Figures 50 present the evolution of the spectral emissivity for $[0]_8$ and for normal incidence. These figures highlight the noise for wavelengths lower than 0.5 $\lambda_{Wien}(T)$. Even if the measurement has been done in a range of 2-15 µm by a step of 0.1 µm, only the measurement in the useful spectrum will be presented in the following.

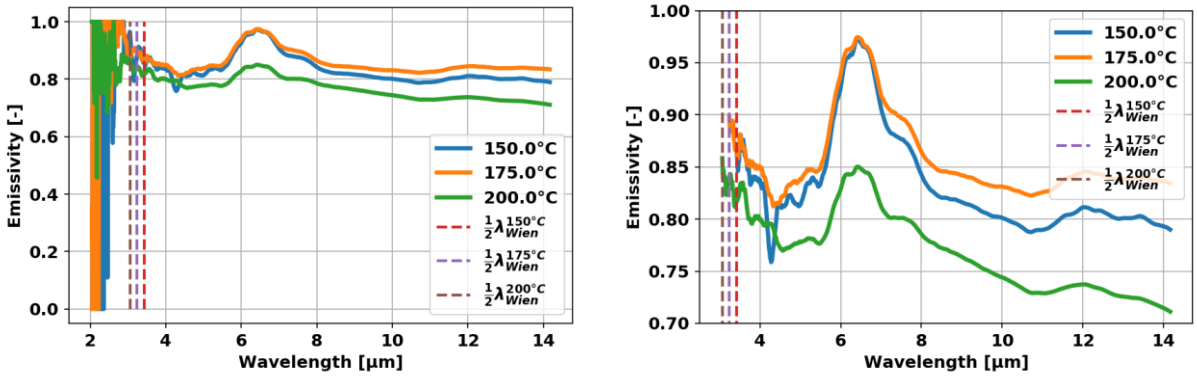

a/ Emissivity from 2 µm to 15 µm

b/ Emissivity only on the useful spectrum

Figure 50 – Evolution of the normal spectral emissivity for $[0]_8$ for temperature [150,175,200]°C

Each measurement is deduced from the mean of 32 acquisition points. The spectrum is then filtered by a centred moving average method. For each imposed temperature, a stabilization time of 1500 s is imposed to the furnace before the first radiation acquisition and the measurement has been done in air at ambient pressure.

5.3. Results for normal incidence

Figures 51 present the evolution of the spectral emissivity for $[0]_8$ and $[90]_8$.

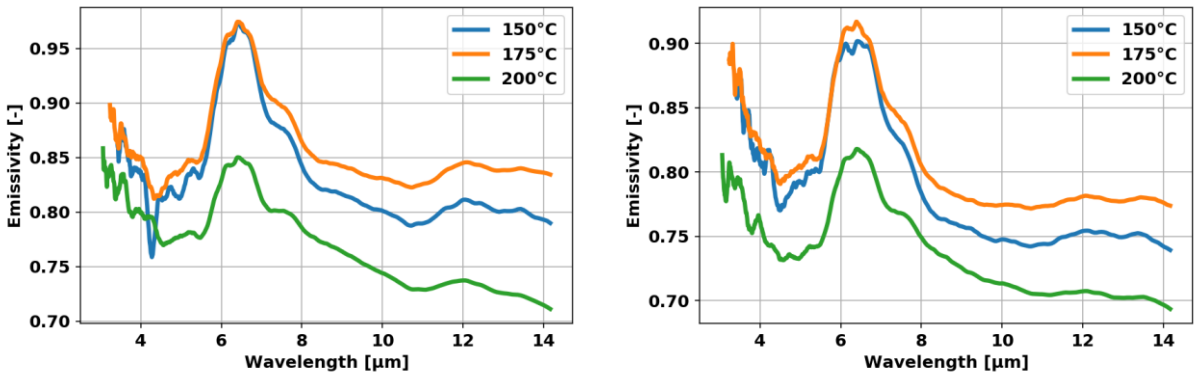

a/ Influence of the temperature on the spectral emissivity for $[0]_8$ sample and for normal incidence

b/ Influence of the temperature on the spectral emissivity for a $[90]_8$ sample and for normal incidence

Figure 51 – Evolution of the spectral emissivity for $[0]_8$ and $[90]_8$ for temperature [150,175,200]°C and for normal incidence

These figures highlight a decrease of the spectral emissivity for temperature close to the glass transition temperature. They also mention a similar trend for the 2 orientations as expected. Nevertheless a surprising low discrepancy between longitudinal and transverse measurement is observed. This difference is only due to the results disparity which is quite important from one sample to another and mainly the consequence of the material surface condition. The error measurement is estimated to around 5% by using test on reference samples with known emissivity coating for these temperatures and emissivity ranges. Hence these measurements can be used to estimate the influence of the surface condition. The Figures 52-54 compare the results for the 3 different temperatures between $[0]_8$ and $[90]_8$ and highlight the good agreement between the two orientations by taking into account the error measurement.

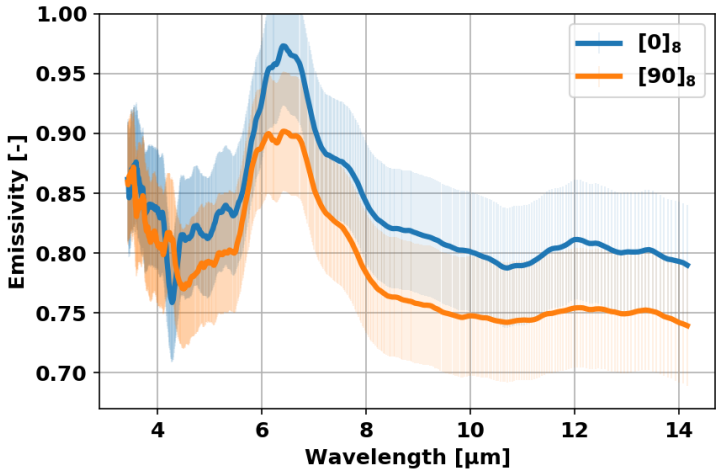

Figure 52 – Comparison of the spectral emissivity for normal incidence for $[0]_8$ and $[90]_8$ samples at 150°C

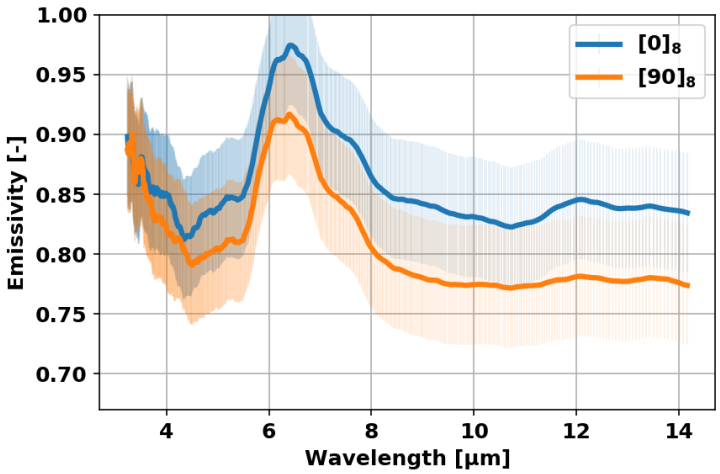

Figure 53 - Comparison of the spectral emissivity for normal incidence for $[0]_8$ and $[90]_8$ samples at 175°C

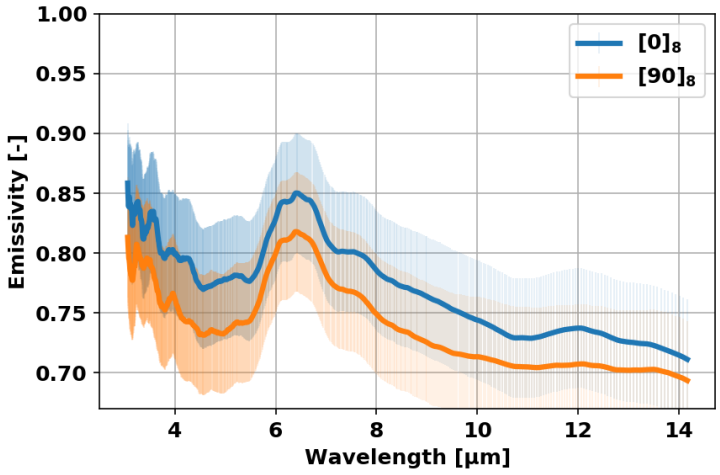

Figure 54 - Comparison of the spectral emissivity for normal incidence for $[0]_8$ and $[90]_8$ samples at 175°C

5.4. Results for angular incidence

The angular spectral emissivity has been measured for the three same temperatures, for the two same different orientations and for 3 different angles 45°, 60° and 75°. Figures 55-57 present the influence of the temperature on the spectral spectrum for 3 studied angles for $[0]_8$ composite laminates. Figures 58-60 present the influence of the temperature on the spectral spectrum for 3 studied angles for $[90]_8$ composite laminates. The Figures 61-63 present the influence of angular incidence on the spectral emissivity for the 3 different imposed temperatures. With the increase of the angular incidence, the spectral emissivity decreases. Nevertheless, the influence of the angular incidence on the evolution of the spectral emissivity is more important for $[0]_8$ than for $[90]_8$. Moreover the evolution of the spectral emissivity with the angular incidence is not Lambertian. Concerning the influence of the temperature, it could be considered similar whatever the observation direction is.

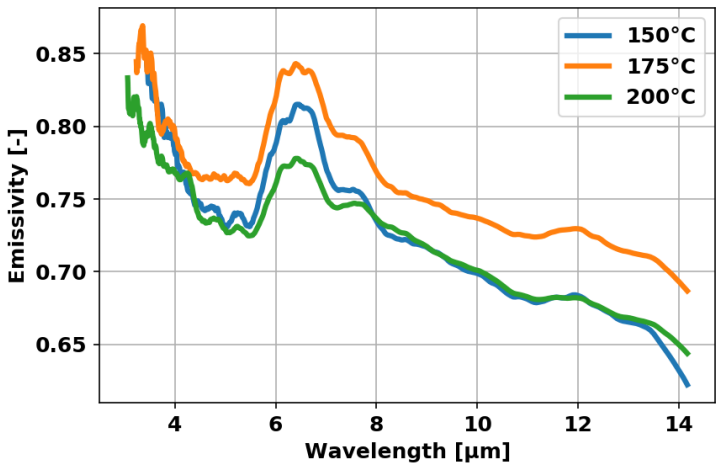

Figure 55 – Influence of the temperature on the spectral emissivity at 45° incidence for $[0]_8$

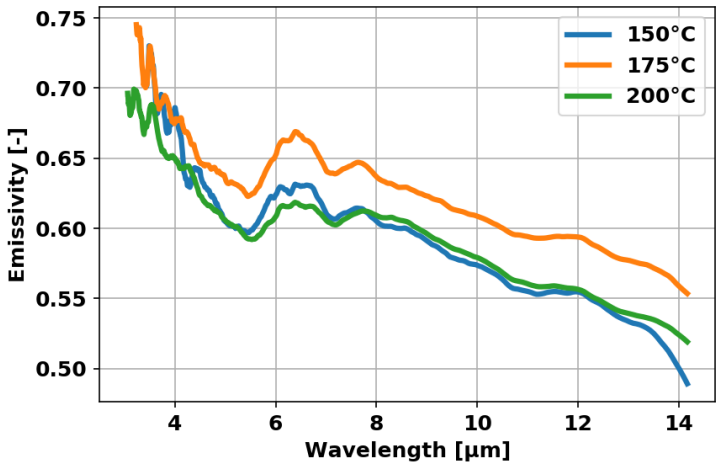

Figure 56 – Influence of the temperature on the spectral emissivity at 60° incidence for $[0]_8$

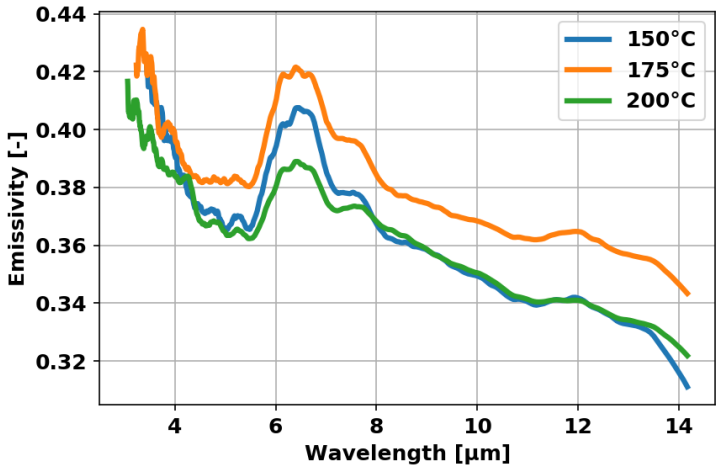

Figure 57 – Influence of the temperature on the spectral emissivity at 75° incidence for $[0]_8$

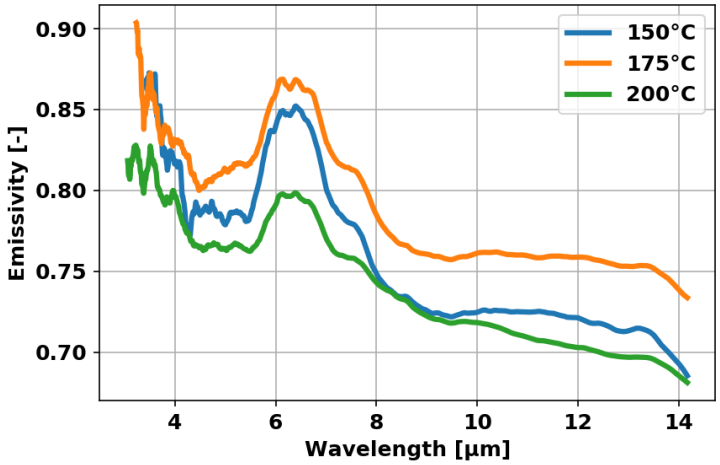

Figure 58 – Influence of the temperature on the spectral emissivity at 45° incidence for $[90]_8$

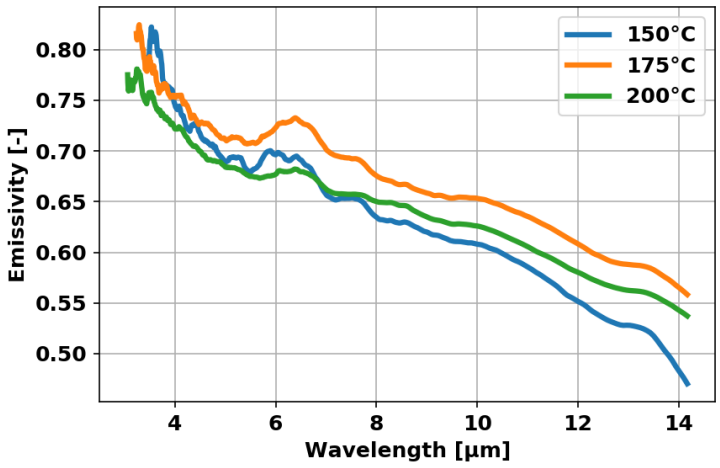

Figure 59 – Influence of the temperature on the spectral emissivity at 60° incidence for $[90]_8$

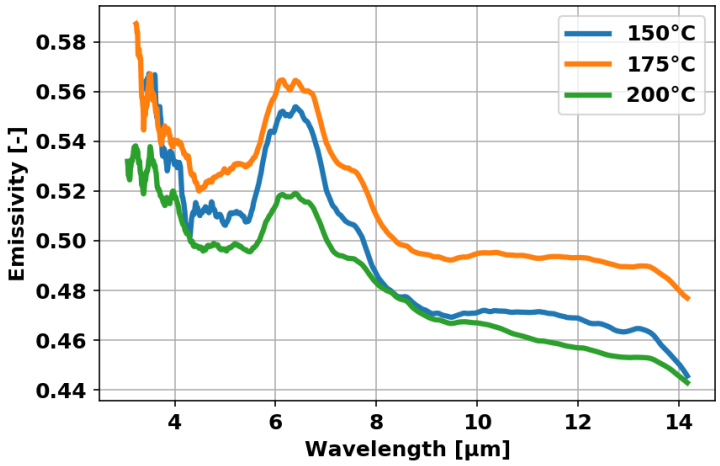

Figure 60 – Influence of the temperature on the spectral emissivity at 75° incidence for $[90]_8$

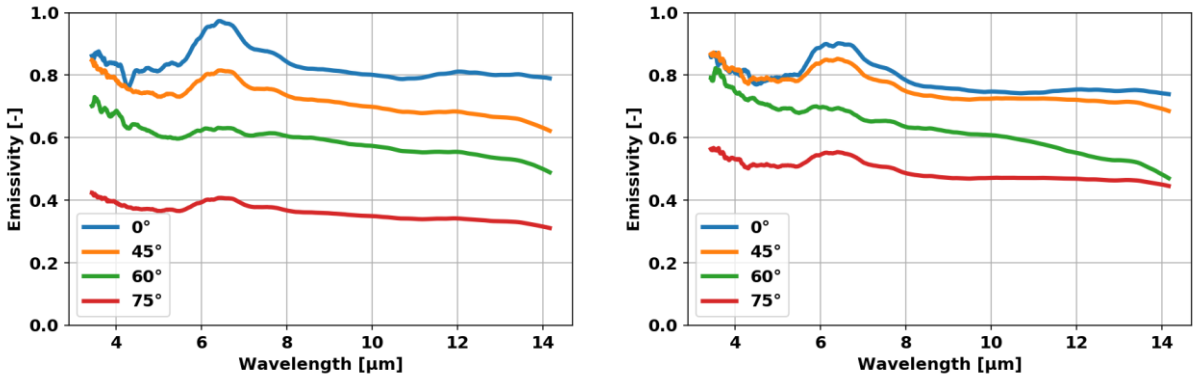

a/ Spectral emissivity for $[0]_8$ samples **b/ Spectral emissivity for $[90]_8$ samples**

Figure 61 – Influence of the angular incidence on the spectral emissivity at 150°C

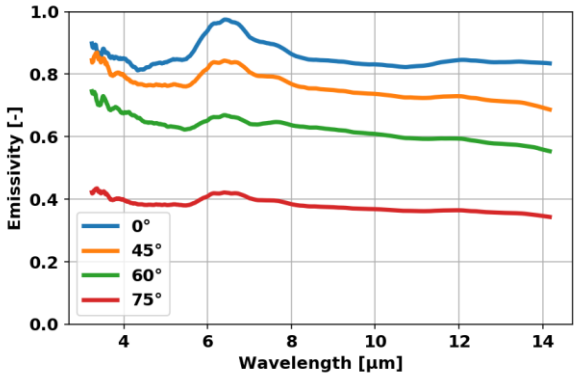

a/ Spectral emissivity for $[0]_8$ samples

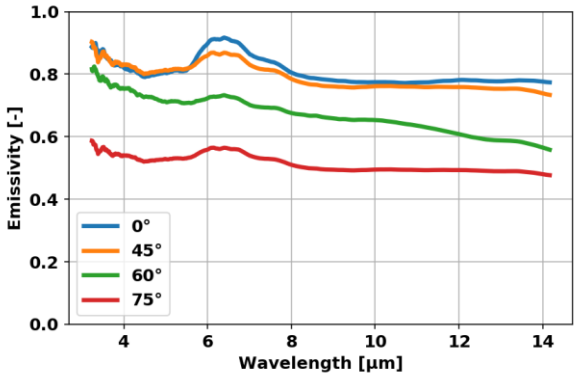

b/ Spectral emissivity for $[90]_8$ samples

Figure 62 – Influence of the angular incidence on the spectral emissivity at 175°C

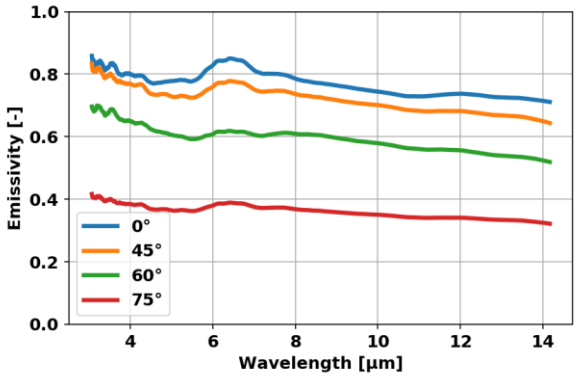

a/ Spectral emissivity for $[0]_8$ samples

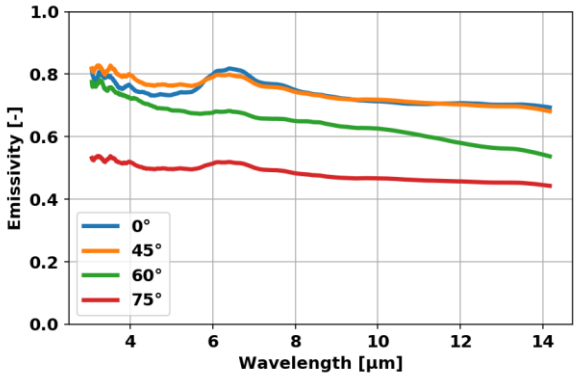

b/ Spectral emissivity for $[90]_8$ samples

Figure 63 – Influence of the angular incidence on the spectral emissivity at 200°C

6 THERMAL CONDUCTIVITY TENSOR AND HEAT CAPACITY OF THE CHARRED MATERIAL

6.1. Experimental methodology

6.1.1. BLADE facility description

The BLADE facility named from the French ''Banc Laser de cAractérisation et de DEgradation'' (characterisation and decomposition laser facility) and presented in Figure 64, is devoted, first, to the characterisation of thermo-physical properties of anisotropic materials [3] and second, to the analysis of the thermal response during decomposition of charring materials [4].

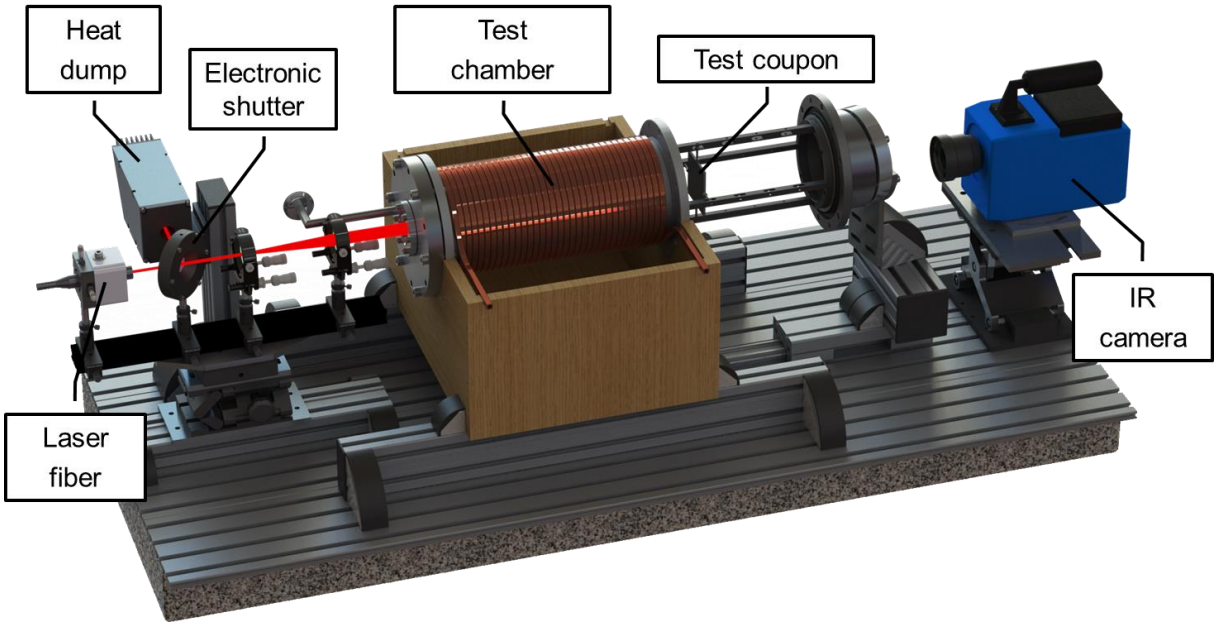

Figure 64 - Illustration of the BLADE facility: setup and instrumentation

Even if the apparatus is original, its principle is simple (Figure 65). A square-shaped ($80 \times 80\ mm^2$) test coupon is located within an air-filled pressure- and temperature-regulated test chamber. The specimen holder consists of 4 small nylon screws for the coupon to stand up straight with minimum contact and thermal loss by conduction. A continuous laser is used to heat up the front side of the test coupon. The laser generates a Gaussian monochromatic beam at the wavelength of $\lambda = 1080\ nm$, collimated at $\emptyset = 21.8\ mm$ at $1/e^2$ and with a maximum power of $50\ W$. The exposure time is accurately controlled with an electronic reflective shutter the diaphragm of which either directs the beam towards a heat dump or opens to heat the coupon up. The transient temperature at the back (unheated) side of the test coupon is measured using quantitative infrared thermography from the test coupon at the initial cold temperature, then during the heating phase up to the cooling phase when the shutter diaphragm is closed and the laser switched off.

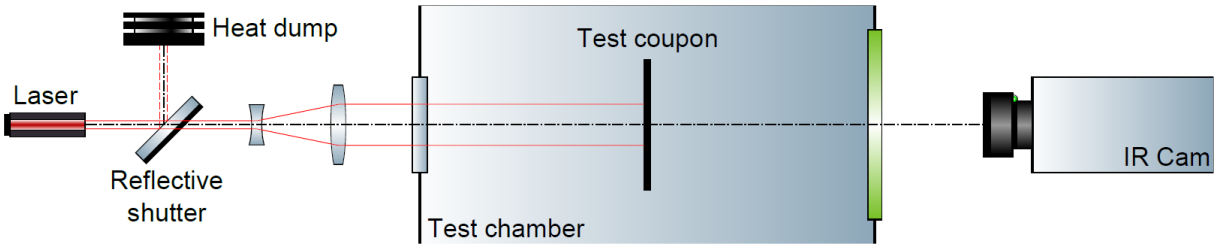

Figure 65 - Principle of the experiments: thermo-physical characterisation and laser-induced decomposition of charring materials

A key feature of the apparatus is an accurate control of the test conditions with respect to some conventional standard tests. The temperature regulation is applied to the chamber outer cylindrical surface using a coolant fluid flowing through a copper tubing coil. The heat transfer from the coil to the chamber is governed by conduction: a thermally conductive compound ensures a good contact and glass wool (not represented in Figure 64) isolates the test chamber from the surrounding environment. Within the test chamber, the temperature regulation of the test coupon is governed only by radiation. The inner surface of the test chamber is coated with a high emissivity black paint to maximise the exchanges. Moreover, the internal pressure is decreased by a vacuum pump that runs continuously during the experiments. The nominal value is set down to $5\,mBar$ $(500\,Pa)$ which is low enough to avoid any convective heat transfer and prevent volatiles from flaming. Indeed, the determination of the convective heat transfer coefficient would have been very difficult even in a simple geometrical configuration. Moreover, constant values or conventional correlations may not be representative enough to model the convective exchanges with the surrounding environment either for natural convection or forced convection if an exhaust hood is used.

Another key feature of the BLADE facility consists in using a laser instead of a flame to heat the coupon up during the experiment. As mentioned in the introduction, fire is a complex phenomenon and the heat flux magnitude and distribution on the material exposed surface may be very difficult to assess accurately and reliably. Instead, the laser provides a heat source, stable in space and time, and characterised experimentally preliminary to the tests. The Gaussian distribution of the beam creates a non-uniform heating on the exposed surface which helps revealing the anisotropic behaviour of such composite laminates.

6.1.2. Measurement technique

The temperature measurement is based upon the quantitative infrared thermography technique included in the BLADE facility. The infrared camera is a FLIR SC7210 equipped with a mid-wave $[3-5\,\mu m]$ high sensitivity InSb detector, $320 \times 256\,pixels$ resolution, low noise and high dynamic range. The camera offers an accurate external triggering feature which allows synchronisation of the image capture to other external devices such as the electronic shutter.

With respect to the expected temperature increase on the back surface of the test coupon, different integration times are used with specific calibrations for each temperature range to cover accurately the behaviour of the material with a reliable temperature resolution. The accuracy is given at $\pm 1°C$ of the temperature expressed in $°C$ between $[0 - 100°C]$ and $\pm 1\,\%$ above. The reconstruction of the instantaneous camera images is then processed from the data at the four integration times to assess for each pixel of the field of interest the right temperature according to its range.

The acquisition frequency is $50\ Hz$; consequently, the time period between each reconstructed image is $0.02\ s$.

The thermal analysis only relies on this technique for the measurements to remain non-intrusive, and for the test conditions at the material surfaces to be well-known.

6.2. Measurements overview and global properties analysis

6.2.1. Preparation of the test coupons

The specimens tested in the BLADE facility and presented in this study are prepared and conditioned from the panels provided by CEiiA. Water jet cutting is used to prepare the test coupons to the required dimensions for the BLADE facility.

The coupons can be seen in Figure 66. One surface is smooth while the other is rough due to the manufacturing process.

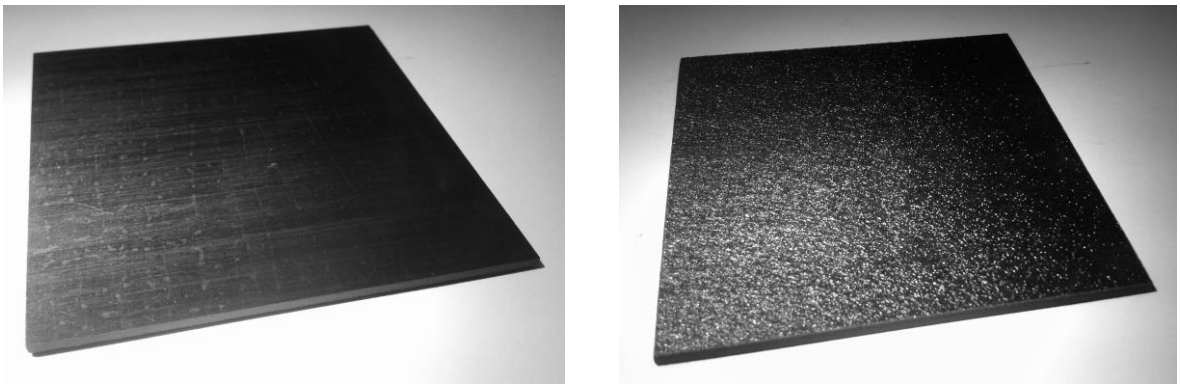

(a) Smooth surface (b) Rough surface

Figure 66 - Water jet cut test coupons before charring

One panel is used for each layout to assess the thermophysical properties of the material. The associated references are given in Table 4:

Coupon reference	Stacking sequence	Dimensions
3809A_FSS_P7_P208-01_SS02#01	$[0]_8$	$80 \times 80 \times 2.1\ \mathrm{mm}^3$
3809A_FSS_P7_P227-01_SS06#01	[45/90/-45/0]s	$80 \times 80 \times 2.1\ \mathrm{mm}^3$

Table 4 - Reference of the virgin test coupons

The stacking sequence of the quasi-isotropic (denoted QI) coupons is: $[45/90/-45/0]_s$

The stacking sequence of the unidirectional (denoted UD) coupons is: $[0]_8$

The coupons are then cured at $350\ °C$ during $5\ h$ to achieve the fully charred state of the material for thermal properties characterisation. The coupons are held tight between aluminium honeycombs in order to limit deformation and pressure increase by helping volatiles to be released from the materials.

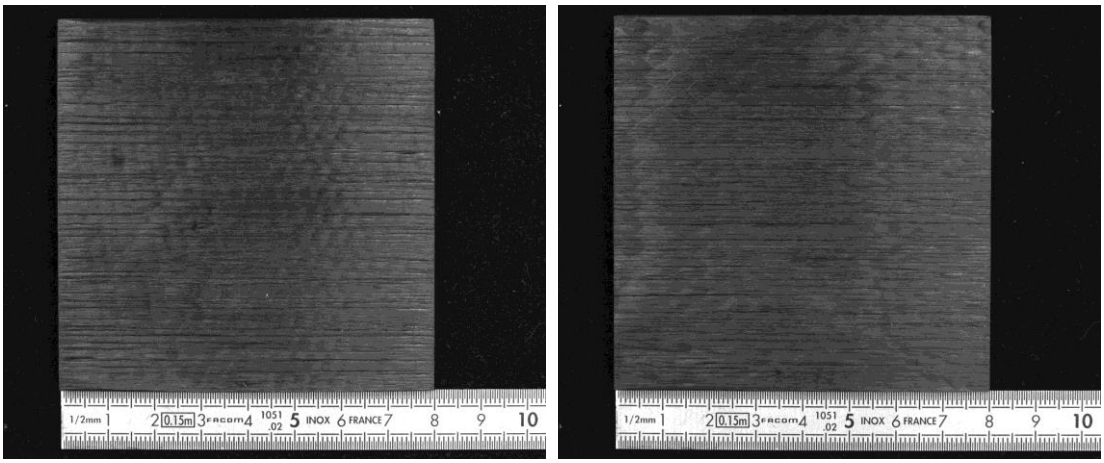

(a) Smooth surface (left UD, right QI)

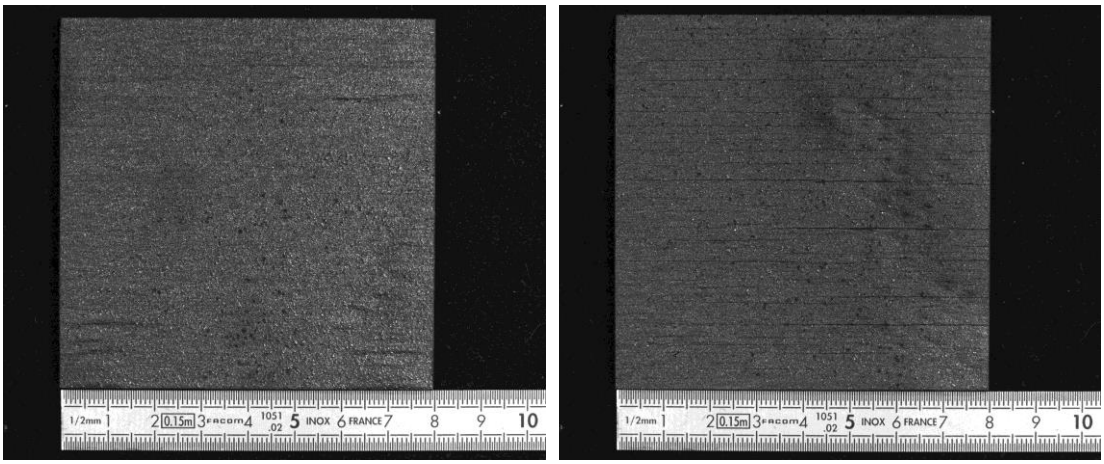

(b) Rough surface (left UD, right QI)

Figure 67 - Water jet cut test coupons after charring

Stacking sequence	Initial mass [mg]	Dimensions	Final mass [mg]	Effective charred density [kg/m3]
$[0]_8$	21.4730	$80.03 \times 79.46 \times 2.76\ \text{mm}^3$	17.9040 $(-16.62\ \%)$	1020
$[45/90/-45/0]_s$	21.1853	$80.07 \times 80.10 \times 2.82\ \text{mm}^3$	17.4654 $(-17.56\ \%)$	966

Table 5 - Reference of the charred test coupons

For all the tests presented hereafter, the infrared thermography is performed on the smooth surface of the material. As a consequence, the heat flux generated by the laser is applied on the rough surface.

6.2.2. Test matrix

The test matrix for the thermophysical properties assessment consists in performing 3 repeatability tests for each temperature applied on the test chamber as for the virgin material. Two temperature levels are chosen within the operating range of the BLADE facility because the thermal properties of the virgin material follow a first-order polynomial form.

The test matrix is detailed in Table 6.

Test #	*Stacking sequence*	$T_{chamber}$ [°	$I_{laser}\ [A]$	$t_{laser}\ [s]$	$t_{acq}\ [s]$	$f_{acq}\ [Hz]$	$T_{atm}\ [°C]$
214	QI	22	12	5	60	50	23.9
215	QI	22	12	10	80	50	23.9
216	QI	22	12	10	80	50	23.9
217	UD	22	12	10	80	50	23.9
218	UD	22	12	10	80	50	23.9
219	UD	22	12	10	80	50	23.9
220	UD	70	12	10	50	50	24.9
221	UD	70	12	10	50	50	25.2
222	UD	70	12	10	50	50	25.2
223	ISO	70	12	10	50	50	25.4
224	ISO	70	12	10	50	50	25.3
225	ISO	70	12	10	50	50	25.5

Table 6 - Test matrix for the thermophysical properties assessment of the charred material

6.2.3. Test protocol

They are placed successively within the test chamber regulated at the initial temperature ($T_{chamber}$) and the pressure is lowered down to $5\,mBar$ for all the experiments. Temperature stabilisation of the specimens is ensured before each test to begin. It is essential to note that the thermal exchanges with the chamber walls only result from radiative heat transfer not only initially but also during the whole test since convective heat transfer is avoided. The orientation of each test coupon in the experiment is

precisely performed by aligning the fibre direction of the first ply of the laminate along the horizontal direction.

The test protocol simply consists in running the IR acquisition $1\,s$ before subjecting the specimen to the laser heat flux during $5\,s$. The laser generates a constant, steady but non-uniform heat flux that creates a thermal loading locally on the centre of the material front surface. Finally, the IR camera keeps on measuring the temperature up to $t = 30\,s$ while the laser is switched off and the test coupon is cooled down thanks to radiative exchanges with the chamber walls.

6.2.4. Optimisation process

It is important to notice that both the heating phase and the cooling phase are important in the optimisation process because the first is relevant to the thermal response during the laser exposure and the second is relevant to thermal losses due diffusion within the material and radiation with the test chamber. Agreement on both phases ensures a good accuracy considering the thermal loading and boundary conditions.

Input data for the optimisation process to assess the thermophysical properties are then a couple of tests performed at different initial temperature. The material density is assumed to be known at the given values listed in Table 2. The test coupon exact dimensions are used to model the material numerically. The computational grid is based on the pixels distribution of the region of interest the IR images to model the material surface. The grid is then extruded in the through-thickness direction with a number of cells calculated with respect of a relevant Fourier number to ensure stability of the computation with the direct heat conduction solver THIDES.

Temperature dependency is evaluated with different choices for the couples of tests. The thermal behaviour laws are then calculated on the whole temperature range available with the BLADE facility from the batch of optimisation computations.

One optimisation computation with a couple of test results takes about 8 to 10 hours of CPU-time to converge to the right thermophysical properties. As a consequence, all tests detailed in Table 6 have not been used to assess the properties. Instead, repeatability is evaluated from the 3 test results performed at the same initial temperature. And then, one out of the three tests is used for each initial temperature condition. As a result, only 2 tests are used for the optimisation process for each test coupon.

6.2.5. Optical surface properties

Emissivity and absorptivity must be characterized in order to convert the signal from the IR camera to quantitative temperatures. Those optical surface properties must be assessed as a function of the wavelength and of the decomposition state. Moreover, because the front and back surfaces are different (smooth or rough) due to the manufacturing process, measurements shall be done on both surfaces. The ply orientation has no effect on virgin properties but when the coupon is fully charred, fibres are visible

and they can affect the measurements. Therefore, measurements are performed on both orientations (0° and 90°) to consider both coupon possible orientation during the experiments.

Values in Figure 68 are used for temperature conversion on charred material characterisations and also on laser and fire-induced decomposition experiments. Virgin material characterisation requires black paint coating.

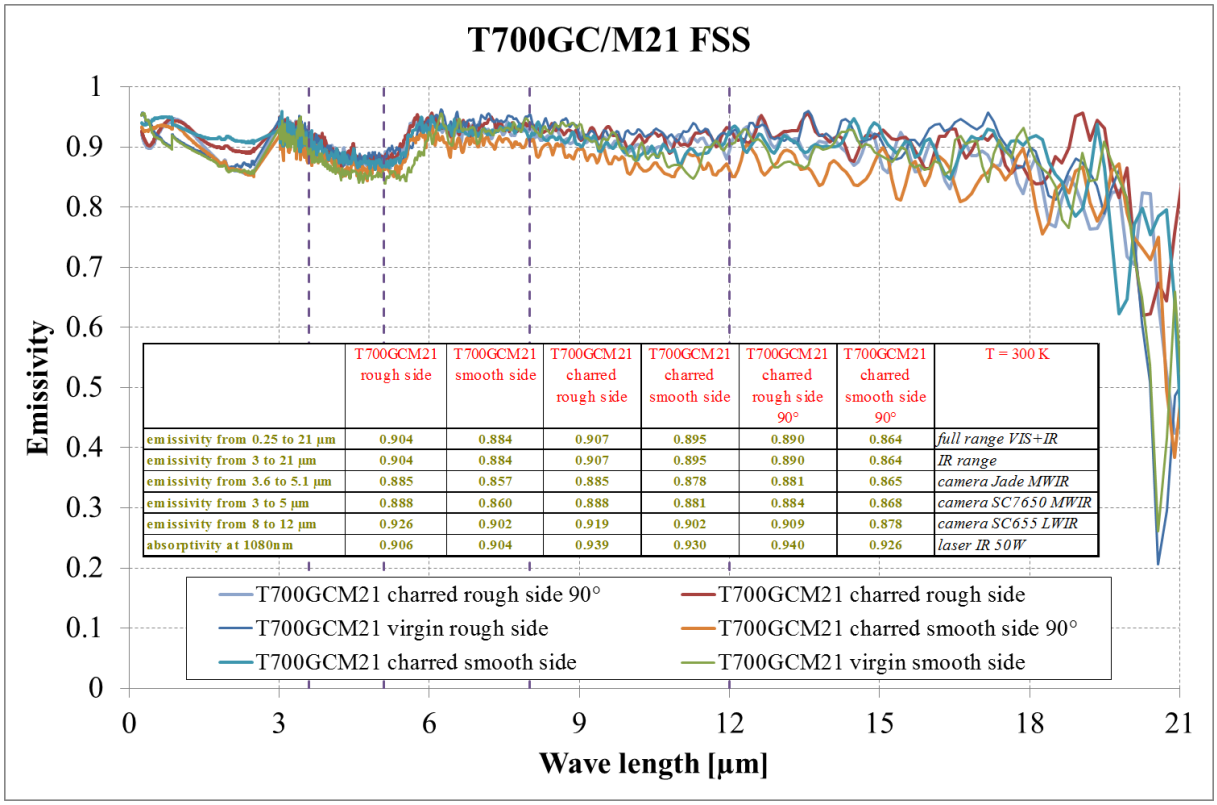

	T700GCM21 rough side	T700GCM21 smooth side	T700GCM21 charred rough side	T700GCM21 charred smooth side	T700GCM21 charred rough side 90°	T700GCM21 charred smooth side 90°	T = 300 K
emissivity from 0.25 to 21 µm	0.904	0.884	0.907	0.895	0.890	0.864	*full range VIS+IR*
emissivity from 3 to 21 µm	0.904	0.884	0.907	0.895	0.890	0.864	*IR range*
emissivity from 3.6 to 5.1 µm	0.885	0.857	0.885	0.878	0.881	0.865	*camera Jade MWIR*
emissivity from 3 to 5 µm	0.888	0.860	0.888	0.881	0.884	0.868	*camera SC7650 MWIR*
emissivity from 8 to 12 µm	0.926	0.902	0.919	0.902	0.909	0.878	*camera SC655 LWIR*
absorptivity at 1080nm	0.906	0.904	0.939	0.930	0.940	0.926	*laser IR 50W*

Figure 68 – Emissivity/Absorptivity measurements on virgin and charred composite surfaces

6.2.6. Measurements analysis

The results presented in the sections hereafter from Figure 69 to Figure 70 for the quasi-isotropic laminate and from Figure 71 to Figure 72 for the unidirectional laminate. For each chamber temperature, the figures show:

a) The thermal response on the back surface measured by the infrared thermography camera when the maximum temperature is reached for the third of the triplicate tests;
b) The temperature evolution extracted from the infrared measurements at different locations from the centre on a horizontal profile for the third of the triplicate tests;
c) The comparison of the temperature evolution on the horizontal profile for the 3 triplicate tests;
d) The temperature discrepancies with respect to the first test.

As described in the test matrix (Table 6), the exposure time and acquisition time have been adjusted to ensure a good signal-over-noise ratio.

The temperature measurements are affected by the charring process whatever the stacking sequence. The orthotropic diffusion of the temperature is still clearly noticeable if the two stacking sequences are compared. Both signals are noisier than those measured on the virgin material. Such response is induced by internal damage within the material such as micro-cracks that affect temperature diffusion. The identification of the thermal properties of such damaged materials should be difficult to perform because the thermal model used to compute the heat transfer is based on the continuous medium approach which may not be relevant anymore or may not result in accurate properties.

The reproducibility of the measurements is very satisfactory whatever the test conditions or stacking sequences.

6.2.6.1. Charred quasi-isotropic T700GC/M21

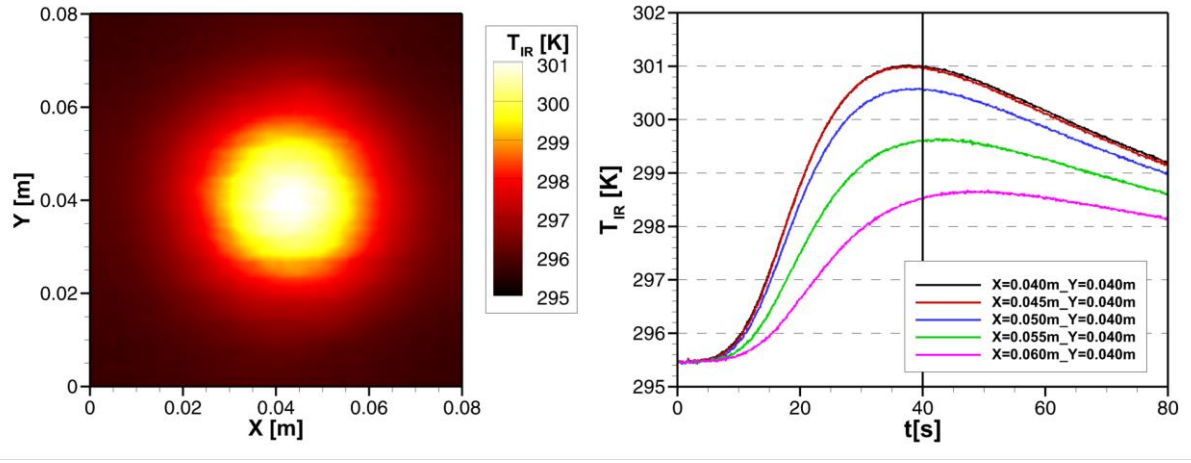

(a) Thermal response measured on the back surface at $t = 40\ s$

(b) Temperature evolution at different locations from the centre of the back surface

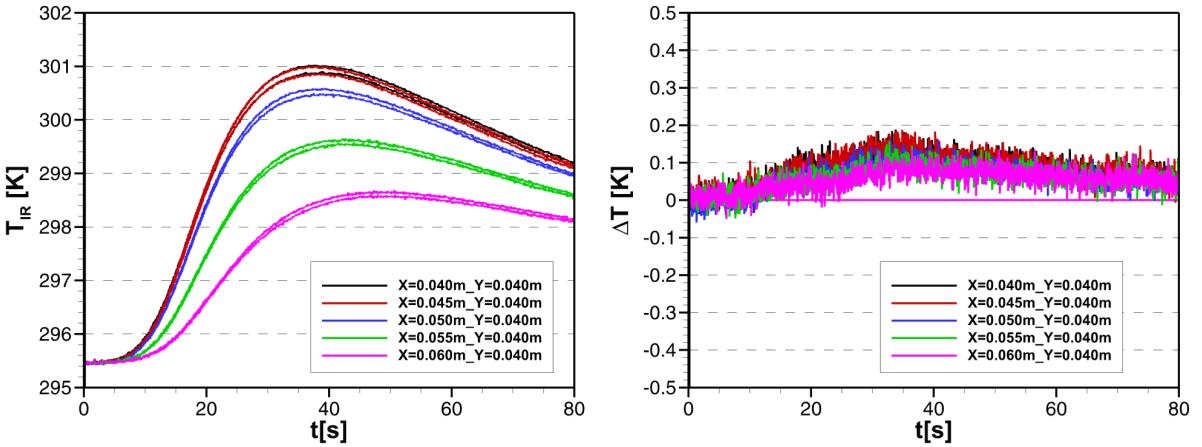

(c) Reproducibility of the measurements

(d) Measurement discrepancies with respect to the first test

Figure 69 – BLADE tests for charred T700GC/M21-QI at $T_{chamber} = 22\ °C$

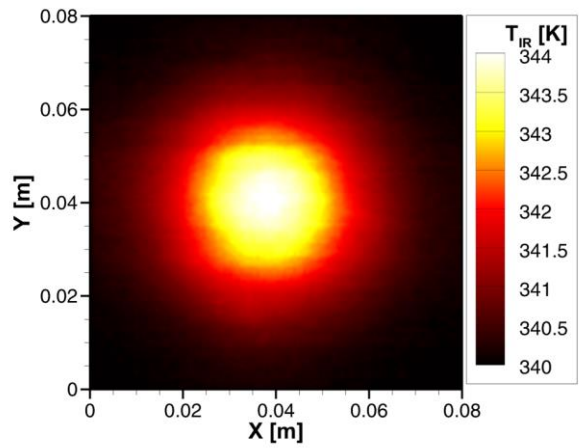

(a) Thermal response measured on the back surface at $t = 40\ s$

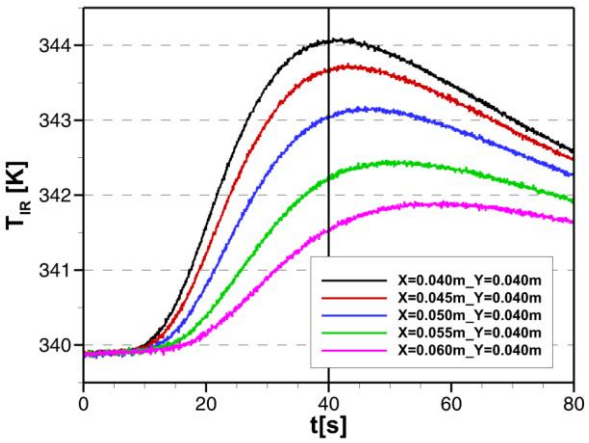

(b) Temperature evolution at different locations from the centre of the back surface

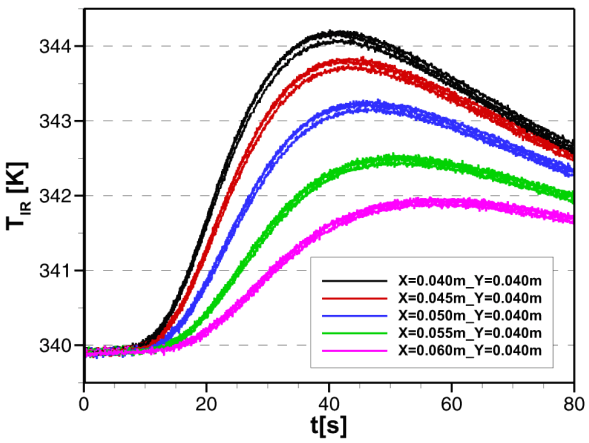

(c) Reproducibility of the measurements

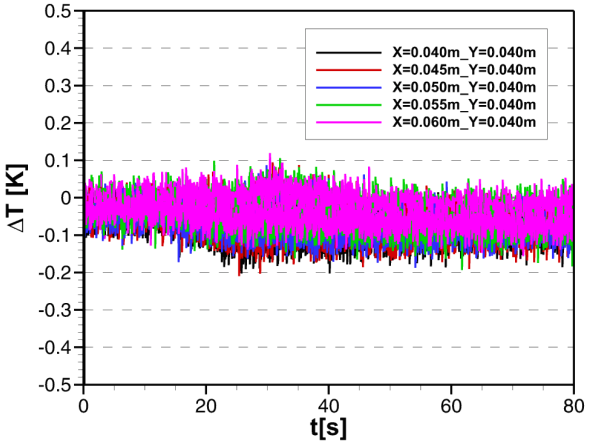

(d) Measurement discrepancies with respect to the first test

Figure 70 – BLADE tests for charred T700GC/M21-QI at $T_{chamber} = 70\ °C$

6.2.6.2. Charred unidirectional T700GC/M21

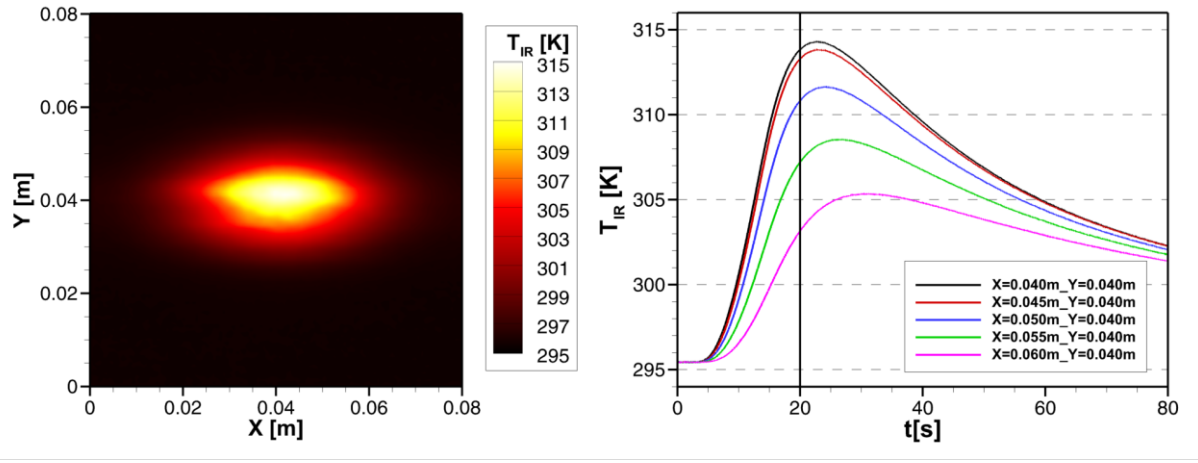

(a) Thermal response measured on the back surface at $t = 20\ s$

(b) Temperature evolution at different locations from the centre of the back surface

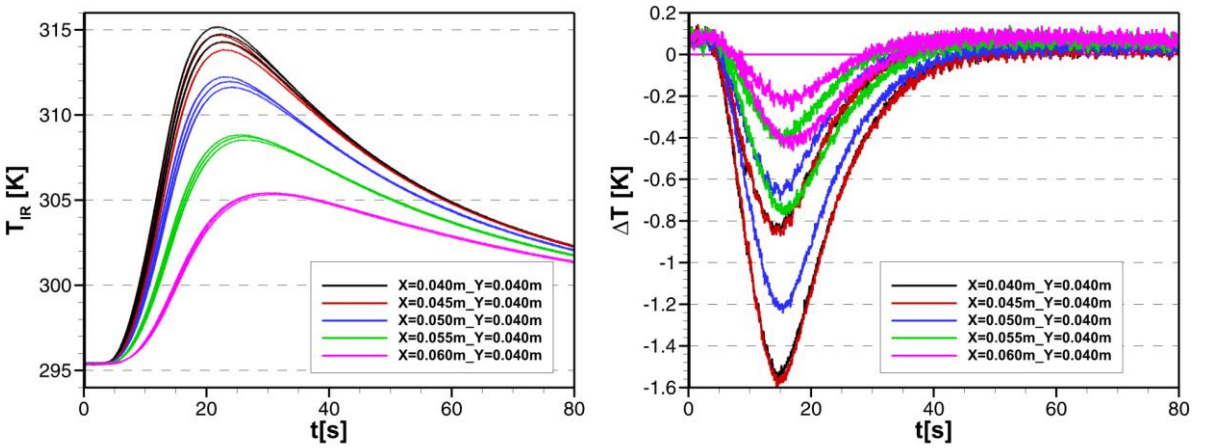

(c) Reproducibility of the measurements

(d) Measurement discrepancies with respect to the first test

Figure 71 – BLADE tests for charred T700GC/M21-QI at $T_{chamber} = 22\ °C$

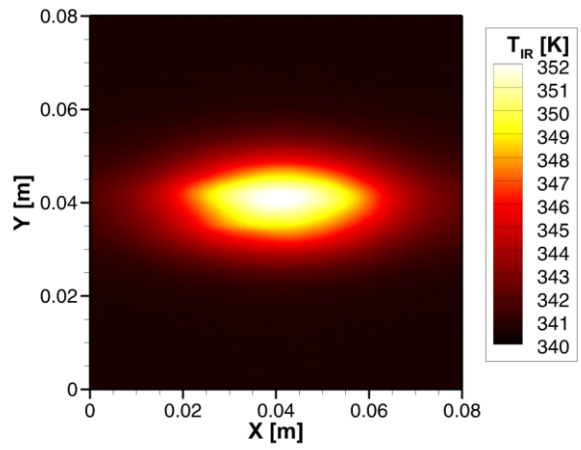

(a) Thermal response measured on the back surface at $t = 30\ s$

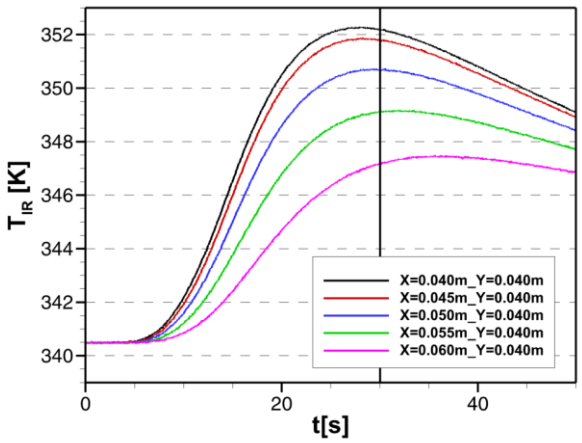

(b) Temperature evolution at different locations from the centre of the back surface

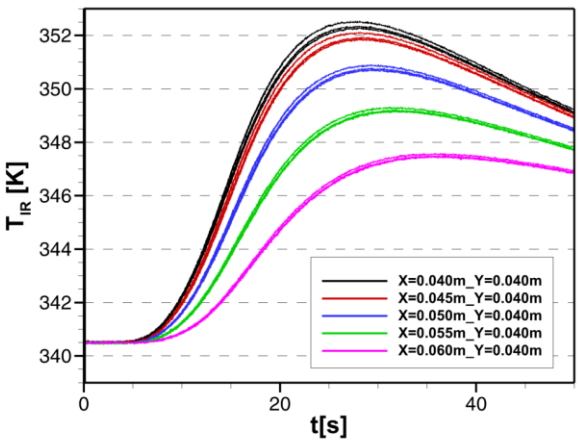

(c) Reproducibility of the measurements

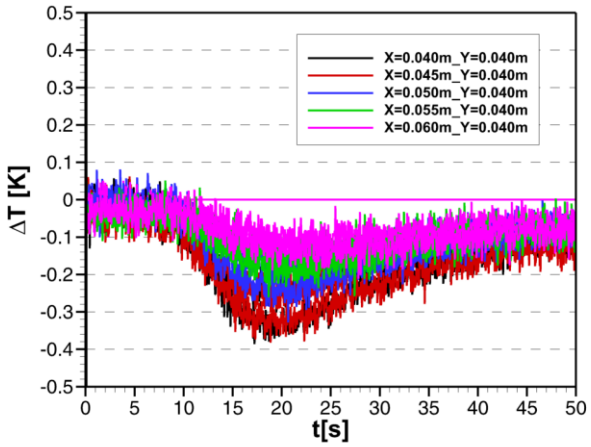

(d) Measurement discrepancies with respect to the first test

Figure 72 – BLADE tests for charred T700GC/M21-QI at $T_{chamber} = 70\ °C$

6.2.7. Thermophysical properties of the charred composite laminates

6.2.7.1. Charred quasi-isotropic T700GC/M21

Figure 73 and Figure 74 show the convergence of the properties assessment algorithm concerning:

a) the functional (temperature difference on the back surface between IR thermographic measurements and the optimal computation);
b) the specific heat;
c) the three main components of the thermal conductivity tensor.

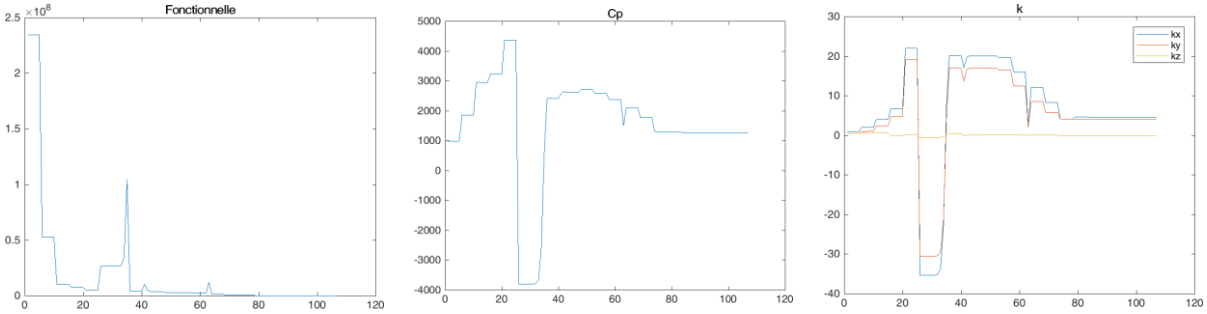

(a) Functional (b) Specific heat (c) Thermal conductivities

Figure 73 – Convergence of the properties assessment algorithm for test #216

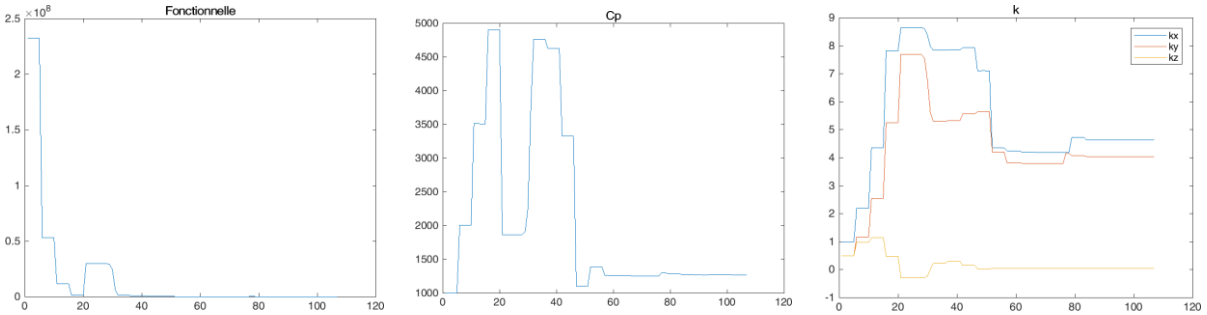

(a) Functional (b) Specific heat (c) Thermal conductivities

Figure 74 – Convergence of the properties assessment algorithm for test #225

Figure 75 exhibits the results of the optimisation process for both tests considered for the properties assessment with from left to right:

- temperature map measured by the thermographic camera when the maximum temperature is achieved;
- temperature map computed by the model with the optimal properties at the same moment;
- comparison of the temperature evolutions extracted from the centre of the back surface associated with the temperature difference between measurement and computation at the same location.

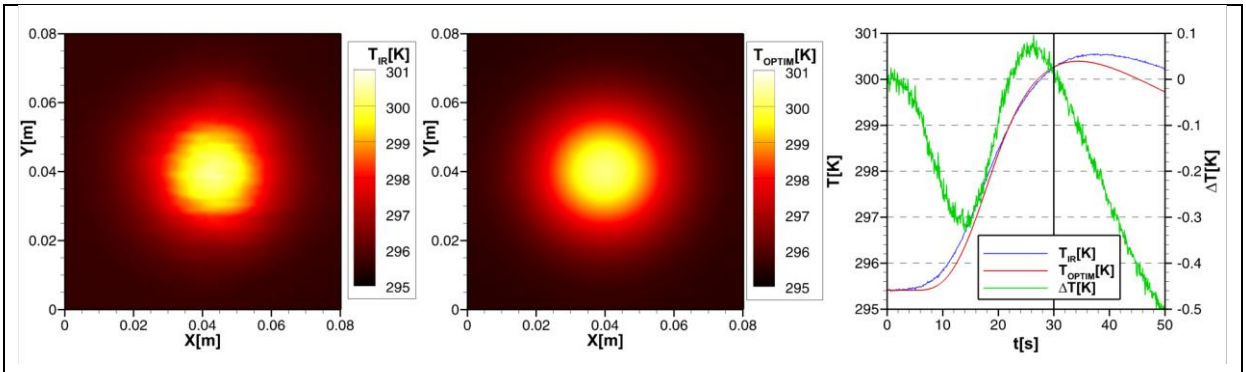

(a) Results for test #216

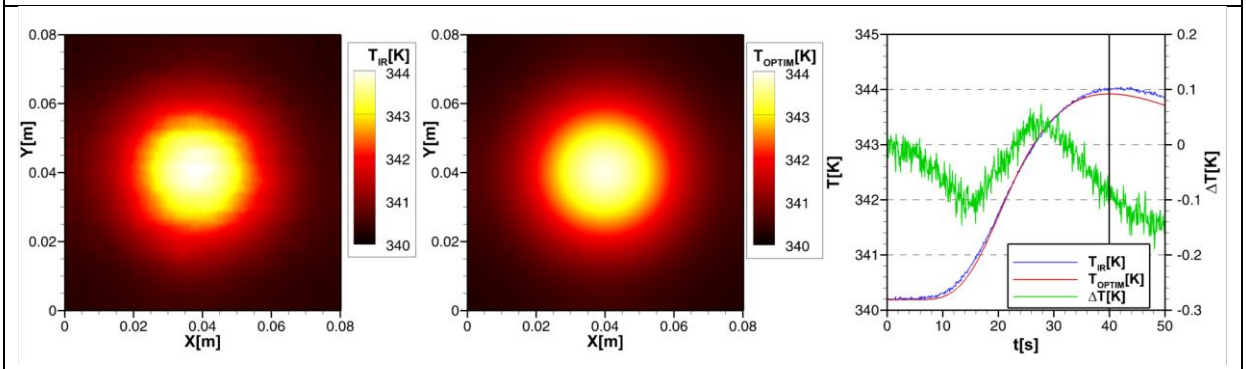

(b) Results for test #225

Figure 75 – Results of the properties optimisation process for the charred T700GC/M21-QI

The results are satisfactory on both temperature levels applied by the test chamber. The thermal behaviour of the material is clearly different at these two temperature levels while the laser heating is strictly identical in both cases. As a consequence, the identified properties should be different.

The identified properties are listed in Table 7 for the T700GC/M21 charred composite laminate with the quasi-isotropic stacking sequence.

Property	22 °C	70 °C
Specific heat C_P $[J/kg/K]$	1275	1256
Thermal conductivity k_x $[W/m/K]$	4.65	4.20
Thermal conductivity k_y $[W/m/K]$	4.05	3.80
Thermal conductivity k_z $[W/m/K]$	0.59E-01	0.45E-01

Table 7 – Thermal properties identified for the charred T700GC/M21-QI

6.2.7.2. Charred unidirectional T700GC/M21

On Figure 76 and Figure 77 are plotted the convergence of the properties assessment algorithm concerning:

a) the functional (temperature difference on the back surface between IR thermographic measurements and the optimal computation);
b) the specific heat;
c) the three main components of the thermal conductivity tensor.

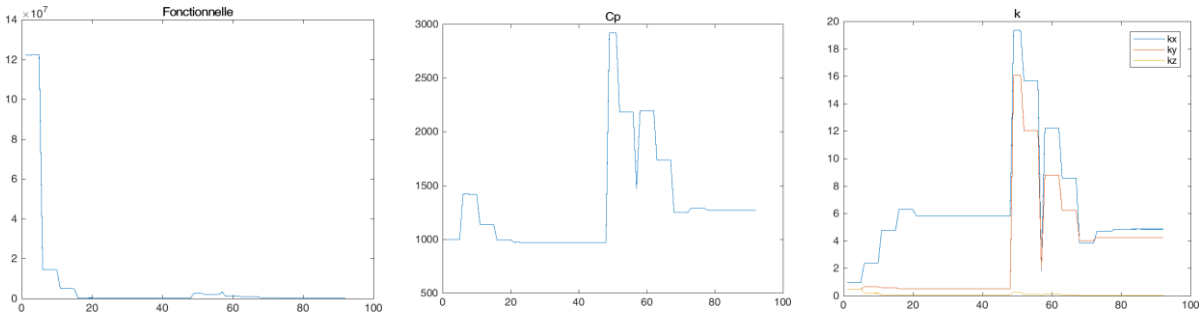

(a) Functional (b) Specific heat (c) Thermal conductivities

Figure 76 – Convergence of the properties assessment algorithm for test #219

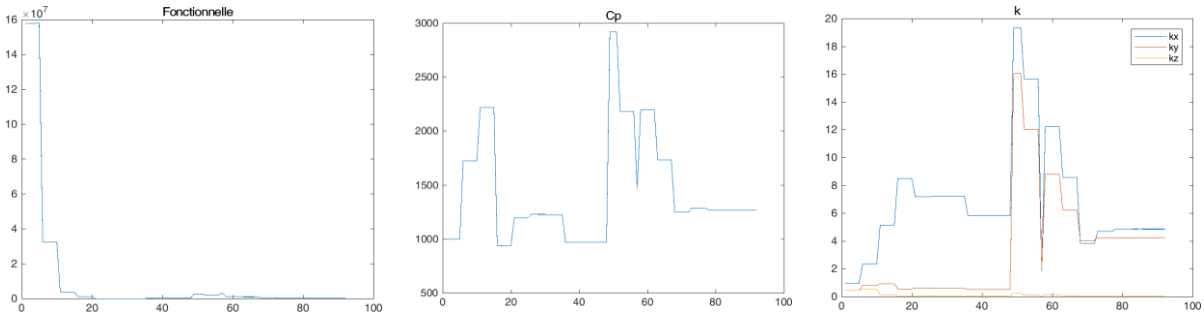

(a) Functional (b) Specific heat (c) Thermal conductivities

Figure 77 – Convergence of the properties assessment algorithm for test #222

Figure 78 shows the results of the optimisation process for both tests considered for the properties assessment from left to right:

- temperature map measured by the thermographic camera when the maximum temperature is reached;
- temperature map computed by the model with the optimal properties at the same moment;
- comparison of the temperature evolutions extracted from the centre of the back surface associated with the temperature difference between measurement and computation at the same location.

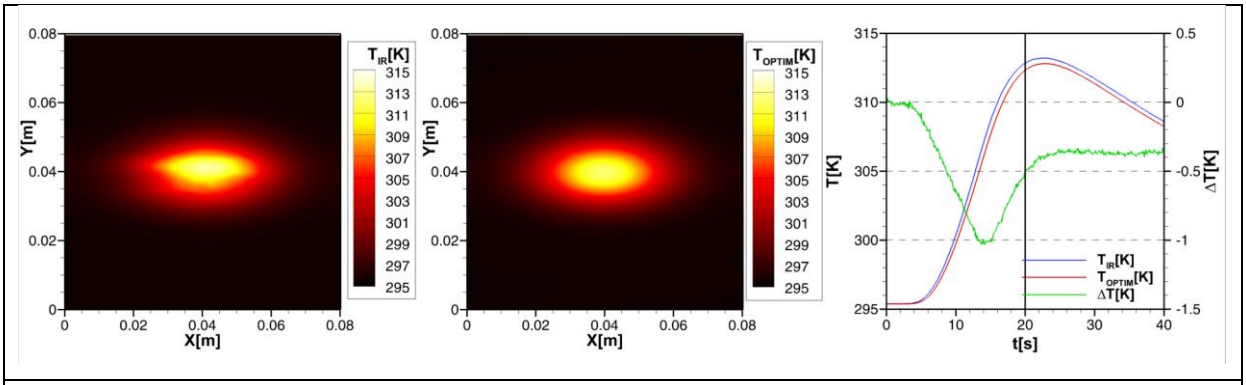

(a) Results for test #219

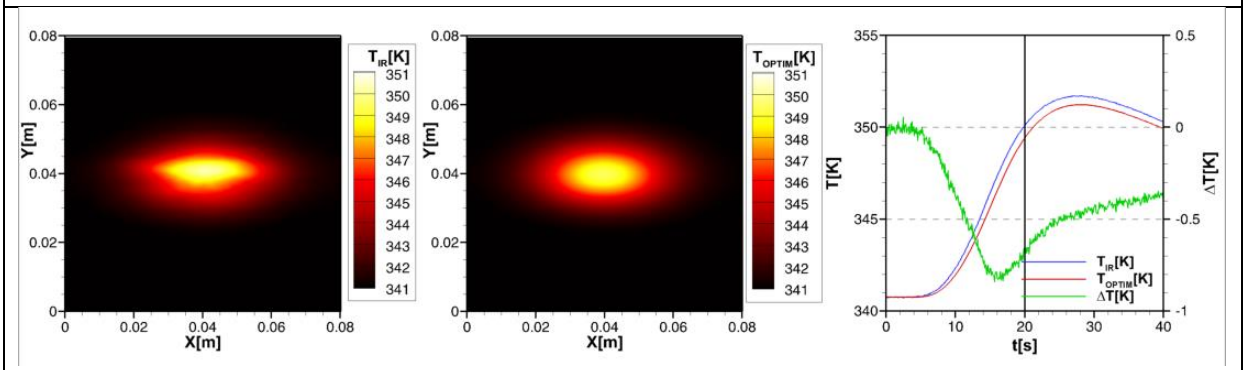

(b) Results for test #222

Figure 78 – Results of the properties optimisation process for the charred T700GC/M21-UD

The results are satisfactory on both temperature levels applied by the test chamber. The thermal behaviour of the material is clearly different at these two temperature levels while the laser heating is strictly identical in both cases. As a consequence, the identified properties should be different.

The identified properties are listed in Table 8 for the T700GC/M21 charred composite laminate with the unidirectional stacking sequence.

Property	22 °C	70 °C
Specific heat C_P $[J/kg/K]$	973	1231
Thermal conductivity k_x $[W/m/K]$	5.85	7.25
Thermal conductivity k_y $[W/m/K]$	5.30e-01	6.25E-01
Thermal conductivity k_z $[W/m/K]$	0.98E-01	0.86E-01

Table 8 – Thermal properties identified for the charred T700GC/M21-UD

7 LASER-INDUCED DECOMPOSITION

7.1. Experimental methodology

7.1.1. BLADE facility

The BLADE facility, depicted in section6.1.1, can be used as well for the analysis of the thermal response of decomposing composite materials [4]. The decomposition is induced by a laser the power of which is set high enough (up to $255\ kW/m^2$) to activate chemical reactions identified in section 3. Longer exposure time is applied on the material in order to investigate the transient thermal response on the back surface of the test coupon using thermographic measurements. Several integration times are programmed in the camera to perform the measurements because the temperature increase can be very high at such high heat flux. Each integration time is calibrated accurately to cover the associated temperature range. Then the images are combined to extend the dynamic range of the camera and to access to both resolution and accuracy detailed in section 6.1.2.

The test protocol for the laser-induced decomposition is similar to the protocol of properties assessment tests except for the exposure time and acquisition time which are obviously longer.

The laser source is calibrated to the desired maximum heat flux magnitudes.

7.1.2. Test matrix

The test matrix is detailed in Table 9 for the T700GC/M21-QI and Table 10 for the T700GC/M21-UD.

Test #	*Stacking sequence*	$T_{chamber}$ [°	I_{laser} $[A]$	t_{laser} $[s]$	t_{acq} $[s]$	f_{acq} $[Hz]$	T_{atm} $[°C]$
173	QI	22	30	300	400	50	23.2
175	QI	22	25	300	400	50	23.8
177	QI	22	20	300	400	50	23.8
181	QI	22	25	300	400	50	24.1
183	QI	22	30	300	400	50	23.6
186	QI	22	30	300	400	50	23.6
188	QI	22	25	300	400	50	23.7
190	QI	22	20	300	400	50	23.8
192	QI	22	20	300	400	50	23.4
194	QI	22	20	900	1000	50	23.4

Table 9 - Test matrix for laser-induced decomposition analysis of the quasi-isotropic laminate

For all the tests presented hereafter, the infrared thermography is performed on the rough surface of the material. As a consequence, the heat flux generated by the laser is applied on the smooth surface to make easier visualisations of the exposed surface after the tests.

For identical conditions applied by the laser on the coupon front surface, the temperature increases more for the unidirectional laminate than for the quasi-isotropic (see section 7.2.2). As a consequence, the highest heat flux was not applied for the unidirectional laminate because the measured temperature did exceed the maximum calibrated temperature.

$Test\ \#$	$Stacking\ sequence$	$T_{chamber}$ [°	$I_{laser}\ [A]$	$t_{laser}\ [s]$	$t_{acq}\ [s]$	$f_{acq}\ [Hz]$	$T_{atm}\ [°C]$
196	UD	22	20	300	400	50	24.6
198	UD	22	20	300	400	50	23.6
200	UD	22	20	300	400	50	23.6
202	UD	22	25	300	400	50	23.4
204	UD	22	25	300	400	50	23.7
206	UD	22	25	300	400	50	23.8

Table 10 - Test matrix for laser-induced decomposition analysis of the unidirectional laminate

The intensity values used of the laser are associated to the following maximum heat flux magnitudes:

- $I_{laser} = 20\ A$ corresponds to a maximum heat flux density of $53.7\ kW/m^2\ \pm 0.1\ kW/m^2$
- $I_{laser} = 25\ A$ corresponds to a maximum heat flux density of $76.2\ kW/m^2\ \pm 0.3\ kW/m^2$
- $I_{laser} = 30\ A$ corresponds to a maximum heat flux density of $101.2\ kW/m^2\ \pm 0.6\ kW/m^2$

7.1.3. Laser calibration

The laser calibration is performed by an inverse heat conduction method developed at ONERA. The heat flux distribution is assessed using a reference material made of pure titanium the thermal properties of which are well known.

Figure 79 shows the result of the laser calibration for the maximum laser intensity $I_{laser} = 30\ A$:

- top/left: temperature map measured by the infrared thermographic camera on the back surface of the titanium coupon at $t = 5\ s$;
- top/right: temperature map computed by the inverse algorithm on the back surface of the titanium coupon at $t = 5\ s$;
- bottom/left: heat flux distribution generated by the laser source on the front surface of the titanium coupon at $t = 5\ s$;
- bottom/right: comparison of temperature evolutions at the centre of the back surface of the material (measurements in red symbols, inverse thermal computation in red line) associated with the maximum heat flux evolution at the centre of the front surface (theoretical step signal in blue line, inverse thermal computation in blue symbols).

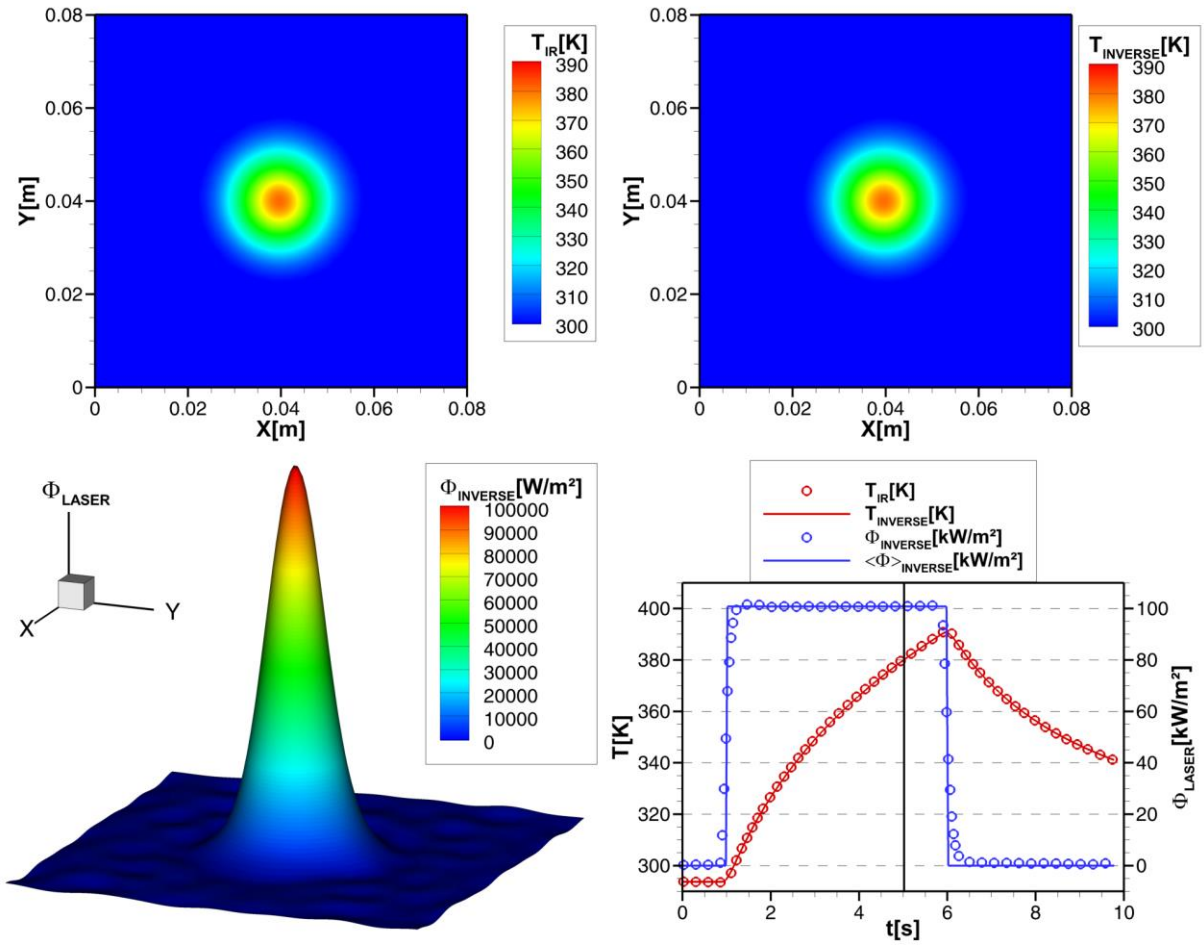

Figure 79 – Heat flux identification for $I_{laser} = 30\ A$ and $\Phi_{laser} = 101.2\ kW/m^2$

7.2. Experimental measurements analysis

The laser induced decomposition is the second application of the BLADE facility. Only the heat flux magnitude and the exposure time are changed with respect to the thermal properties assessment application. As a result of the high heat flux applied onto the material surface, the thermal response on the back surface is driven by:

- the heat diffusion within the material as a result of the equilibrium of the input laser flux and the thermal loss by radiation (convection is avoided by the vacuum condition within the test chamber);
- consumed or produced volume energies resulting from endothermal and exothermal chemical reactions respectively;
- internal mechanical damage.

7.2.1. Laser induced decomposition of the quasi-isotropic T700GC/M21

The following sections exhibit the results of the experimental measurements performed on the quasi-isotropic stacking sequence of the T700GC/M21 composite laminate.

Each test coupon is measured accurately in size and mass to identify the effective density and control the thickness because it can affect the thermal behaviour measured in the back surface and the reproducibility of the results. The values are listed in Table 11.

$Test\ \#$	$\Phi_{laser}\ [kW/m^2]$	$t_{laser}\ [s]$	$m_0\ [g]$	$L_x\ [mm]$	$L_y\ [mm]$	$L_z\ [mm]$	$\rho\ [kg/m^3]$
173	53.7	300	21.3158	79.98	80.03	2.25	1480.08
175	53.7	300	21.3081	80.00	79.89	2.26	1475.21
177	53.7	300	21.3580	79.98	80.01	2.23	1496.68
181	76.2	300	21.4575	79.89	80.05	2.27	1478.09
183	76.2	300	21.3030	79.85	80.00	2.24	1488.77
186	76.2	300	21.3698	80.00	79.99	2.25	1484.20
188	101.2	300	21.4628	80.07	79.99	2.26	1482.77
190	101.2	300	21.3853	79.99	79.97	2.27	1472.74
192	101.2	300	21.3884	79.91	80.01	2.27	1473.69
194	53.7	900	21.3182	80.02	80.01	2.28	1460.40

Table 11 – Dimensional measurements of the quasi-isotropic test coupons

For each heat flux magnitude and laser exposure time, the next figures depict:

- on the left hand side, the temperature map measured on the back surface when the maximum temperature is reached;
- on the right hand side, the temperature evolution as a function of time probed at different locations from the centre of the back surface every $5\ mm$.

After each set of triplicate tests, reproducibility is evaluated by comparing the temperature evolution as a function of time of each test performed at the same experimental condition. The superimposition of the different curves should highlight any discrepancy on the thermal behaviour of the test coupons.

Finally, the table sums up the mass loss measured before and after the tests to provide additional information about the decomposition rate and the reproducibility of the tests.

7.2.1.1. $\Phi_{laser} = 53.7\ kW/m^2$ during $t_{laser} = 300\ s$

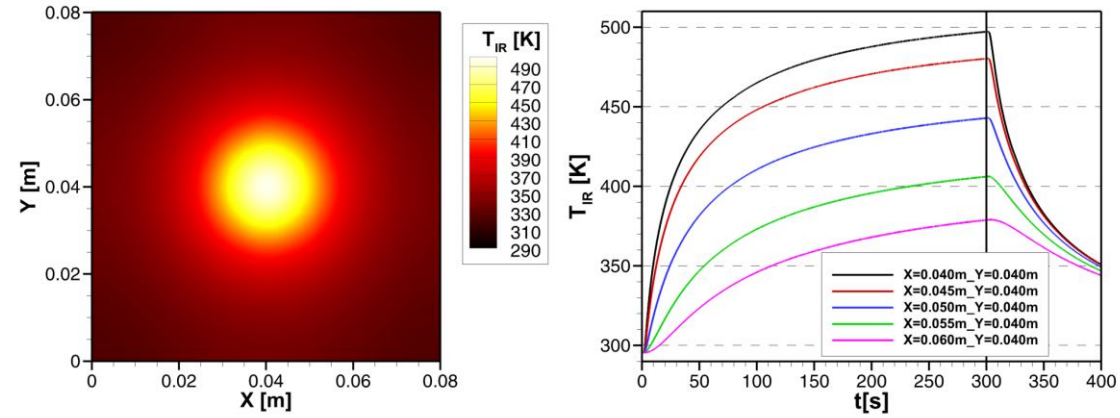

(a) Test #177

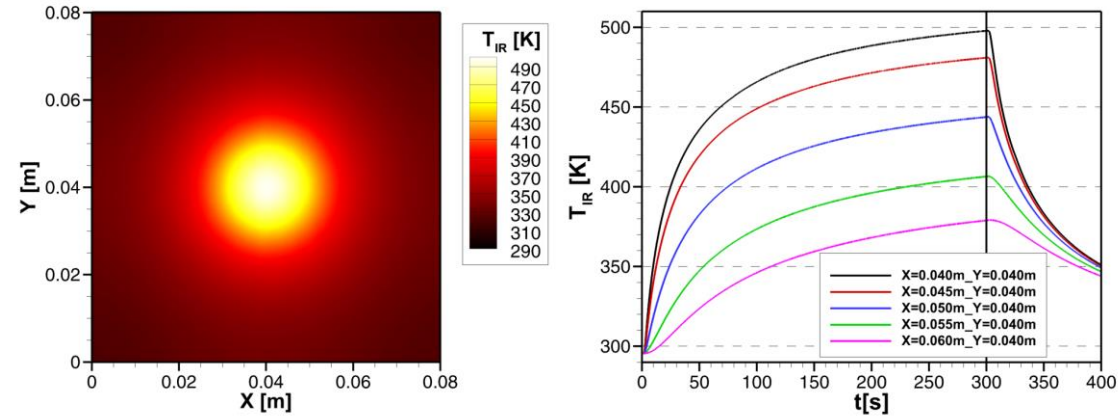

(b) Test #190

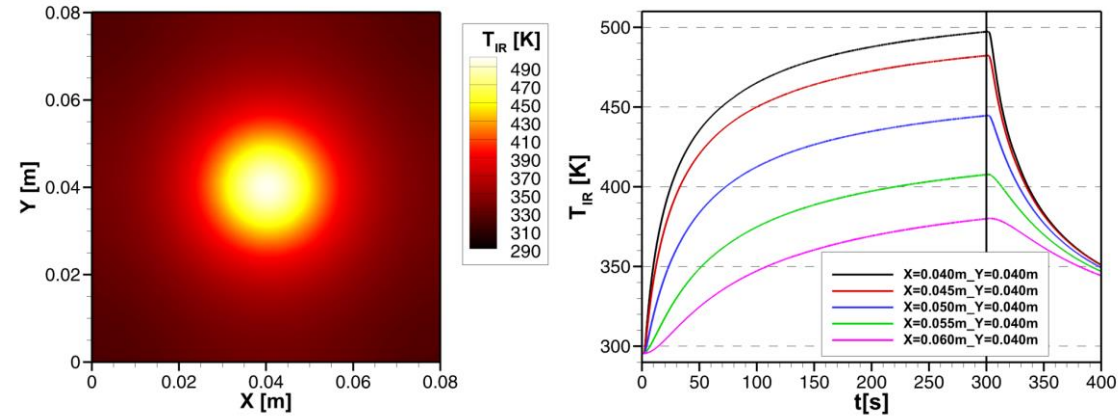

(c) Test 192

Figure 80 – Triplicate measurements of laser-induced decomposition at $\Phi_{laser} = 53.7\ kW/m^2$ during $t_{laser} = 300\ s$ on T700GC/M21-QI test coupons

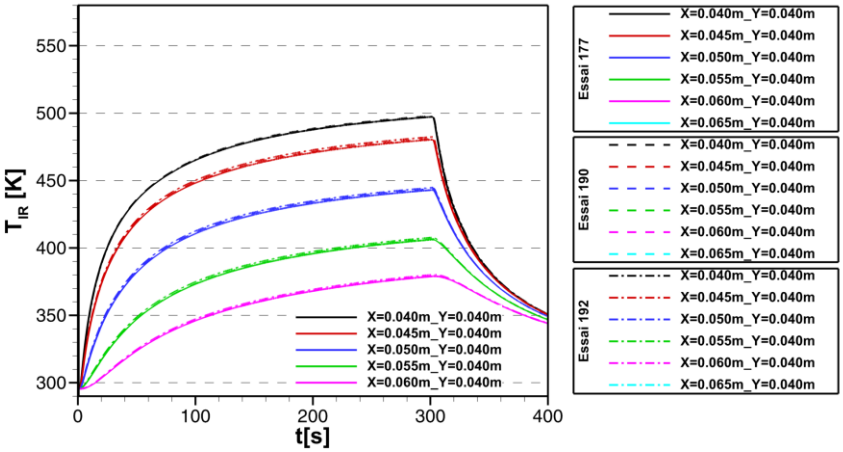

Figure 81 – Triplicate measurements reproducibility of laser-induced decomposition at $\Phi_{laser} = 53.7\ kW/m^2$ during $t_{laser} = 300\ s$ on T700GC/M21-QI test coupons

Material	Config	# Test	Φ_{laser} (kW/m²)	t_{laser} (s)	m_0 (g)	m_f (g)	Δm (mg)	Δm (%)
T700GC/M21	[0/45/90/-45]s	177	53.7	300	21.3580	21.3509	7.1	0.03
T700GC/M21	[0/45/90/-45]s	190	53.7	300	21.3853	21.3770	8.3	0.04
T700GC/M21	[0/45/90/-45]s	192	53.7	300	21.3884	21.3813	7.1	0.03

Table 12 – Pre- and post-test mass measurements for laser-induced decomposition at $\Phi_{laser} = 53.7\ kW/m^2$ during $t_{laser} = 300\ s$ on T700GC/M21-QI test coupons

A $200\ K$ temperature increase on the back surface is induced by the laser heat flux magnitude of $53.7\ kW/m^2$ after $300\ s$ of continuous laser exposure. The thermal behaviour is perfectly reproduced in all triplicate tests without any sign of internal mechanical damage. The mass loss is almost identical in all three tests.

7.2.1.2. $\Phi_{laser} = 76.2\ kW/m^2$ during $t_{laser} = 300\ s$

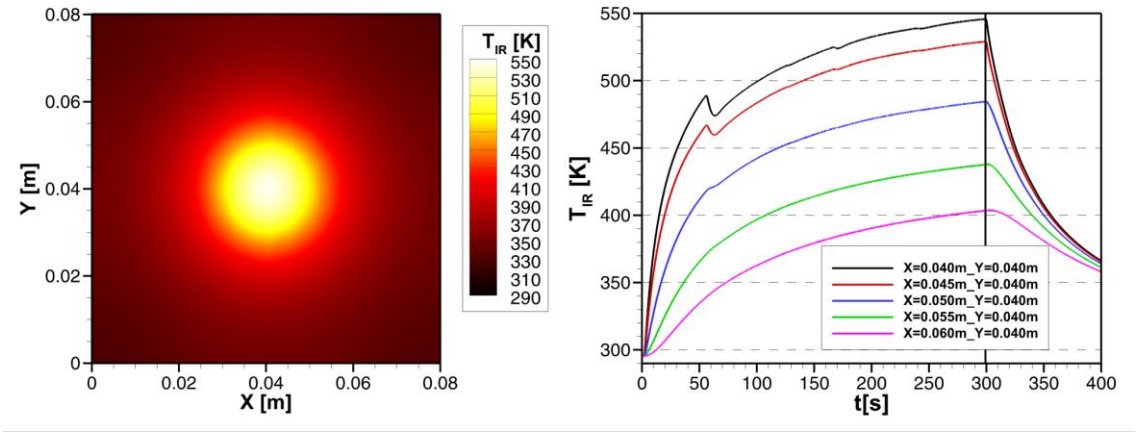

(a) Test #175

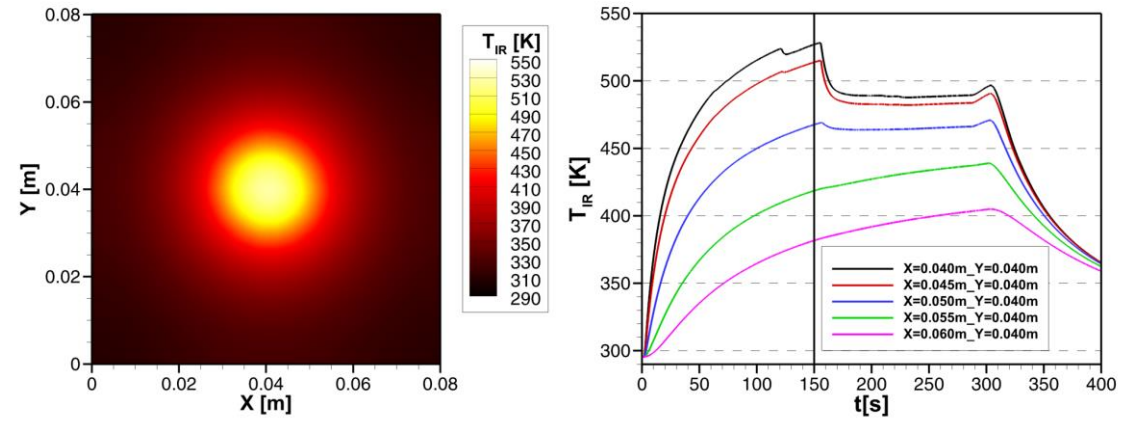

(b) Test #181

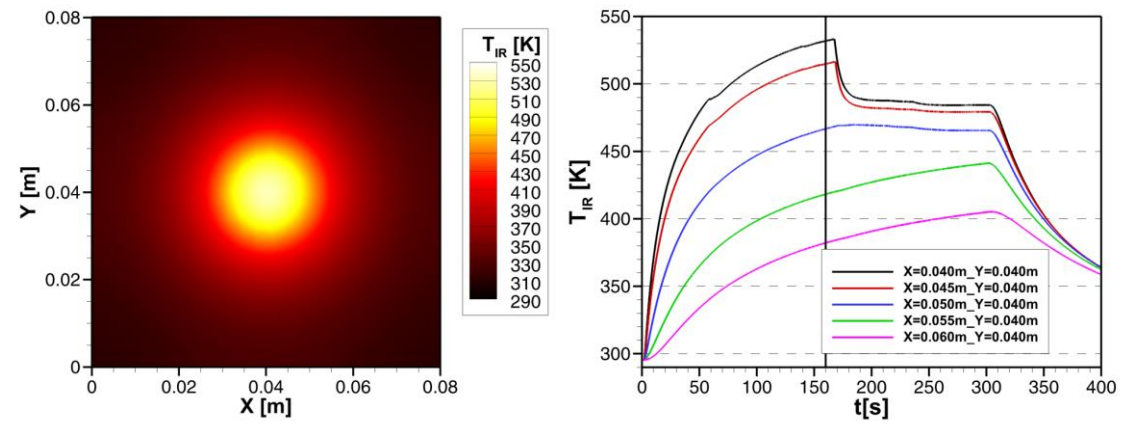

(c) Test 188

Figure 82 – Triplicate measurements of laser-induced decomposition at $\Phi_{laser} = 76.2\ kW/m^2$ during $t_{laser} = 300\ s$ on T700GC/M21-QI test coupons

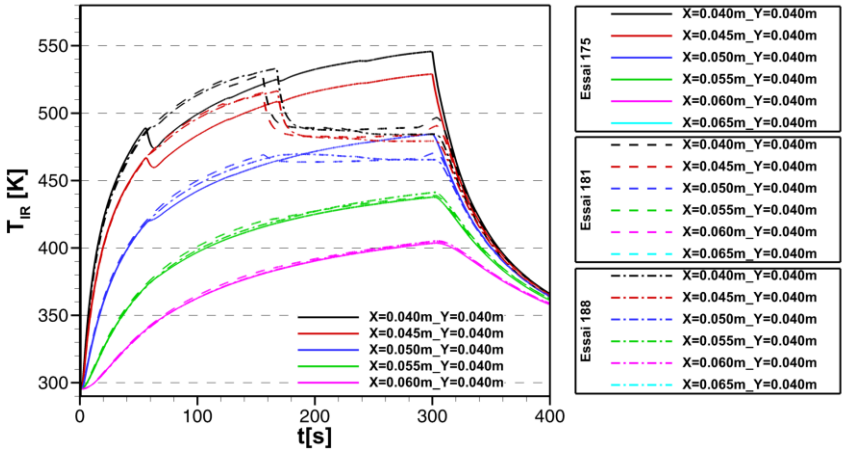

Figure 83 – Triplicate measurements reproducibility of laser-induced decomposition at $\Phi_{laser} = 76.2\ kW/m^2$ during $t_{laser} = 300\ s$ on T700GC/M21-QI test coupons

Material	Config	# Test	Φ_{laser} (kW/m²)	t_{laser} (s)	m_0 (g)	m_f (g)	Δm (mg)	Δm (%)
T700GC/M21	[0/45/90/-45]s	175	76.2	300	21.3081	21.2942	13.9	0.07
T700GC/M21	[0/45/90/-45]s	181	76.2	300	21.4575	21.4454	12.1	0.06
T700GC/M21	[0/45/90/-45]s	188	76.2	300	21.4628	21.4496	13.2	0.06

Table 13 – Pre- and post-test mass measurements for laser-induced decomposition at $\Phi_{laser} = 76.2\ kW/m^2$ during $t_{laser} = 300\ s$ on T700GC/M21-QI test coupons

A $250\ K$ temperature increase on the back surface is induced by the laser heat flux magnitude of $76.2\ kW/m^2$ after $300\ s$ of continuous laser exposure. The thermal behaviour is perfectly reproduced in all triplicate tests without any sign of internal mechanical damage in the first $50\ s$ of the experiments. Then temperature decays suddenly on the back surface. However, onset exposure time or temperature can vary significantly between the test while laser and test chamber conditions are identical. The temperature decay is the thermal signature of an internal damage called delamination where any interface between plies can be degraded and cracked. The cracks create a thermal barrier preventing heat to diffuse in the through thickness direction. As a consequence, the temperature decreases while the laser is still heating the front surface with a continuous heat flux. The post-delamination behaviour of the test coupons is significantly different. The magnitude of the damage and/or the number of events can often vary depending on the material microstructure. The magnitude of the temperature decay is directly related to the thickness of the cracks. But temperature on the back surface does not provide enough information to identify the number of crack and the thickness location within the laminate.

The mass loss remains almost identical in all three tests.

7.2.1.3. $\Phi_{laser} = 101.2\ kW/m^2$ during $t_{laser} = 300\ s$

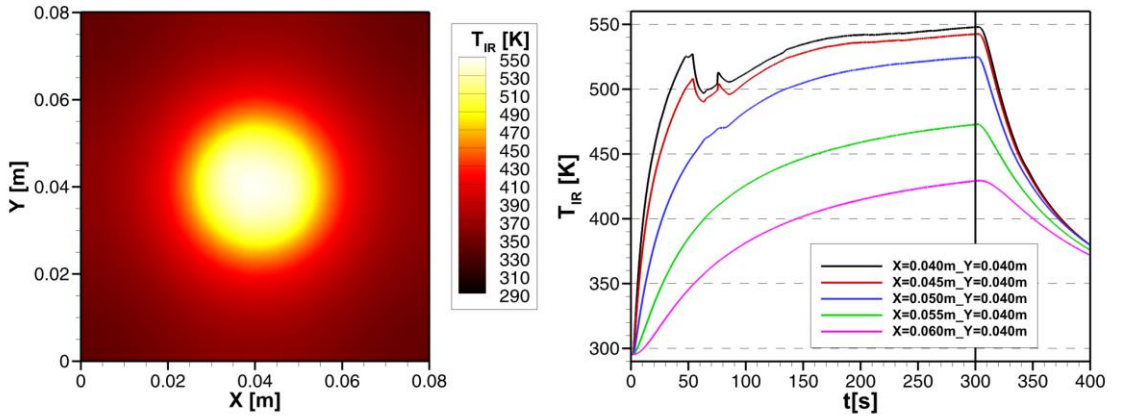

(a) Test #173

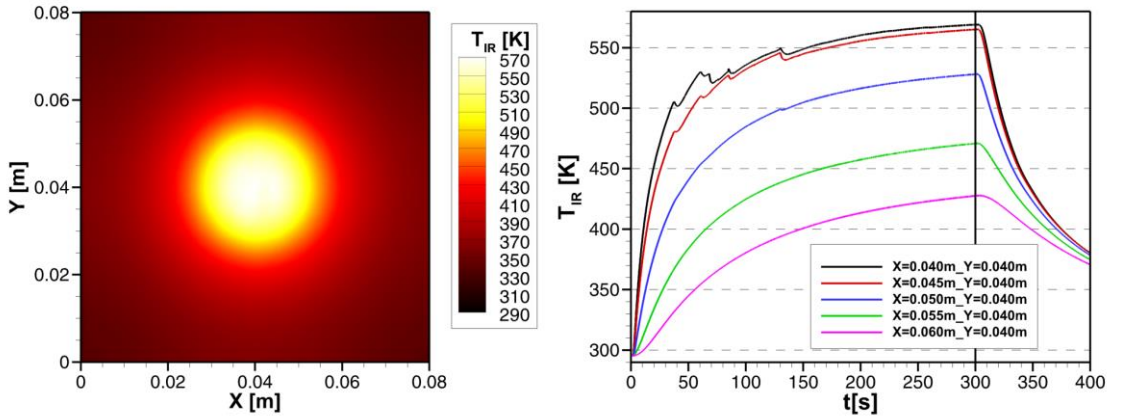

(b) Test #183

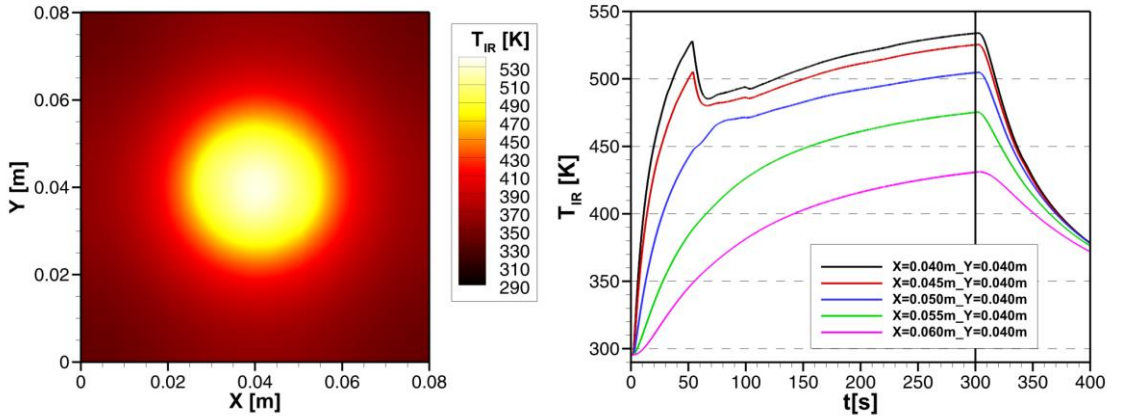

(c) Test 186

Figure 84 – Triplicate measurements of laser-induced decomposition at $\Phi_{laser} = 101.2\ kW/m^2$ during $t_{laser} = 300\ s$ on T700GC/M21-QI test coupons

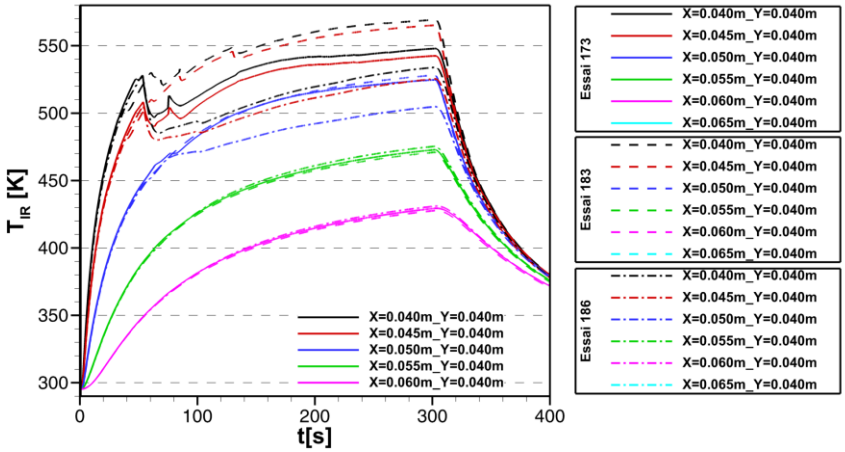

Figure 85 – Triplicate measurements reproducibility of laser-induced decomposition at $\Phi_{laser} = 101.2\ kW/m^2$ during $t_{laser} = 300\ s$ on T700GC/M21-QI test coupons

Material	Config	# Test	Φ_{laser} (kW/m²)	t_{laser} (s)	m_0 (g)	m_f (g)	Δm (mg)	Δm (%)
T700GC/M21	[0/45/90/-45]s	173	101.2	300	21.3158	21.2782	37.6	0.18
T700GC/M21	[0/45/90/-45]s	183	101.2	300	21.3030	21.2687	34.3	0.16
T700GC/M21	[0/45/90/-45]s	186	101.2	300	21.3698	21.3324	37.4	0.18

Table 14 – Pre- and post-test mass measurements for laser-induced decomposition at $\Phi_{laser} = 101.2\ kW/m^2$ during $t_{laser} = 300\ s$ on T700GC/M21-QI test coupons

A $270\ K$ temperature increase on the back surface is induced by the laser heat flux magnitude of $101.2\ kW/m^2$ after $300\ s$ of continuous laser exposure. The thermal behaviour is perfectly reproduced in all triplicate tests without any sign of internal mechanical damage in the first $40\ s$ of the experiments. Then temperature decays suddenly on the back surface. The reproducibility out of the damaged area is very good with small effect on the thermal response $15\ mm$ away from the centre of the back surface.

The mass loss remains very similar in all three tests.

7.2.2. Laser induced decomposition of the unidirectional T700GC/M21

The following sections show the results of the experimental measurements performed on the unidirectional stacking sequence of the T700GC/M21 composite laminate.

Each test coupon is measured accurately in size and mass to identify the effective density and control the thickness because it can affect the thermal behaviour measured in the back surface and the reproducibility of the results. The values are listed in Table 15.

$Test\ \#$	$\Phi_{laser}\ [kW/m^2]$	$t_{laser}\ [s]$	$m_0\ [g]$	$L_x\ [mm]$	$L_y\ [mm]$	$L_z\ [mm]$	$\rho\ [kg/m^3]$
196	53.7	300	21.4284	79.99	79.95	2.25	1489.20
198	53.7	300	21.5199	79.99	79.92	2.29	1469.99
200	53.7	300	21.6729	80.05	80.01	2.30	1471.24
202	76.2	300	21.6873	80.02	80.07	2.28	1484.58
204	76.2	300	21.5004	80.02	79.91	2.29	1468.29
206	76.2	300	21.6229	80.02	80.07	2.30	1467.30

Table 15 – Dimensional measurements of the unidirectional test coupons

For each heat flux magnitude and laser exposure time, the figures depict:

- on the left hand side, the temperature map measured on the back surface when the maximum temperature is reached;
- on the right hand side, the temperature evolution as a function of time probed at different locations from the centre of the back surface every $5\ mm$.

After each set of triplicate tests, reproducibility is evaluated by comparing the temperature evolution as a function of time of each test performed at the same experimental condition. The superimposition of the different curves should highlight any discrepancy on the thermal behaviour of the test coupons.

Finally, the table sums up the mass loss measured before and after the tests to provide additional information about the decomposition rate and the reproducibility of the tests.

7.2.2.1. $\Phi_{laser} = 53.7\ kW/m^2$ during $t_{laser} = 300\ s$

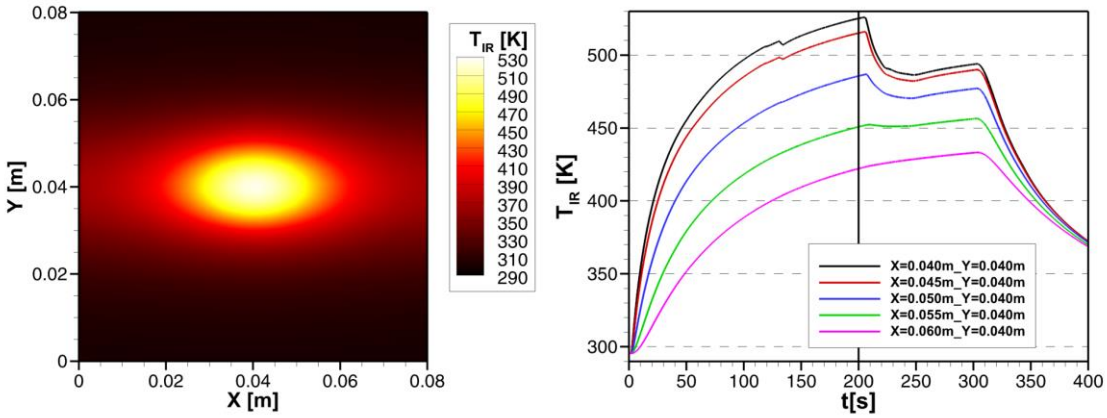

(a) Test #196

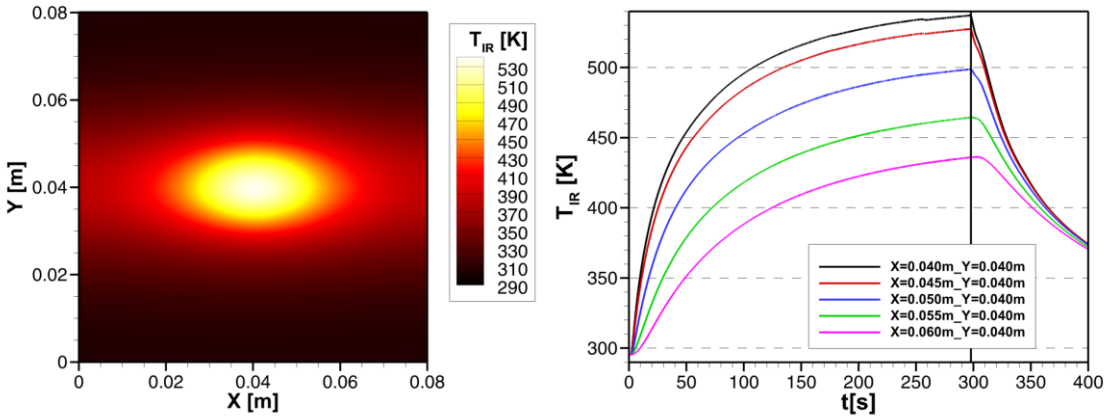

(b) Test #198

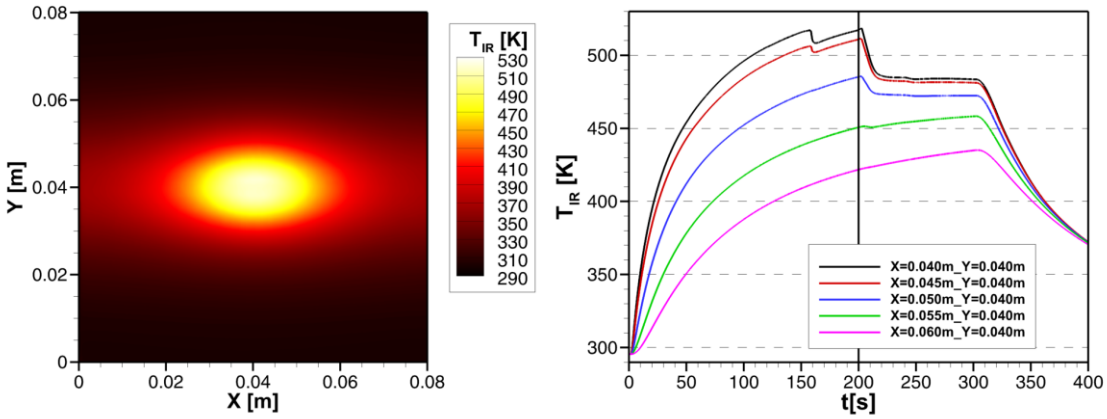

(c) Test 200

Figure 86 – Triplicate measurements of laser-induced decomposition at $\Phi_{laser} = 53.7\ kW/m^2$ during $t_{laser} = 300\ s$ on T700GC/M21-UD test coupons

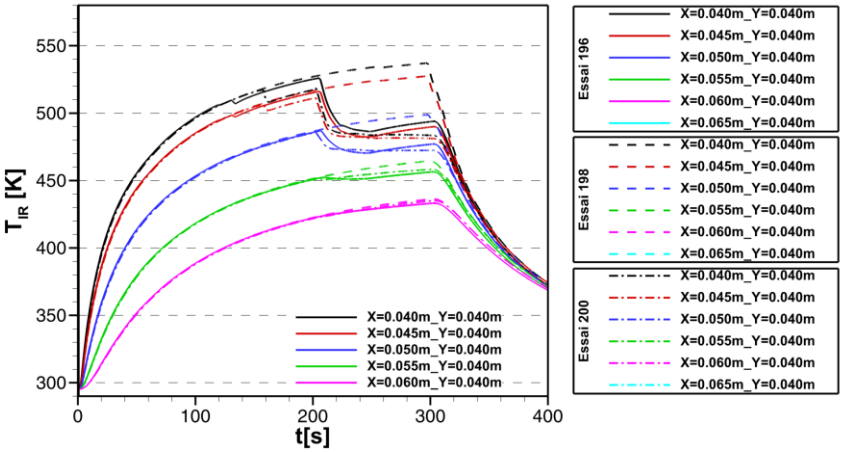

Figure 87 – Triplicate measurements reproducibility of laser-induced decomposition at $\Phi_{laser} = 53.7\ kW/m^2$ during $t_{laser} = 300\ s$ on T700GC/M21-UD test coupons

Material	Config	# Test	Φ_{laser} (kW/m²)	t_{laser} (s)	m_0 (g)	m_f (g)	Δm (mg)	Δm (%)
T700GC/M21	[0]8	196	53.7	300	21.4284	21.4158	12.6	0.06
T700GC/M21	[0]8	198	53.7	300	21.5199	21.5131	6.8	0.03
T700GC/M21	[0]8	200	53.7	300	21.6729	21.6640	8.9	0.04

Table 16 – Pre- and post-test mass measurements for laser-induced decomposition at $\Phi_{laser} = 53.7\ kW/m^2$ during $t_{laser} = 300\ s$ on T700GC/M21-UD test coupons

Despite an undamaged behaviour of the quasi-isotropic laminate, the unidirectional stacking sequence presents a different behaviour under the laser heat flux magnitude of $53.7\ kW/m^2$ and $300\ s$ of continuous laser exposure. A $240\ K$ temperature increase is measured on the back surface. The thermal behaviour is perfectly reproduced in all triplicate tests before signs of internal mechanical damage appear. The mass loss is affected by the onset of delamination damage. Almost undamaged test coupon #198 has a lower mass loss than the other two damaged test coupons subjected to identical heat load. The crack onset within the laminate induces an insulating gas layer that may result in higher temperature on the exposed surface. As a consequence, the decomposition by pyrolysis is increased in the area ahead of the crack and, the mass loss is observed higher.

7.2.2.2. $\Phi_{laser} = 76.2\ kW/m^2$ during $t_{laser} = 300\ s$

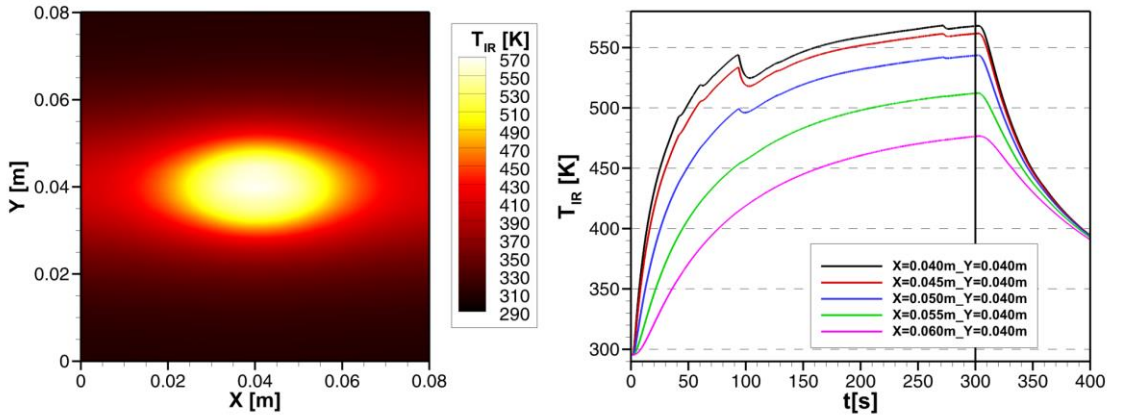

(a) Test #202

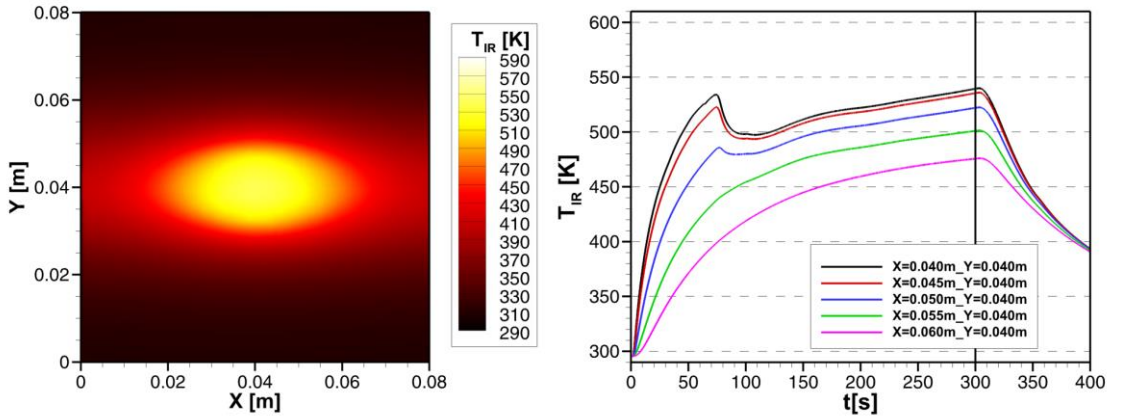

(b) Test #204

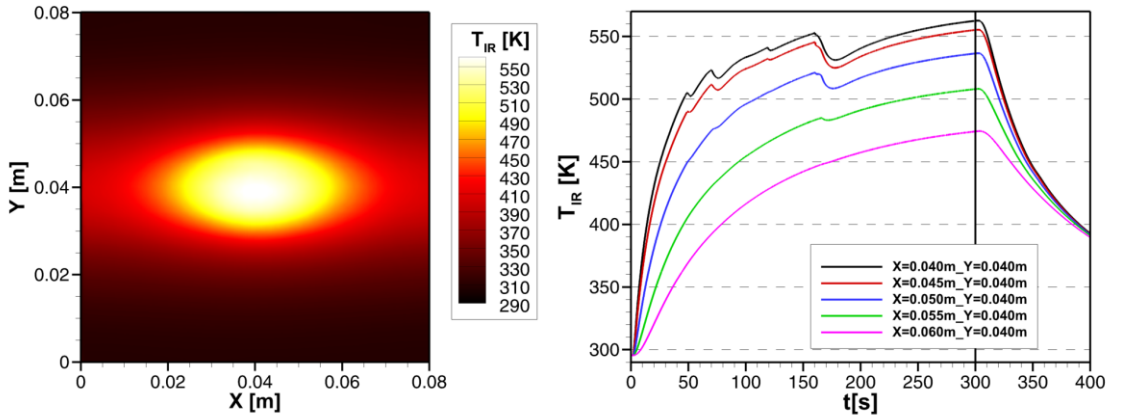

(c) Test 206

Figure 88 – Triplicate measurements of laser-induced decomposition at $\Phi_{laser} = 76.2\ kW/m^2$ during $t_{laser} = 300\ s$ on T700GC/M21-UD test coupons

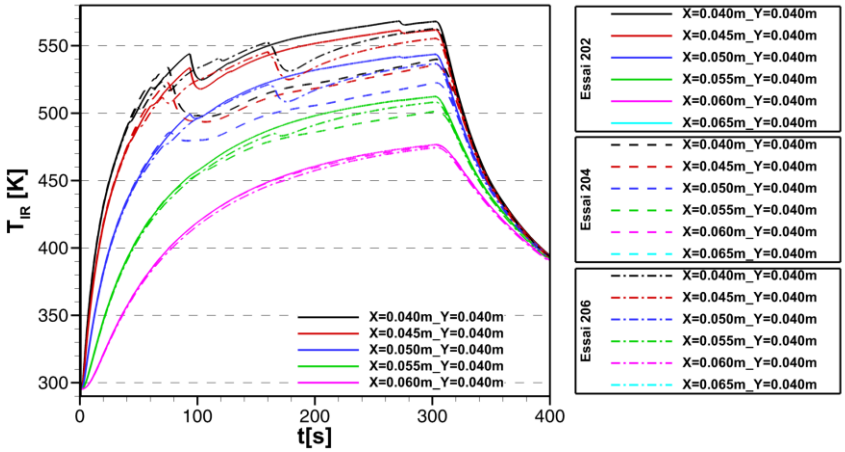

Figure 89 – Triplicate measurements reproducibility of laser-induced decomposition at $\Phi_{laser} = 76.2\ kW/m^2$ during $t_{laser} = 300\ s$ on T700GC/M21-UD test coupons

Material	Config	# Test	Φ_{laser} (kW/m²)	t_{laser} (s)	m_0 (g)	m_f (g)	Δm (mg)	Δm (%)
T700GC/M21	[0]8	202	76.2	300	21.6873	21.6639	23.4	0.11
T700GC/M21	[0]8	204	76.2	300	21.5004	21.4768	23.6	0.11
T700GC/M21	[0]8	206	76.2	300	21.6229	21.6009	22.0	0.10

Table 17 – Pre- and post-test mass measurements for laser-induced decomposition at $\Phi_{laser} = 76.2\ kW/m^2$ during $t_{laser} = 300\ s$ on T700GC/M21-UD test coupons

A $270\ K$ temperature increase on the back surface is induced by the laser heat flux magnitude of $76.2\ kW/m^2$ after $300\ s$ of continuous laser exposure. The thermal behaviour is perfectly reproduced in all triplicate tests without any sign of internal mechanical damage in the first $40\ s$ of the experiments. Then temperature suddenly decays on the back surface. The magnitude of the temperature decay is not related to the magnitude of the thermal load. It may result from the relaxation of internal stresses that depends on the microstructure and crack location.

The mass loss remains almost identical in all three tests.

7.2.3. Thermal behaviour sensibility analysis

The next sections compare the sensitivity of test conditions onto the thermal behaviour of the material.

7.2.3.1. Thermal behaviour as a function of the heat flux magnitude

Figure 90 shows the thermal behaviour of the material as a function of the heat flux magnitude applied on the front surface of the test coupons. Only temperature at the centre of the back surface is plotted in order to easily compare the results and different coloured lines are used for each heat flux.

Whatever the stacking sequence, the heat rate is increasing as the heat flux magnitude of the laser is increasing as well. Temperature increases faster for unidirectional test coupons than for quasi-isotropic ones given a similar heat flux.

The curves describe the stochastic behaviour of the delamination damage onset and growth within CFRP laminate materials.

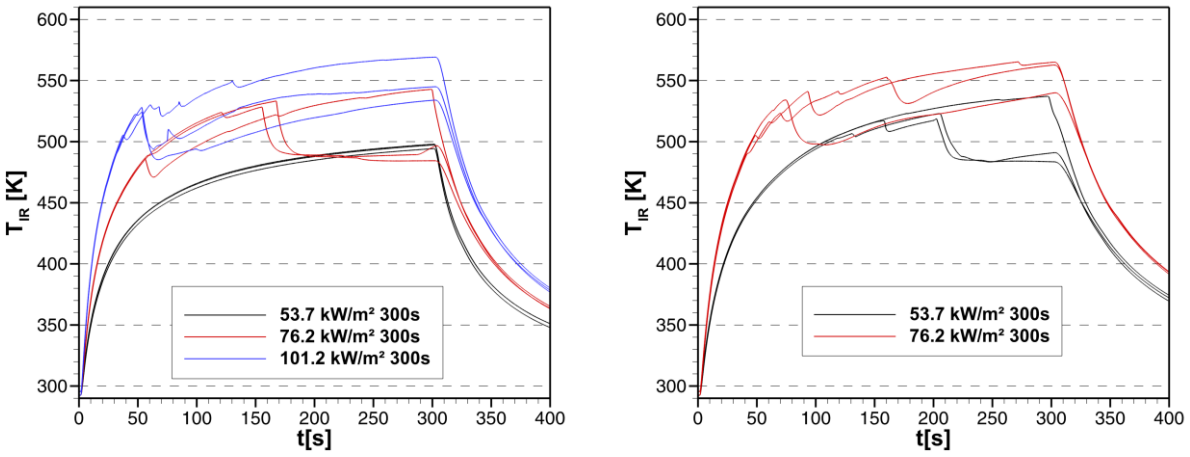

(a) T700GC/M21-QI (b) T700GC/M21-UD

Figure 90 – Thermal response at the centre of the back surface as a function of the maximum laser heat flux density applied on the front surface of the test coupons

7.2.3.2. Thermal behaviour as a function of the laser exposure time

Figure 91 shows the thermal behaviour of the material as a function of the laser exposure time at the lowest heat flux magnitude. Tests were only conducted on quasi-isotropic test coupons because this specific condition does not induce any delamination damage during the experiments. As a consequence, effects of heat transfer, thermochemical transformations and energetics, and volatile transport can be investigated without any interaction with mechanical damage. The reproducibility in the first phase is perfect and no sign of delamination appears on the following $600\ s$ of laser exposure. The mass loss is twice higher than for test coupons exposed during $300\ s$. These tests should be perfect candidates for the pyrolysis model validation.

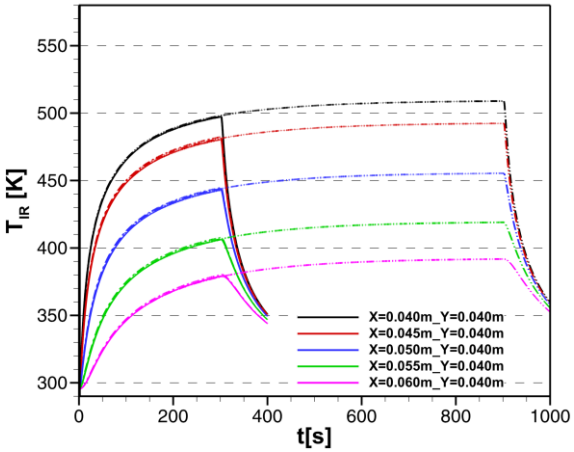

Figure 91 - Thermal response at the centre of the back surface as a function of the laser exposure time applied on the front surface of the QI test coupons $\Phi_{laser} = 53.7\ kW/m^2$

Material	Config	# Test	Φ_{laser} (kW/m²)	t_{laser} (s)	m_0 (g)	m_f (g)	Δm (mg)	Δm (%)
T700GC/M21	[0/45/90/-45]s	194	53.7	900	21.3182	21.3045	13.7	0.06

Table 18 – Pre- and post-test mass measurements for laser-induced decomposition at $\Phi_{laser} = 53.7\ kW/m^2$ during $t_{laser} = 600\ s$ on T700GC/M21-QI test coupon #194

8 FIRE-INDUCED DECOMPOSITION

8.1. Experimental methodology

8.1.1. FIRE facility

The FIRE facility was developed to investigate the thermal response of composite materials exposed to fire with a focus on the interactions between the flame and pyrolysis volatiles resulting from the decomposition of the material.

The name FIRE comes from the acronym Flame-wall Interaction Research Experiment. The facility is presented in Figure 92.

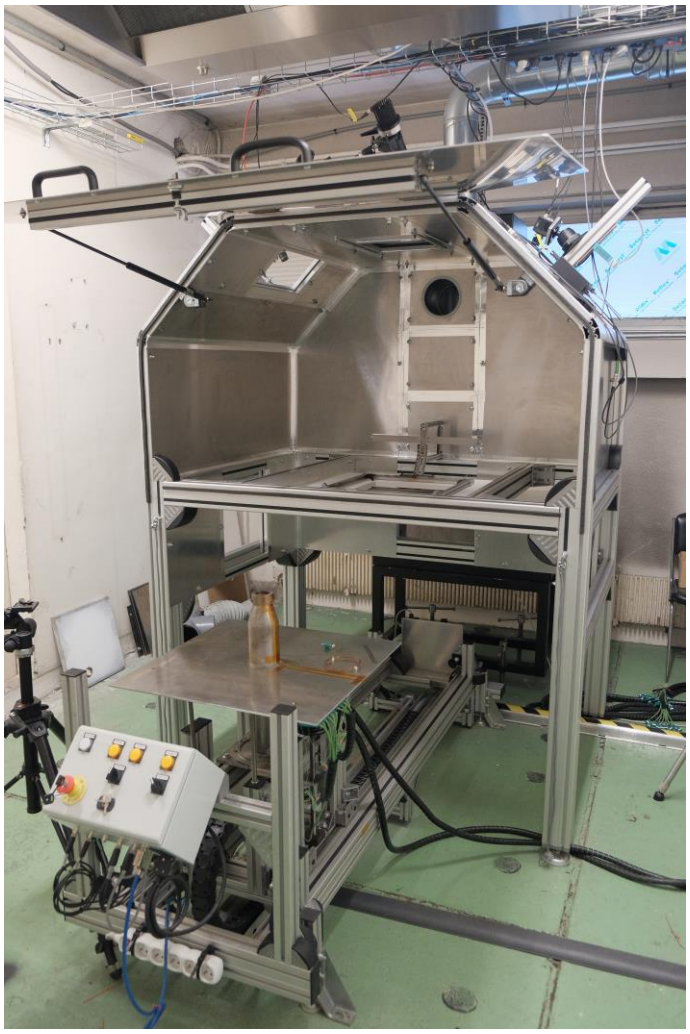

Figure 92 – FIRE facility

It is composed of:

- a gas burner providing a vertical premixed air-propane flame;

- a linear slide rail guiding system to move the burner from the outside position (for ignition and thermal stabilisation) to the inside position just below the test coupon;
- A main chassis which is divided into:
    - an upper part above the test coupon where measurements are made on the unexposed surface (infrared thermography, digital image correlation) as well as mass loss using a Roberval balance configuration;
    - a lower part where optical visualisations and measurements can be performed through dedicated windows on the side exposed to fire.
- two exhaust hoods to extract air, smoke and fumes when the burner is outside the main chassis as well as when the burner is shifted below the test coupon during the tests.

The facility is fully controlled with a LabView-based programme that automatically starts the test and the acquisition with all measurements in sync.

8.1.2. Instrumentation

The main interest of the FIRE facility is to simultaneously perform different measurements during the test in order to correlate the dynamic behaviour of the flame with the thermal, chemical and mechanical behaviour of the material. A series of sensors and measurements techniques are carried out in the FIRE facility, all of them are non-intrusive measurements:

- mass flow rate meters for both air and propane.
- thermocouples for temperature measurements:
    - on the burner wall;
    - on the horizontal metal plate below;
    - in the gas inlet of the burner;
    - in the exhaust hood inside the chassis.
- position sensors to accurately record when the burner is below the coupon and it gets back outside. Signals are used for measurements synchronisation.
- infrared thermography to measure the transient thermal behaviour on the back surface of the material when it is exposed to fire.
- digital image correlation to measure the deformation of the back surface of the test coupon using a random speckle pattern blue light projection and 2 cameras in a stereoscopic configuration.
- high precision electromagnetic compensation weighing module to measure the mass loss during the experiment.
- high resolution camera to visualise the flame impinging onto the material surface.

Laser Doppler Velocimetry (LDV) or Particle Image Velocimetry (PIV) can be performed in the gas phase area to assess the fire dynamics.

8.1.3. Test matrix

The test matrix is detailed in Table 19 for the T700GC/M21-QI.

Test #	Coupon reference	Fuel/air ratio	Mass flow rate $[g/s]$	t_{fire} $[s]$	t_{acq} $[s]$	f_{acq} $[Hz]$	T_{atm} $[°C]$
011	3809A_FSS_P7_P233-01_SS06#08	1.2	4.2	60	120	10	21.8
012	3809A_FSS_P7_P233-01_SS06#07	1.2	4.2	60	120	10	22.4
013	3809A_FSS_P7_P233-01_SS06#07	1.2	4.2	60	120	10	22.8
014	3809A_FSS_P7_P233-01_SS06#19	1.2	4.2	30	60	10	22.7
015	3809A_FSS_P7_P233-01_SS06#18	1.2	4.2	30	100	10	22.5
016	3809A_FSS_P7_P233-01_SS06#17	1.2	4.2	30	100	10	23.1
017	3809A_FSS_P7_P233-01_SS06#15	1.2	4.2	30	150	10	23.6
018	3809A_FSS_P7_P233-01_SS06#16	1.2	4.2	60	150	10	23.8
019*	3809A_FSS_P7_P233-01_SS06#14	1.2	4.2	30	100	10	23.6

Table 19 - Test matrix for fire-induced decomposition analysis of the quasi-isotropic laminate

All tests are performed with the same burner settings in order to generate the same flame. Only the exposure time is changed. All coupons were exposed to the fire on the smooth surface.

* Test #019 was added to the test matrix to investigate the material behaviour exposed to the fire on the rough surface.

Concurrently, tyre debris impact tests were performed on thicker panels (16-ply quasi-isotropic laminates) at different impact velocities to damage the material. Damages were characterised using infrared non-destructive inspection. Damaged panels were finally sent back to fire tests to investigate how the internal damage will affect the material response to fire.

The second test matrix is detailed in Table 20.

Test #	Coupon reference	Impact velocity $[m/s]$	Fuel/air ratio $[-]$	Mass flow rate $[g/s]$	t_{fire} $[s]$	t_{acq} $[s]$	f_{acq} $[Hz]$	T_{atm} $[°C]$
024	V01_01	150	1.2	4.2	180	270	10	20.7
025	V02_02	186	1.2	4.2	120	210	10	19.6
026	V02_03	185	1.2	4.2	180	270	10	19.6
027	V3_01	171	1.2	4.2	150	240	10	18.8
028	V01_02	158	1.2	4.2	150	240	10	19.3
029	V02_01	171	1.2	4.2	150	240	10	19.1

Table 20 – Second test matrix for fire-induced decomposition analysis of damaged quasi-isotropic laminates

Longer fire exposure can be applied on thicker panels. Exposure time was adjusted on the three first tests and a compromise was chosen for the three last tests.

It is important to notice that unfortunately the two series of tests cannot be compared because the material thickness is different. However, the procedure IMPACT > NDI > FIRE gives relevant information to

analyse the results of the second series of tests. Moreover, the random feature of the damage onset and growth during FIRE tests would have made comparisons difficult to perform.

8.2. Phenomenology of the material response

Figure 93 shows an overview of the successive events occurring during the fire exposure onto the composite test coupon. Photographs are captured using Fujifilm camera (1frame/s, 16Mpx, 35mm, f/2, ISO1600, 1/3200s).

First, the gas burner is moved below the test coupon when thermal stabilisation is reached. The flame is blue with a noticeable flame front. The material heating begins but without any visible material response.

Few seconds later, yellow flames appear on the material surface. Temperature within the material must be high enough to activate pyrolysis with significant release of gaseous volatiles. The colour is related to an incomplete combustion and soot radiation. As a consequence, effect of volatiles ignition can be easily dissociated from the flame generated by the burner that remains perfectly unchanged.

The growth of volatiles off-gassing and combustion continues in the third step to become significant in the fourth step with a quasi-steady state regime.

At the end of the exposure time, the burner is moved away from the material but temperature within the material is still high enough to keep on decomposing the matrix and releasing burning volatiles.

At the end of the experiment, self-extinguishing time can be evaluated.

Figure 93 – Overview of the successive events occurring during the fire exposure onto the composite test coupon

From the photographs, two interesting pieces of information can be extracted: the ignition time and the self-extinguishing time. The values are reported in

024	V01_01	180	29	45
025	V02_02	120	22	40
026	V02_03	180	20	Unavailable data
027	V03_01	150	32	32
028	V01_02	150	25	23
029	V02_01	150	25	34

Table 21 with a $\pm 1\ s$ accuracy.

Test #	*Coupon reference*	t_{fire} $[s]$	*Ignition time [s]*	*Self − extinguishing time [s]*
011	3809A_FSS_P7_P233-01_SS06#08	60	Unavailable data	
012	3809A_FSS_P7_P233-01_SS06#07	60	20	38
013	3809A_FSS_P7_P233-01_SS06#07	60	17	24
014	3809A_FSS_P7_P233-01_SS06#19	30	16	54
015	3809A_FSS_P7_P233-01_SS06#18	30	15	7
016	3809A_FSS_P7_P233-01_SS06#17	30	19	10
017	3809A_FSS_P7_P233-01_SS06#15	30	18	27
018	3809A_FSS_P7_P233-01_SS06#16	60	15	36
019	3809A_FSS_P7_P233-01_SS06#14	30	15	13
Damaged panels (tyre debris impact)				
024	V01_01	180	29	45
025	V02_02	120	22	40
026	V02_03	180	20	Unavailable data
027	V03_01	150	32	32
028	V01_02	150	25	23
029	V02_01	150	25	34

Table 21 – Ignition time and self-extinguishing time measured during the FIRE tests

Before analysing the thermal response, the effect of the internal damage induced by the impact onto the fire behaviour of the material can be observed on the photographs by comparing with the behaviour of virgin test coupons detailed in Figure 93. Although the impactor was shot at the centre of the test coupon, non-destructive inspector showed that the internal damage topology can be off-centred. The internal damage can thus affect the gas release at the material surface as a consequence of an off-centred thermal response. For instance, test #025 shows a gas phase ignition located on one side of the material surface as illustrated in Figure 94. At the beginning of this experiment, the internal thermal conditions within the laminate are non-uniform. Delamination induced by the impact prevents heat to diffuse through the area

where cracks are located. The thermal insulation of the cracked layer causes the temperature on the surface exposed to fire to rise faster in the damaged area. The gas phase is released first in the damaged area and the ignition occurs earlier in the experiment (Table 21). The dissymmetry remains until the off-gassing reaches a steady state with significant gas release on the whole surface of the material.

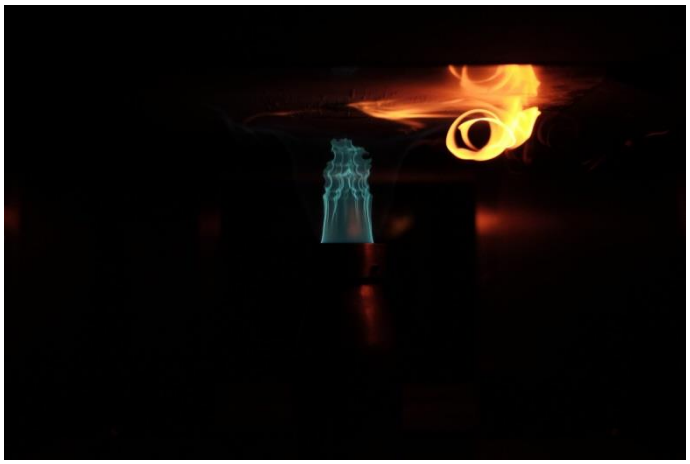

Figure 94 – Internal damage affecting the gas release and ignition on the material surface during test#025

As a result, the effect of the internal damage induced by preliminary impacts can only be observed before fire induced damages occur and expand onto the whole material surface.

Another effect of the internal damage induced by the impact can be observed for damages located in the first surface ply on the side exposed to fire. Non-destructive inspection shows small cracks on the surface of some coupons. For instance, surface cracks can be observed on test #028 as illustrated in Figure 95. The focus in Figure 95(b) shows that the gas phase is released preferentially through the surface crack.

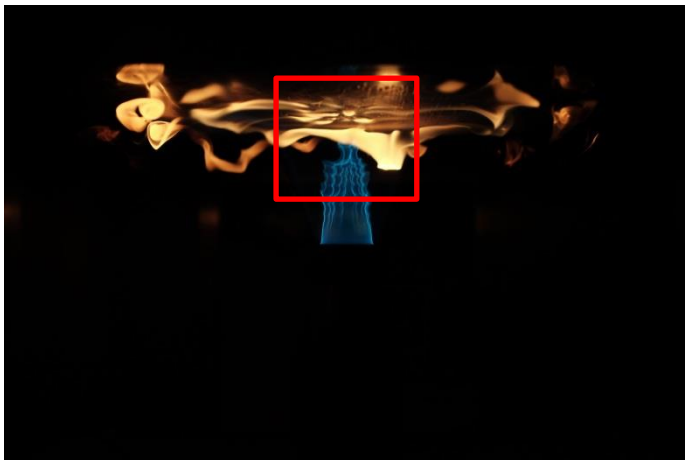

(a) Gas phase ignition on the material surface

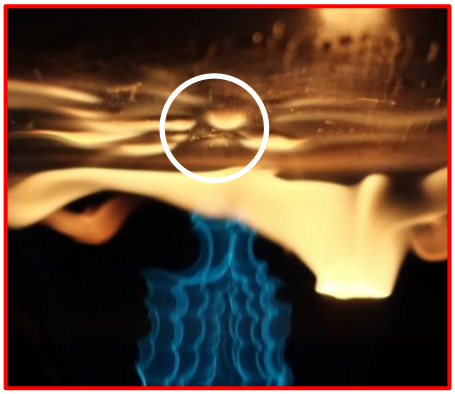

(b) Focus on the gas release area

Figure 95 – Surface cracks causing preferential gas release areas on the material surface during test#028

Visualisation of the exposed surface offers significant information about the material behaviour that can be correlated in time to the other measurements.

8.3. Thermal response analysis

8.3.1. Virgin 8-ply panels

Figure 96 to Figure 104 present the results from the thermographic temperature measurements performed on the unexposed surface of the composite test coupons. The 9 different plots are ranked according to the fire exposure time from $t_{fire} = 60\ s$ (Figure 96 to Figure 99) to $t_{fire} = 30\ s$ (Figure 100 to Figure 104).

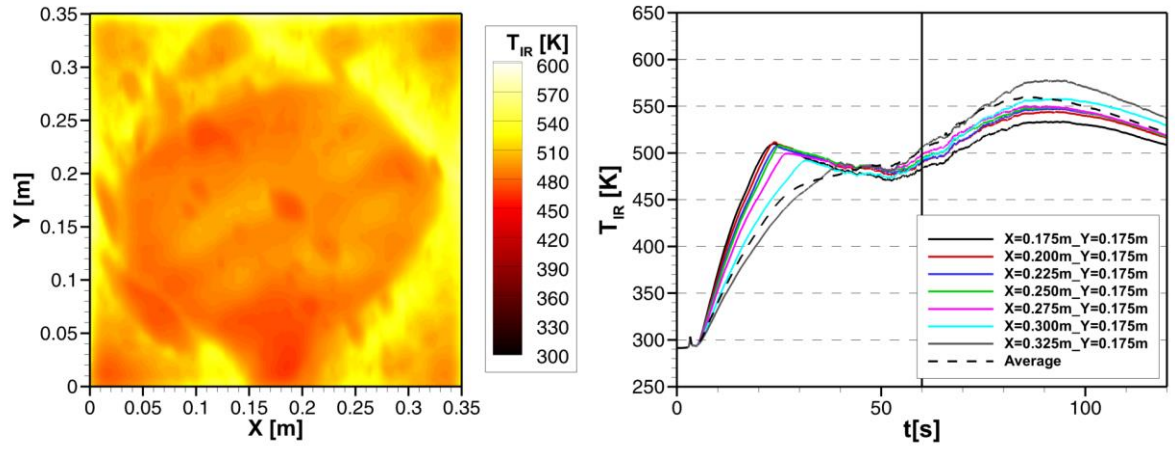

Figure 96 - Fire-induced decomposition during $t_{fire} = 60\ s$ - Test #011

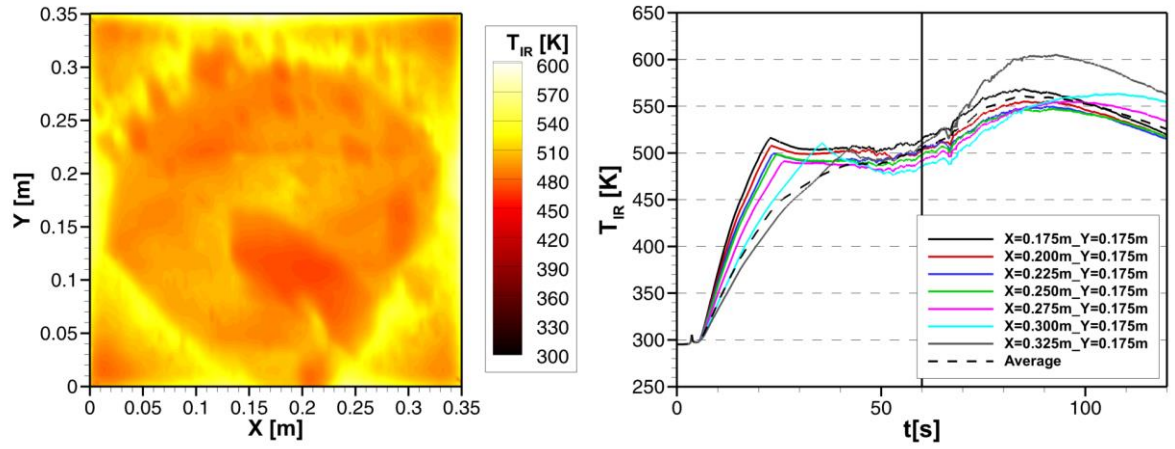

Figure 97 - Fire-induced decomposition during $t_{fire} = 60\ s$ - Test #012

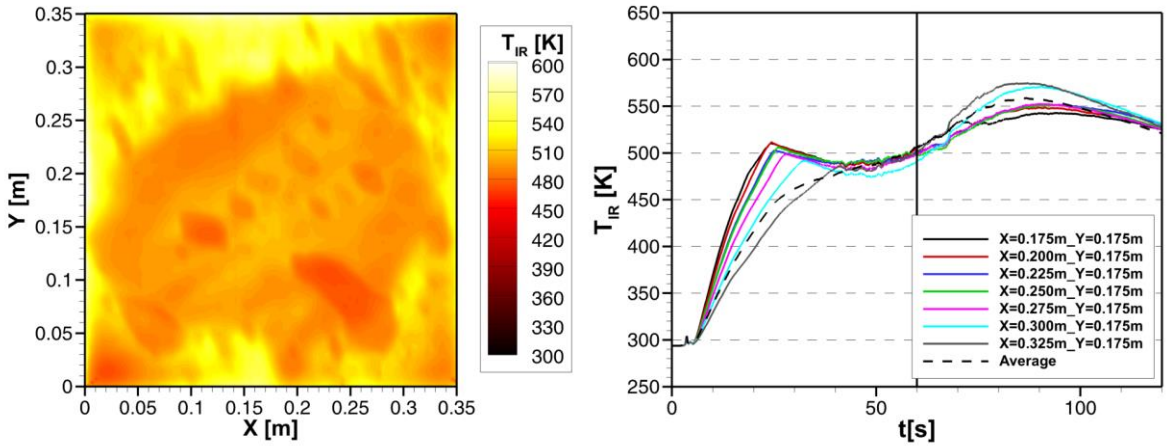

Figure 98 - Fire-induced decomposition during $t_{fire} = 60\ s$ - Test #013

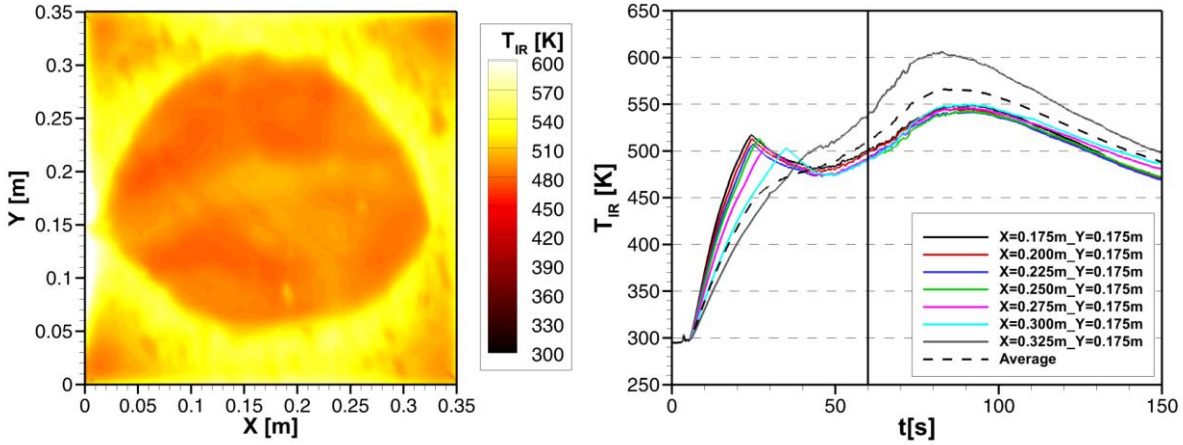

Figure 99 - Fire-induced decomposition during $t_{fire} = 60\ s$ - Test #018

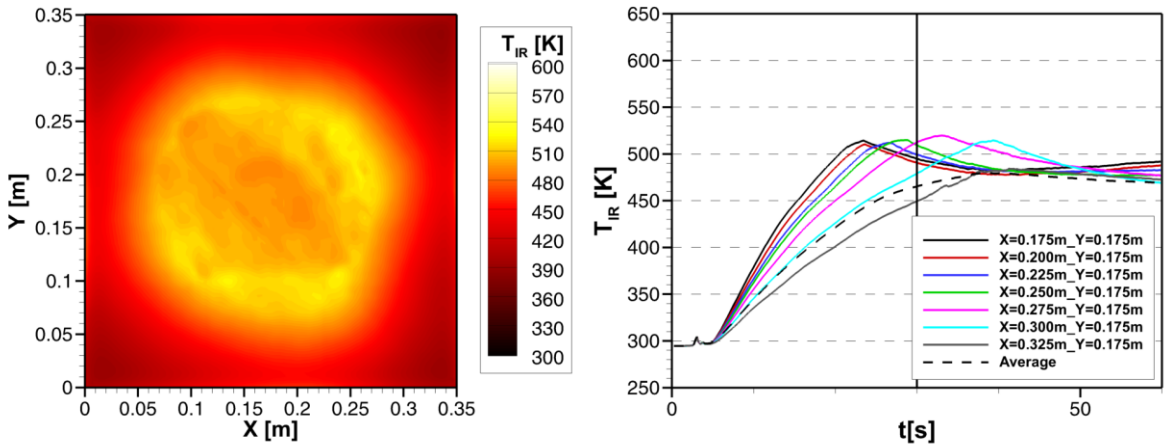

Figure 100 - Fire-induced decomposition during $t_{fire} = 30\ s$ - Test #014

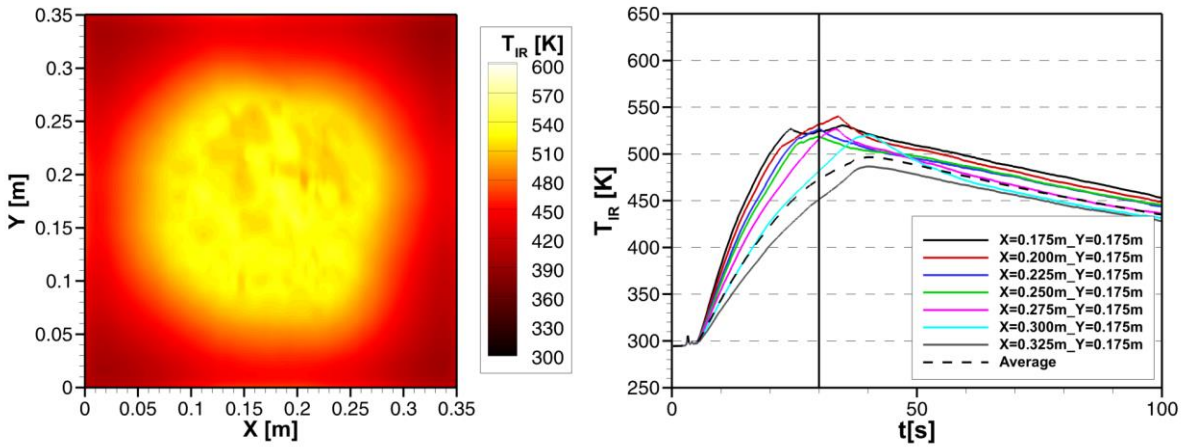

Figure 101 - Fire-induced decomposition during $t_{fire} = 30\ s$ - Test #015

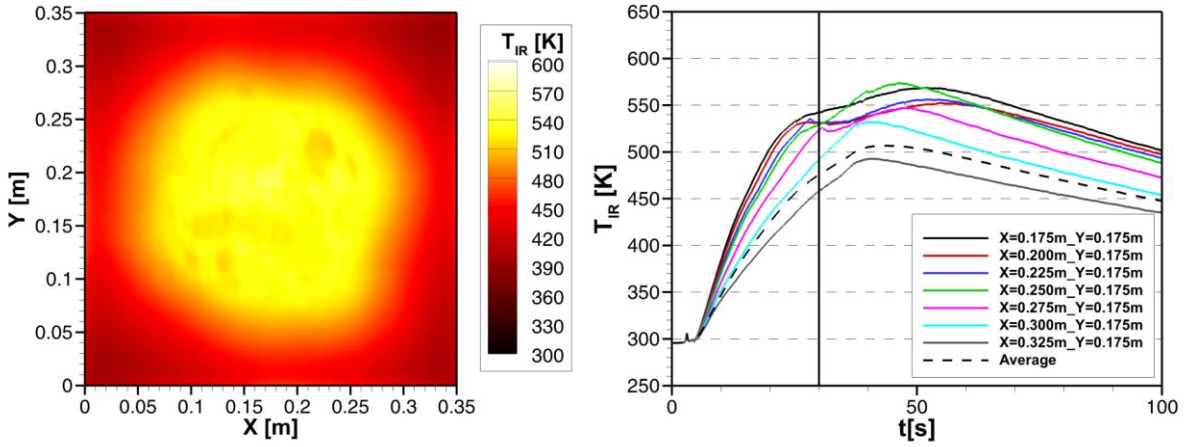

Figure 102 - Fire-induced decomposition during $t_{fire} = 30\ s$ - Test #016

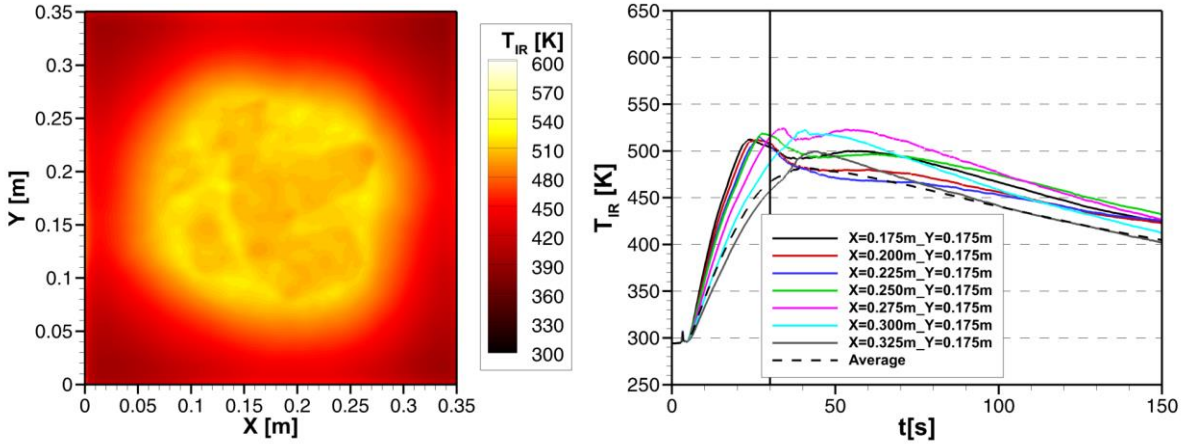

Figure 103 - Fire-induced decomposition during $t_{fire} = 30\ s$ - Test #017

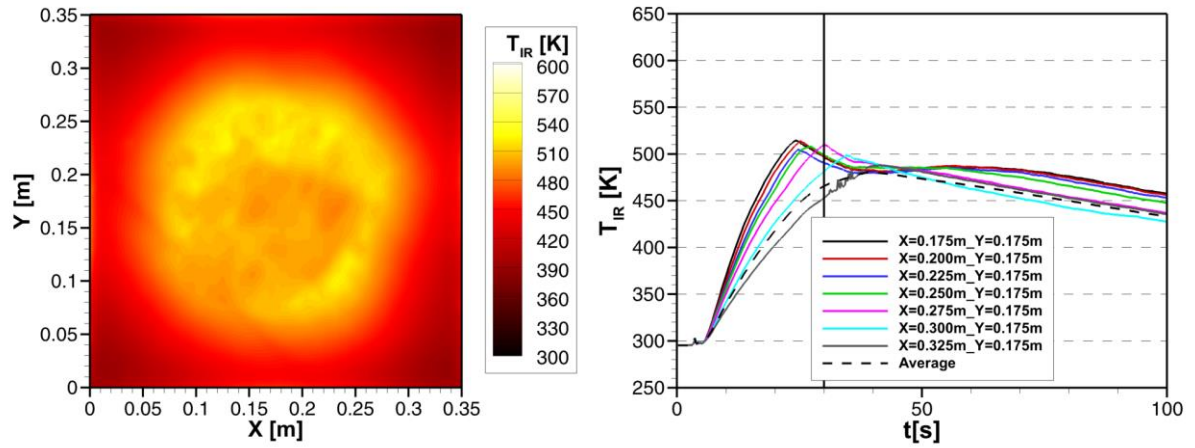

Figure 104 - Fire-induced decomposition during $t_{fire} = 30\ s$ - Test #019

The picture on the left hand side of each figure shows the temperature map measured on the back surface at the end of the fire exposure time. On the right hand side, the temperature evolution as a function of time is plotted at different locations from the centre of the back surface (every $25\ mm$) using the same template as for BLADE results (section 7.2).

However, another curve is added to the plot with a dashed line. It exhibits the average temperature computed on the whole material surface as a function of time.

Many interesting features can be observed through these data:

- Because the flame inlet conditions are controlled and unchanged for the different tests, the reproducibility of the flame is granted. As a consequence, the material response in the first $25\ s$ is identical in all tests presented from Figure 96 to Figure 104.
- At $t_{fire} \approx 25\ s$, an important temperature decay is observed in the time evolution although the fire is still impinging the front surface. The delamination damage noticed in laser-induced decomposition tests in the BLADE facility is obviously also observed in the fire-induced decomposition tests. The thermal signature of delamination on the unexposed surface is a sudden temperature decay induced by an interlaminar rupture. It results in the creation of a gas layer that prevents heat to diffuse in the through-thickness direction. This phenomenon can be observed in the temperature maps. The delaminated area is characterised by colder temperature at its centre than on the sides.
- While the delamination onset appears to be reproducible, the growth of the delamination and the post-delamination behaviour of the material differ in all tests. It may depend on the material microstructure. With a pure radiative heat source in the BLADE facility, stochastic post-delamination behaviours were observed in section 7.2. The complexity of induced phenomena increases significantly with a fire heat source. Flame dynamics induces unsteady behaviour at the

material surface that may also differ from one test to another while the average thermal solicitation is still unchanged.

- The average temperature plot shows that homogenisation of the temperature occurs during the experiment because local and average temperature are very close at the end of the experiment. It may be correlated to the ignition of pyrolysis volatiles because the heat flux space distribution induced by the burner itself is centred with a very low contribution on the coupons edges. Ignition of pyrolysis volatiles helps homogenising the heat flux distribution. As a consequence, temperature on the exposed surface becomes more uniform.
- The difference concerning the material behaviour whether the smooth surface or the rough surface is exposed to fire is not significant with regard to the performed tests and conditions. Values of surface optical properties are too close to result in significant changes about radiative heat loss with the environment. Effect of roughness on the exposed surface needs to be investigated more precisely to assess relevant conclusions.

8.3.2. Damaged 16-ply panels

Figure 96 to Figure 110 present the results from the thermographic temperature measurements performed on the unexposed surface of the damaged composite test coupons.

The results are presented at three successive exposure time values during each experiment in order to discriminate either the thermal response is due to the initial damage or the fire-induced damage.

The picture on the left hand side of each figure shows the temperature map measured on the back surface. On the right hand side, the temperature evolution as a function of time is plotted at different locations from the centre of the back surface (every $25\ mm$). Another curve is added to the plot with a dashed line. It exhibits the average temperature computed on the whole material surface as a function of time.

For tests #024 and #026, the fire exposure was too long. Decomposition gas release was observed from the sides of the material and momentary ignition of the gas phase was noticed after $t_{exposure} = 150\ s$ on the sides up to the unexposed surface. That is the reason why some temperature profiles close to the coupon side (grey, light blue and purple curves…) show a noisier signal with many peaks. The analysis of such behaviour is very difficult and ignition on the unexposed surface is usually prevented because the heat source is no longer confined to the exposed surface. Nevertheless, the first part of those tests can be analysed like the others.

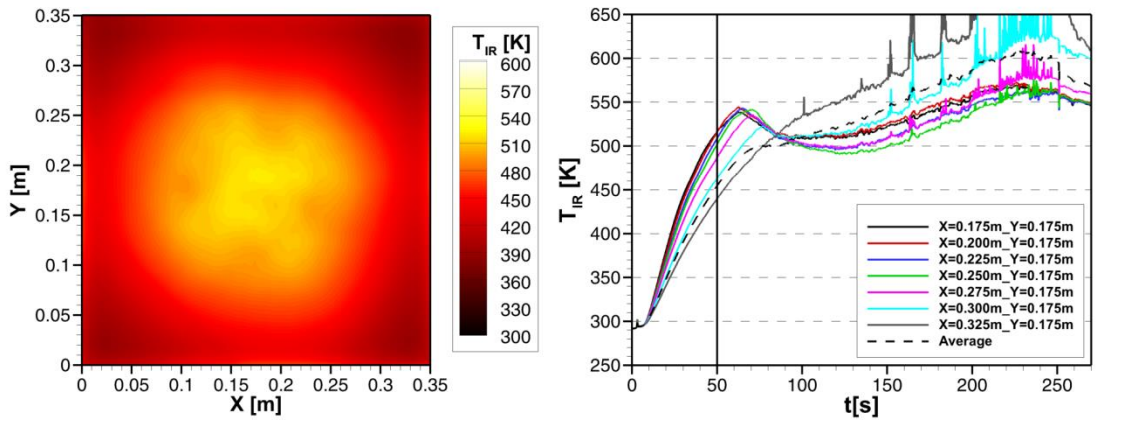

(a) Instantaneous temperature map at $t_{exposure} = 50\ s$

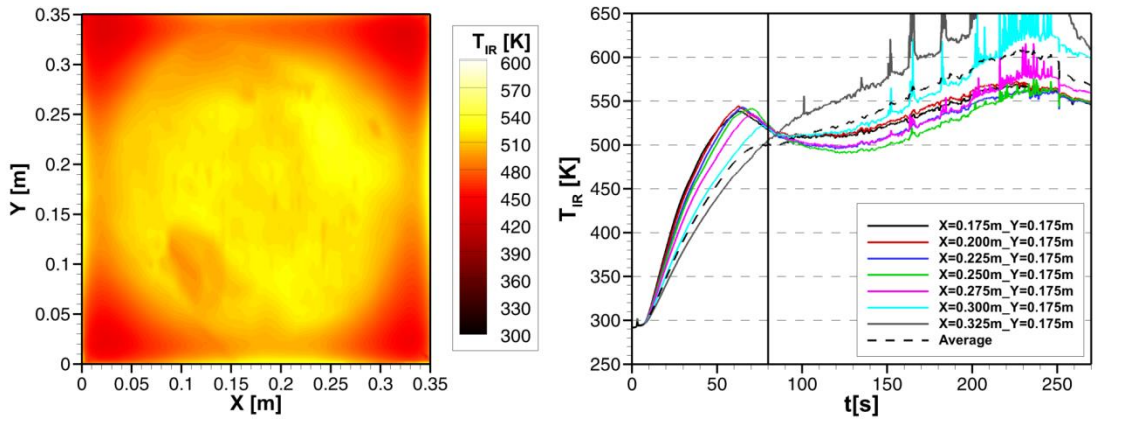

(b) Instantaneous temperature map at $t_{exposure} = 80\ s$

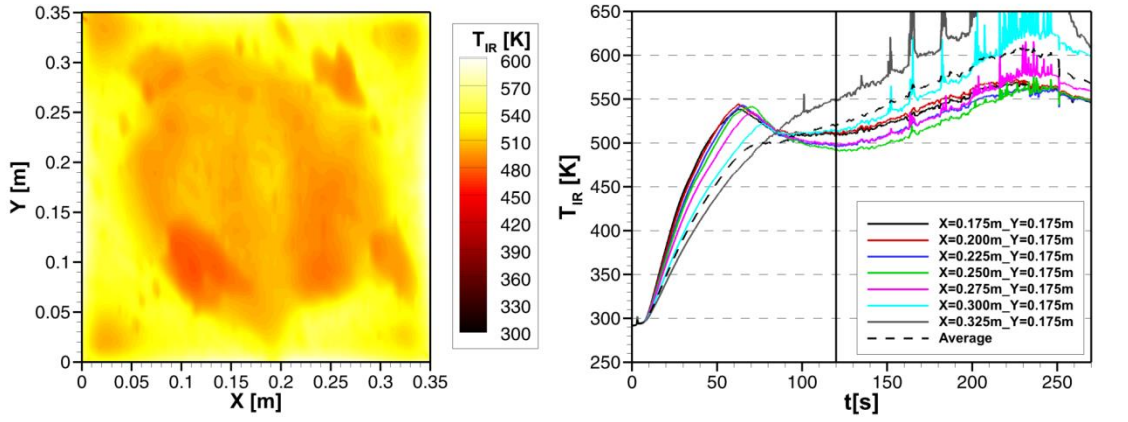

(c) Instantaneous temperature map at $t_{exposure} = 120\ s$

Figure 105 - Fire-induced decomposition during $t_{fire} = 180\ s$ - Test #024

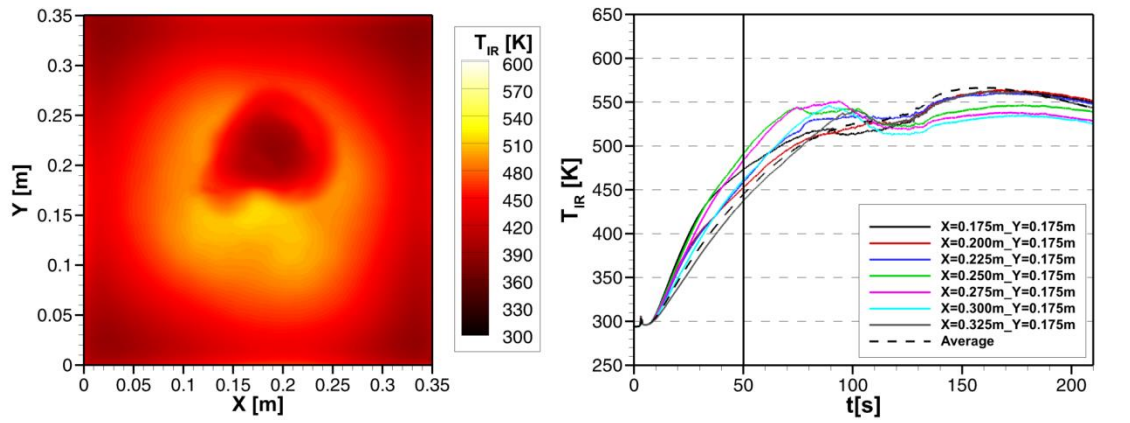

(a) Instantaneous temperature map at $t_{exposure} = 50\ s$

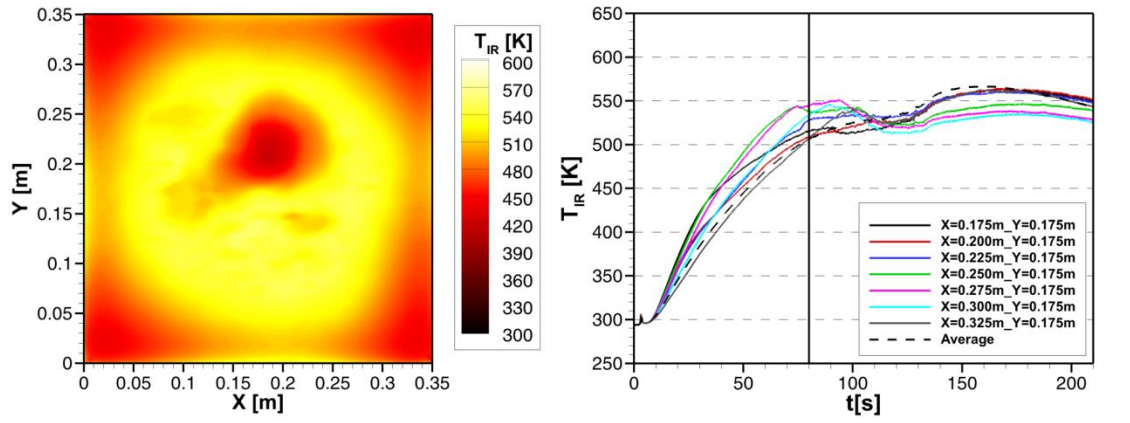

(b) Instantaneous temperature map at $t_{exposure} = 80\ s$

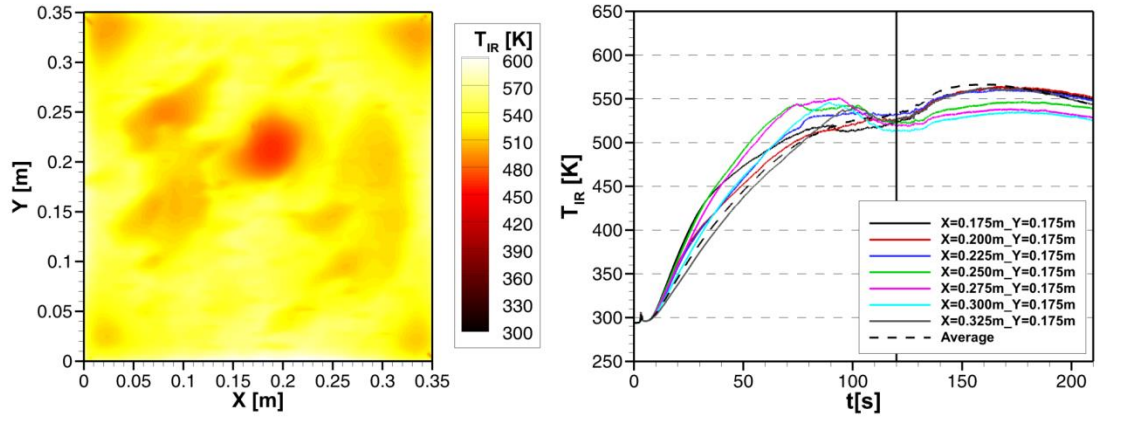

(c) Instantaneous temperature map at $t_{exposure} = 120\ s$

Figure 106 - Fire-induced decomposition during $t_{fire} = 120\ s$ - Test #025

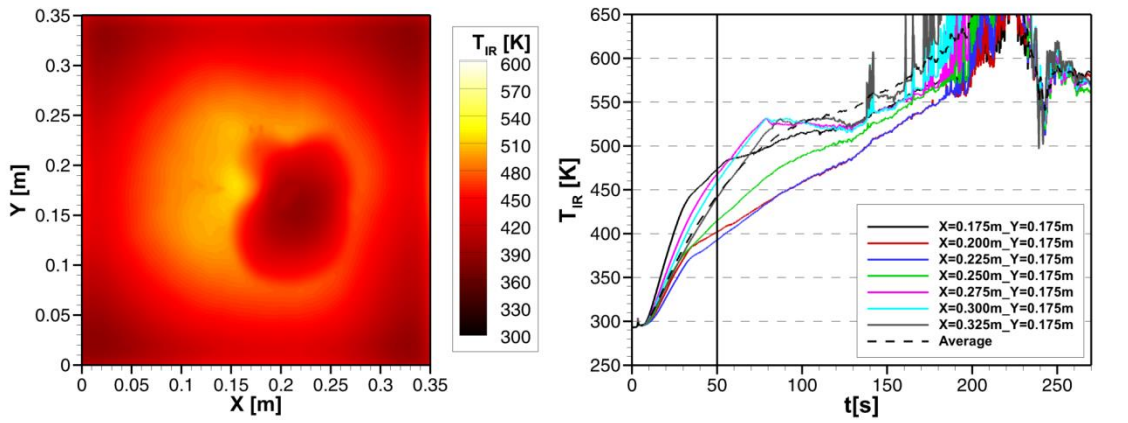

(a) Instantaneous temperature map at $t_{exposure} = 50\ s$

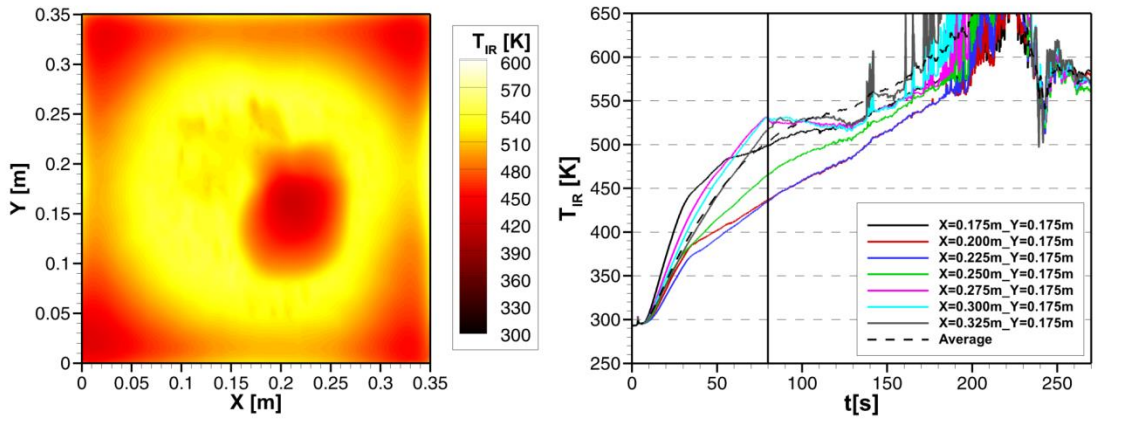

(b) Instantaneous temperature map at $t_{exposure} = 80\ s$

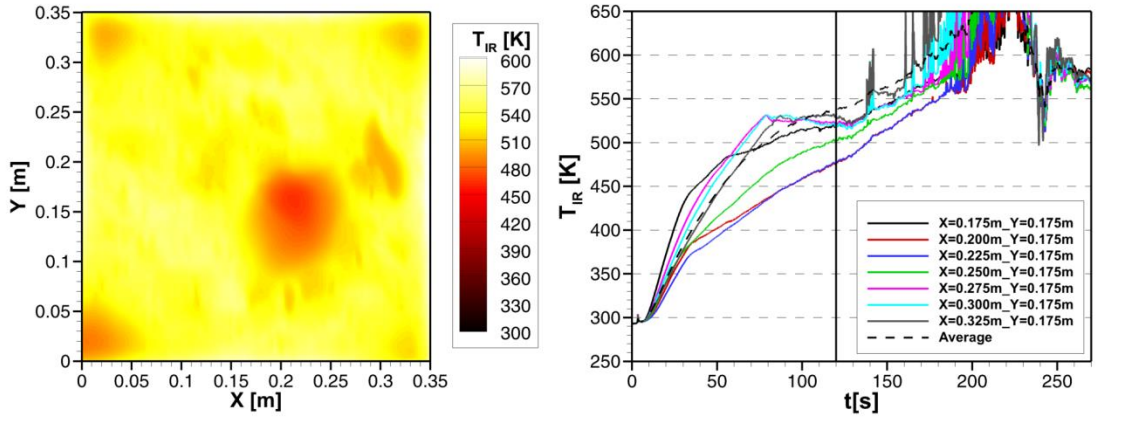

(c) Instantaneous temperature map at $t_{exposure} = 120\ s$

Figure 107 - Fire-induced decomposition during $t_{fire} = 180\ s$ - Test #026

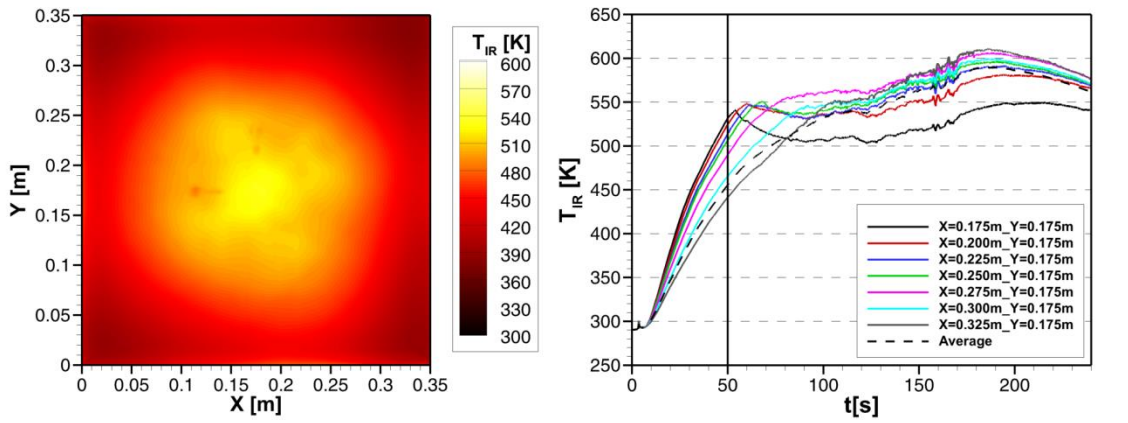

(a) Instantaneous temperature map at $t_{exposure} = 50\ s$

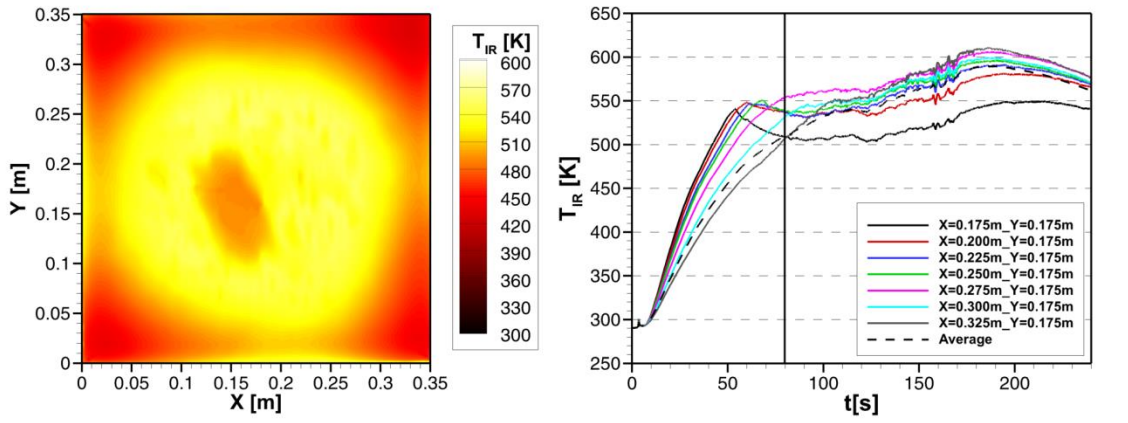

(b) Instantaneous temperature map at $t_{exposure} = 80\ s$

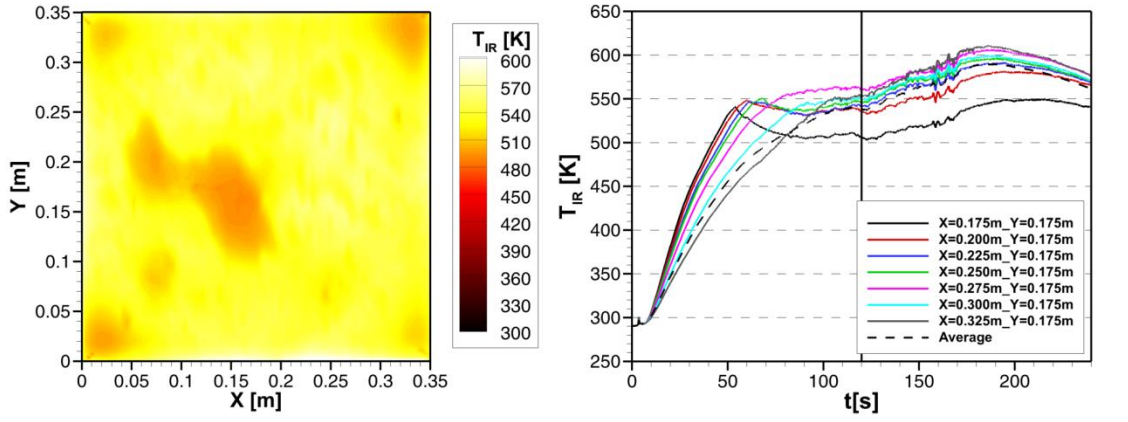

(c) Instantaneous temperature map at $t_{exposure} = 120\ s$

Figure 108 - Fire-induced decomposition during $t_{fire} = 150\ s$ - Test #027

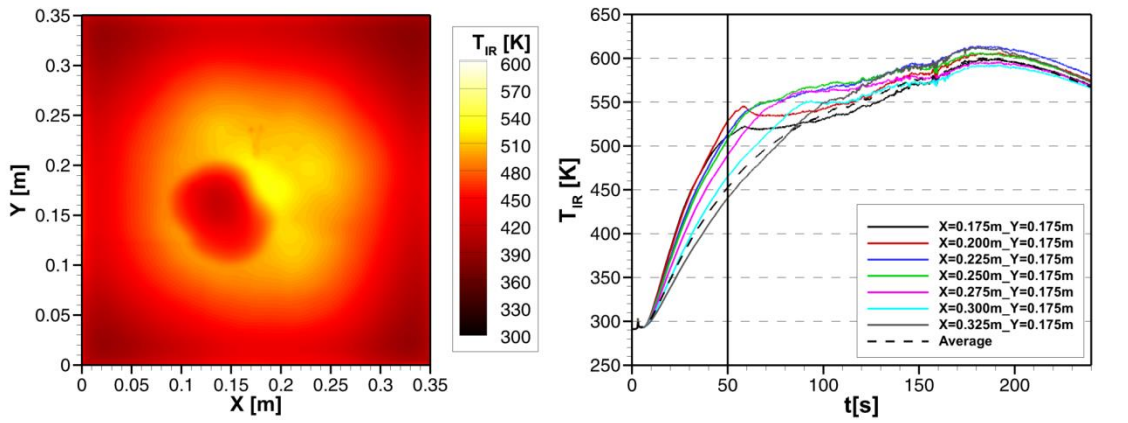

(a) Instantaneous temperature map at $t_{exposure} = 50\ s$

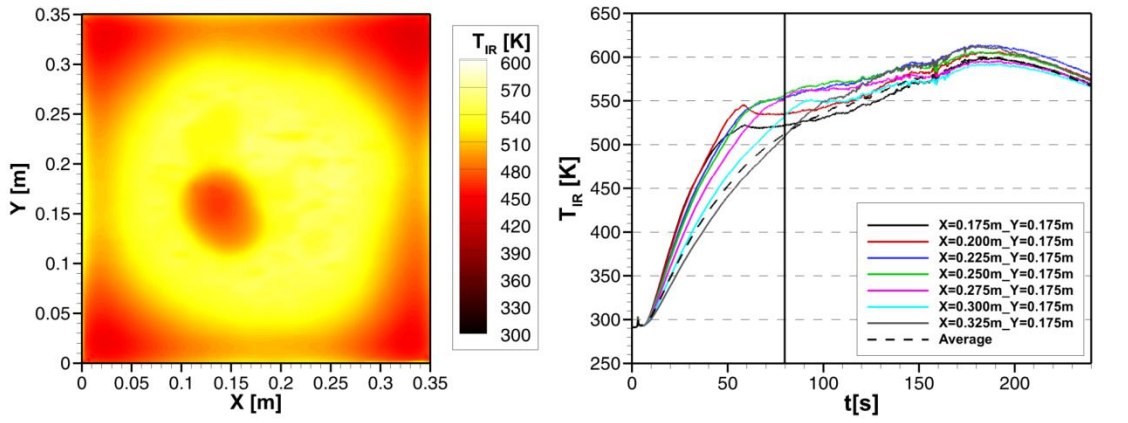

(b) Instantaneous temperature map at $t_{exposure} = 80\ s$

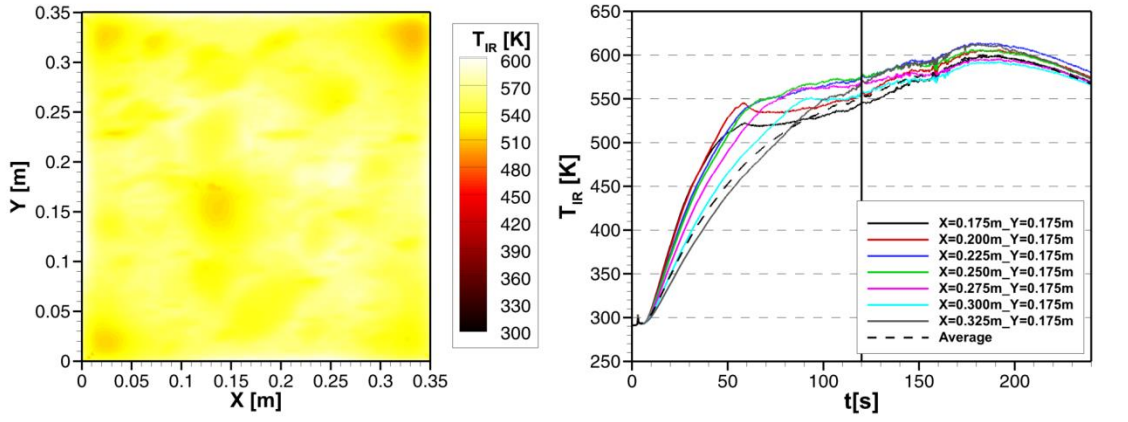

(c) Instantaneous temperature map at $t_{exposure} = 120\ s$

Figure 109 - Fire-induced decomposition during $t_{fire} = 150\ s$ - Test #028

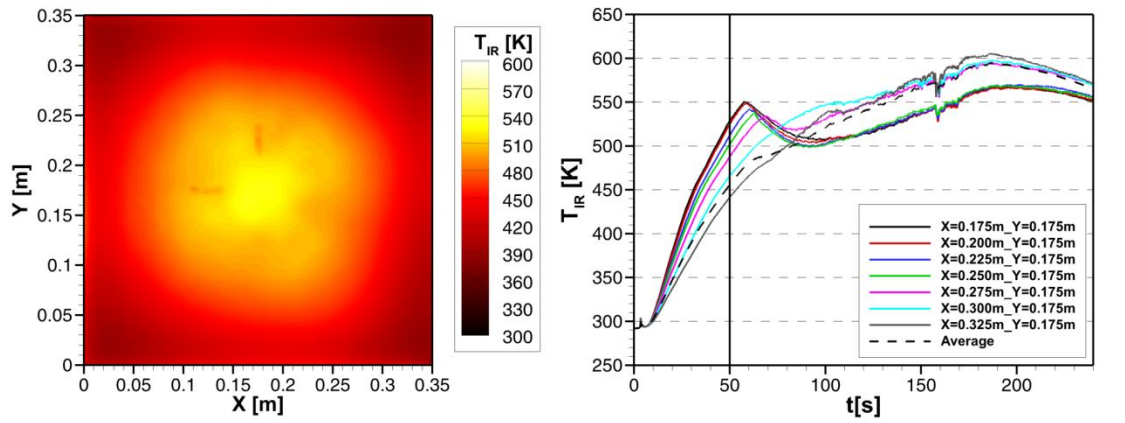

(a) Instantaneous temperature map at $t_{exposure} = 50\ s$

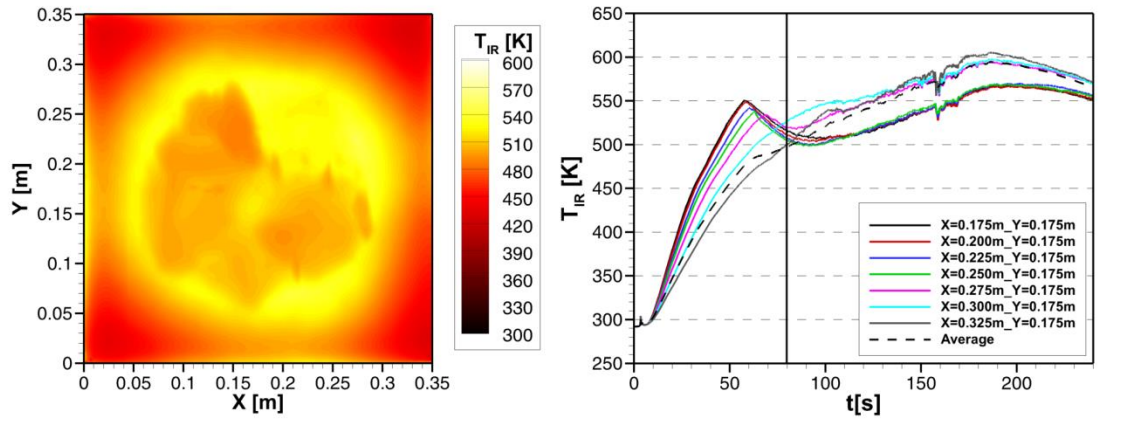

(b) Instantaneous temperature map at $t_{exposure} = 80\ s$

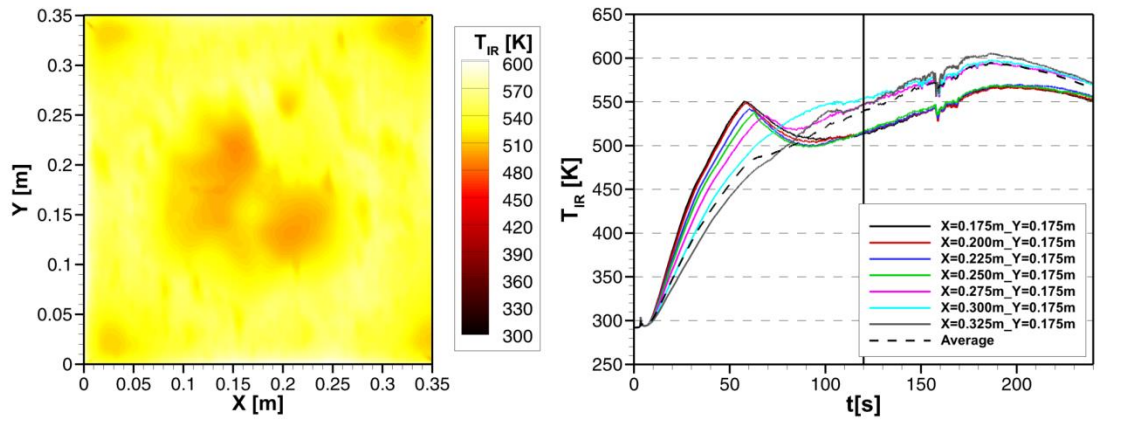

(c) Instantaneous temperature map at $t_{exposure} = 120\ s$

Figure 110 - Fire-induced decomposition during $t_{fire} = 150\ s$ - Test #029

The six tests can be categorised according to the thermal response on the unexposed surface:

- For low impact velocities, almost no damage is observed on the panels by the NDI and an undamaged thermal behaviour is expected during the measurements.
- For higher impact velocities, significant internal damage is observed by the NDI and the thermal behaviour should be affected by the cracks as it would be by a fire-induced delamination damage.
- For intermediate impact velocities, damage can be located on the surface ply only without affecting the thermal response on the unexposed surface. Heat diffusion in the through-thickness direction will smooth any local discontinuity and the thermal behaviour will be similar to an undamaged behaviour.

Only two different behaviours are observed in the first phase of the measurements:

- The thermally-undamaged test coupons (#024 in Figure 96, #027 in Figure 99 and #029 in Figure 110) show a thermal behaviour similar to undamaged panels tested previously in D7.7. The maximum temperature is measured at the centre of the back surface (black line on the right plot) during the experiment.
- For the three others (#025 in Figure 106, #026 in Figure 107 and #028 in Figure 100), the shape and dimension of the initial internal damage can be observed at the beginning of the experiments. The temperature at the centre (black line on the right plot) is no longer the highest and the thermal response is affected by the damage.

Fire-induced damage occurs in second phase of the experiments with a significant temperature decay measured on the unexposed surface while the flame is still impinging the exposed surface.

Finally, when the burner is moved away from the coupon and the self-extinguishing time is reached, the temperature starts to decrease on the material unexposed surface.

8.4. Mass loss measurements

Figure 111 shows the mass loss measurements performed in the FIRE facility with test conditions detailed in Table 19. The 9 different plots are ranked according to the fire exposure time from $t_{fire} = 60\ s$ for Figure 111 (a-d) to $t_{fire} = 30\ s$ for Figure 111 (e-i).

The black symbols represent the raw data measured by the weighing module. At $t_{fire} = 0\ s$, an positive offset is observed on all curves. At $t_{fire} = 60\ s$ (or respectively $t_{fire} = 30\ s$), a similar but negative offset is observed. This phenomenon is related to the pressure force driven by the burner gas flow impinging the surface of the test coupon. As a consequence, the data, extracted during the period where the coupon is exposed to the fire, are shifted upward due to this pressure constraint.

The processing of the mass loss signal then consists in identifying the pressure shift on all curves and in removing the offset when the burner is below the coupon. The raw data with the pressure correction is plotted in blue symbols in Figure 111. Theoretically, the corrected data must reach the baseline measured before and after the test. Most tests verified this criterion.

Finally, the corrected data are filtered to remove noise using a frequency based filter (non-dimensional factor f is given on the curves). The red curves give the filtered data to analyse the time evolution and mass loss magnitude for the different tests.

Some oscillations are noticed on some tests despite the filtering of the signal. The oscillations can be also observed on the raw data if the filter removed points too far away from the baseline. These oscillations are related to stresses relaxation of the composite coupon during the test. Reasons might be found in the buckling phenomenon despite the clamps that hold the coupon on the four corners.

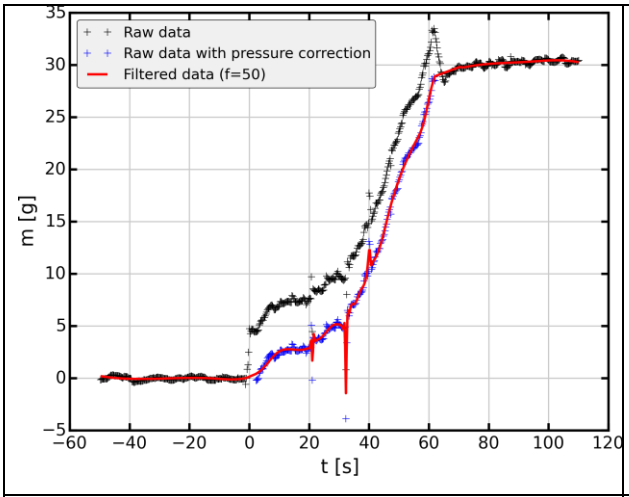

(a) Test #011

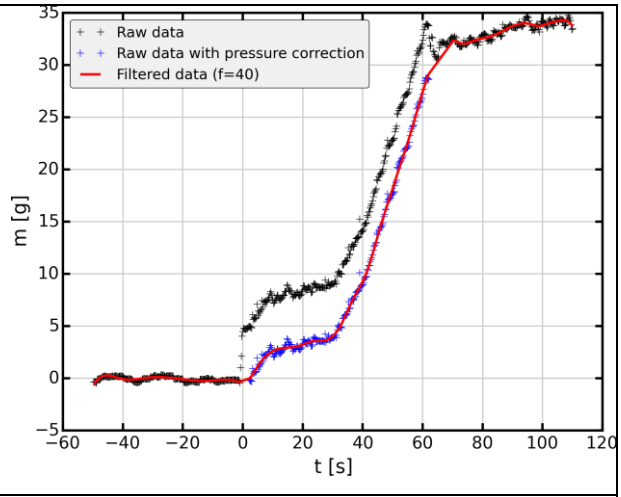

(b) Test #012

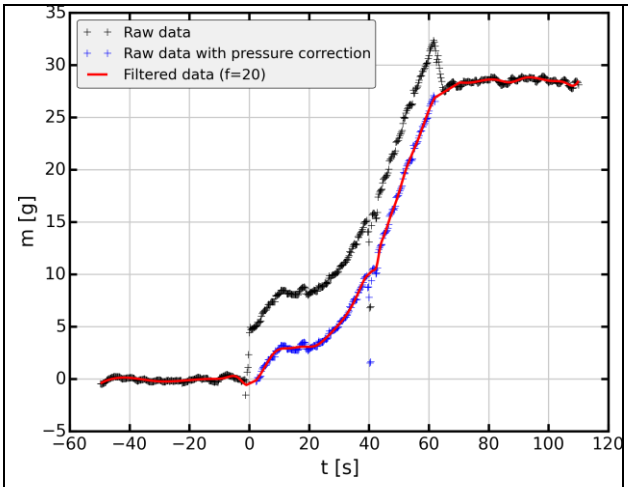

(c) Test #013

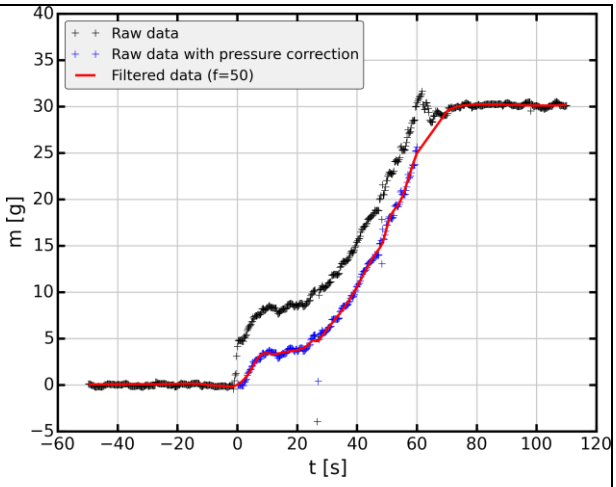

(d) Test #018

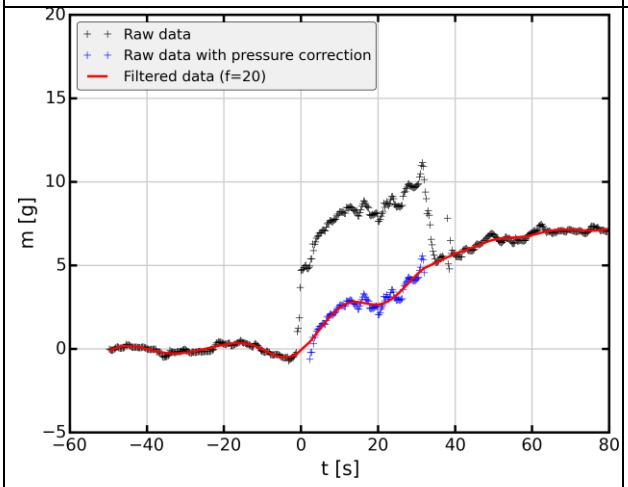

(e) Test #014

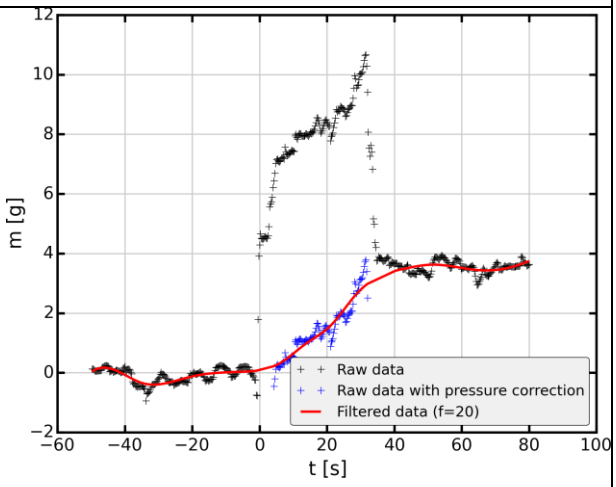

(f) Test #015

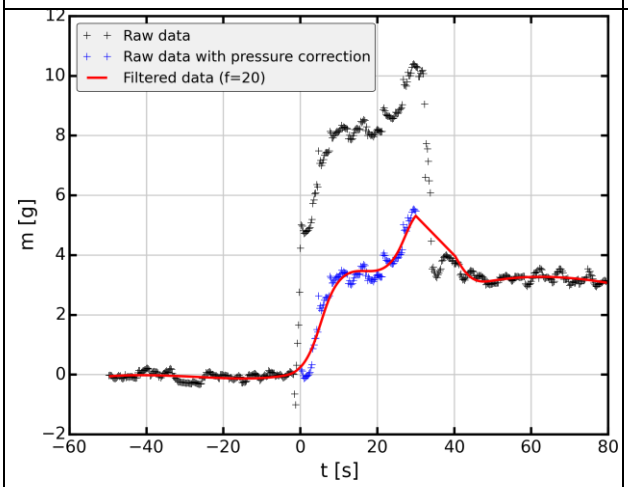

(g) Test #016

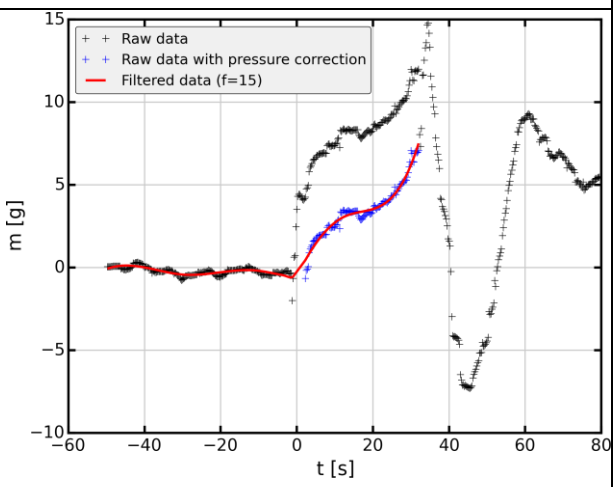

(h) Test #017

Future Sky Safety has received funding from the EU's Horizon 2020 Research and Innovation Programme, under Grant Agreement No. 640597.

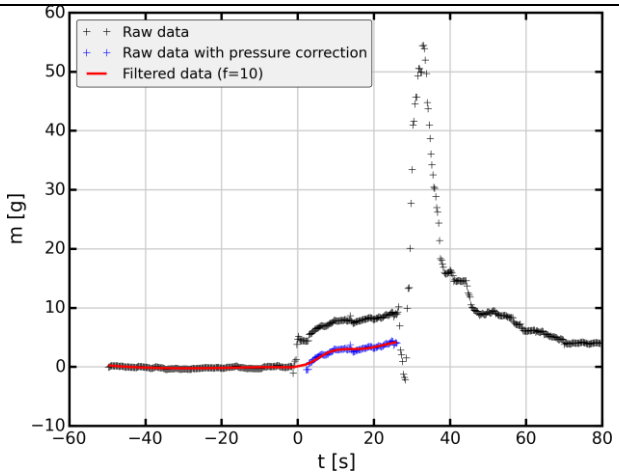

(i) Test #019

Figure 111 – Mass loss measurements performed on 9 test coupons exposed to a fire during $t_{fire} = 60\ s$ (a-d) and $t_{fire} = 30\ s$ (e-i)

The reproducibility of the results is very satisfactory with $\Delta m_{max} = [25 - 30\ g]$ for $t_{fire} = 60\ s$ and $\Delta m_{max} = [4 - 7\ g]$ for $t_{fire} = 30\ s$. The exposure time has a significant effect on the mass loss. The first $30\ s$ of fire heating correspond to a transient phase where temperature increases and pyrolysis starts. The behaviour on the next $30\ s$ shows a linear trend which may be related to the quasi-steady state observed in Figure 93. The mass loss slope increases significantly during this phase which may be the result of the heat flux contribution of the volatile ignition onto the material exposed surface.

On most tests, the mass loss keeps on increasing slightly after the burner is moved away from the test coupon. This feature is related first to the still high temperature within the material and second to remaining flames that can sustain the decomposition until self-extinguishing.

8.4.1. Damaged composite panels

Figure 111 shows the mass loss measurements performed in the FIRE facility with test conditions detailed in Table 20 considering damaged test coupons.

Despite the stresses relaxation occurring within the material as detailed previously for virgin composite panels, another undesired effect is observed on tests #027 and #029 with a negative mass loss at the beginning of the experiment. It should be related to a residual contact between the test coupon and the ceramic plate around the coupon holder. This contact prevents the coupon to apply its entire weigh force on the balance. For test #027, the contact should have occurred just after the burner has reached its final position under the coupon because the pressure force is clearly noticeable and the mass loss measurement gets back to the baseline in the second part of the test. For test #029, the contact should have occurred when the coupon was placed on the holder. The pressure force correction results in a

corrected mass loss higher than the raw data. As a consequence, this particular test cannot be analysed and it is considered as failed.

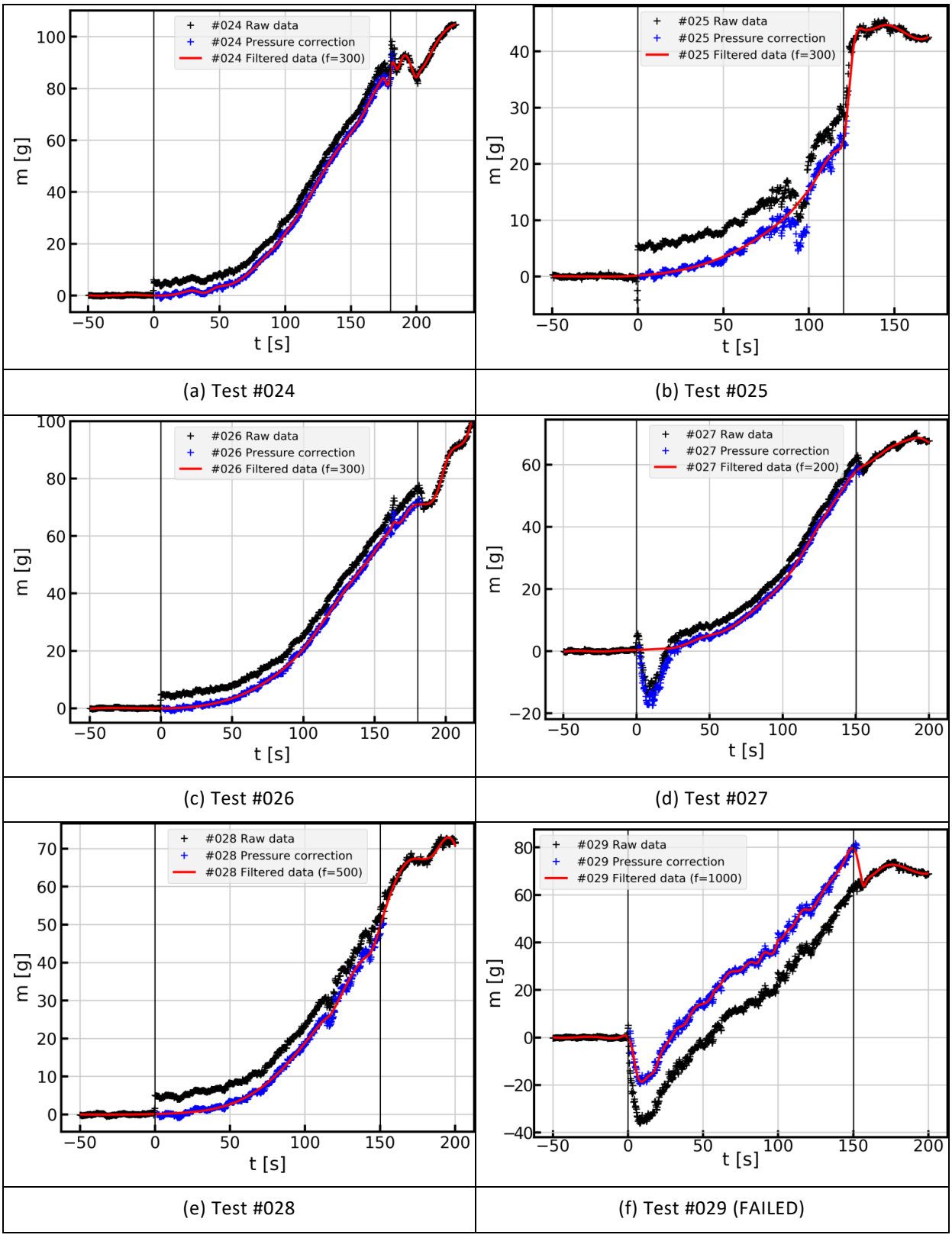

Figure 112 – Mass loss measurements performed on 6 damaged test coupons exposed to a fire from $t_{fire} = 120\ s$ up to $t_{fire} = 180\ s$

The comparison in Figure 113 of all tests but test #029 shows that the reproducibility of the measurements is not as satisfactory as for the undamaged panels tested in the previous.

The mass loss rate seems to be slightly higher for the test coupons where NDI showed almost no damage (tests #024 and #027). As a consequence, damage induced by impacts can slightly delay the overall decomposition of the material during the test. The insulating effect of the internal cracks prevents temporarily the decomposition of the material part located after the cracks. But if the exposure time is high enough, fire-induced damages will prevail and drive the material behaviour.

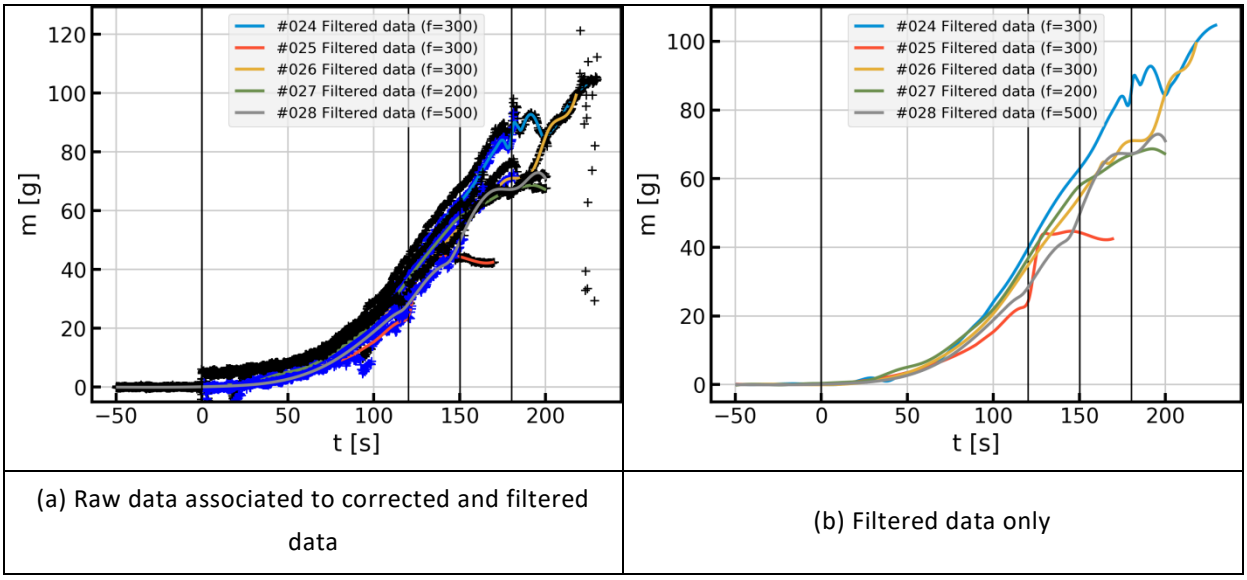

(a) Raw data associated to corrected and filtered data

(b) Filtered data only

Figure 113 – Mass loss measurement comparison

8.5. Preliminary delamination damage analysis

Digital Image Correlation (DIC) is used to measure the deformation of the back surface of the test coupon using a random speckle pattern blue light projection and 2 cameras in a stereoscopic configuration.

This technique is carried with ONERA in-house software for both image acquisition and correlation processing. However, although the FIRE test facility was not developed during Future Sky Safety project, the DIC method implementation into the facility was performed during Future Sky Safety. As a consequence, some work still remains to calibrate the two cameras and correct all optical flaws, to process automatically all sets of images in order to assess the surface deformation. It is important to recall that for a $150\ s$ acquisition:

- 750 images are recorded by each camera at the frequency of $5\ Hz$.
- Each $5\ Mpx$ image has a file size of $5\ Mo$.

As a consequence, the volume of data to process is $7.5\ Go$. It should require high computation resources.

However, the raw image analysis highlights some interesting features concerning the onset and growth of delamination damage with is the main interest of the method. Figure 114 gives an example of images from the DIC measurement technique during fire-induced decomposition and shows the delamination damage onset for test #014. The software will then correlate the initial background image with each of the following images to assess the deformation.

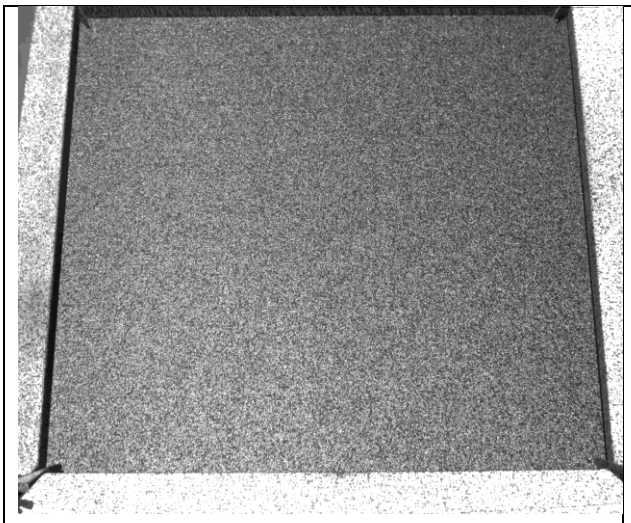

(a) Camera A – initial background image

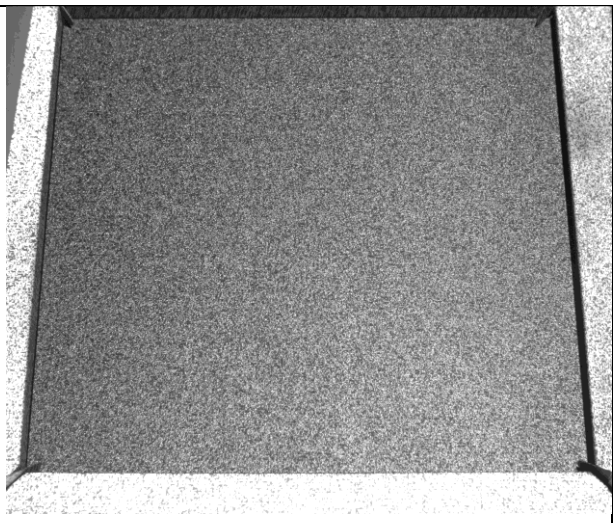

(b) Camera B – initial background image

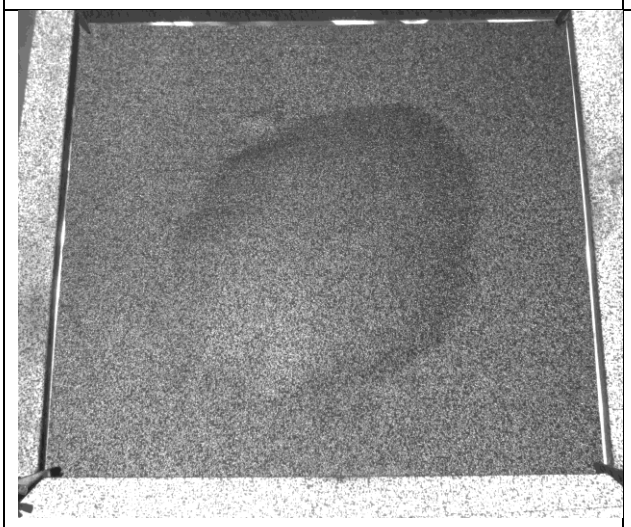

(c) Camera A – delamination image

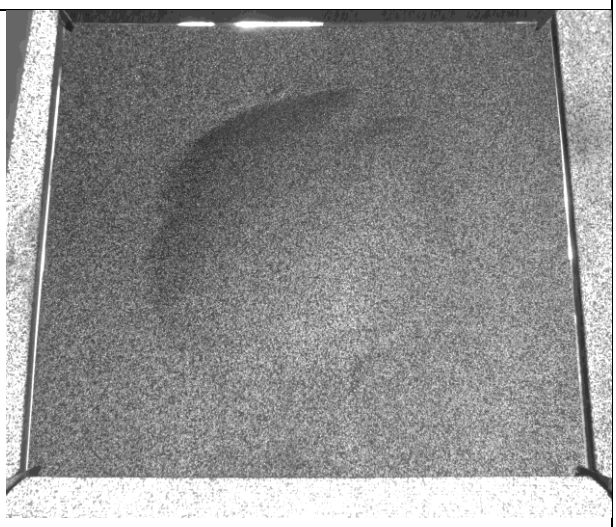

(d) Camera B – delamination image

Figure 114 – Example of images from the DIC measurement technique during fire-induced decomposition and delamination damage onset (Test #014)

ONERA's on-going work will also consist in combining the deformation with the infrared thermographic measurements for 3D temperature reconstruction.

9 MECHANICAL AND THERMO-MECHANICAL TESTING

9.1. Thermal expansion characterization

9.1.1. Experimental procedure and test matrix

The purpose of this experimental study is to characterize the evolution of the thermal expansion of the material as function of the temperature. The SETSYS Evolution testing device from SETARAM (Figure 115) has been used for the dilatometric measurements. Silica probe has been used for the coupon associated with thermocouples type K and P for temperature measurement. One thermocouple is used for controlling the temperature evolution in the furnace and another one is used for monitored the sample temperature. For such device, the gas ambiance can be imposed. In this experimental campaign, air and neutral gas (nitrogen or argon) have been used in order to evaluate the influence of the oxidation chemical reaction on the thermal expansion.

Figure 115 – Dilatometric measurement : SETSYS Evolution testing device from SETARAM

The Table 22 presents the test matrix and the length of the sample. All the coupons have been cutting from the 3809A_FSS_P7_P204-01_SS02 plate which is a $[0]_8$ stacking sequence composite laminate and have a width of 10 mm.

Name	Length [mm]	Orientation	Enceinte Temperature [°C]	Gas
P204-01-L1	19.86	Fiber	20→150→20→250→20	Air
P204-01-L2	19.74	Fiber	20→150→20→250→20	Air
P204-01-L3	19.74	Fiber	20->150->20->250->20	Air
P204-01-T1	10.11	Transverse Fiber	20→125→20→250→20	Air
P204-01-T2	10.10	Transverse Fiber	3x[20→100→20]→250→20	Air
P204-01-T3	10.01	Transverse Fiber	20→250→50→600	Nitrogen

Name	Length [mm]	Orientation	Enceinte Temperature [°C]	Gas
P204-01-T4	9.75	Transverse Fiber	20→250→50→600→50→250→20	Argon
P204-01-T5	9.75	Transverse Fiber	20→250→50→600→50→250→20	Argon
P204-01-T6	9.75	Transverse Fiber	20→150→50→250→20	Air
P204-01-T7	10.18	Out of plane	20→250→50→250→20	Air
P204-01-ep1	2.27 2.28	Out of plane	20→150→20→250→20// 20→800→20	Air Air
P204-01-ep2	2.24	Out of plane	20→125→20→250→20	Air
P204-01-ep3	2.25	Out of plane	20→250→50→600	Argon
P204-01-ep4	2.11	Out of plane	20→150→50→250→20	Argon
P204-01-ep5	2.24	Out of plane	20→150→50→250→20	Air
P204-01-ep6	2.24	Out of plane	20→150→50→250→20	Air

Table 22 - Test matrix for thermal expansion characterization

The idea of this test matrix was to select a temperature lower than the glass transition temperature (T_G ≈ 200°C), another one after the T_G but before the temperature of pyrolysis of the matrix and a last one after this pyrolysis temperature (≈ 380°C).

Complex temperature cycling permits to check the effect of the temperature history loading on the apparent thermal expansion behaviour. For example, P204-01-T2 sample has been tested with 3 cycling between ambient temperature and 100°C in order to check if the thermal expansion behavior is reversible.

All the results present hereafter the evolution of the thermal strain versus the temperature of the sample. This experimental thermal strain ε_{th} is defined as:

$$\varepsilon_{th} = \frac{\Delta L}{L_0}$$

Where ΔL is the displacement measured by the device and L_0 is the initial sample length.

In order to take into account the effect of the thermal expansion of the probe, a “blank line” is performed before each temperature cycling on a reference sample. Nevertheless, due to the temperature imposed and the value of the displacement measured in our test campaign, this correction could be neglected. For measure the displacement, a very low force is applied to the sample by a mass of 5 g for all the samples except for P204-01-ep3 for which a mass of 10 g was imposed.

9.1.2. Results

9.1.2.1. Thermal expansion in the fiber direction

The Figure 116 presents the evolution of the longitudinal thermal strain as function of the sample temperature. From this result is could be conclude that the coefficient of thermal expansion (CTE) in the fiber direction can be considered as null as expected.

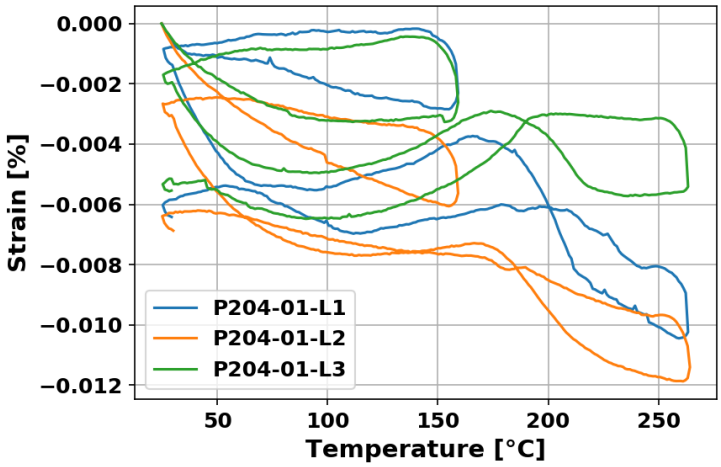

Figure 116 – Evolution of the longitudinal thermal strain as function of the temperature

9.1.2.2. Thermal expansion in the transverse fibre direction

The Figure 121 presents the evolution of the transverse thermal strain as function of the sample temperature in air ambiance. We can observe that before the T_G, the thermal expansion behavior seems to be reversible and presents a linear trend. Just before reaching for the first time the glass transition temperature, the material exhibits a quite strange behavior with a plateau for the evolution of the thermal strain. After this plateau and for temperature greater than glass transition, the evolution of the thermal strain is quite linear with the temperature growth but presents an effective tangent CTE higher than for temperature below T_G. After reaching 250°C and during the cooling phase, the material exhibits an hysteresis in the thermal expansion behavior with a "residual strain" of -0.2% at ambient temperature. For the next thermal cycling between ambient temperature and 250°C, the effective thermal strain behavior of the material in the transverse direction is bilinear and reversible. The apparent tangent CTE is lower before T_G than after.

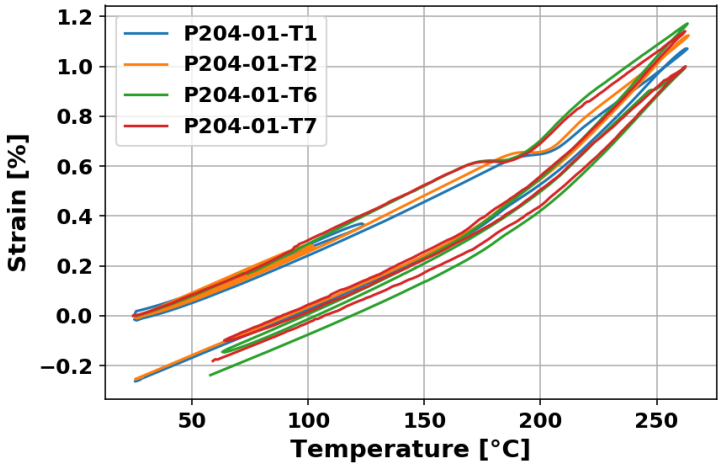

Figure 117 – Evolution of the transverse thermal strain as function of the temperature in air ambiance

The Figure 122 presents the thermal strain evolution as function of the temperature under inert atmosphere. The same evolution is observed before 250°C in neutral ambiance than in oxidizing atmosphere. After 250°C, the thermal train continue to increase but with a non linear trend until a sudden fall. For P204-01-T3, the sample collapses and the test is aborting by the buckling of the coupon (Figure 119). The P204-01-T3, is the only coupon what collapses during our test campaign but it also the only one on which a mass of 10 g was applied versus 5 g for the other coupons. Nevertheless, 10 g is equivalent to a compression stress of 4444 Pa on the material which is very low. For the other samples, after this fall, the thermal strain is decreasing during heating and seems to converge to a plateau. During the cooling phase, the apparent tangent CTE is very low.

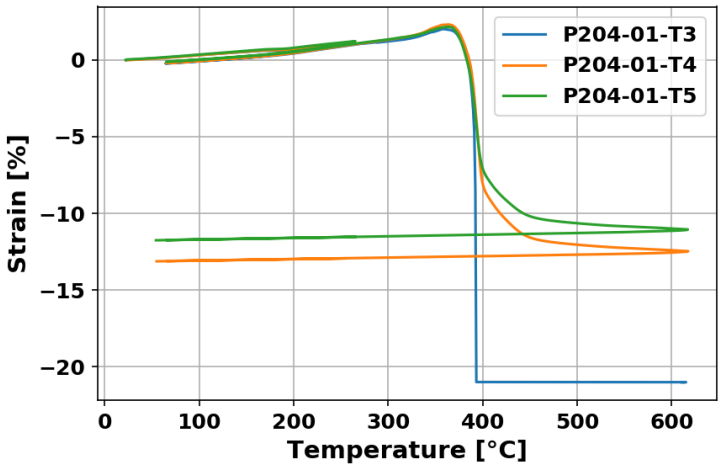

Figure 118 – Evolution of the transverse thermal strain as function of the temperature in neutral ambiance

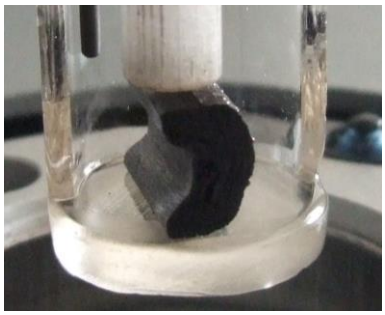

Figure 119 – Buckling of the P204-01-T3 sample after 380°C

This temperature of collapse of the coupon is coherent with the thermal degradation of the material. The TGA highlights a global reaction at around 380°C (653 K) and corresponding to the pyrolysis reaction of the matrix. One can conclude from this result that the material is very brittle in charred state.

The Figure 123 confirms the excellent agreement between test performed at air ambiance and at inert ambiance.

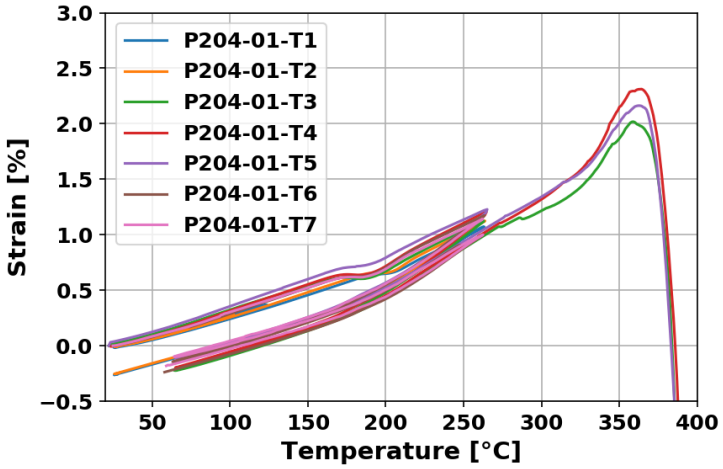

Figure 120 – Comparison of the evolution of the transverse thermal strain as function of the temperature at air or inert ambiance

9.1.2.3. Thermal expansion in the out of plane direction

The Figure 121 presents the evolution of the out of plane thermal strain as function of the sample temperature in air ambiance. We can observe a similar trend for the evolution of the out of plane thermal strain than for the transverse thermal strain.

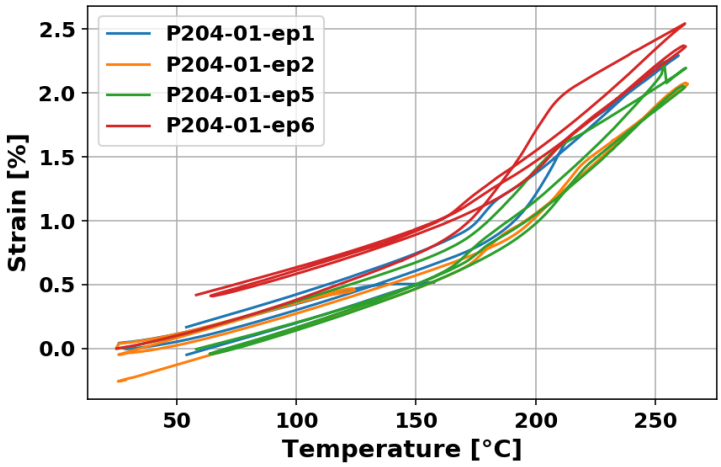

Figure 121 – Evolution of the out of plane thermal strain as function of the temperature in air ambiance

The Figure 122 presents the thermal strain evolution as function of the temperature under inert atmosphere and the evolution of the thermal strain is also similar than the evolution of the transverse thermal strain. A fall of the thermal strain is also measured at 380°C corresponding to the temperature of the pyrolysis of the matrix.

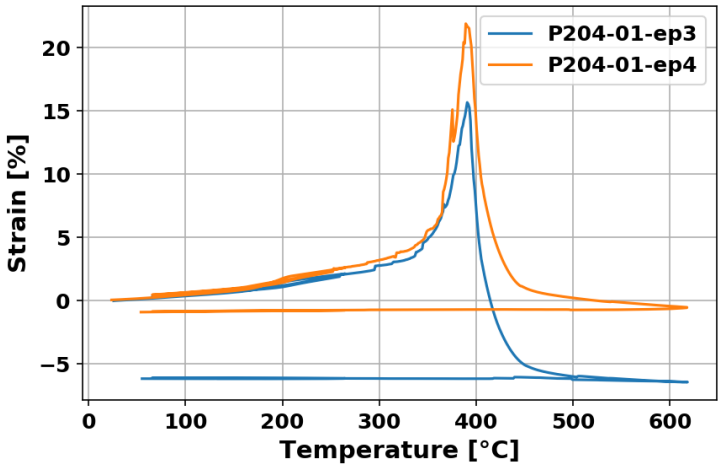

Figure 122 – Evolution of the transverse thermal strain as function of the temperature in neutral ambiance

The Figure 123 confirms the excellent agreement between test performed at air ambiance and at inert ambiance.

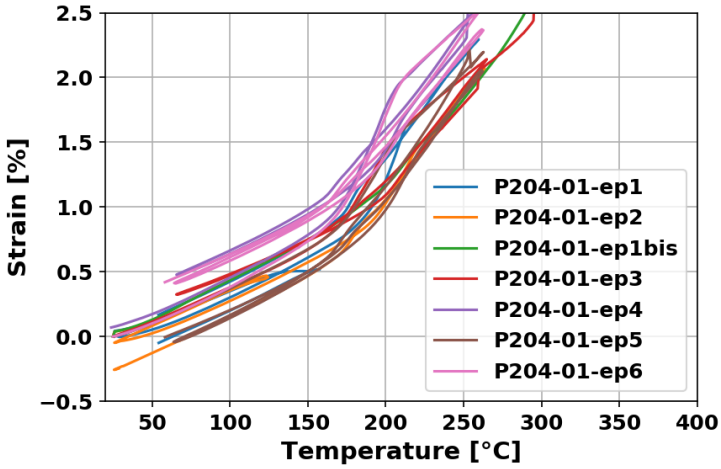

Figure 123 – Comparison of the evolution of the transverse thermal strain as function of the temperature at air or inert ambiance

9.1.2.4. Comparison between transverse and out of plane thermal expansion

The Figure 124 compares the evolution of transverse and the out of plane thermal strains. This Figure highlights the higher influence of the temperature on the out of plane thermal expansion than for the transverse one.

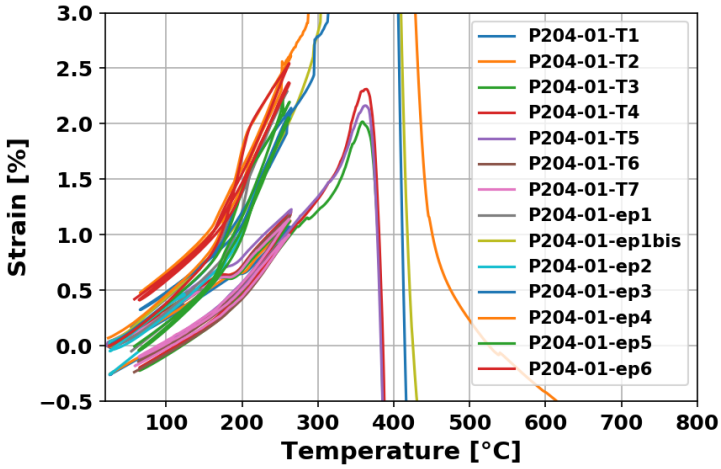

Figure 124 – Comparison of the evolution of the transverse and out of plane thermal strain as function of the temperature

The Figures 125-126 presents the evolution of the sequent CTE defined by:

$$\alpha_{seq} = \frac{\varepsilon_{th}(T) - \varepsilon_{th}(T_o)}{T - T_o}$$

where T_o is a reference temperature. In our case, T_0 = 180°C.

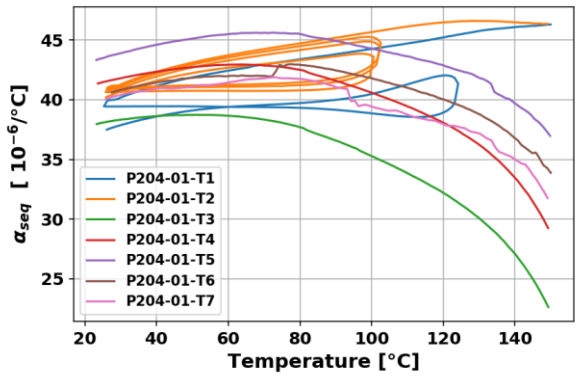

a/ Evolution of the sequent transverse CTE 20°C-150°C

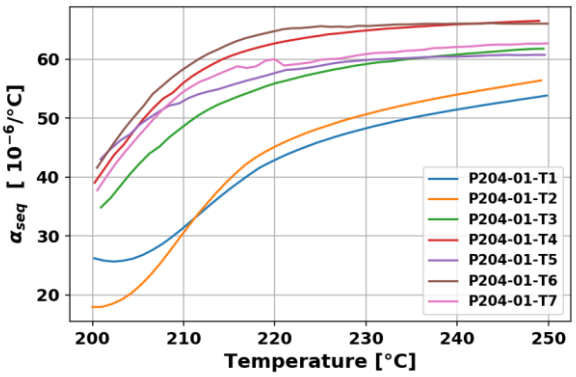

b/ Evolution of the sequent transverse CTE 200°C-250°C (first cycle)

Figure 125 – Evolution of the sequent transverse CTE as function of the temperature

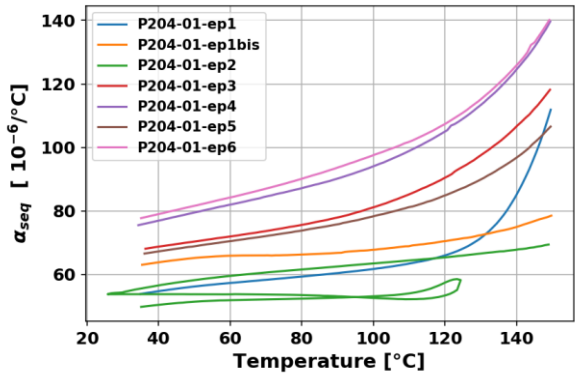

a/ Evolution of the sequent out of plane CTE 20°C-150°C

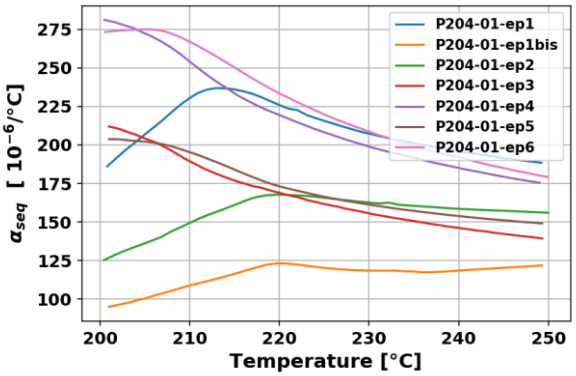

b/ Evolution of the sequent out of plane CTE 200°C-250°C (first cycle)

Figure 126 – Evolution of the sequent transverse CTE as function of the temperature

These figures highlight the difficulty to characterize the sequent CTE for values higher than T_G. This is the reason why, the linear CTE for the transverse and out of plane direction have been characterized between 20°C and 120°C. The Figures 127-128 present the characterisation of these coefficients by linear regression of the evolution of the transverse and out of plane thermal strains between 20°C and 120°C. Tables 23-24 resume the linear CTE values.

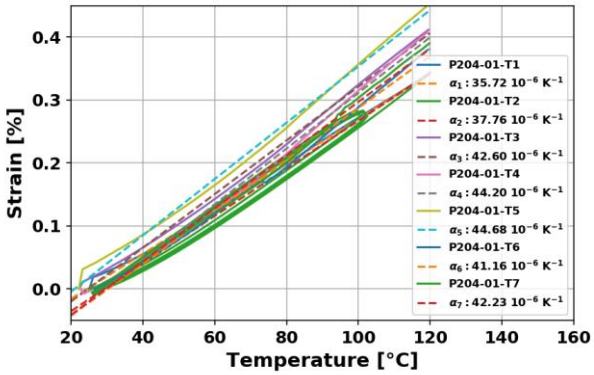

a/ Linear regression of the transverse CTE between 20°C and 120°C

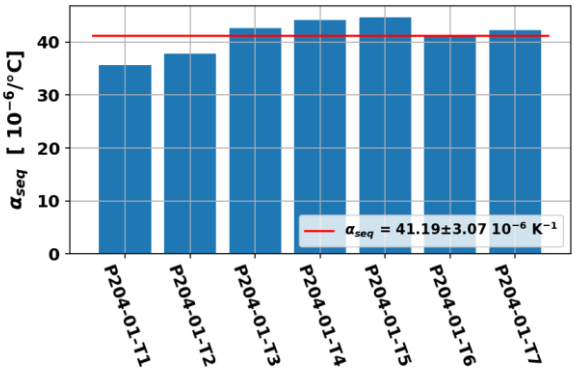

b/ Distribution of transverse linear CTE

Figure 127 – Linear transverse CTE for T700GC/M21

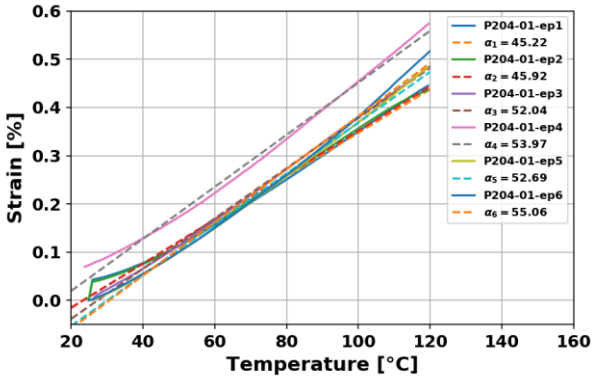

a/ Linear regression of the out of plane CTE between 20°C and 120°C

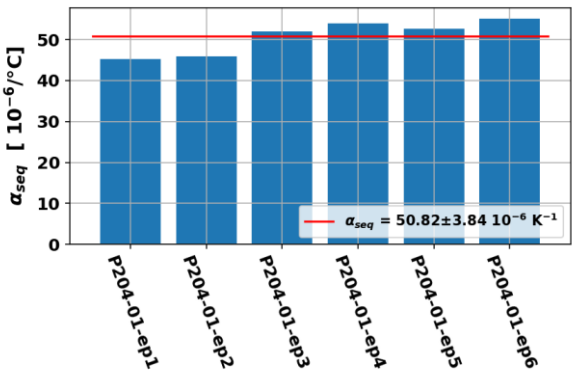

b/ Distribution of out of plane linear CTE

Figure 128 – Linear transverse CTE for T700GC/M21

Name	Linear CTE [10^{-6} K^{-1}]
P204-01-T1	35.72
P204-01-T2	37.76
P204-01-T3	42.60
P204-01-T4	44.20
P204-01-T5	44.68
P204-01-T6	41.16
P204-01-T7	42.23
CTE (mean, std)	41.19±3.07

Table 23 – Linear coefficient of thermal expansion in transverse direction

Name	Linear CTE [10^{-6} K^{-1}]
P204-01-ep1	45.22
P204-01-ep2	45.92
P204-01-ep3	52.04
P204-01-ep4	53.97
P204-01-ep5	52.69
P204-01-ep6	55.06
CTE (mean, std)	50.82 ±3.84

Table 24 – Linear coefficient of thermal expansion in out of plane direction

9.2. Static mechanical tests

9.2.1. Experimental technics and methods

The purpose of this study is to characterize the influence of the temperature on the apparent static behavior of the selected Carbon/Epoxy material. Two different configurations have been used in this study. One dedicated to tensile tests on standard tensile coupons with no tabs. In this case, The geometry of the coupon as recommended in ASTM D3039 or in ISO 527 is :

- For 0° unidirectional laminates 15 mm width x 250 mm long x 2.25 mm thick
- For 90° unidirectional or $[\pm 45]_{4s}$ laminates 25 mm width x 250 mm long x 2.25 mm thick

Figure 129-130 present the set up use for performing static test on a Zwick electromechanical testing machine ZW150 with a 150 kN high capacity. In order to apply a specified temperature, a climate chamber has been used as illustrated on Figure 129-130. In order de validate the strength of some laminates, a hydraulic testing machine from MASER with a 500°kN high capacity have been used (Figure).

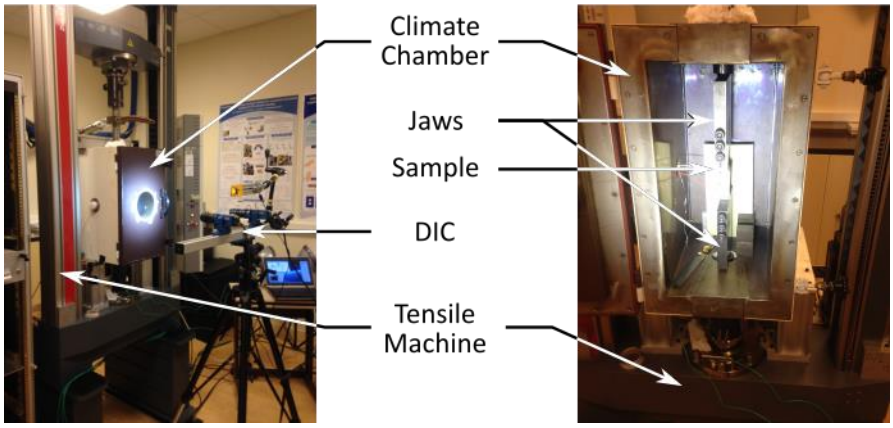

Figure 129 – Experimental setup used for the static mechanical characterization of laminates at different temperatures.

In order to check the temperature inside the climate chamber, the temperature is monitored on a reference coupon close to the test sample as mentioned on Figure 130. The mechanical test is applied only after the temperature stabilization inside the climate chamber. The waiting time necessary depends on the setpoint temperature defined. It takes up to 2 hours before achieving the temperature of 200°C (figure 132) for example for the P210-5.

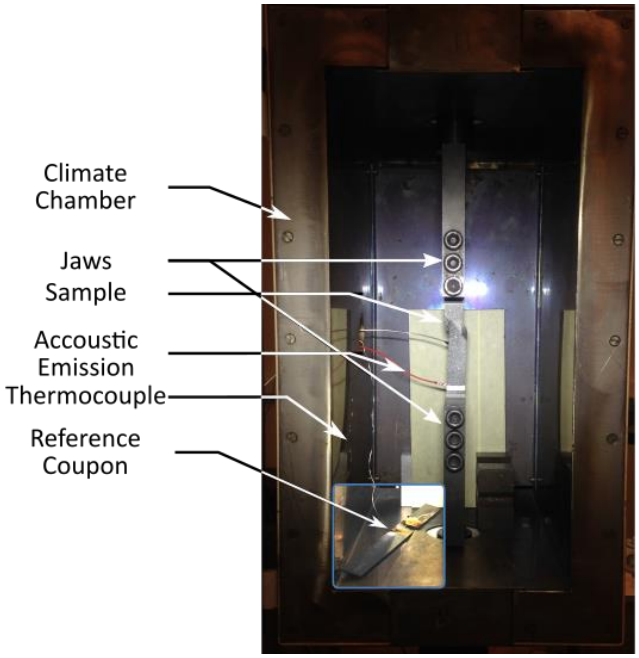

Figure 130 – Experimental setup used for the static mechanical characterization of laminates at different temperatures.

Figure 131 – Experimental setup used for the static mechanical characterization of laminates on the hydraulic testing machine MASER 50T.

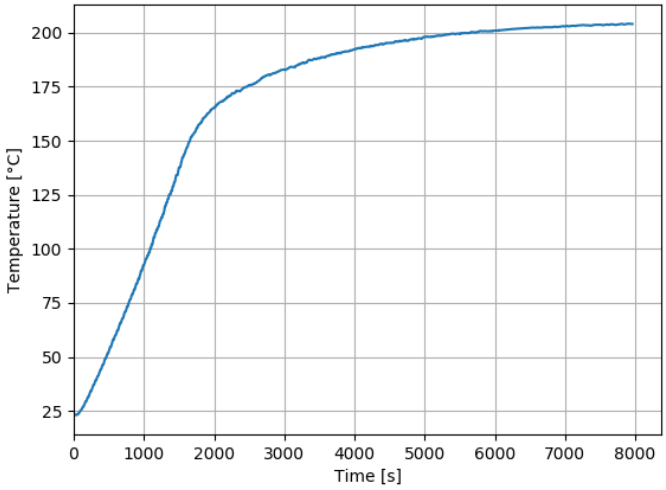

Figure 132 – Waiting time evolution of the temperature applied to a 0° unidirectional laminate before applying mechanical loading on P210-5 sample.

The strain measurement is performed by using Digital Image Correlation. The "VIC-3D" system provided by "correlated solutions" is used. 2048x2048 images are taken with a frame rate of 1 image per second. Coupons surface are covered with a speckle realized thanks to blank and black paint. The strain of the sample is averaged on virtual gauge that covers all the gage area of the coupon (Figure 133). Only few samples have been monitored with acoustic emission.

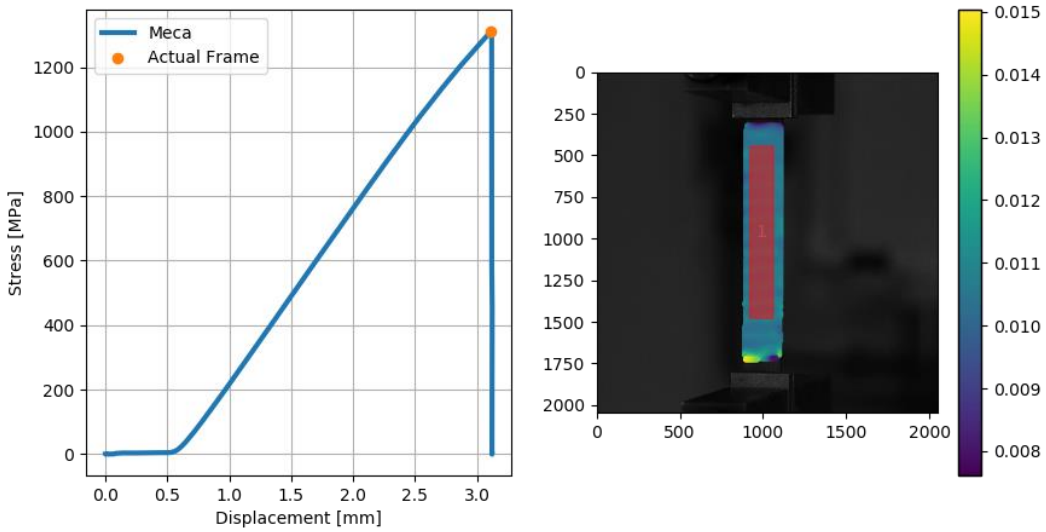

Figure 133 – Virtual strain gauge for tensile test on 0° unidirectional (P210-1 coupon). The area of the strain gauge is in red on figure.

9.2.2. Thermomechanical properties in the fiber axis for static tensile test

Thermomechanical loading have been applied on 0° unidirectional 8 plies laminate manufactured by CEIIA. The test matrix of the mechanical tests is described in the Table 25. Tests follow the recommendations of the EN ISO 527 normative procedure.

Reference Plate	Coupon Reference	Loading rate	Temperature	Stacking Sequence	width
3809A_FSS_P7_P210-01_SS02	P210-1	1. mm/min	ambient	$[0°]_8$	15 mm
3809A_FSS_P7_P210-01_SS02	P210-2	1. mm/min	ambient	$[0°]_8$	15 mm
3809A_FSS_P7_P210-01_SS02	P210-3	1. mm/min	145°C	$[0°]_8$	15 mm
3809A_FSS_P7_P210-01_SS02	P210-4	1. mm/min	145°C	$[0°]_8$	15 mm
3809A_FSS_P7_P210-01_SS02	P210-5	1. mm/min	205°C	$[0°]_8$	15 mm
3809A_FSS_P7_P210-01_SS02	P210-7	1. mm/min	ambient	$[0°]_8$	15 mm
3809A_FSS_P7_P210-01_SS02	P210-8	1. mm/min	ambient	$[0°]_8$	15 mm
3809A_FSS_P7_P210-01_SS02	P210-9	1. mm/min	ambient	$[0°]_8$	15 mm

Reference Plate	Coupon Reference	Loading rate	Temperature	Stacking Sequence	width
3809A_FSS_P7_P210-01_SS02	P210-10	1. mm/min	180°C	$[0°]_8$	15 mm
3809A_FSS_P7_P210-01_SS02	P210-6	1. mm/min	180°C	$[0°]_8$	15 mm

Table 25 – Test matrix for 0° unidirectional laminates

The Figure 134 shows the evolution of the longitudinal and transverse strain versus the applied strain.

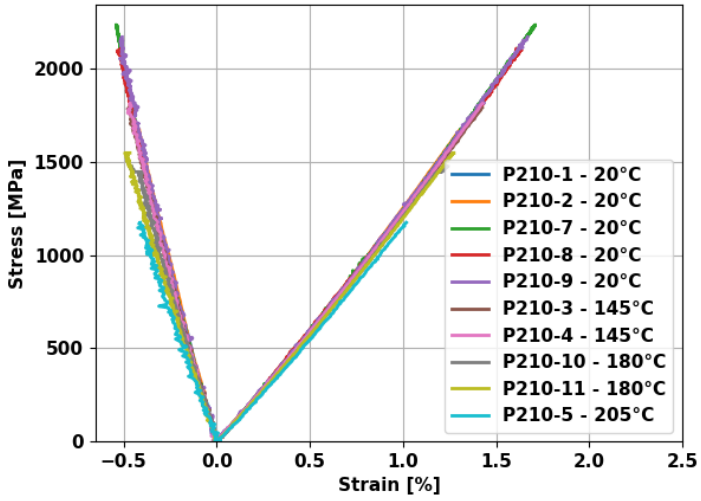

Figure 134 – Stress strain curve of 0° unidirectional laminates for 20°C , 145°C, 180°C and 205°C.

Whatever the applied temperature, the response of the material is linear until the final rupture. The very low increase of the modulus is observed thanks to the alignment of the fibers. It can be considered that the behavior in the fiber direction is elastic linear. The results exhibit a very low influence of the temperature on the mechanical behavior in the fiber direction. Concerning the failure stress, the values obtained couldn't be considered as pertinent since:

- For tests at ambient and 145°C, splitting cracks have been observed (Figure 135)
- For tests at 205°C, sliding of the coupon in the jaws have been observed (Figure 136)

We can notice for coupons P210-7, P210-8 and P210-9, the hydraulic testing machine was used and the elastic behavior of the coupons exhibit is similar to the test obtain with the electromechanical machine. Nevertheless, the ultimate strength is higher for these coupons than for tests performed on coupons P210-1 and P210-2. Hence, only the longitudinal Young modulus and Poison ratio have been reported in Table 26.

Coupon Reference	Temperature	Stacking Sequence	Young Modulus	Poison ratio
P210-1	ambient	$[0°]_8$	113.67 GPa	0.33

Coupon Reference	Temperature	Stacking Sequence	Young Modulus	Poison ratio
P210-2	ambient	$[0°]_8$	117.43 GPa	0.33
P210-7	ambient	$[0°]_8$	117.06 GPa	0.33
P210-8	ambient	$[0°]_8$	118.25 GPa	0.34
P210-9	ambient	$[0°]_8$	119.22 GPa	0.32
P210-3	145°C	$[0°]_8$	111.81 GPa	0.34
P210-4	145°C	$[0°]_8$	112.68 GPa	0.34
P210-10	180°C	$[0°]_8$	111.60 GPa	0.38
P210-11	180°C	$[0°]_8$	112.40 GPa	0.39
P210-5	205°C	$[0°]_8$	107.73 GPa	0.42

Table 26 – Young and poison ratio for 0° unidirectional laminates according to ISO 527

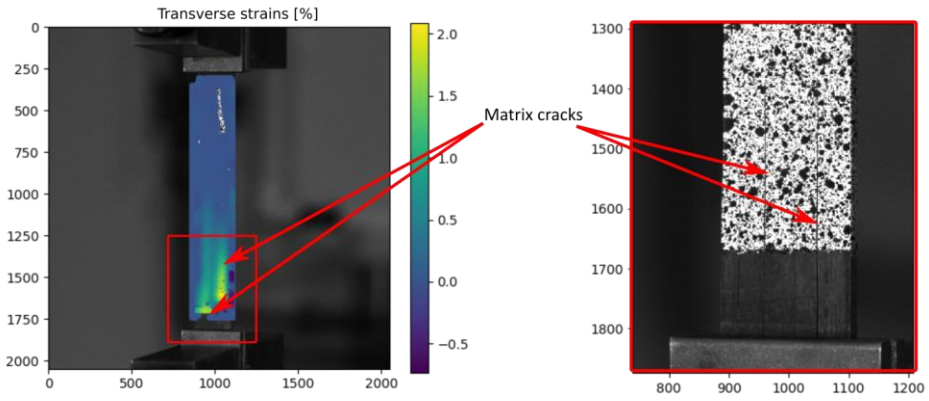

Figure 135 – Fracture mode for 0° unidirectional laminate due to splitting cracks in the grip (P210-1) for tensile test at ambient temperature

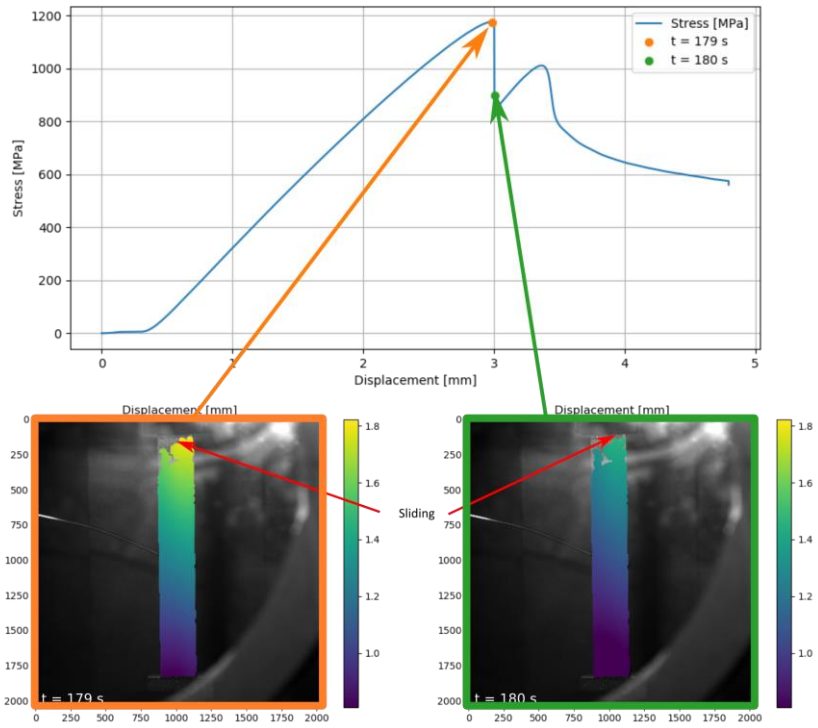

Figure 136 – Sliding in the grip of 0° unidirectional laminate coupons (P210-5) for tensile test at 205°C. Vertical displacement fields before and after the sliding.

Figure 137 presents the evolution of the normalized Young modulus and the normalized Poison ratio as function of the temperature. These curves exhibit the influence of the temperature on the Poison ratio and confirm its low influence on the Young modulus.

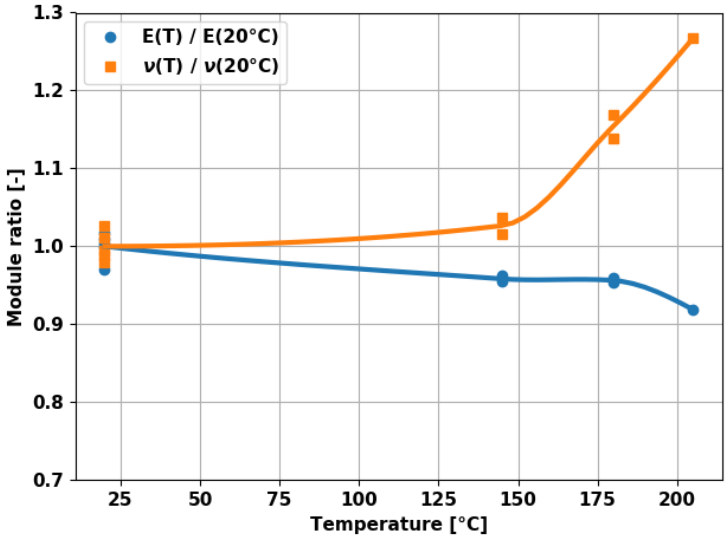

Figure 137 – Evolution of the normalized Young Modulus and the normalized Poison ratio as function of the temperature

9.2.3. Thermomechanical properties in the transverse axis for static tensile test

Thermomechanical loading have been applied on 90° unidirectional 8 plies laminate manufactured by CEIIA. The test matrix of the mechanical tests is described in the Table 27. Tests follow the recommendations of the EN ISO 527 normative procedure.

Reference Plate	Coupon Reference	Loading rate	Temperature	Stacking Sequence	width
3809A_FSS_P7_P213-01_SS03	P213-2	1. mm/min	ambient	$[90°]_8$	25 mm
3809A_FSS_P7_P213-01_SS03	P213-3	1. mm/min	ambient	$[90°]_8$	25 mm
3809A_FSS_P7_P213-01_SS03	P213-4	1. mm/min	140°C	$[90°]_8$	25 mm
3809A_FSS_P7_P213-01_SS03	P213-5	1. mm/min	140°C	$[90°]_8$	25 mm
3809A_FSS_P7_P213-01_SS03	P213-6	1. mm/min	80°C	$[90°]_8$	25 mm
3809A_FSS_P7_P213-01_SS03	P213-7	1. mm/min	80°C	$[90°]_8$	25 mm

Table 27 – Test matrix for 90° unidirectional laminates

The Figure 138 shows the evolution of the longitudinal and transverse strain versus the applied strain. These curves show the high influence of the temperature on the transverse behavior. Polymer matrix composite are well known to exhibit non-linear behavior for shear or transverse loading due to the viscous behavior of the polymer. At high temperature, this viscous behavior of the matrix is exacerbated and explains not only the loss of the apparent Young modulus (reported in Table 28) but also the nonlinear behavior for transverse loading. The stress strain curve is less linear for transverse loading at 140°C than at ambient temperature. The strength is also highly dependent of the temperature. A good repeatability is observed for the data with a higher scattering for the strength value.

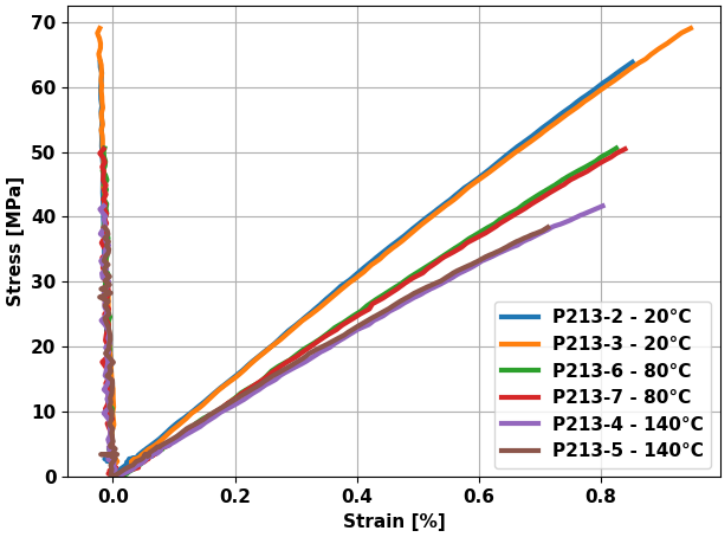

Figure 138 – Stress strain curve of 90° unidirectional laminates for 20°C , 80°C and 140°C.

Transverse Young modulus and the transverse strengths for the tested coupon have been reported in Table 28.

Coupon Reference	Temperature	Stacking Sequence	Young Modulus	Transverse Strength
P213-2	ambient	$[90°]_8$	7.73 GPa	65 MPa
P213-3	ambient	$[90°]_8$	7.92 GPa	70 MPa
P213-4	140°C	$[90°]_8$	5.73 GPa	42 MPa
P213-5	140°C	$[90°]_8$	5.85 GPa	39 MPa
P213-6	80°C	$[90°]_8$	6.42 GPa	51 MPa
P213-7	80°C	$[90°]_8$	6.43 GPa	51 MPa

Table 28 – Transverse Young modulus and transverse strength for 90° unidirectional laminates according to ISO 527

In the first batch of the test results for this project [10], DMA tests have been performed on small sample of 90° unidirectional laminates. The Figure 139 present the comparison of the Young modulus estimated by DMA tests and by the actual experimental test campaign. A very good agreement is observed between these two data sets and confirms the continuous decrease of the transverse Young modulus measured by DMA tests as function of the temperature increase.

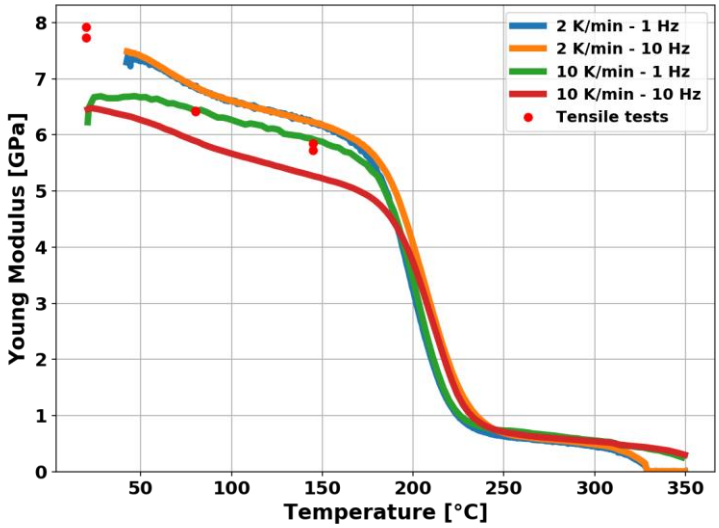

Figure 139 – Comparison between the characterization of the transverse Young modulus tensile performed with DMA tests on $[90]_8$ and the presented data

9.2.4. Thermomechanical properties for in plane shear loadings for static tensile test

Thermomechanical loading have been applied on $[\pm 45°]_{4s}$ laminate manufactured by CEIIA. The test matrix of the mechanical tests is described in the Table 31. Tests follow the recommendations of the ASTM D 3518 normative procedure.

Reference Plate	Coupon Reference	Loading rate	Temperature	Stacking Sequence	width
3809A_FSS_P7_P219-01_SS04	P219-1	1. mm/min	ambient	$[\pm 45°]_{4s}$	25 mm
3809A_FSS_P7_P219-01_SS04	P219-2	1. mm/min	ambient	$[\pm 45°]_{4s}$	25 mm
3809A_FSS_P7_P219-01_SS04	P219-3	1. mm/min	140°C	$[\pm 45°]_{4s}$	25 mm
3809A_FSS_P7_P219-01_SS04	P219-4	1. mm/min	140°C	$[\pm 45°]_{4s}$	25 mm
3809A_FSS_P7_P219-01_SS04	P219-5	1. mm/min	80°C	$[\pm 45°]_{4s}$	25 mm
3809A_FSS_P7_P219-01_SS04	P219-6	1. mm/min	80°C	$[\pm 45°]_{4s}$	25 mm

Table 29 – Test matrix for $[\pm 45°]_{4s}$ laminates

The Figure 140 shows the evolution of the longitudinal and transverse strain versus the applied strain. These curves show the high influence of the temperature on the transverse behavior. Polymer matrix composite are well known to exhibit non-linear behavior for shear or transverse loading due to the viscous behavior of the polymer. At high temperature, this viscous behavior of the matrix is exacerbated and explains not only the loss of the apparent Young modulus (reported in Table 30) but also the nonlinear behavior for transverse loading. The stress strain curve is less linear for transverse loading at 140°C than at ambient temperature. The strength is also highly dependent of the temperature.

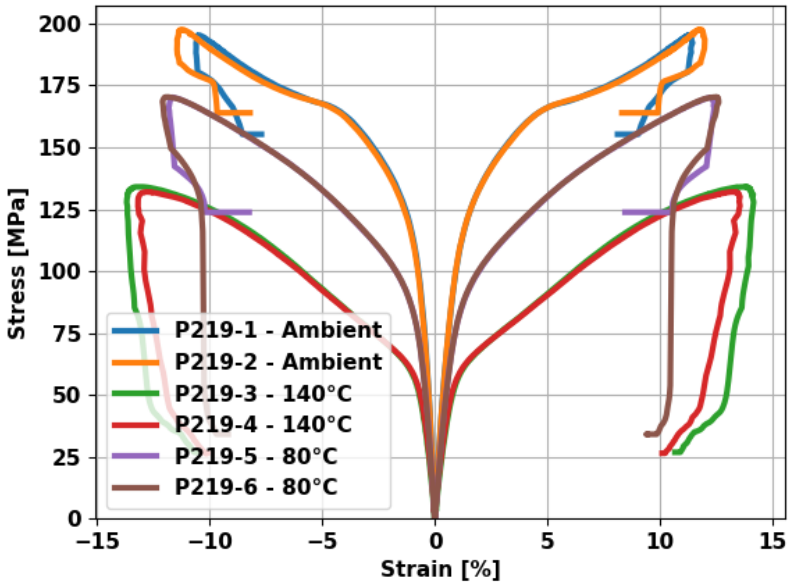

Figure 140 – Stress strain curve of $[\pm 45°]_{4s}$ laminates for 20°C , 80°C and 140°C.

The shear Young modulus and the shear strengths for the tested coupon have been reported in Table 30.

Coupon Reference	Temperature	Stacking Sequence	Shear Modulus	Shear Strength	Maximal shear strain
P219-1	ambient	$[\pm 45°]_{4s}$	3501 MPa	98 MPa	11.01 %
P219-2	ambient	$[\pm 45°]_{4s}$	3550 MPa	99 MPa	11.70 %
P219-3	140°C	$[\pm 45°]_{4s}$	1899 MPa	67 MPa	13.91 %
P219-4	140°C	$[\pm 45°]_{4s}$	1925 MPa	66 MPa	13.35 %
P219-5	80°C	$[\pm 45°]_{4s}$	2703 MPa	85 MPa	12.10 %
P219-6	80°C	$[\pm 45°]_{4s}$	2724 MPa	85 MPa	12.33 %

Table 30 – Shear modulus and shear strength according to ASTM D 3518

Only two samples have been monitored with Acoustic Emission. The Figure 141 presents the evolution of the normalized cumulative energy and the instant on the strain stress curve of the material when an

acoustic event occurs. These curves confirm that the nonlinear behavior in shear for low stress is only due to the viscous behavior of the matrix and not due to matrix transverse cracking. The matrix damage only appears after around a shear stress in the material of 60 MPa.

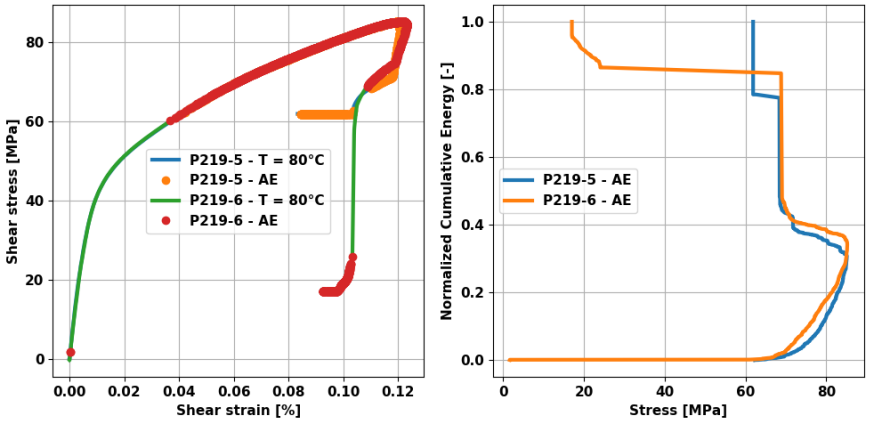

Figure 141 – Evolution of the acoustic emission events for $[\pm 45°]_{4s}$ laminates at 80°C.

9.2.5. Thermomechanical properties for quasi-isotrope laminate submitted to static tensile test

Thermomechanical loading have been applied on $[45/90/-45/0]_s$ laminate manufactured by CEIIA. The test matrix of the mechanical tests is described in the Table 31. Tests follow the recommendations of the ASTM D 3518 normative procedure.

Reference Plate	Coupon Reference	Loading rate	Temperature	Stacking Sequence	width
3809A_FSS_P7_P229-01_SS06	P229-1	1. mm/min	ambient	$[45/90/-45/0]_s$	25 mm
3809A_FSS_P7_P229-01_SS06	P229-2	1. mm/min	ambient	$[45/90/-45/0]_s$	25 mm
3809A_FSS_P7_P229-01_SS06	P229-3	1. mm/min	145°C	$[45/90/-45/0]_s$	25 mm
3809A_FSS_P7_P229-01_SS06	P229-4	1. mm/min	145°C	$[45/90/-45/0]_s$	25 mm
3809A_FSS_P7_P229-01_SS06	P229-5	1. mm/min	180°C	$[45/90/-45/0]_s$	25 mm
3809A_FSS_P7_P229-01_SS06	P229-6	1. mm/min	180°C	$[45/90/-45/0]_s$	25 mm

Reference Plate	Coupon Reference	Loading rate	Temperature	Stacking Sequence	width
3809A_FSS_P7_P229-01_SS06	P229-7	1. mm/min	ambient	$[45/90/-45/0]_s$	25 mm
3809A_FSS_P7_P229-01_SS06	P229-9	1. mm/min	ambient	$[45/90/-45/0]_s$	25 mm
3809A_FSS_P7_P253-01_SS06	P253-1	1. mm/min	ambient	$[45/90/-45/0]_s$	25 mm

Table 31 – Test matrix for $[45/90/-45/0]_s$ laminates

The Figure 142 shows the evolution of the longitudinal and transverse strain versus the applied strain. These curves show the few influence of the temperature on the apparent behavior of the laminate. Polymer matrix composite are well known to exhibit non-linear behavior for shear or transverse loading due to the viscous behavior of the polymer. Nevertheless at the macroscopic scape for a quasi isotrope, the apparent Young modulus (reported in Table 32) is few influenced by the temperature (Figure 143). The same remark could be made for the apparent strength (Figure 144). Moreover, we can observe a quasi constant value of the longitudinal ultimate strain (Table 32 and Fig 145).

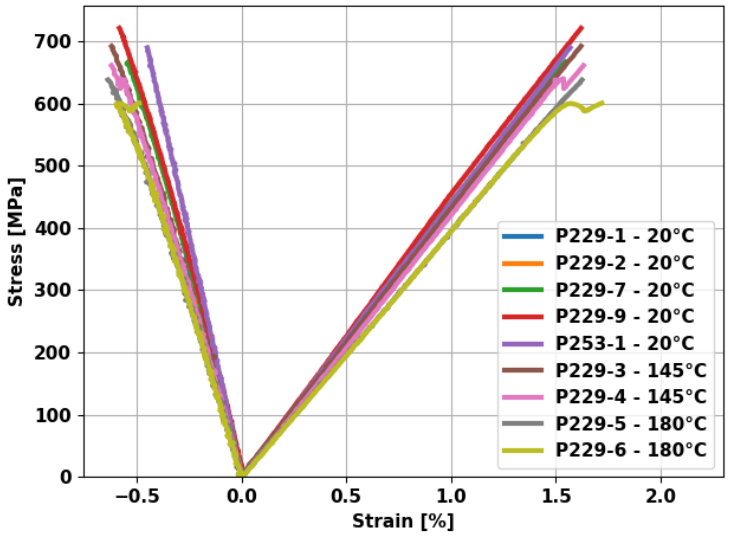

Figure 142 – Stress strain curve of $[45/90/-45/0]_s$ laminates for 20°C , 80°C and 140°C.

Coupon Reference	Temperature	Stacking Sequence	Young Modulus	Strength	Maximal axial strain
P229-1	20°C	$[45/90/-45/0]_s$	42.72 GPa	> 635 MPa	> 1.47 %
P229-2	20°C	$[45/90/-45/0]_s$	43.69 GPa	> 633 MPa	> 1.47 %

Coupon Reference	Temperature	Stacking Sequence	Young Modulus	Strength	Maximal axial strain
P229-7	20°C	$[45/90/-45/0]_s$	43.82 GPa	> 667 MPa	> 1.55 %
P229-9	20°C	$[45/90/-45/0]_s$	44.88 GPa	721 MPa	1.62 %
P253-1	20°C	$[45/90/-45/0]_s$	44.58 GPa	690 MPa	1.57 %
P229-3	145°C	$[45/90/-45/0]_s$	42.84 GPa	692 MPa	1.62 %
P229-4	145°C	$[45/90/-45/0]_s$	40.98 GPa	661 MPa	1.63 %
P229-5	180°C	$[45/90/-45/0]_s$	38.96 GPa	638 MPa	1.63 %
P229-6	180°C	$[45/90/-45/0]_s$	39.50 GPa	601 MPa	1.72 %

Table 32 – Apparent young modulus and strength according to ASTM D 3518 for $[45/90/-45/0]_s$

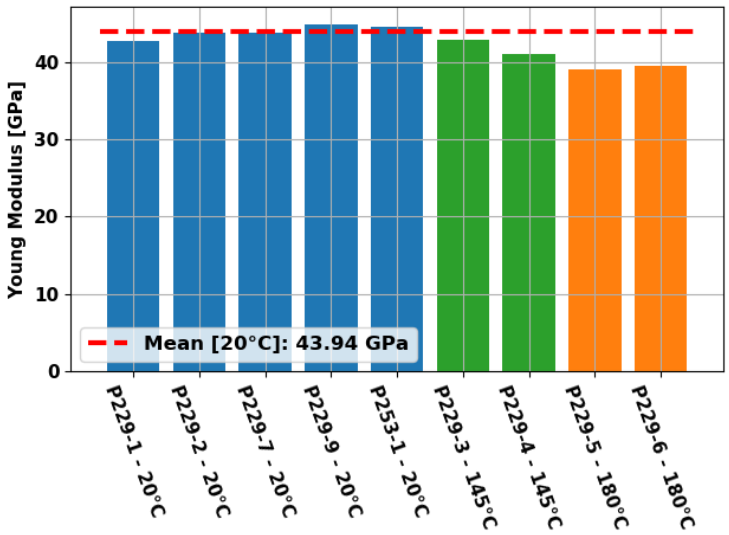

Figure 143 – Distribution of young modulus for quasi isotropic laminate

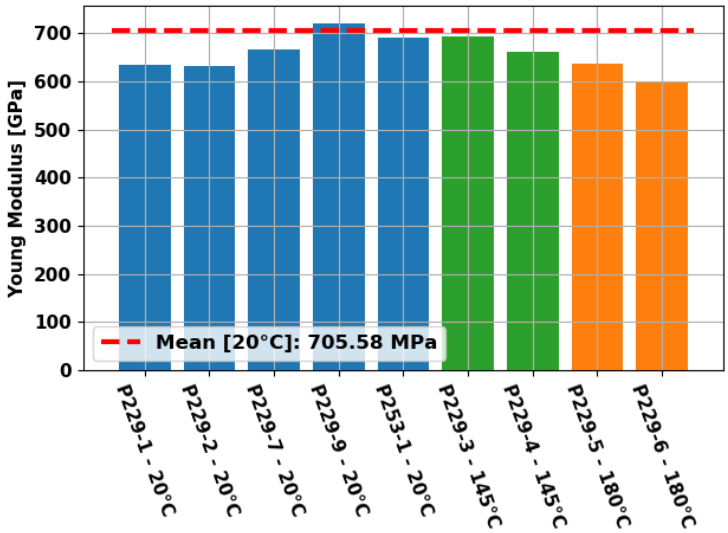

Figure 144 – Distribution of strength modulus for quasi isotropic laminate

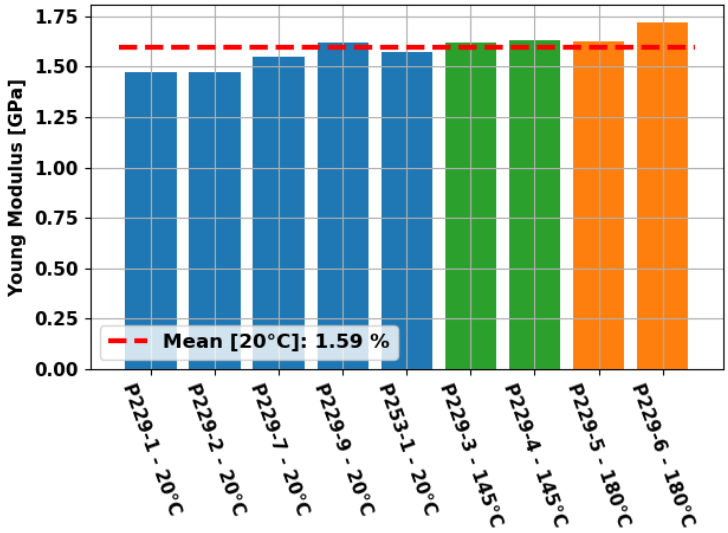

Figure 145 – Distribution of ultimate strain for quasi isotropic laminate

Only four samples have been monitored with Acoustic Emission (P253-1, P229-7, P229-5, P229-6). The Figure 146 presents the evolution of the normalized cumulative energy (the normalization is made for an applied strain on the laminate of 1.55%) and the instant on the strain stress curve of the material when an acoustic event occurs. We can observe on these figures, the delay on the onset of damage due to the decrease of the thermal curing stress for tests performed in temperature on sample P229-5 and 6. At 180°C, these curing stresses are relaxed and can be neglected but at ambient temperature, there are not null and have a huge impact on the onset of the matrix transverse cracking in 90° plies.

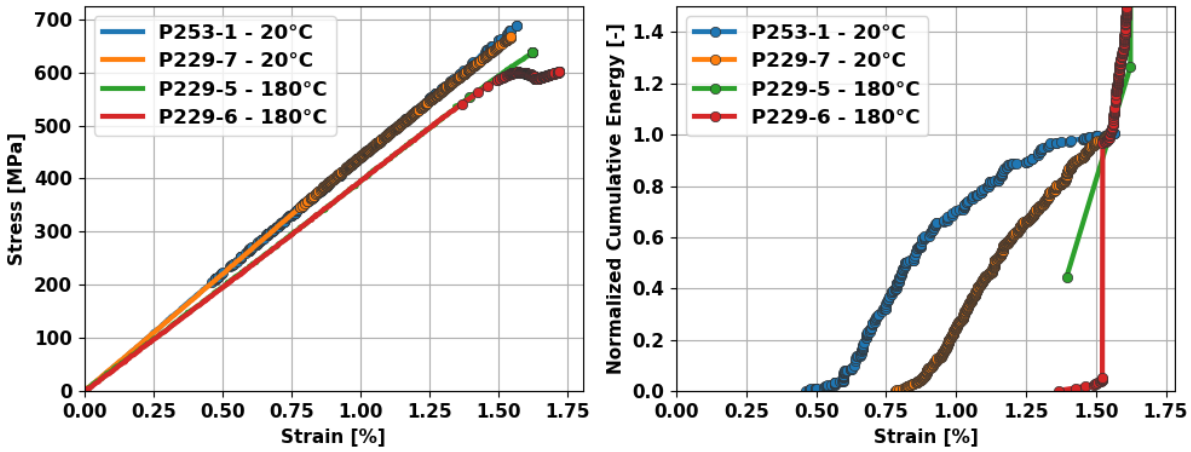

Figure 146 – Evolution of the acoustic emission events for quasi isotropic laminate

9.2.6. Thermomechanical properties on the interfaces

The purpose of this experimental study is to characterize the evolution of the interfacial properties with the increase of the temperature. In order to achieve such objective, Onera has developed a new experimental procedure to limit the drawbacks of using a climate chamber to impose a temperature on the sample. Indeed, the waiting time to attempt the desired temperature could modify the strength of the interface. It is then mandatory to reduce this waiting time. This is the reason why the INJECT bench uses the Joule heating phenomenon to increase the heating rate. In the case of the characterization of the interface toughness, the INJECT bench is based on a end-notched flexure (ENF) test configuration. The idea is to impose an electric current inside the material in order increase the temperature thanks to the quite high electric resistance of carbon/epoxy laminates.

The Figure 147 presents the INJECT setup for ENF test. A 2D Digital Image Correlation is used to monitored the displacement of the sample and an IR camera is used for monitored the temperature inside the material. The current is injected inside the material on the two extremities of the sample and only in the upper arm of the sample. In order to reduce the contact electric resistance, these extremities are beveled by a polishing machine for increasing the injected surface.

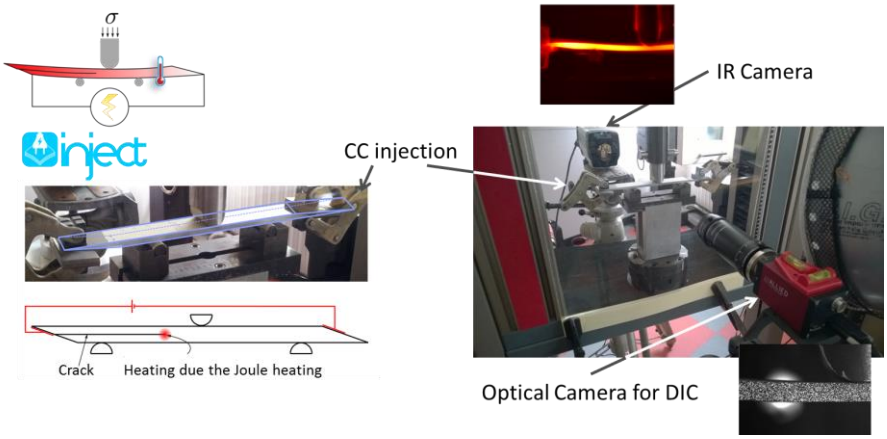

Figure 147 – INJECT bench for characterizing the toughness in mode II by ENF test

As recommended in the ASTM D 7905 standard, the compliance methods is used to estimate the thougness of the interface. To succeed in, the coupon is place at a distance of a_o of 20 mm, 30 mm and 40 mm from left roller (148) and the crack is only propagated for the 30 mm configurations. The 2 others configurations are only mandatory for characterizing the stiffness of the sample.

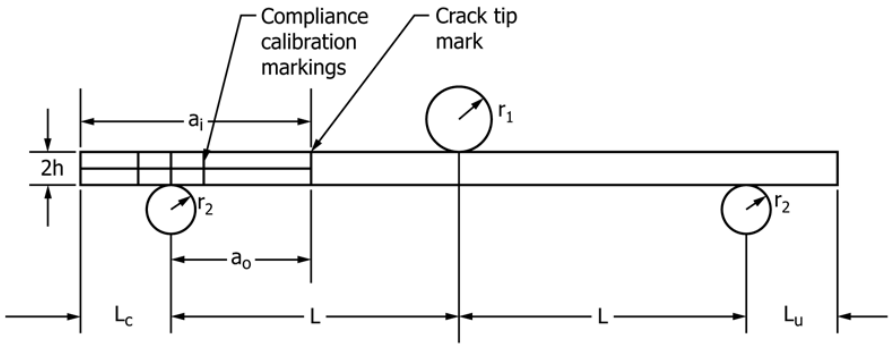

Figure 148 – ENF Specimen, Fixture, and Dimensions [11]

Figures 149-150 present the force/displacement curves for the two samples P203-1 and P203-2 for the Non-Precracked (NPC) configuration and the Precracked (PC) configuration. These samples have been tested at ambient temperature. A good repeatability of the expirement is observed even if a high decrease in the maximum force is monitored between NPC and PC configuration. Thanks to these data, it is then very easy to determine the apparent toughness by the compliance method [11]:

$$C = A + m\,a^3$$

In witch C is the compliance of the coupon and a is the crack length. The coefficients, A and m, are determined using a linear least squares regression analysis of the compliance, C, versus crack length cubed (Figures 152-153). The determined values are reported in Table 33.

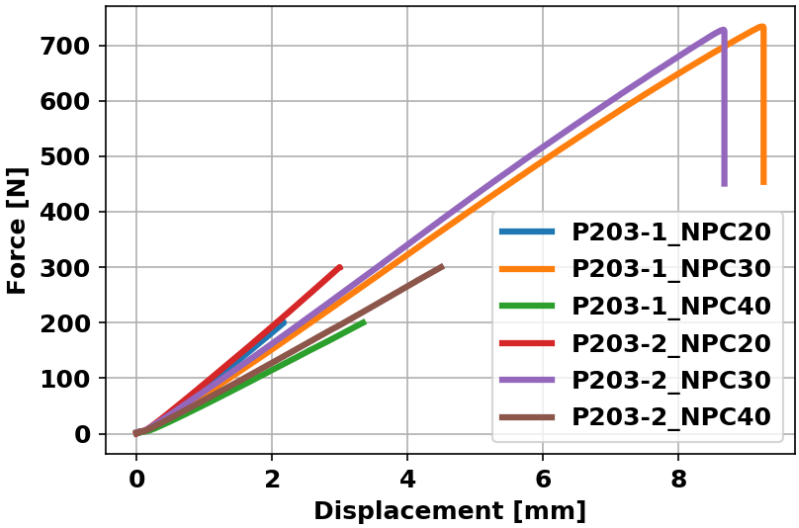

Figure 149 – Force displacement curve for the Non-Precracked (NPC) configuration at ambient temperature

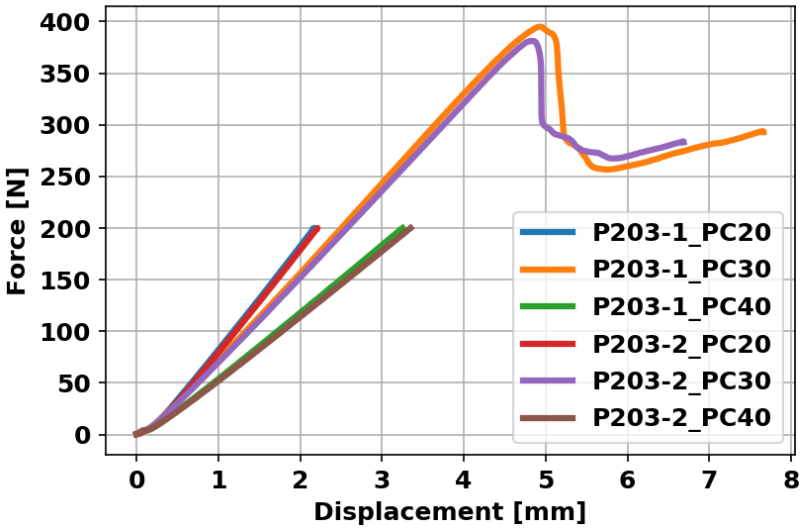

Figure 150 – Force displacement curve for the Precracked (PC) configuration at ambient temperature

Coupons P203-3-P203-6 have been tested by injected power (30-50 W) inside which induced an average temperature close to the crack tip between 70 to 95°C. The temperature field in the sample is not homogenous due to the presence of the roller. Thanks to the Digital Image Correlation system (DIC) and to IR camera, we are able to monitor the temperature in the sample by projection of the temperature field on the DIC field. Hence we can estimate an average temperature on the DIC field (Figure 151). This average temperature is reported in Table 33 and on Figures 154-157.

In order to use the same methodology for determining the fracture toughness, a waiting time of 260 s is respecting before applying any displacement loading and this waiting time ensures a stabilized

temperature in the coupon. Figures 154-157 presents the evolution of the temperature in the coupon and the mechanical loading for Non-Precracked (NPC) and Precracked (PC) configuration. Nevertheless, due to the electric contact resistance and its evolution due to the local pyrolysis of the resin, the temperature inside the material can decrease. Moreover, in some case, the contact is lost and the temperature fall dramatically. For example in the P203-5 NPC configuration case, the contact was lost just before the propagation of the crack and the temperature before the crack propagation was closed to the ambient temperature. This is the reason why, Table 33 reports the average temperature at the propagation of the crack.

The estimation of the toughness of the sample is similar than for the ambient configuration. The compliance of the sample is identified with the crack tip positioned at 20 mm and 40 mm and the propagation of the crack tip is only performed for an initial crack length of 30 mm.

The Figures 152-153 exhibit the influence of the real position of the initial crack length on the estimation of A and m parameters in the compliance method. Thanks to optical and thermal observations, we can precisely identify the initial crack tip position (Figure 158) and then have a better agreement of the compliance evolution with theoretical evolution (Figures 152-153). It is true for NPC configurations but not for PC configurations.

Coupon Reference	Temperature NPC/PC	Power	Stacking Sequence	m NPC/PC	G_{II} NPC	G_{II} PC
P203-1	ambient	-	$[0°_4//0°_4]$	1.03/0.96 $[10^{-7}\ N^{-1}mm^{-2}]$	3010 J/m^2	814 J/m^2
P203-2	ambient	-	$[0°_4//0°_4]$	0.888/1.01 $[10^{-7}\ N^{-1}mm^{-2}]$	2537 J/m^2	798 J/m^2
P203-3	71°C/69°C	50 W	$[0°_4//0°_4]$	1.37/1.13 $[10^{-7}\ N^{-1}mm^{-2}]$	1474 J/m^2	960 J/m^2
P203-4	92°C/86°C	50 W	$[0°_4//0°_4]$	1.23/1.12 $[10^{-7}\ N^{-1}mm^{-2}]$	1180 J/m^2	826 J/m^2
P203-5	30°C/87°C	30 W	$[0°_4//0°_4]$	1.03/1.29 $[10^{-7}\ N^{-1}mm^{-2}]$	2456 J/m^2	819 J/m^2
P203-6	71°C/67°C	30 W	$[0°_4//0°_4]$	0.917/1.11 $[10^{-7}\ N^{-1}mm^{-2}]$	1510 J/m^2	645 J/m^2

Table 33 – Determination of the Mode II Interlaminar Fracture Toughness for P203-1-6

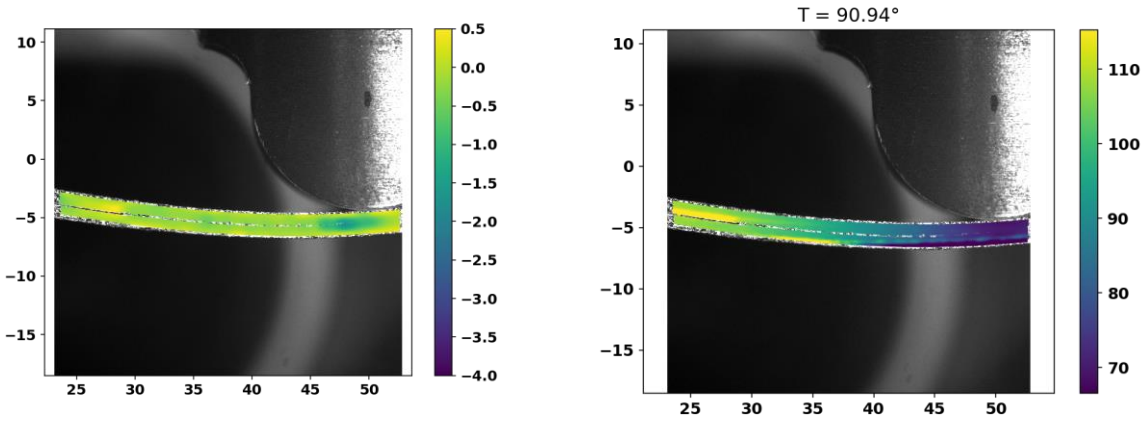

a/ Shear strain [%] b/ Temperature field [°C]

Figure 151 – Temperature and shear strain fields in sample P203-4 just after the propagation of the crack tip in the NPC configuration

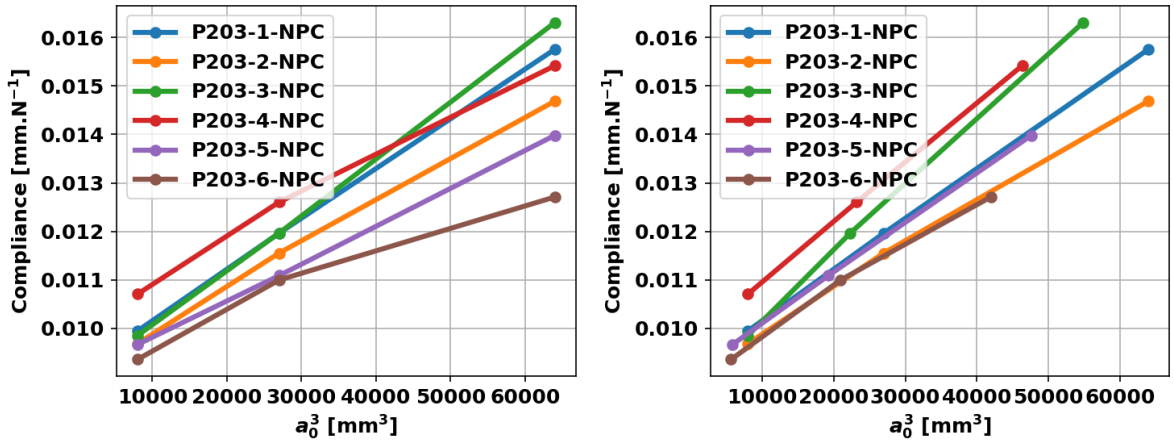

Figure 152 – Determination of the A and m parameter from the evolution of the compliance for NPC configuration by considering the theoretical crack length or the experimental one

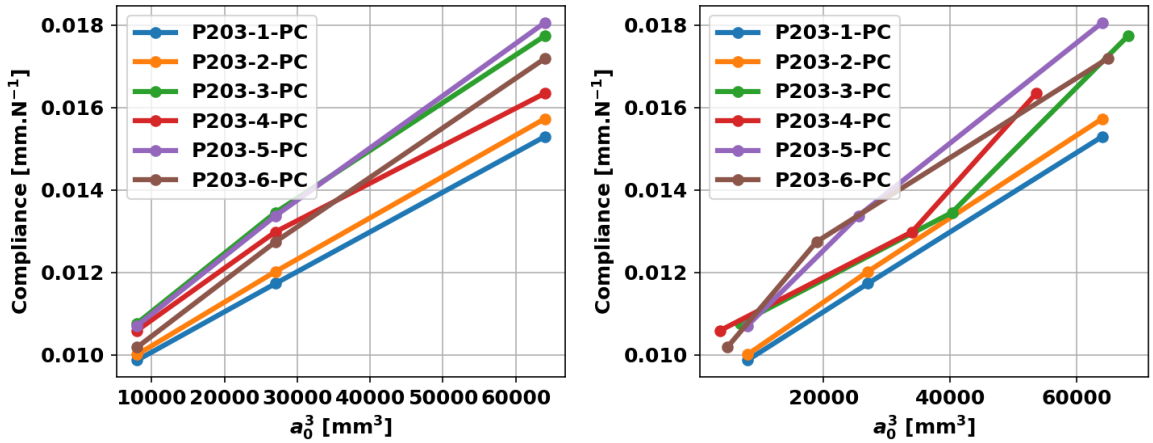

Figure 153 – Determination of the A and m parameter from the evolution of the compliance for PC configuration by considering the theoretical crack length or the experimental one

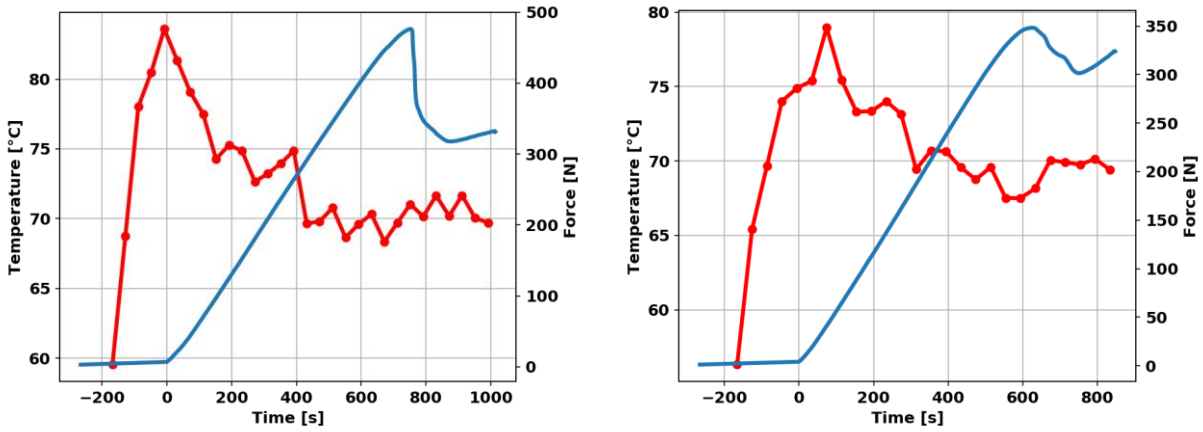

a/ P203-3 NPC **b/ P203-3 PC**

Figure 154 – Evolution of the temperature in P203-3 for NPC and PC configurations

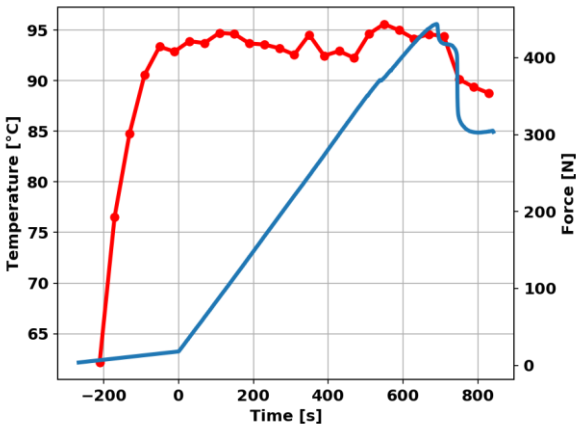

a/ P203-4 NPC

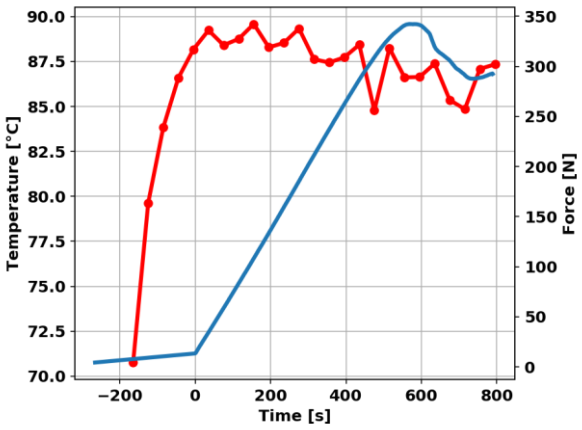

b/ P203-4 PC

Figure 155 – Determination of the A and m parameter for P203-4

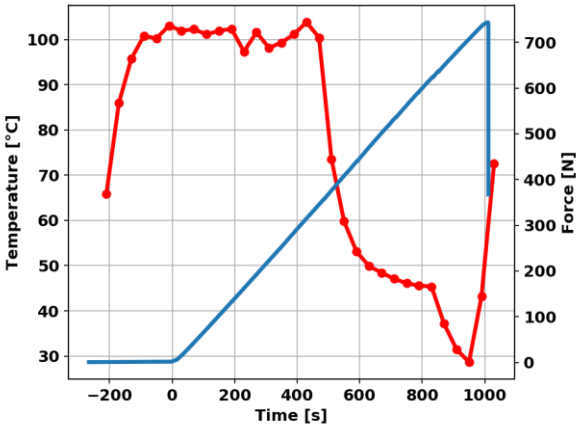

a/ P203-5 NPC

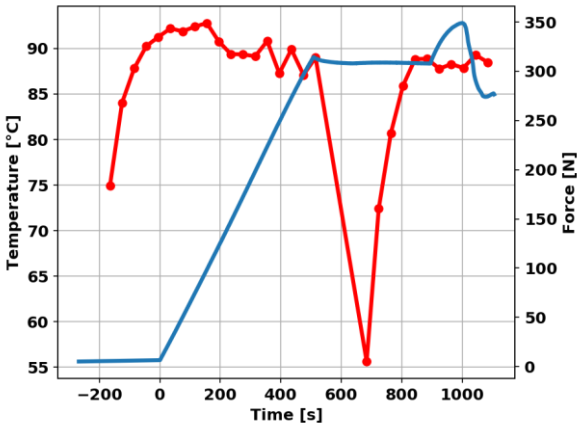

b/ P203-5 PC

Figure 156 – Determination of the A and m parameter for P203-5

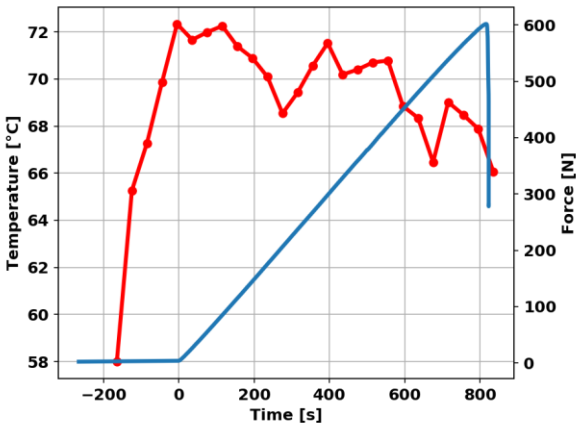

a/ P203-6 NPC

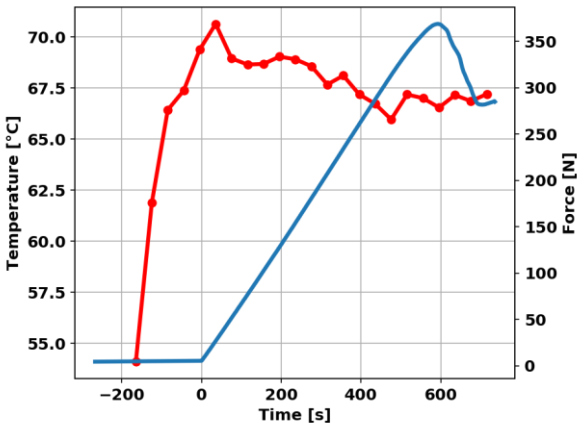

b/ P203-6 PC

Figure 157 – Determination of the A and m parameter for P203-6

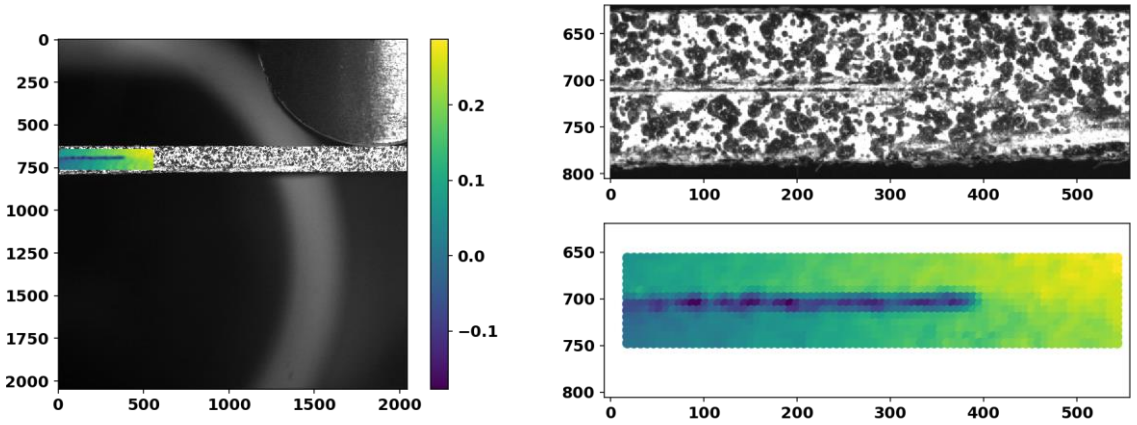

a/ Displacement field in P203-4 NPC

b/ Comparison between optical observation and DIC in P203-4 NPC

Figure 158 – Determination of the initial crack tip in P203-4

Figures 159 compare the force displacement curves for all the samples. For NPC configuration, a clear difference between tests performed at ambient or in temperature is observed. For ambient temperature, a brittle fracture occurs than a more ductile fracture is observed for samples tested in temperature. Moreover, the peak force for test performed in temperature is much lower than for tests performed at ambient temperature. For PC configurations, all samples present the quite same fracture behaviour even if the fracture of sample tested in temperature seems to be more ductile. Whatever the curve shape, the peak force is similar for all the samples and imply a quite similar toughness.

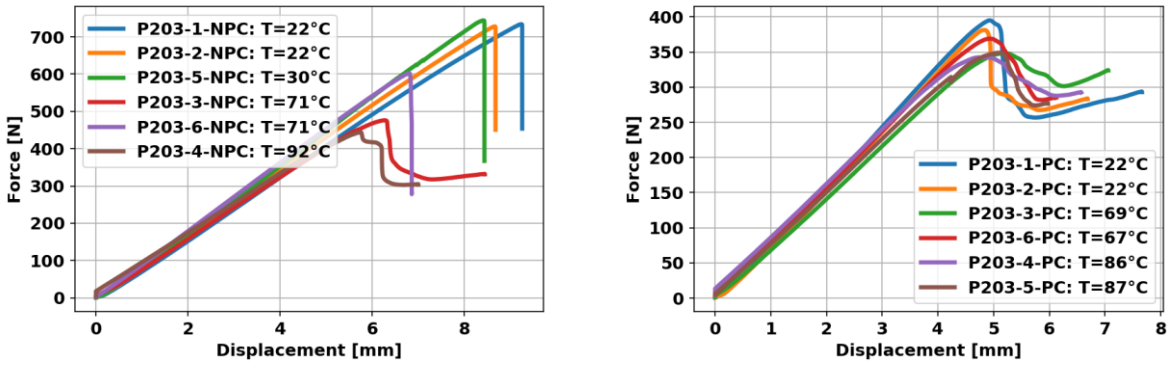

a/ NPC configuration

b/ PC configuration

Figure 159 – Comparison of the force displacement curve for all the samples in NPC or PC configuration

Figures 160-161 confirm the precedent analysis and as reported in Table 33, the temperature have a highly influence on the G_{II}^{c} for NPC configurations but it has a very low influence for the PC configuration. Two hypotheses can be proposed. The first one concerns the shape of the crack front. Even if in NPC configuration the crack tip is artificial, the geometry of the crack is controlled and straight. After the first propagation, it is not ensured that the crack tip remains straight. The compliance evolution in PC

configuration is strange and consolidates this hypothesis. The second hypothesis concerns the temperature field at the crack tip. The presence of Teflon in NPC configuration can change the temperature field in the vicinity of the crack front and could explain the difference between NPC and PC configuration. Complementary analyses like NDT or micro fractography can explain this difference on the influence of the temperature on the delamination propagation.

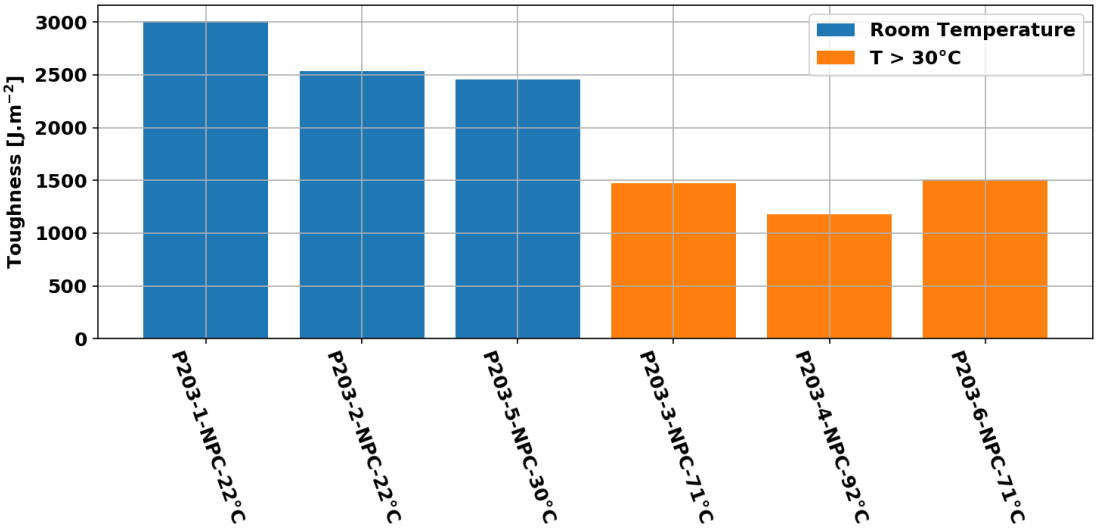

Figure 160 – Influence of the temperature on the toughness in mode II on NPC configurations

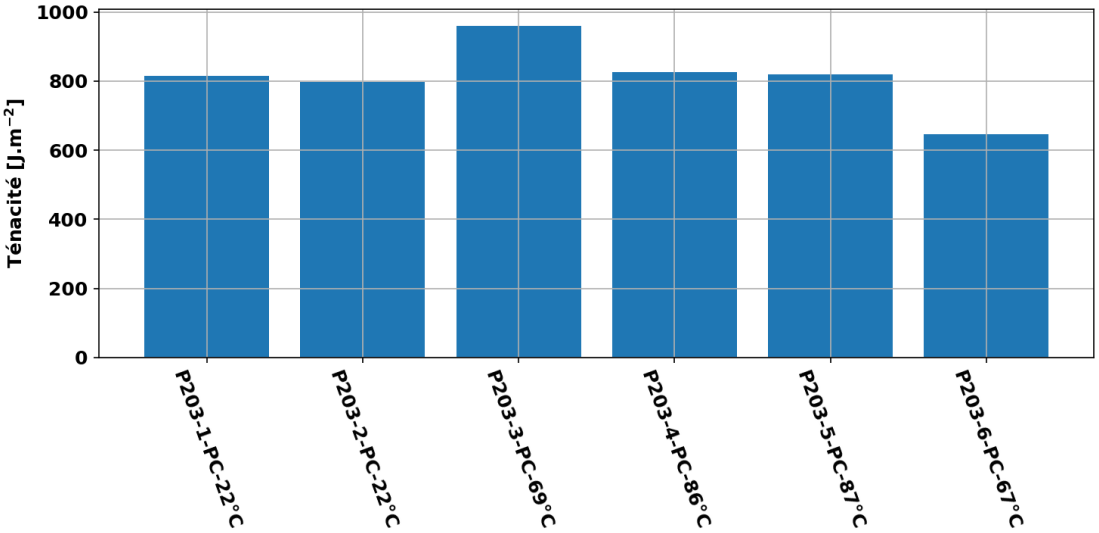

Figure 161 – Influence of the temperature on the toughness in mode II on NPC configurations

9.3. Dynamic tensile tests

The purpose of this experimental study is to characterise the evolution of carbon/epoxy material tensile shear behaviour with respect to the increase of the temperature and strain rate. For that purpose an Instron environmental chamber has been modified in order to be used on a hydraulic jack. As shown in Figure 162, the modification of the environmental chamber has been done in order to only apply the heating on the composite specimen nor on the whole experimental setup.

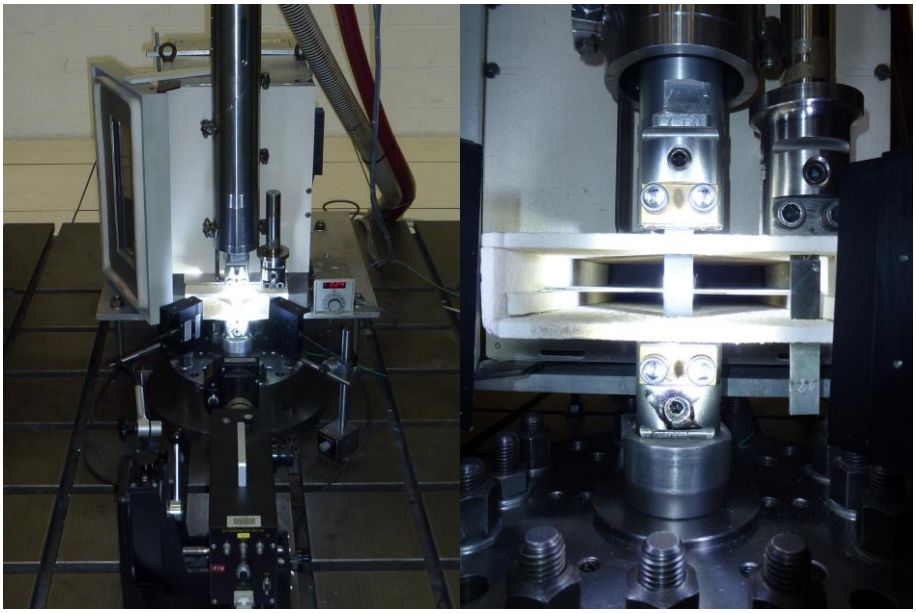

Figure 162 – Experimental setup used for the mechanical characterization of $[\pm 45°]_{2s}$ laminates at different strain rates and temperatures.

With this experimental setup, tests have been performed for four different temperatures (20°C, 70°C, 120°C and 170°C) and three different loading rates (1 mm/s, 100 mm/s and 2m/s). For each configuration, at least three tests have been performed in order to evaluate the discrepancies. The load measurement is performed with a piezoelectric load cell. The longitudinal and transverse strains are measured with strain gauges glued on opposite faces of the sample. Moreover, the longitudinal strain is also evaluated with an optical extensometer thanks to two black and white transitions painted on the composite surface. Finally, the temperature in the modified environmental chamber is monitored with a thermocouple embedded in a reference coupon, as shown in Figure 163. Before to start the mechanical testing, a reasonable waiting time has been used in order to assume a thermal equilibrium in the coupon.

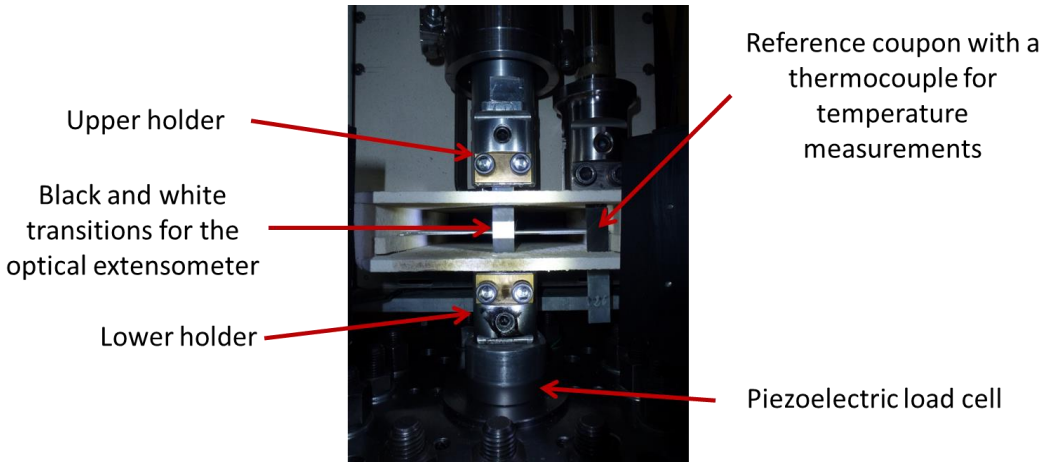

Figure 163 – Zoom on the experimental setup

In the sequel, the analysis of the experimental results is firstly done for each tested temperature and a final discussion on the temperature influence is done. The evaluation of the shear modulus is based on the ISO 14129 normative procedure. The strain rates are evaluated on the same strain interval.

9.3.1. Test performed at 20°C

These tests have been performed without environmental temperature regulation at room temperature. Tests have been performed at three different loading rates: 1 mm/s, 100 mm/s and 2 m/s. Test results are plotted in Figure 164 and mechanical properties are summarised in Table 34. The three selected loading rates are leading to strain rates between $6.9*10^{-3}$ s^{-1} and 19.2 s^{-1}.

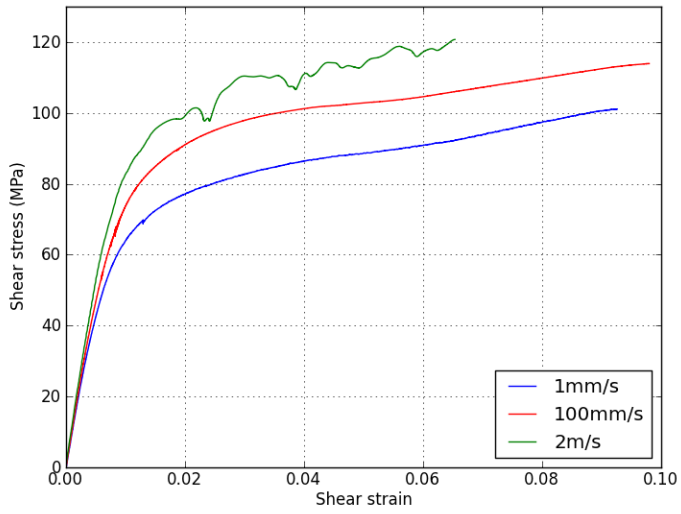

Figure 164 – Shear stress-strain curves for the test performed at 20°C at different loading rates.

Loading rates	Strain rate [s^{-1}]	G_{12} [MPa]	σ_{max} [MPa]	ε_{max} [%]
1 mm/s	$6.9*10^{-3}$ ± 6.6%	4820 ± 6.5%	208 ± 4%	10.1 ± 16.4%
100 mm/s	$6.04*10^{-1}$ ± 3.4%	5190 ± 5.2%	233 ± 2%	10.4 ± 8.8%
2 m/s	19.2 ± 1%	5440 ± 3.4%	232 ± 3.3%	9.02 ± 3.4%

Table 34 – Results of the mechanical characterization performed at room temperature for different loading rates.

The results clearly exhibit a rate dependency with for example an increase of the shear modulus with respect to the loading rate. Concerning the maximum longitudinal stress, an increase is observed between the two first speeds followed by a plateau between the second and the higher loading speed. For the maximum longitudinal strain, which is evaluated with the optical extensometer, a small increase is firstly observed followed by a decrease for the higher loading rate.

9.3.2. Test performed at 70°C

For the three speeds, the previously described environmental chamber has been used in order to perform tests with a controlled temperature of 70°C.

Tests have been performed at three different loading rates: 1 mm/s, 100 mm/s and 2 m/s. Test results are plotted in Figure 165 and mechanical properties are summarised in Table 35. The three selected loading rates are leading to strain rates between $8.5*10^{-3}$ s^{-1} and 14.4 s^{-1}.

The results also exhibit a rate dependency, similar to the one observed at room temperature. The shear modulus and the maximum longitudinal stress increase with respect to the loading rate. For the maximum longitudinal strain, which is evaluated with the optical extensometer, a small increase is firstly observed followed by a decrease for the higher loading rate.

Loading rates	Strain rate [s^{-1}]	G_{12} [MPa]	σ_{max} [MPa]	ε_{max} [%]
1 mm/s	$8.5*10^{-3}$ ± 2.6%	4000 ± 2.6%	192 ± 4.3%	13 ± 6.4%
100 mm/s	$8.7*10^{-1}$ ± 6.7%	4200 ± 2.4%	221 ± 1.2%	13.5 ± 12.4%
2 m/s	14.4 ± 1.7%	4897 ± 0.6%	232 ± 1.6%	11 ± 11.2%

Table 35 – Results of the mechanical characterization performed at 70°C for the different loading rates.

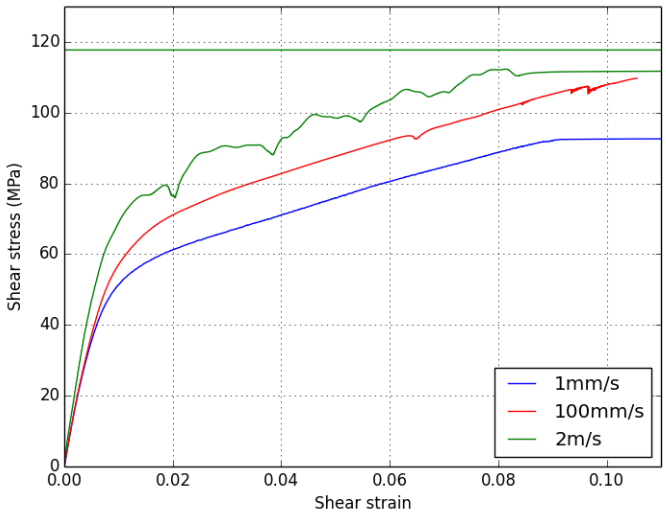

Figure 165 – Shear stress-strain curves for the test performed at 70°C at different loading rates.

9.3.3. Test performed at 120°C

For the three speeds, the previously described environmental chamber has been used in order to perform tests with a controlled temperature of 120°C.

Tests have been performed at three different loading rates: 1 mm/s, 100 mm/s and 2 m/s. Test results are plotted in Figure 166 and mechanical properties are summarised in Table 36. The three selected loading rates are leading to strain rates between $9.2*10^{-3}$ s^{-1} and 14.5 s^{-1}. A premature failure of the strain gauge is observed for all the tested speeds at this temperature. This explains the use of a redundant strain measurement with the optical extensometer which allows the measurement of the maximum strain.

The results also exhibit a rate dependency, similar to the one observed at room temperature. The shear modulus and the maximum longitudinal stress increase with respect to the loading rate. For the maximum longitudinal strain, which is evaluated with the optical extensometer, almost no variation is observed for this temperature.

Loading rates	**Strain rate [s^{-1}]**	**G_{12} [MPa]**	**σ_{max} [MPa]**	**ε_{max} [%]**
1 mm/s	$9.2*10^{-3}$ ± 1.9%	3040 ± 1.9%	157 ± 2.5%	12.3 ± 11.6%
100 mm/s	$7.2*10^{-1}$ ± 6.1%	3620 ± 4%	184 ± 2.7%	12.6 ± 8.9%
2 m/s	14.5 ± 14.5%	3940 ± 8.7%	198 ± 1.5%	12.1 ± 7.4%

Table 36 – Results of the mechanical characterization performed at 120°C for the different loading rates.

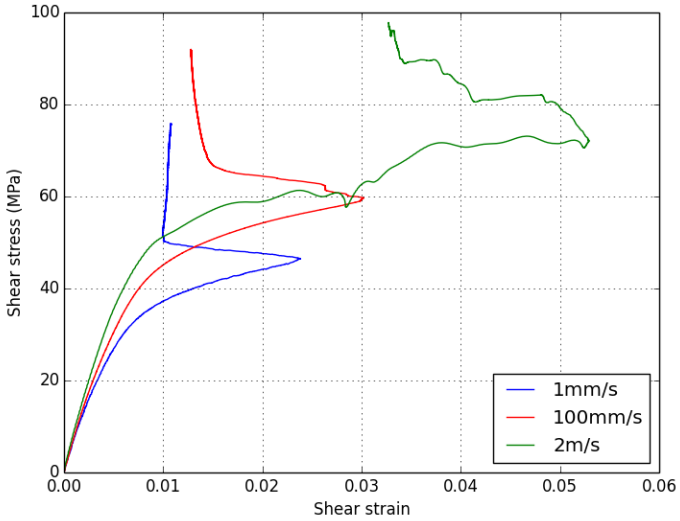

Figure 166 – Shear stress-strain curves for the test performed at 120°C at different loading rates.

9.3.4. Test performed at 170°C

For the three speeds, the previously described environmental chamber has been used in order to perform tests with a controlled temperature of 170°C.

Tests have been performed at three different loading rates: 1 mm/s, 100 mm/s and 2 m/s. Test results are plotted in Figure 167 and mechanical properties are summarised in Table 37. The three selected loading rates are leading to strain rates between $1.8*10^{-2}$ s^{-1} and 19.7 s^{-1}. For these tests at temperature close to the vitreous transition, the discrepancy of experimental results is higher. The behaviour of such material is known to evolve quickly for these temperatures which can explain the higher discrepancy.

Loading rates	**Strain rate [s^{-1}]**	**G_{12} [MPa]**	**σ_{max} [MPa]**	**ε_{max} [%]**
1 mm/s	$1.8*10^{-2}$ ± 18.8%	1020 ± 33%	115 ± 13.3%	-
100 mm/s	1.62 ± 15.2%	1730 ± 8%	156 ± 2.1%	-
2 m/s	19.7 ± 8%	2060 ± 9.5%	164 ± 2.4%	-

Table 37 – Results of the mechanical characterization performed at 170°C for the different loading rates.

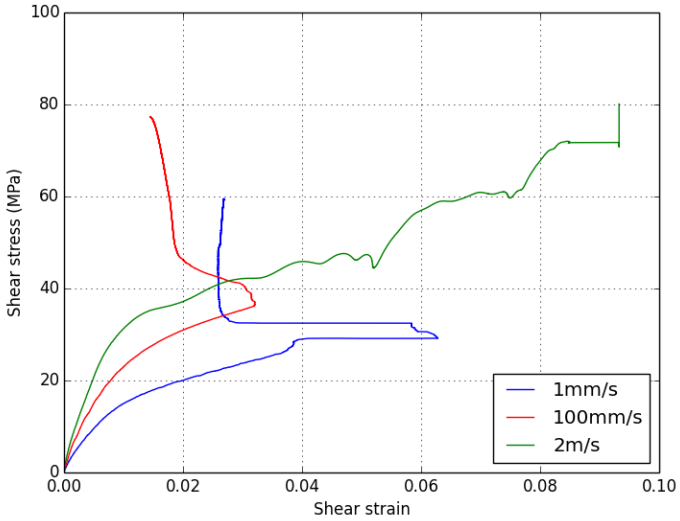

Figure 167 – Shear stress-strain curves for the test performed at 170°C at different loading rates

Despite this, the results also exhibit a rate dependency, similar to the one observed previously. The shear modulus and the maximum longitudinal stress increase with respect to the loading rate. For the maximum longitudinal strain, which is evaluated with the optical extensometer, almost no variation is observed for this temperature.

9.3.5. Influence of the temperature increase

The experimental results previously described have been analysed regarding the loading rate dependency. For a fixed strain rate, the influence of the temperature increase can also be analysed. In order to highlight the influence of temperature, all the results concerning the shear modulus (G_{12}) and the maximum longitudinal stress (σ_{max}) have been summarised respectively in Table 38 and Table 39.

G_{12} [MPa]	**20°C**	**70°C**	**120°C**	**170°C**
1 mm/s	4820 ± 6.5%	4000 ± 2.6%	3040 ± 1.9%	1020 ± 33%
100 mm/s	5190 ± 5.2%	4200 ± 2.4%	3620 ± 4%	1730 ± 8%
2 m/s	5440 ± 3.4%	4897 ± 0.6%	3940 ± 8.7%	2060 ± 9.5%

Table 38 – Combined influence of strain rate and temperature on the shear modulus.

σ_{max} [MPa]	**20°C**	**70°C**	**120°C**	**170°C**

1 mm/s	208 ± 4%	192 ± 4.3%	157 ± 2.5%	115 ± 13.3%
100 mm/s	233 ± 2%	221 ± 1.2%	184 ± 2.7%	156 ± 2.1%
2 m/s	232 ± 3.3%	232 ± 1.6%	198 ± 1.5%	164 ± 2.4%

Table 39 – Combined influence of strain rate and temperature on the maximum longitudinal stress.

The temperature increase leads to a decrease of the shear modulus and of the maximum stress. This result is in good agreement with the literature of organic matrix composite and of polymers materials.

The Figure 168 clearly exhibits the strong influence of the temperature on the linear as well as on the nonlinear behaviour of such materials.

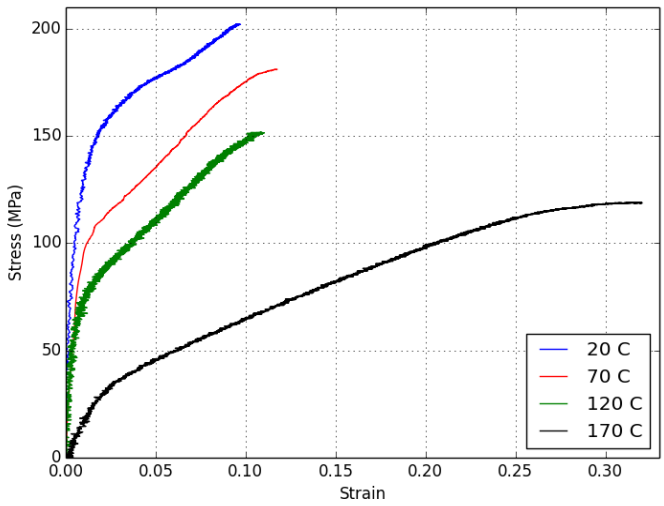

Figure 168 – Shear stress-strain curves for the test performed at 1mm/s at different temperatures.

9.4. Dynamic tensile tests on charred material

The objective of this specific study is to better understand the influence of the degradation of the material on its mechanical behaviour. For that purpose, an experimental procedure has to be proposed to obtain the charred material and a specific experimental setup has to be design in order to be able to apply the mechanical loading on the degraded material.

9.4.1. Experimental procedure for charred material

The procedure is based on the experimental results obtained in this project combined with the modelling tool MoDeTheC developed by ONERA. In this project, two configurations have been considered:

- Apply the degradation procedure on each coupon before the mechanical testing
- Apply the degradation procedure on a plate before manufacturing the coupons

After a first analysis, it appears that at least 5 hours are required to obtain a charred coupon. In this case, the experimental campaign would have been time consuming. Consequently, it has been decided to apply the degradation procedure on a plate in a furnace. Consequently, the procedure described in section 4 to obtain a fully charred specimen is also used for this study.

This procedure has been applied to T700GC/M21 $[\pm 45°]_{2s}$ composite plate in regulated furnace. Two plates have been degraded for this study. The initial mass of the first plate was 116,2 g and the mass after degradation was 97,5 g, leading to a mass loss of 16.1%. For the second plate, the initial mass was 116 g and the mass after degradation was 96,8 g, leading to a mass loss of 16,6%. The percentage of mass loss is slightly lower than the one predicted by the numerical tool but remains acceptable.

9.4.2. Design of the specific experimental setup

After the degradation, the material is fragile and difficult to cut. In order to obtain coupons from the plate, a diamond saw has been used to cut the specimens. A special attention has been paid in order to not extend the delamination between ply which can be observed on the degraded composite plate. To be able to apply a mechanical load on such a brittle and weak material, specific holders have been designed. As shown in Figure 169, the specific holders are fixed to the hydraulic jack with the threaded axle. The degraded material is glued to the holder with an epoxy adhesive which is injected within the 4 mm diameter hole.

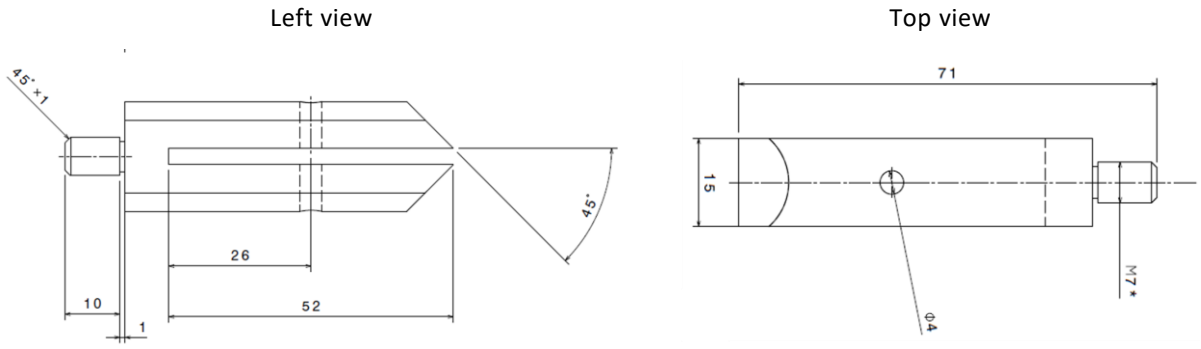

Figure 169 – Geometry of the specific holders design to apply the mechanical loading on charred specimens.

As shown in Figure 170, tests have been performed on a hydraulic jack. The longitudinal displacements of the upper and lower holder have been measured with Keyence laser transducers. The longitudinal strain of the specimen is measured with a strain gauge glued on the specimen surface. Finally, the load apply to the specimen is measured with a piezoelectric load cell.

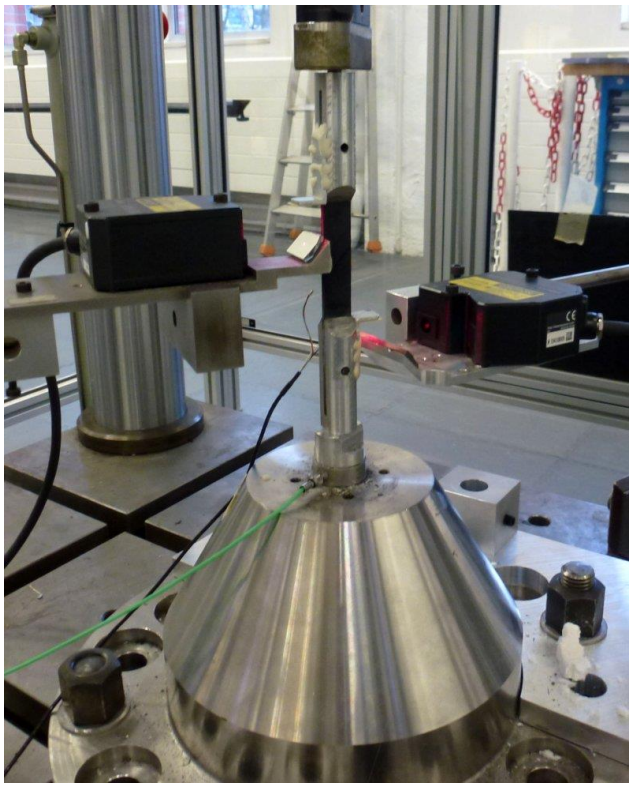

Figure 170 – Experimental setup.

9.4.3. Tests results

For this study, tests have been performed at three different loading rates: 6 mm/min, 60 mm/min and 600 mm/min.

First of all a preliminary test have been performed with two strain gauges, each one glued on opposite face of the coupon. Results of this test performed at the lower loading rates are plotted in Figure 171.

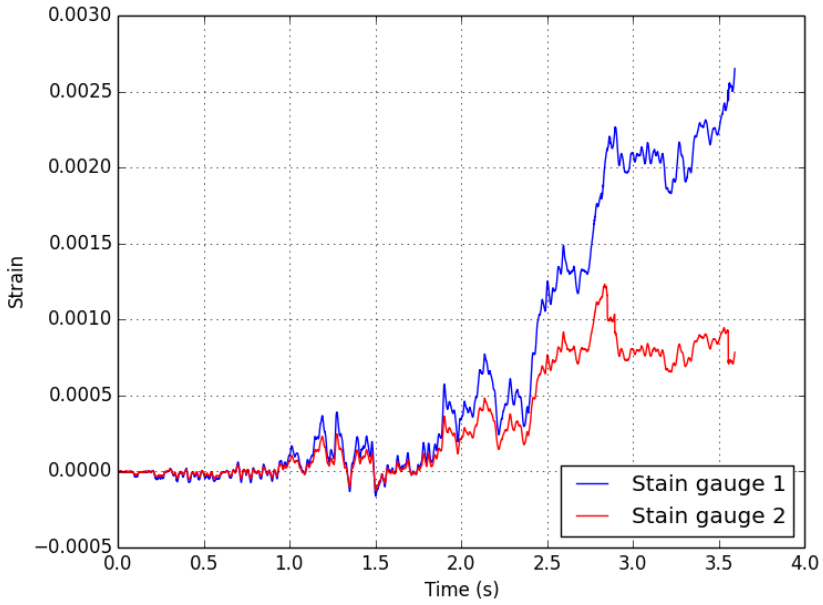

Figure 171 – Evolution of the measured strain for two stain gauges glued on opposite faces of the specimen at the lower loading rate (6 mm/min).

It can be noticed that very small strain are measured during this test. At the beginning of the test, the two strain gauges are close but the two measurements quickly diverge. At the end the test, the second strain gauge measure two times more strain than the first one. This can be explained by the fact that some of the plies of the specimen are delaminated and also strain gauges are not easy to glue on the charred material because of its local heterogeneity. In the sequel, a comparison of stress-strain curves at different loading rates will be done but one has to keep in mind that the strain measurement with such specimens is not as precise as the strain measurement on virgin material. Moreover, as the displacement of the lower and upper holder is measured, a global strain can also be evaluated based on these two quantities. One also has to be careful concerning this global strain, some authors have shown that the strain is not homogeneous on the whole free length of a $[\pm 45°]_{2s}$ laminate.

A comparison of tests results obtained at two different loading rates, 6 mm/min and 600 mm/min, is done in Figure 172. On this figure, the stress-strain curves are plotted with the two different technics for the strain measurement: the global strain based on displacement and the local strain based on strain gauge. Firstly, the two measurement technics are close even if the global strain evolution is affected by some disturbances at the higher loading rate. However, this figure clearly exhibits that the behaviour of the charred material is not affect by the loading rate increase contrary to the virgin material. This behaviour can also be compared to the one of the virgin material with for example Figure 164. It can be observed that after degradation, the behaviour becomes brittle without nonlinear behaviour.

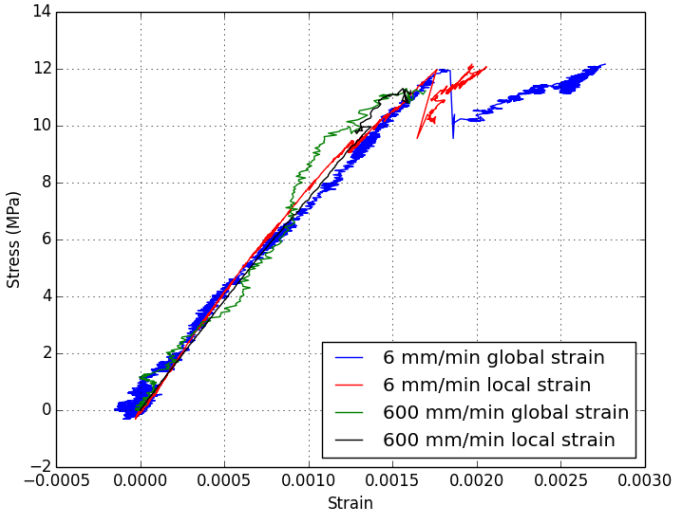

Figure 172 – Comparison of the stress-strain curves obtained with the two measurement technics at two different loading rates.

The same tendency is observed for the maximum stress applied to the charred material. Regarding the discrepancy observed on these values, it is assumed that no rate is observed for the charred material. The magnitude of these values can be compared to the ones of the virgin material summarised in Table 39. A sharp decrease of the maximum stress is observed for the charred material.

Loading rates	**σ_{max} [MPa]**
6 mm/min	11.8 ± 33%
60 mm/min	9.46 ± 11%
600 mm/min	13.3 ± 16%

Table 40 – Results of the evolution of the maximum stress applied on charred material at the different loading rates.

As a conclusion, the charred material behaviour is brittle with a very low strength compared to the virgin material.

9.5. In-plane compression [ONERA Lille]

The purpose of this experimental study is to characterize the evolution of carbon/epoxy material compressive behaviour with respect to the increase of the temperature. Two material directions are investigated: 0° and 90°. As it was previously described in a previous deliverable (FSS_P7_ONERA_D7.4), a specific procedure has been developed based on the two coexisting normative procedures: ASTM D3410 and ASTM D695. It is based on mixed solution for applying the load to the specimen. Indeed, the specimen is loaded by shear and end loadings. To be able to apply the loading at high temperature, metallic tabs are used. The experimental setup is described in Figure 173. Tests have been performed on an Instron electromechanical testing device equipped

with a furnace. The furnace temperature is monitored during the test with a thermocouple, independent of the furnace temperature regulation system. The load is measured with a ±300 kN load cell.

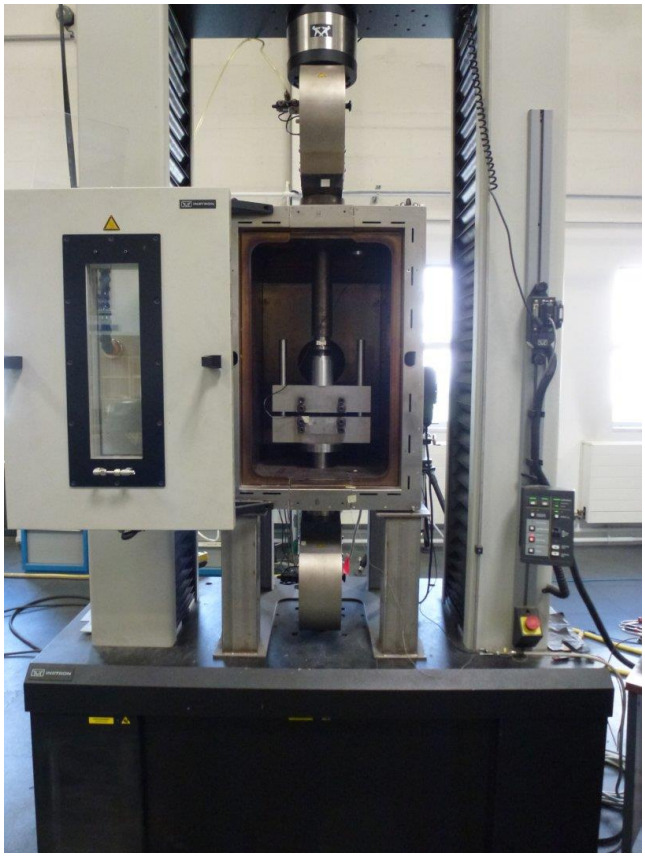

Figure 173 – Experimental setup used for the compressive test at high temperatures.

9.5.1. Tests on 90° specimens

The experimental investigation has been done for various temperatures and various loading rate. Four temperatures have been tested: 20°C, 120°C, 180°C and 220°C. Between each tests a sufficient time is waited in order to start each tests with an equivalent initial condition in terms of furnace initial temperature. Two different loading speeds have been tested: 0,5 mm/min and 100 mm/min. At least three specimens have been tested for each configuration. The strain of the specimen is measured with a 350Ω strain gauge (QFLA-2-350-11).

A comparison of the different stress-strain curves obtained for the tests performed at 0.5 mm/min is plotted in Figure 174.

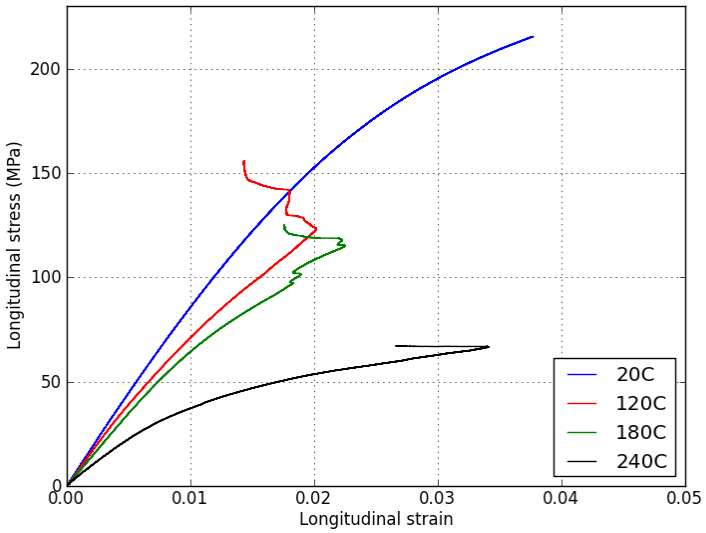

Figure 174 – Stress-strain curves of the compressive tests performed at 0.5 mm/min on 90° specimens for different furnace temperatures.

Results clearly exhibit that the material behaviour is strongly temperature dependant. For example, a sharp decrease of the apparent modulus is observed. Due to the premature failure of the stain gauge which is visible for the tests performed at temperature higher than the room one, the influence of environmental temperature on the nonlinear behaviour cannot be analysed. The variations of the apparent modulus and the maximal stress applied to the specimen with respect to the temperature are summarised in Table 41. First of all, the results obtained at room temperature are in agreement with the literature. The temperature increase implies a sharp decrease of the mechanical properties particularly regarding the strength of the ply in this direction which is 3 times lower at 240°C than at room temperature.

Temperature	**E_{22} [MPa]**	**σ_{max} [MPa]**
20°C	8910 ± 1,7%	218 ± 1,4%
120°C	8260 ± 5,6%	151 ± 3.2%
180°C	7170 ± 2%	122 ± 5.5%
240°C	4795 ± 3,5%	70 ± 4,3%

Table 41 – Results of the mechanical characterization performed at 0.5 mm/min for different environmental temperatures.

The experimental investigation at 100 mm/min has been performed on a smaller number of coupons due to the number of specimens used to validate the protocol. Consequently, only two specimens have been used instead of three, except for 240°C where only one test has been performed.

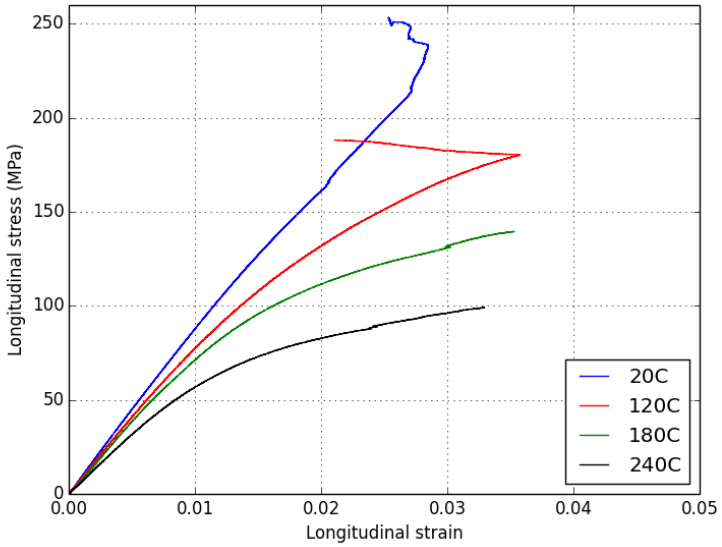

Figure 175 – Stress-strain curves of the compressive tests performed at 100 mm/min on 90° specimens for different furnace temperatures.

Results of this experimental investigation are plotted in Figure 175. As it was previously observed for the tests performed at 0,5 mm/min, the mechanical behaviour is strongly affected by the temperature increase. The apparent modulus and the maximum stress applied to the specimen decrease with respect to the temperature increase. The evolution of these two quantities is sum up in Table 42.

Temperature	**E_{22} [MPa]**	**σ_{max} [MPa]**
70°C	9240 ± 1%	254 ± 0,5%
120°C	8210 ± 2,3%	185 ± 1,6%
180°C	7890	141 ± 0,5%
240°C	6470	99

Table 42 – Results of the mechanical characterization performed at 100 mm/min for different environmental temperatures.

These values can be compared to those obtained for the tests performed at 0,5 mm/min summarized in Table 41. The comparison exhibits a loading rate effect on these two quantities. For example, an increase between 15% and 20% is observed for the maximum stress applied to the specimen between the two experimental investigations.

9.5.2. Tests on 0° specimens

Compressive tests on 0° laminates are difficult to perform, even more at high temperature. After a preliminary study, the previously used experimental setup has been modified to ensure an optimal application of the load

on the specimen. As shown in Figure 176, some parts have been added to ensure an optimal application of the load.

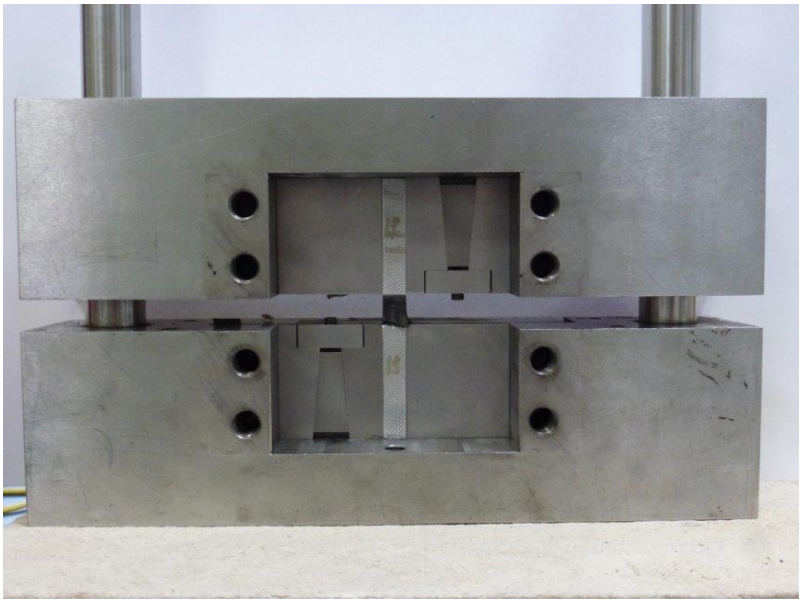

Figure 176 – Specific experimental setup used for the 0° compression tests.

This new experimental setup avoids the deformation of the specimen due to Poisson effect in the holder. As it can be noticed in Figure 176, aluminum tabs are glued to the specimens to apply the load.

For the tests performed at room temperature, the strain is measured with 120Ω YFLA2 strain gauges. The results obtained for the three tested specimens are plotted in Figure 177.

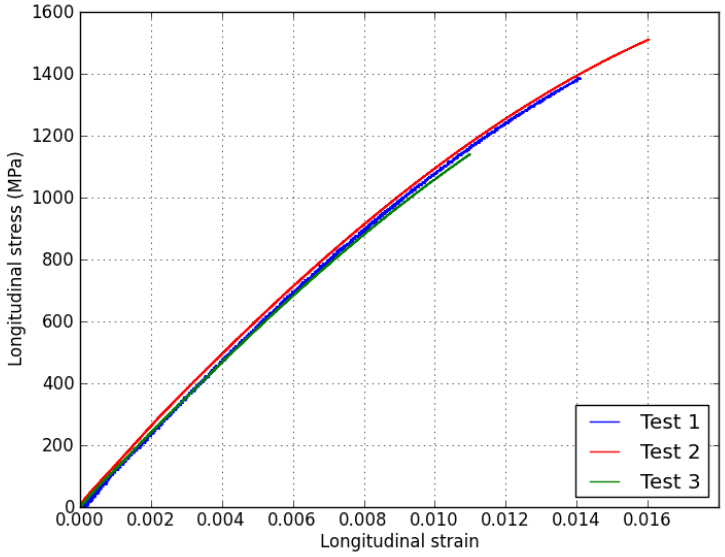

Figure 177 – Stress-strain curves of compressive tests performed on 0° laminates at room temperature.

For these tests performed at 0,5 mm/min, a longitudinal modulus of 122 GPa ± 4% is obtained. Regarding the maximum loading applied to the specimen a higher discrepancy is observed in Figure 177. A mean value of 1350 MPa ± 15% is obtained. The values given by the manufacturer are 119 GPa for the longitudinal compressive modulus and 1465 MPa for the maximum stress. The results obtained with the specific experimental setup proposed in this study are consistent with the properties given by the manufacturer.

To study the influence of temperature on these properties, a first experimental investigation has been performed with a furnace temperature of 120°C. In this case, the strain of the specimen is measured with a 350Ω strain gauge (QFLA-2-350-11). The results obtained for the three tested specimens are plotted in Figure 178. Tests have been also performed at 0,5 mm/min. In this case the value of the longitudinal modulus is not modified, a mean value of 121 GPa ± 1,2% is obtained. A decrease of the maximum stress applied to the specimen can be observed by comparing Figure 177 and Figure 178. For an environmental temperature of 120°C, a mean value of 1230 GPa ± 4,1% is obtained for the maximum stress applied to the specimen. Compared to the results obtained at room temperature, a decrease of 10% is obtained for the maximum stress at 120°C.

Tests at higher temperature (180°C and 240°C) have been performed but the results cannot be exploited due to premature failure outside of the free length of the specimen. At these temperatures, the stiffness of the aluminium tabs seems to decrease and allows deformation in the applied loading part of the specimen leading to premature failure. Stiffer tabs are currently tested and if new results are obtained, they will be added in the WP 7.1 final deliverable.

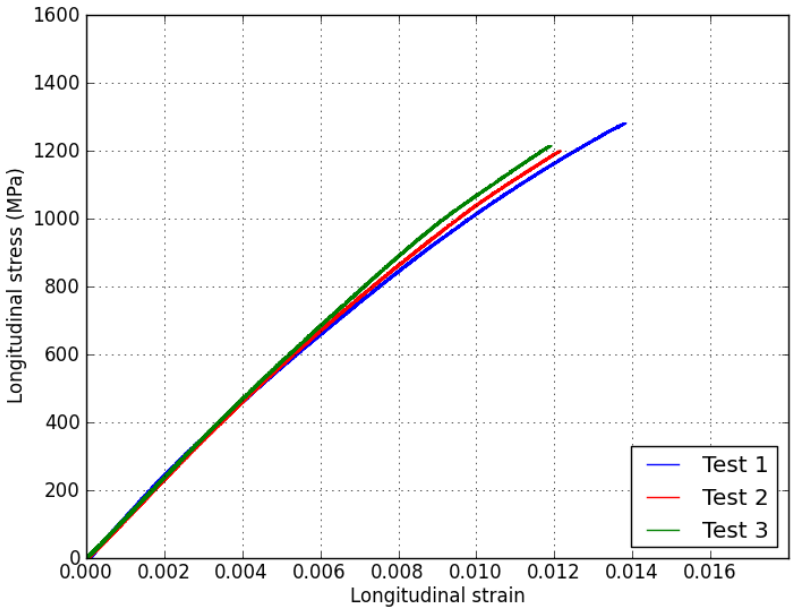

Figure 178 – Stress-strain curves of compressive tests performed on 0° laminates at room temperature.

10 ACHIEVEMENT OF THE TYRE DEBRIS IMPACT ONTO COMPOSITE PANELS

The objective of this specific study is to assess the stiffened panels of the virgin and charred material for the impact loading. For that purpose, an experimental procedure has been developed for tyre debris impact onto composite panels. The gas gun will be used to perform the tyre impact and the experimental design has been modified to set up displacement or strain field measurements during its impact. The modification allows measuring the field measurements using the Digital Image Correlation (DIC) method during the impact test (100 m/s <impact velocity <200 m/s).

10.1. Gas gun facility

The gas gun is the test facility used in Onera to perform the tyre impact. The gas gun facility (Photo 179) is constituted of a compressed air tank controlled by a high-speed electro-valve that is connected to a 50 mm diameter and 2 m long gun. A breech at the valve/gun interface permits the loading of the projectile and support. Windows placed along the protection box permits to film the projectile before and after its impact. The 400x400mm testing area is made of a vertical rigid wall on which is fixed the 2 points bending device. Impacts are performed on targets consisting in 450x330mm composite panels, which are freely supported on two 20mm diameter steel cylinders separated by a 350 mm distance.

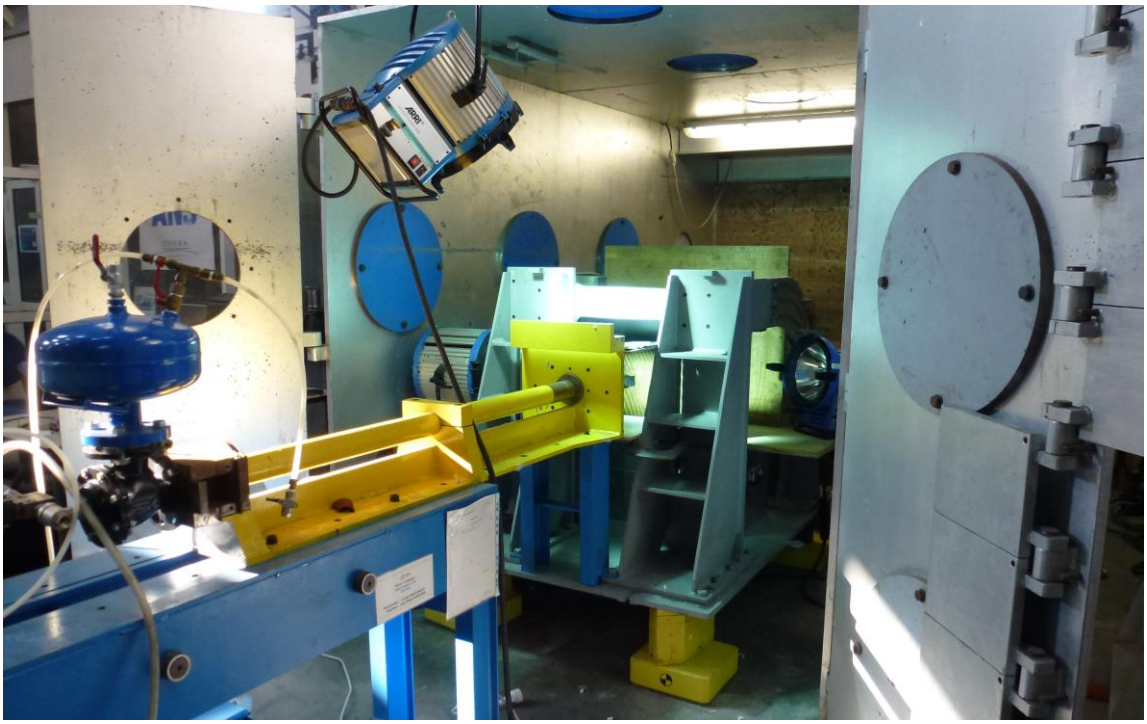

Photo 179: Test facility - Gas gun

10.2. Projectiles

The tyre debris projectile is fabricated from aircraft type of Michelin France (Figure 177). The projectiles consist of cylindrical shape (Ø=30mm – H=15mm). The average mass of the projectile was 40.2g (dispersion 1.9%) respectively. They are supported and guided in the gun thanks to foam sabots specifically designed so that the projectile does not suffer any damage during the acceleration phase up to the ejection from the gun. The end of the gun is equipped with a specific component which ensures that almost no debris of the sabot may follow the projectile and potentially perturb the measurements.

Figure 180: Type debris

10.3. Boundaries conditions of panel composite

The specimens dimensions of the composite panels are: height = 350 mm and width = 350 mm. The fixation enables a two-point bending response of the panel, and the bending distance is fixed at 300mm. The impact velocity will be defined according to expected damage up to 200 m/s thanks to pre-test analysis lead with aluminum panels T351 -2024. The impact will be always in the middle of the specimen.

10.4. Measurements during the test

10.4.1. Strain gauges measurements

All specimens are equipped with strain gauges bonded on the rear face, at a 30 mm distance from the plate center according to 2 perpendicular axes (horizontal and vertical) illustrated in the Figure 177.

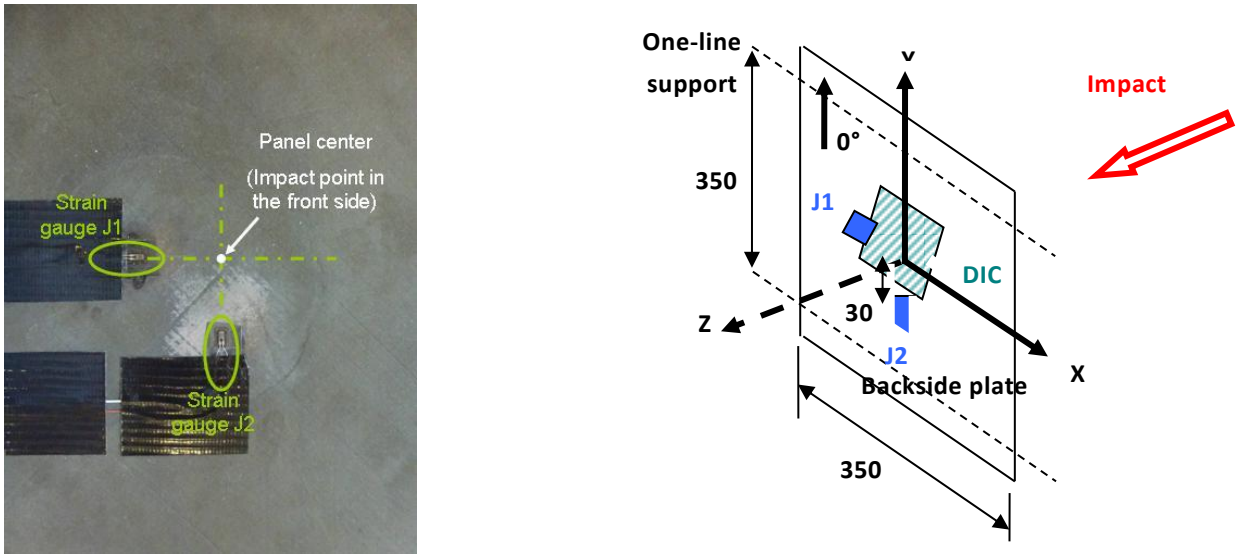

Figure 181: Strain gauge positions

Future Sky Safety has received funding from the EU's Horizon 2020 Research and Innovation Programme, under Grant Agreement No. 640597.

10.4.2. Displacement and strain fields measurements

The optical method is applied to measure the displacement and the strain fields during the impact thanks to the Digital Image Correlation (DIC) method in the impact tests.

Photo 182: Pattern in the specimen back side

Two cameras PHOTRON SAX are installed in the rear of the device, and allow capturing a part of panel back skin through this window. The frame rate is 36000 images par second with a resolution of 512x512 pixels. The panels are covered with a random black/white spray pattern, painted over their rear face (Figure 177). The DIC measurement area with this resolution is about 85mmx85mm. The strain gauges and the DIC measurement will be compared to assess the precision of the optical measurements.

10.4.3. Impact configuration

The velocity of the hail before impact is measured by 2 optical barriers, spaced by a 75 mm distance, which permit to acquire a start and stop time thus leading to a measure of the projectile velocity within an accuracy of around 0.1%. The kinematics of the projectile is captured with a Photron RS3000 camera, positioned horizontally, which are implemented with a frame rate of 30000 images par second and a resolution of 256x256 pixels. Video permits to control the initial configuration of the projectile (velocity, incidence) to evaluate the deformation of the target and eventually to follow the trajectory and measure the projectile velocity after impact (Figure 177).

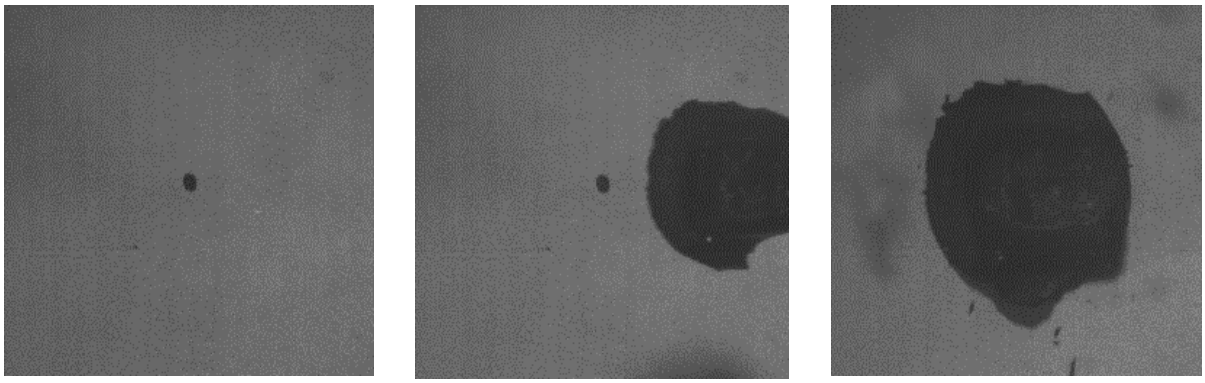

Figure 183 : Evolution of the tyre debris deformation

10.4.4.Non Destructive Inspection

The Non Destructive Inspection has been done after each impact with pulse thermography developed by Onera in order to highlight their internal damages. The Thermographic Signal Reconstruction (TSR) is based on emerging contrast. The principle of this method consists in selecting the best derivative images associated with every given depth range, in order to either qualitatively detect the defects. It has been proposed to project the three best polynomial coefficient images in an RGB basis, in order to build a unique "composite" image of the defects. For delamination-like defects, the best detection was obtained for degree n=7. For these tests, the panel after impact was pulse-heated by two Elinchrom flash lamps delivering a pulse of total energy 6 kJ in 4 ms. The temperature distribution (320×256 pixels) is recorded during 60 s at 100 Hz by a FLIR X6540sc MWIR gamme [1,5 – 5] mm. (Figure 177). The 1st logarithmic derivatives absolute contrast gives the detailed distribution of the delamination in the plate thickness. The panels' analysis in the front and rear sides

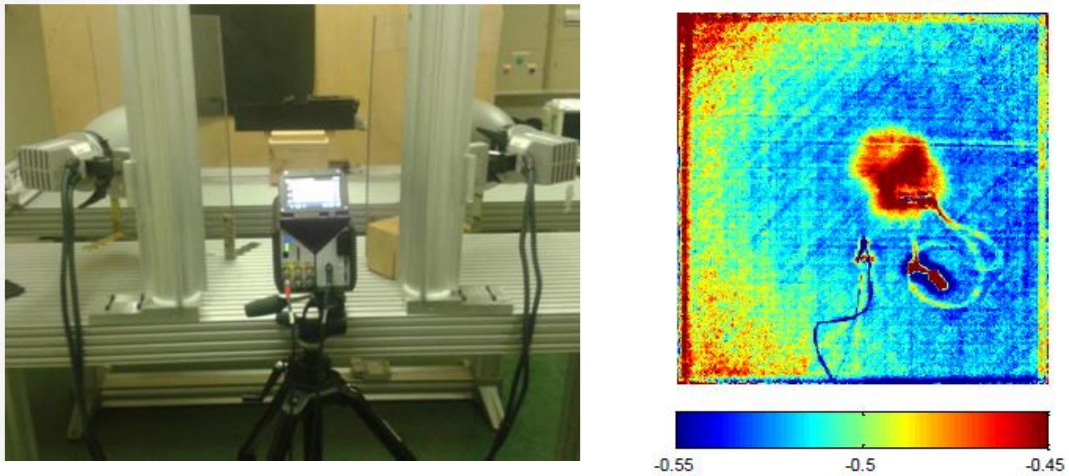

Figure 184: Illustration of the 1st logarithmic derivatives absolute contrast

10.4.5.Test matrix

The main parameters and tests results are summarized in the following table:

Test number	Velocity
V1_01	150 m.s-^{1} ± 1%
V2_01	171 m.s-^{1} ± 1%
V2_02	186 m.s-^{1} ± 1%
V2_02	185 m.s-^{1} ± 1%
V3_01	171 m.s-^{1} ± 1%

Table 43 : Synthesis of the high velocity impact tests tested

The velocity range from 110 to 200 m/s permits to identify the limit velocity without perforation. The objectives are to compare the impact behavior for the charred and virgin material by estimating the limit velocity without target perforation. The first tests were performed onto the flat panels with virgin material at different velocities impact. The panels are supported in the rigs with adhesive tape to avoid their fall.

10.4.6.Analysis of strain gauge measurement

The following figures illustrate the gauges measurements for all impact velocities (Figure 185 and Figure 185). The strain levels globally extend from 1% to -0.6% during the indentation phase (0 <t<100µs) and are globally similar for the both gauges (the laminate is isotropic). The first peak corresponds to the impact of the tyre projectile; it does not evolve with the impact velocity on the studied range. The negative peak of the strains results is caused from the compression wave propagation towards edges free of the panel.

Between 100µs <t<800µs, the tire is fully compressed and apply the load evenly (Figure 185). A global flexure of the panel appears and the strain levels increase with the velocity during this stage. After t>800µs, the panel oscillates and returns to its equilibrium position after about 10 ms (Figure 186).

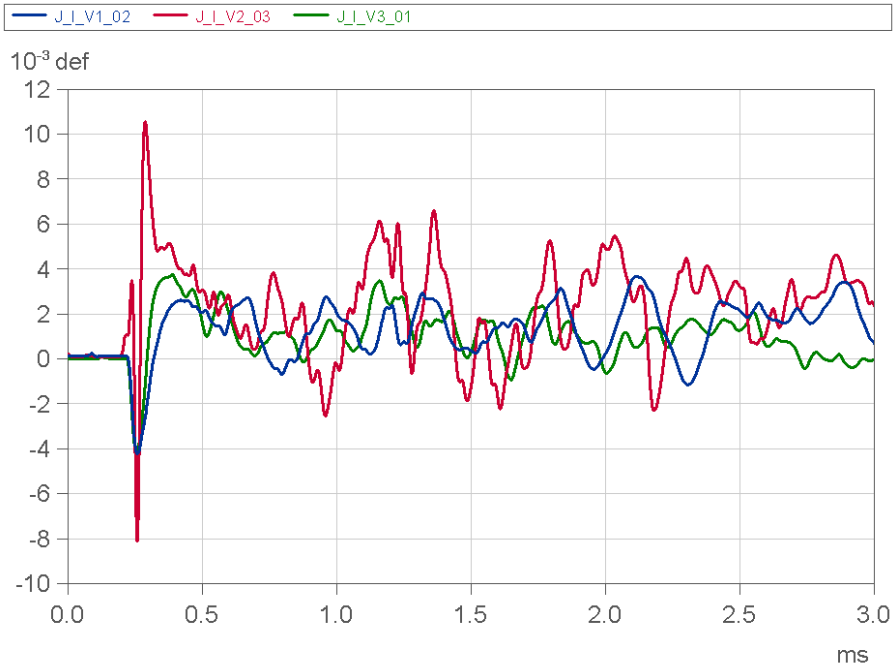

Figure 185: Strain gauges measurements (gauge J1)

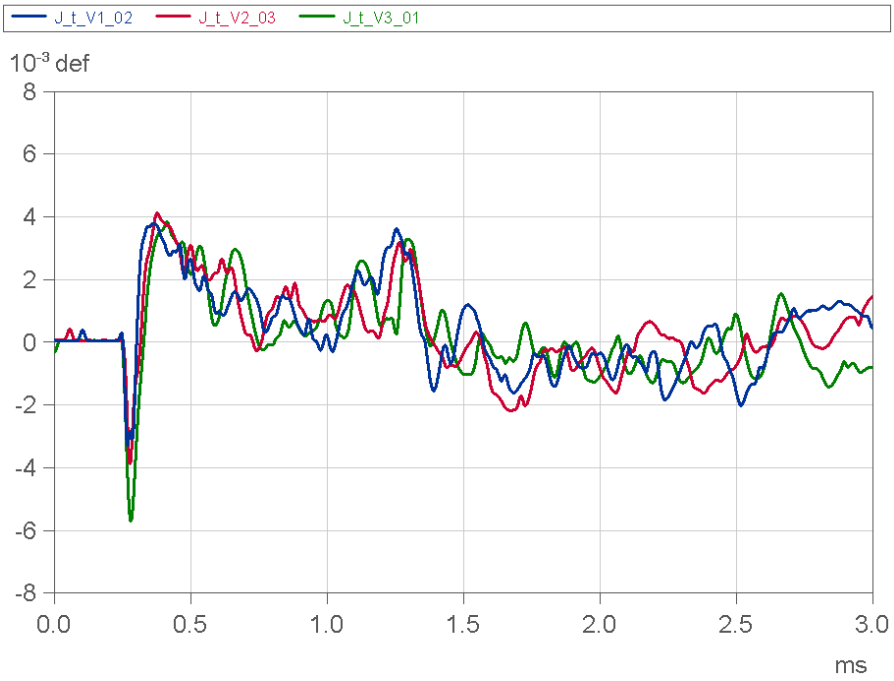

Figure 186: Strain gauges measurements (gauge J2)

10.4.7.Analysis of fields displacement-strain (DIC)

The fields' displacements measurements are computed thanks to the Digital Image Correlation (DIC) method during the test. This method allows measuring the displacement field in the normal direction of the panel. The displacement profile shows a sharp deformation at the apex of the impact zone (Figure 187). The strains obtained by the DIC and the gauges have been compared. A strong correlation between both kinds of measurements is demonstrated. The analysis of the strain and displacement fields shows a first indentation phase on the composite in contact with the projectile. Then a wave propagates from the impact point on the composite structure. This phenomenon appears clearly using the strain fields by the DIC method, while strain gauges do not. After the equilibrium, the panel is subjected to a bending dynamic load which is measured by the DIC method. Such results are illustrated for an impact velocity of 185m/s. It is observed that the maximum deflection of the composite structure always appears during the bending phase.

V =150 m/s (Test V1_02)	**V =171m/s (Test V3_01)**	**V =185 m/s (Test V2_03)**
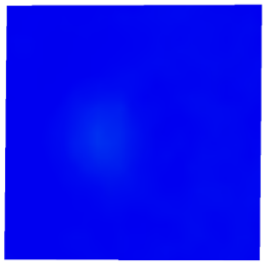		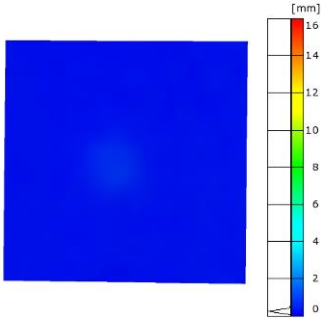
t=0 ms		
	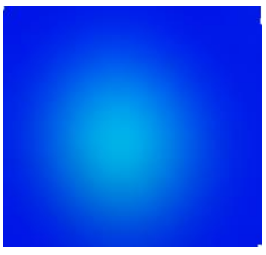	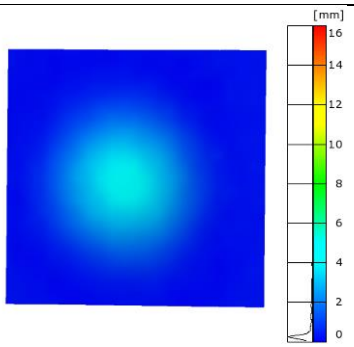
t=28 µs		

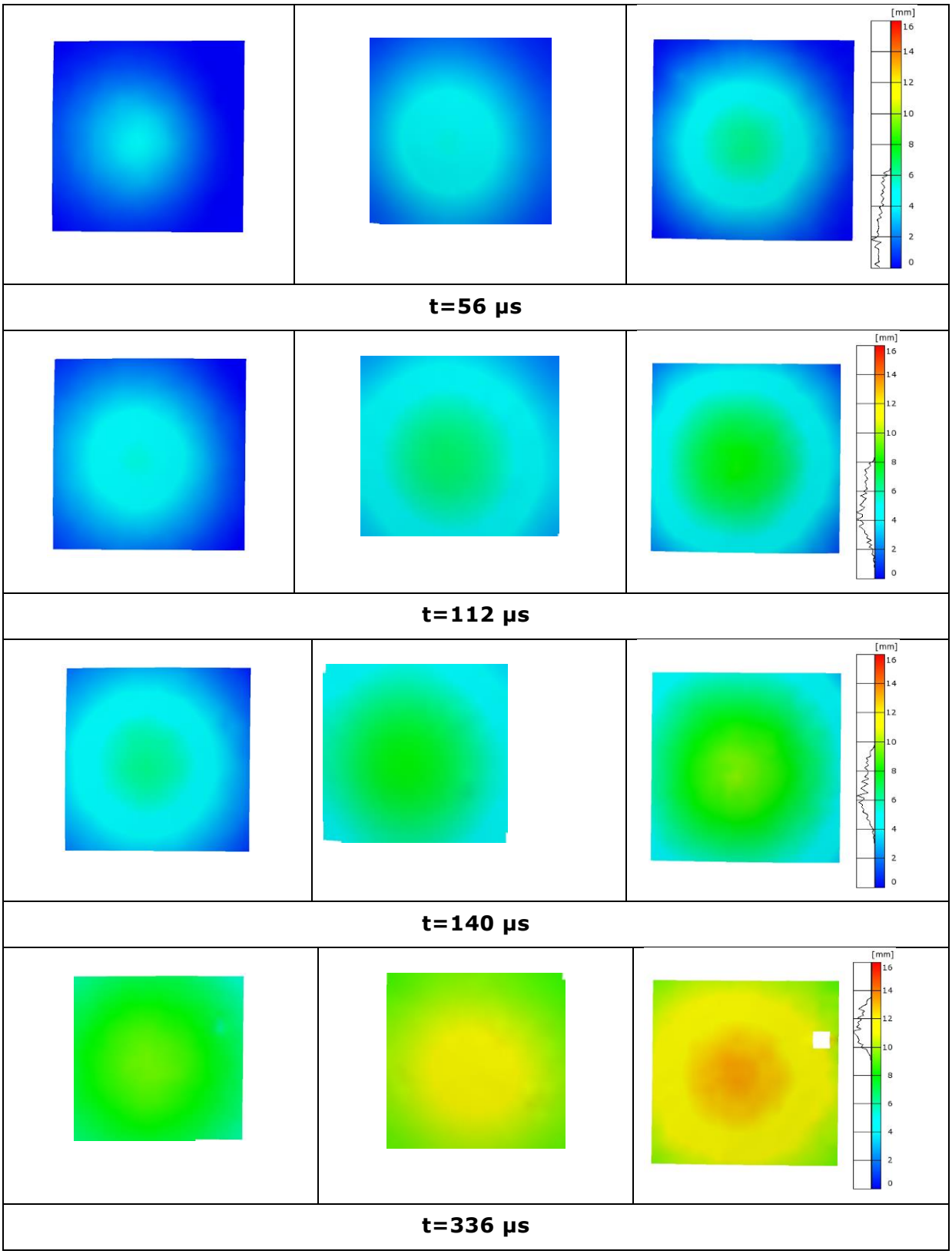

Figure 187: Analysis of the z-displacement field on the flat panel

10.4.8.Analysis of the CND controls for the panel target

All flat panel targets were controlled in order to identify their damage distribution. The following figure shows the shape of the delaminated areas. The damage increases as velocity rise. For the low velocities (v<150m/s, there is no apparent damage in the thickness. Damages s under the projectile are observed, and caused by the wave propagation in the panel thickness. For the higher velocities, damages under the striker are followed by delamination on an important area due to the flexure of the panel.

V =150 m/s (Test V1_02)	**V =171m/s (Test V3_01)**	**V =185 m/s (Test V2_03)**
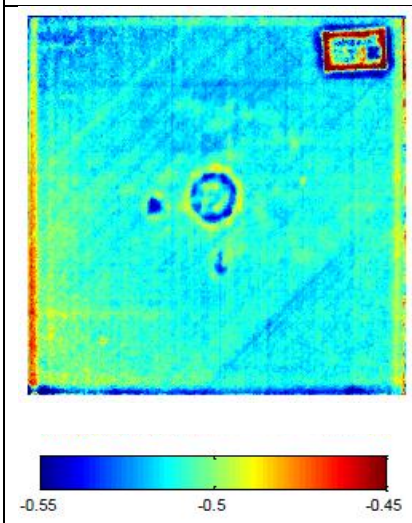	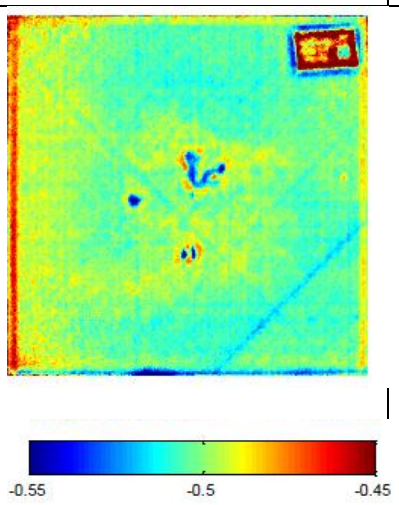	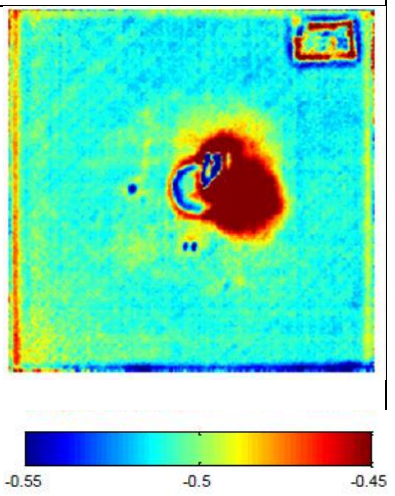
Almost no damage	*Some damage located in the surface ply*	*Damage and delamination across the thickness*

Figure 188: Shape and dimension of the damages area for flat panel

11 AIRBUS D&S EXPERIMENTAL INVESTIGATION

11.1. Test campaign

This report contains thermal characterization results for M21/T700 panels.

11.1.1. Characterization of thermal parameters at high temperature

EADS CASA has developed an internal characterization procedure validated through fire tests in order to obtain emissivity, conductivity, specific heat and in-plane diffusivity. Material involved in the program should be characterized following this procedure at Getafe facilities. The range to be characterized should cover from RT to 1100ºC. Thermal response of the material based on the state of degradation produced by the temperature from the thermal properties of the material.

The method for the characterization is an adaption of the classical Flash Method [17], based on the study of the evolution of temperature of the coupon when submitted to a controlled energy pulse. This method permits the extraction of thermal properties through the different degradation states.

With the proposed test the following properties will be obtained, both for as-received material and degraded:

- α (m2/s) Coefficient of thermal diffusivity.
- ρCp (kg/m3) Volumetric specific heat at constant pressure
- k (w/m K) Thermal conductivity coefficient Derived parameter: $\propto = \frac{\mathbf{k}}{\boldsymbol{\rho Cp}}$
- ε Emissivity (separate from flash method)

Through the direct application of the procedure developed by Airbus D&S these thermal properties of the materials can be determined in a non-intrusive way by means of the application of infrared technology.

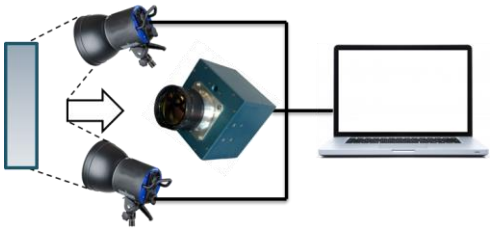

Theoretical background of this method is shown herein [17]:

At the rear surface, where $x = L$, the temperature history can be expressed by:

$$T(L,t) = \frac{Q}{\rho C L}\left[1 + 2\sum_{n=1}^{\infty}(-1)^n \cdot exp\left(\frac{-n^2\pi^2}{L}\alpha t\right)\right] \quad \text{(X1.6)}$$

Two dimensionless parameters, V and ω can be defined:

$$V(L,t) = \frac{T(L,t)}{T_M} \quad \text{(X1.7)}$$

$$\omega = \frac{\pi^2\,\alpha t}{L^2} \quad \text{(X1.8)}$$

T_M represents the maximum temperature at the rear surface. The combination of Eq X1.6-X1.8 yields:

$$V = 1 + 2\sum_{n=1}^{\infty}(-1)^n \cdot exp(-n^2\,\omega) \quad \text{(X1.9)}$$

When $V = 0.5$, $\omega = 1.38$, and therefore:

$$\alpha = \frac{1.38 \cdot L^2}{\pi^2 t_{\frac{1}{2}}} \quad \text{(X1.10)}$$

or:

$$\alpha = 0.1388\,\frac{L^2}{t_{\frac{1}{2}}} \quad \text{(X1.11)}$$

where $t_{½}$ is the time required for the back surface to reach half of the maximum temperature rise.

This expression is used in the case of ideal case without convection loses. In case of having convection an estimation of its effect must be taken into account in order to correct this deviation.

Volumetric Specific heat is obtained with the total energy applied to the flash pulse, Q, the maximum temperature increment measured by the rear camera and the panel thickness, L.

$$c_p\rho = Q/LT_M$$

In order to carry out the determination of the thermal parameters of the panels, before and after the heating, Airbus D&S requested two samples of a size approximated of 300x300 mm.

Test	Specimen name	Orientation/Stack Sequence	Length [mm]	Width [mm]	Thickness [mm]
Laminate	Pyro 1	$(45/90/-45/0)_s$	300.0	300.0	2.1
Laminate	Pyro 2	$(45/90/-45/0)_s$	300.0	300.0	2.1

Table 44 – Characteristic dimensions of the specimens for thermic characterization

Figure 189 – Determination of thermal properties by means of adapted flash method

The determination of these properties is performed in an as-received configuration and in a partial degraded panel state after a fire exposition.

Figure 190 – Determination of thermal properties by means of adapted flash method

11.1.2. Standard Fire tests to establish fire test overall behavior

In order to evaluate the overall behavior of the material when submitted to flame a Standard Fire Test is performed with the requested panels. The fire tests will be performed according to specific normative applicable to aeronautic structures when submitted to fire:

1- ISO 2685:1998(E): “Aircraft- Environmental test procedure for airborne equipment – Resistance to fire in designated fire zones”. [12]
2- FAA'S ADVISORY CIRCULAR Nº 20-135: “Power plant Installation and Propulsion System Component Fire Protection Test Methods, Standards and Criteria”. [13]

Figure 191 – Fire Test performed with calibrated flame and monitoring equipment

In order to carry out the determination of the thermal parameters of the panels, before and after the heating, Airbus D&S requested two samples of a size approximated of 300x300 mm.

Test	Specimen name	Orientation/Stack Sequence	Length [mm]	Width [mm]	Thickness [mm]
Laminate	Pyro 3	$(45/90/-45/0)_s$	690.0	440.0	2.1

Table 45 – Characteristic dimensions of the specimens for FIRE Tests

Standard fire test conditions for this test are:

Test conditions	Value
Fire Duration	15 min
Wind Airspeed	0 kts
Load	0 (daN)
Vibration	0 Hz
Purpose	DEVELOPMENT
Specimen Installation	VERTICAL POSITION
Test Procedure	[15, 16]

Table 46 – Test conditions

11.1.3. Instrumentation

The following thermographic equipment is used for the test realization:

Specifications	FLIR A 325	SC4000 HS	Thermosensorik 320 S
Espectral band	7.5 – 13 ⍰m	3 – 5 ⍰m	0.9 – 1.7 ⍰m
Detector	microbolom. VO_x	InSb	InGaAs
Resolution	320x240	320 x 256 (81920)	320 x 256
Pixel Pitch (⍰m)		30	
Cooling	Not refrigerated	Stirling cycle (77 K)	Thermoelectric (298 K)
Focal Distance	18 mm	25 mm (50 y 100 mm)	50 mm
Number F (F/#)	1.3	2.3	2.0
Instantaneous Field of view (mrad)	1.36	1.0 (0.5 y 0.25)	
Field of view		21.7º V x 17.5º H (25mm)	
Temperature Range	-20 - 1200 ºC		
Dynamic range	15 bits	14 bit	12 bit
Digital Output	Ethernet	Ethernet	LVDS
Transfer rate	Max 60Hz	400 fps @ full frame	150 fps @ full frame
Filter	9,518 - 9,653 µm	3.5 - 4 µm	
Portafilter			4 interchangeable filters, 30 fps per filter
Salida de vídeo			Vía VGA
Trigger I/O			TTL

Future Sky Safety has received funding from the EU's Horizon 2020 Research and Innovation Programme, under Grant Agreement No. 640597.

11.2. Test results

11.2.1. Characterization of thermal parameters at high temperature

The results for M21 /T700 panel tests are summarized in the following table and figure:

Thermal Property	Units	Degradation	M-21/T700	Epoxi [18]
α	m^2/s	As received	5,426E-07	4.58E-07
		Degraded	3,034E-08	1.02E-07
k	W/m·K	As received	0,6887	0.67
		Degraded	0,0621	0.12
ρ·CP	$(J/(m^3 \cdot K))$	As received	1,268E+06	1.55E+06
		Degraded	9,648E+06	1.16E+06
ε		As received	0,965	0.9
		Degraded	0,99	0.99
CP (ρ as received)	J/(kg·K)	As received	901	1050.9
		Degraded	1471	786.5
Transition Temperature Range	ºC	As received	270	300
		Degraded	340	400
ρ	kg/m^3	As received	1407,3	1474.9

Table 47 – Test results

Diffusivity: Conductivity: Volumetric specific heat:

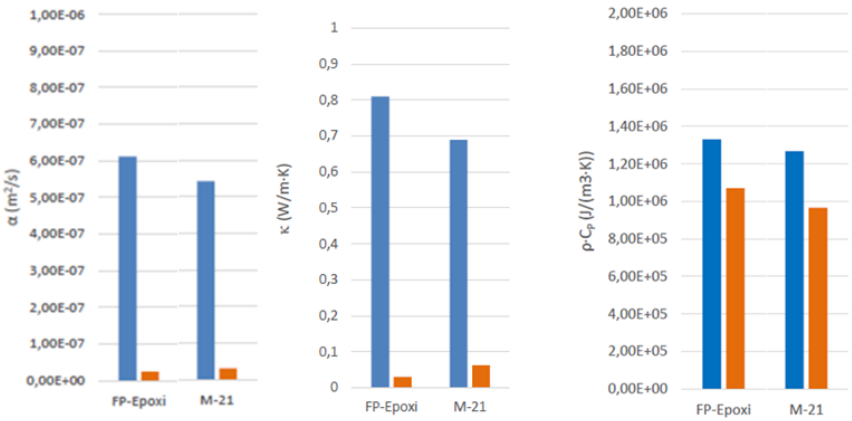

Figure 192 – Panel after standard fire test

Similar results in terms of diffusivity and specific heat have been observed in relation to reference.

11.2.2. Standard Fire tests

11.2.2.1. Calibration

The M21/T700 Specimen has been burnt from a distance of 200 mm instead of 100 mm as stated in [12], in order to have a good frontal view of the panel by the thermal cameras. For this reason, the temperature and the power of the flame with the nozzle at a distance of 200mm from calibration devices has been measured, in addition to calibration measurements.
The resulting applied power heat has been slightly lower than in a pure standard fire test:

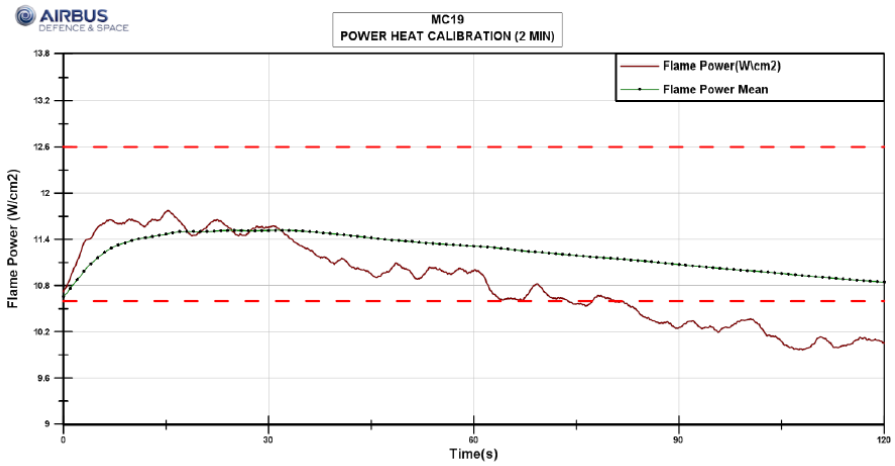

HEAT FLUX DENSITY (W/cm2)		
MAXIMUM	ARITHMETIC MEAN AFTER 30 SEC	TOTAL ARITHMETIC MEAN
11.77	11.52	10.84

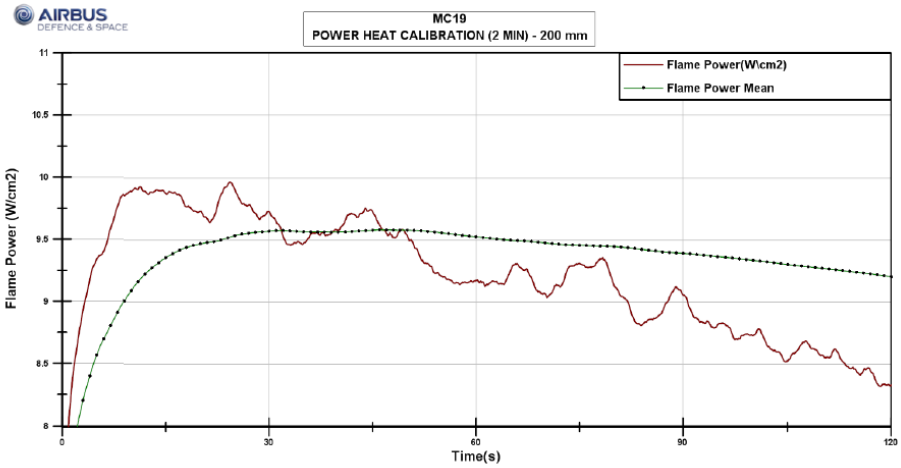

HEAT FLUX DENSITY (W/cm2)		
MAXIMUM	ARITHMETIC MEAN AFTER 30 SEC	TOTAL ARITHMETIC MEAN
9.97	9.59	9.21

Figure 193 – Calibration heat flux at 100mm and 200mm

11.2.2.2. Thermography results throughout the test

Thermographic results during standard fire test of the M21/T700 specimen are depicted in the next figures (time step shown in each figure). Fire tests lasts for 15 min, (900s) from the flame initiation moment up to flame shut down. Some frames have been included after flame out to monitor specimen cool down.

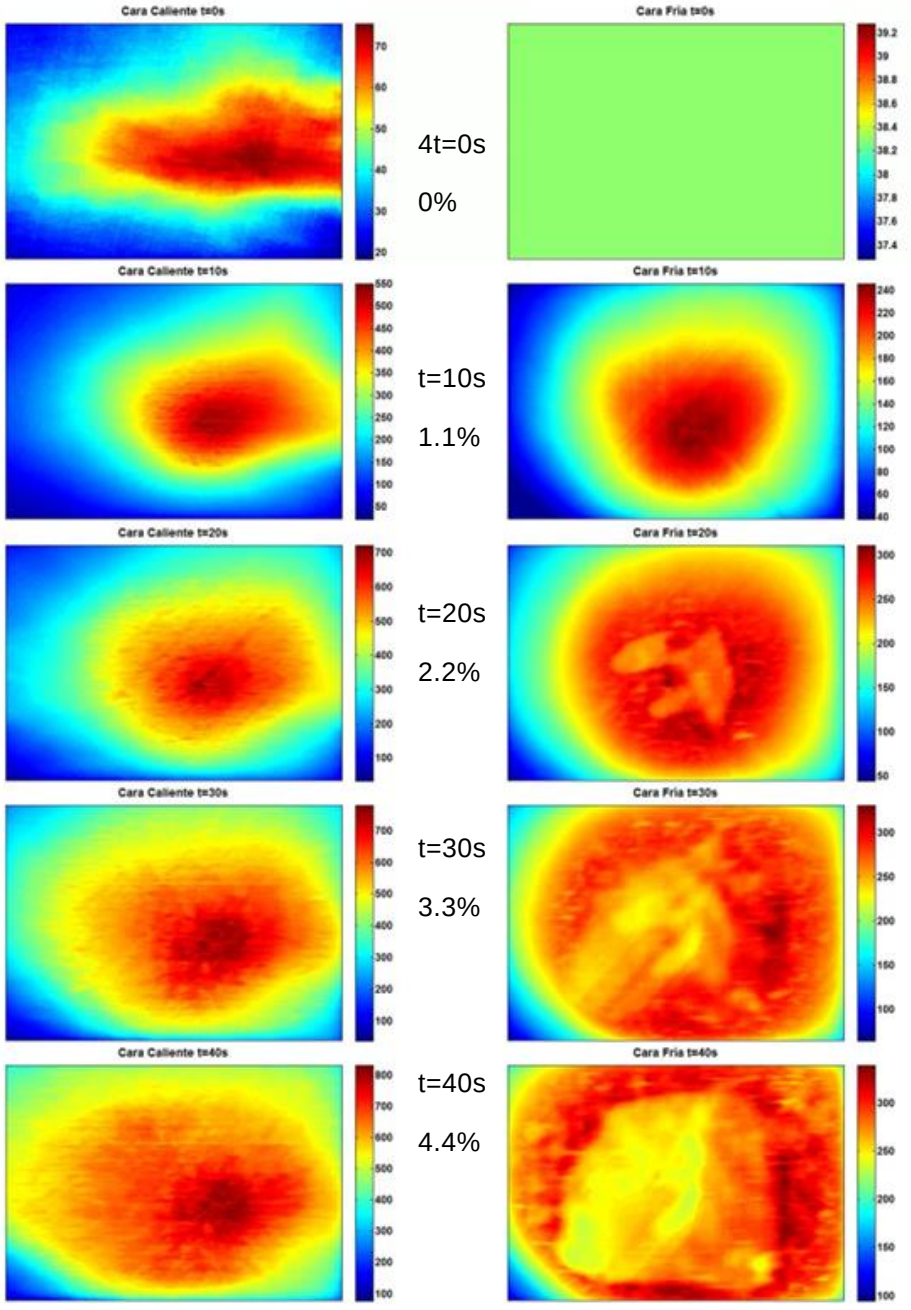

Figure 194 – Hot (left) and cold face(right) temperature plot throughout the test (1)

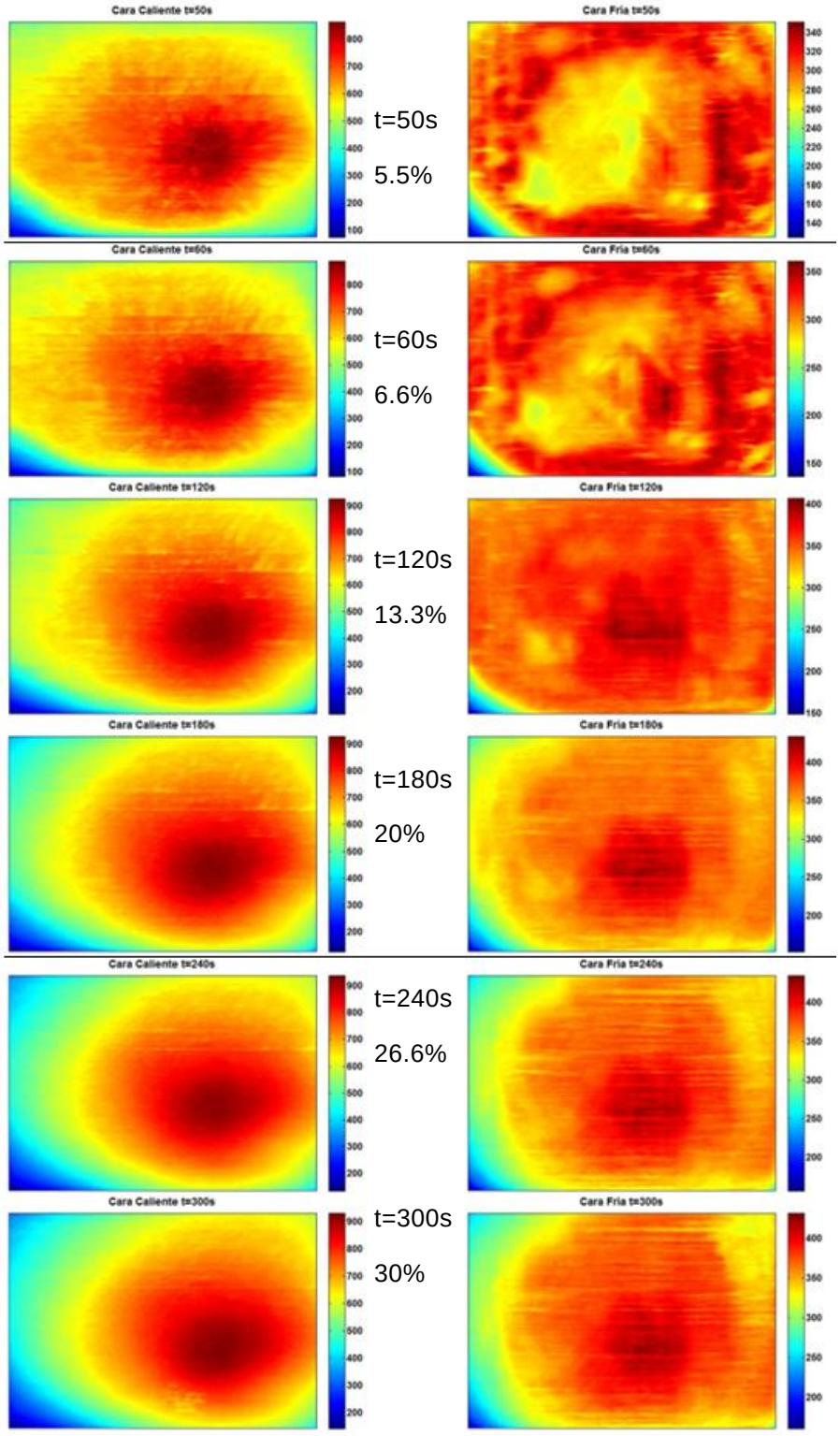

Figure 195 – Hot (left) and cold face(right) temperature plot throughout the test (2)

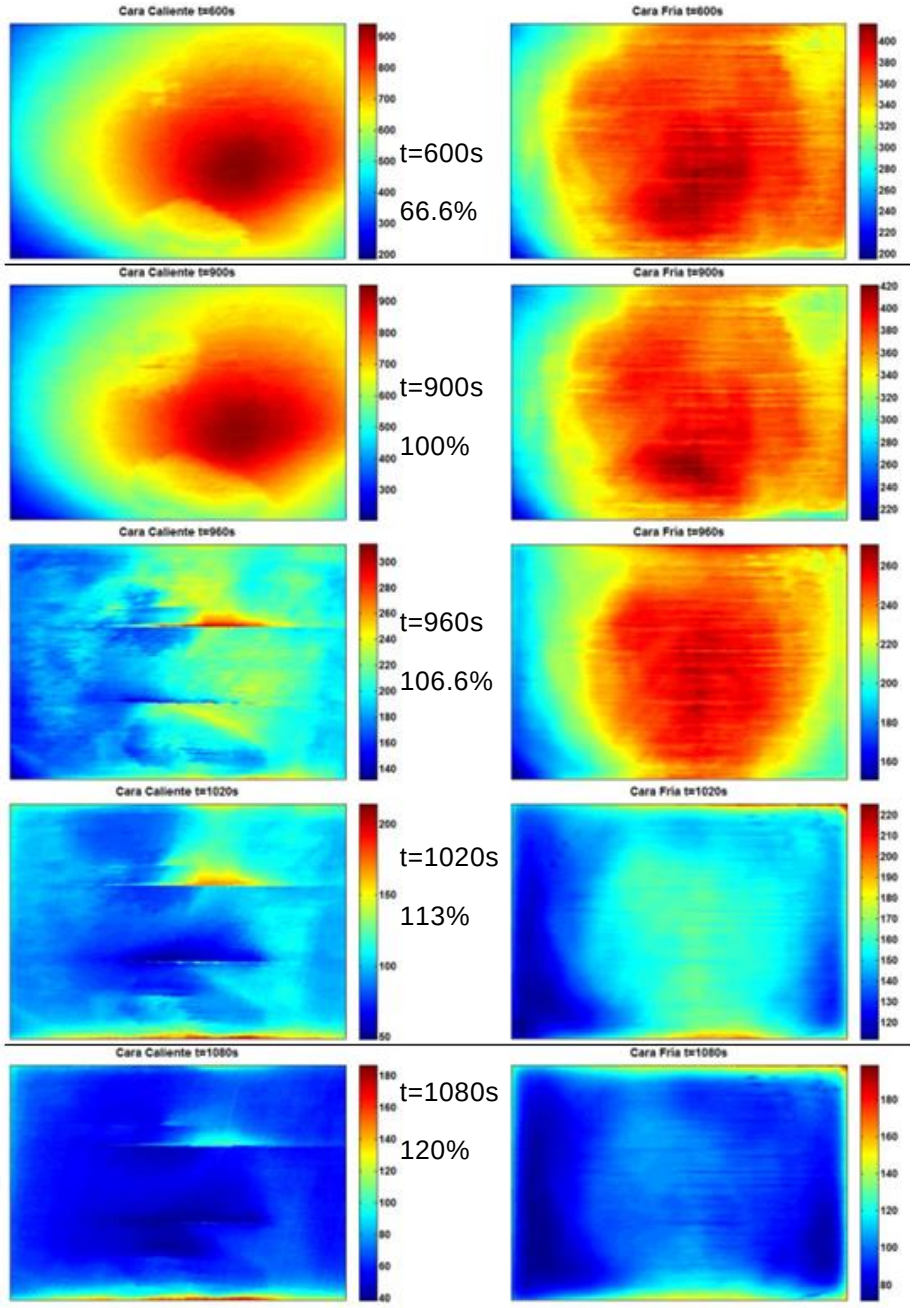

Figure 196 – Hot (left) and cold face(right) temperature plot throughout the test (3)

Figure 197 – Panel after standard fire test (Hot face, RHS; Cold Face LHS))

The summary of obtained temperature and time s to stationary states is the following:

Thermal Property		**Units**	**M21/T700**	**Epoxi [18]**
98% Temperature Percentile in Hot Face	$T_{Hot\ face98\%}$	ºC	915	917
Time to reach $T_{Hot\ face98\%}$	t($T_{Hot\ face98\%}$)	s	510	475
Cold face temperature at t($T_{Hot\ face98\%}$)	$T_{Cold\ face98\%}$	ºC	396	388
98% Temperature Percentile in Cold Face	$T_{Cold\ face98\%}$	ºC	410	412
Time to reach $T_{Cold\ face98\%}$	t($T_{Cold\ face98\%}$)	s	185	-
Stationary temperature difference between hot and cold faces	ΔT_{HF-CF}	ºC	517	496
Std Deviation in ΔT_{HF-CF}		ºC	5	5
Time to reach stationary difference		s	70	100

Other relevant information:

- There was a high emission of fume after flame application
- The flame did not pierce the panel during the test.
- It can be observed a small separation between fibers on flame application panel side
- It can be observed that panel first ply direction is horizontal whilst it's supposed to be at 45º. Possible laminate stacking sequence error or 0º direction mismatch.

12 CONCLUSIONS

Future Sky Safety is a Joint Research Programme (JRP) on Safety, initiated by EREA, the association of European Research Establishments in Aeronautics. The Programme contains two streams of activities: 1) coordination of the safety research programmes of the EREA institutes and 2) collaborative research projects on European safety priorities.

This deliverable is produced by the Project P7 “Mitigating Risks of Fire, Smoke and Fumes”, and belongs to the first work package, aiming at improving characterization capabilities and understanding with respect to the fire and high temperature behaviour of primary structure CFRP materials. Test results from a second batch of T700/M21 tests are presented in this report.

The objective of FSS P7 work package WP7.1 “Understanding and characterising the fire behaviour of primary structure composite materials (epoxy resins, standard CFRP)” is to enhance knowledge concerning the fire behaviour and performance of CFRP primary structure composite materials, in order to better predict safety and survivability issues in case of fire incident or post-crash situation. Such predictions rely on physical models and numerical tools which need to be developed based on exhaustive materials (characterisation) and components (validation) experimental testings. Moreover, WP7.1 produces a comprehensive experimental database for a reference material to be shared by the European research community as a basis for material model development of the fire behaviour and degradation of CFRP materials. The T700GC/M21 material has been proposed to be used in this WP7.1 because a lot of published results already exist about its standard mechanical behaviour which the project can build on. For this purpose, existing testing protocols have to be adapted, improved or invented. FSS P7 deliverable D7.1 “Plan of Experiments – Primary Structures Materials – Final Requirements, Selection and Specification of Materials and Tests” [1] includes a list of complementary tests which could be developed and performed to complete an already existing database with respect to:

- Mechanical and thermo-mechanical properties of virgin and charred material,
- Dynamic degradation phenomena (incl. ignition of combustible gases inside the CFRP laminate) during the fire exposure time,
- Fire resistance of damaged composite panels to direct exposure to flame impact.

This report presents the test results from a second batch of T700/M21 tests.

In the last past years, ONERA has developed a test facility to provide thermo-physical properties characterisation of anisotropic materials. Especially, it can assess simultaneously the specific heat and the 3 main components of the thermal conductivity tensor as a function of temperature. It is based on thermographic measurements of the material thermal response subjected to a pure radiative laser heating. The test facility was carried out on the selected T700GC/M21 CFRP material that was studied in 2 stacking sequences to identify properties at the virgin state (i.e. below glass transition and pyrolysis thresholds) and above.

In precedent studies, the thermal decomposition of epoxy matrix reinforced by carbon fibre composite materials had been performed at ONERA. Three main chemical reactions had been identified: pyrolysis of the matrix, oxidation of the char produced by the pyrolysis of the matrix and oxidation of the fibres. To succeed in, Thermo Gravimetric Analysis (TGA) and Differential Scanning Calorimetry (DSC) experiments had been carried out in order to identify a thermal degradation model adapted to composite materials. In this deliverable, the complementary TGA results for the material manufactured and provided by CEiiA are under the scope.

Heating rates of TGA measurements have also been extended to reach thermal loads of the same order of magnitude than those experienced during a fire event. Kinetic modelling assessed at low heating rates is confronted to high heating rates measurements and shows a significant local thermal non-equilibrium that requires measurements to be analysed out of the conventional thermally thin assumption.

Thermal properties of the CFRP had been assessed experimentally in the previous deliverable for the virgin state of the material onto a temperature range where any chemical reaction is avoided. Complementary TGA measurements have provided kinetic modelling for defining a preparation protocol to reach a fully charred (pyrolysed) state of the material. The protocol has been successfully carried out and thermal characterisations of the charred state have been performed and are presented in this deliverable.

Laser induced decomposition has been developed at ONERA to analyse the thermal response of composite material subjected to a pure radiative heat load. Such original approach can provide relevant information about the material behaviour without any uncertainty regarding the heat flux distribution and its nature. Actually, a fire event induces a heat flux at the material surface the time and space distribution of which is very difficult to assess. Using a stable and coherent heat source provides a very accurate heat flux on the material surface so that the thermal response can be analysed confidently. The experimental facility offers also well controlled boundary conditions, non-intrusive and accurate temperature measurements and avoids any combustion of volatiles that can affect the material behaviour. Results are presented for different heat flux magnitudes and different laser exposure periods.

The mechanical and thermo-mecanical tests performed in this study give access to the evolution of various material properties with the increase of the temperature. These properties are needed in order to be able to model the thermo-mechanical behaviour of composite materials with the temperature increase. Innovative experimental setups and protocols have been used in this project in order to obtain these properties at high temperatures as for example the inject test bench.

To conclude, this report contributes in this project in the production of a comprehensive experimental database for a reference material (T700GC/M21) which can be shared by the European research community as a basis for material model development of the fire behavior and degradation of CFRP materials.

13 REFERENCES

[1] M. Oliveira et al., Future Sky Safety, Plan of Experiments - Primary Structures Materials - Final Requirements, Selection and Specification of Materials and Tests, D7.1, September 2015.

[2] E. Deletombe et al., Future Sky Safey, Project Plan P7 - Mitigating the risk of fire, smoke and fumes (V3.0), D8.1 - Appendix P7, September 2015.

[3] P. Reulet and G. Leplat. An inverse method for experimental determination of temperature dependent thermal conductivities and specific heat of orthotropic materials. In *ITCC 2011 - International Thermal Conductivity Conference*, Chicoutimi, Quebec, CANADA, 2011.

[4] G. Leplat and V. Biasi. Experimental and numerical thermal response analysis of laser-induced composite decomposition. In *FRPM 2015 - 15th Fire Retardancy and Protection of Materials meeting*, Berlin, Germany, 2015.

[5] P. Beauchene, V. Biasi, C. Huchette, G. Leplat, G. Roger, PRF MADMAX : Caractérisation expérimentale des propriétés physiques du T700M21, *Internal Onera Report (in french) RT 2/21100 DMAE/DMSC,* 2016

[6] S. Feih, A. P. Mouritz, Tensile properties of carbon fibres and carbon fibre–polymer composites in fire. *Composites Part A: Applied Science and Manufacturing.* 43, 765–772, 2012

[7] N. Rose, M. Le Bras, S. Bourbigot, R. Delobel, B. Costes, Fire Retardant PolymersComprehensive study of the oxidative degradation of an epoxy resin using the degradation front model. *Polymer Degradation and Stability.* 54, 355–360, 1996

[8] A. De Fenzo, C. Formicola, V. Antonucci, M. Zarrelli, M. Giordano, Effects of zinc-based flame retardants on the degradation behaviour of an aerospace epoxy matrix. Polymer Degradation and Stability. 94, 1354–1363, 2009

[9] C. Huchette, Sur la complémentarité des approches expérimentales et numériques pour la modélisation des mécanismes d'endommagement des composites stratifiés *thesis, Université Paris 6,* 2005.

[10] G. Leplat, A. Deudon, C. Huchette, G. Portemont, E. Deletombe, G. Roger, J. Berthe. Future Sky Safety – D7.4 Primary structure materials – Test Results (first batch), 2016.

[11] ASTM D7905, Standard Test Method for Determination of the Mode II Interlaminar Fracture Toughness of Unidirectional Fiber-Reinforced Polymer Matrix Composites, 2014

[12] ISO 2685:1998(E): “Aircraft- Environmental test procedure for airborne equipment – Resistance to fire in designated fire zones”.

[13] FAA'S ADVISORY CIRCULAR Nº 20-135: “Power plant Installation and Propulsion System Component Fire Protection Test Methods, Standards and Criteria”

[14] TAE-T-NT-160047 “MC19 FIRE TEST RESULTS”

[15] SPO705382_ Issue1.4: Airbus Fire Test Generic Specification

[16] NT-0-SGL-05001_IssueC: Fire Test Laboratory Procedure

[17] ASTM E1461 – 13 “Standard Test Method for Thermal Diffusivity by the Flash Method”

[18] UC3M D16.2 “Characterization of thermo-mechanical behavior of composite materials in fire and empirical determination of their properties”